



**A Systematic Methodology Enabling Marine
Engine Health Assessment by Employing
First-Principles Digital Twins**

Konstantinos - Marios Tsitsilonis

A thesis submitted for the degree of Doctor of
Philosophy


MAY 2023

Declaration of Authenticity and Author's Rights

Declaration of Authenticity and Author's Rights This thesis is the result of the author's original research. It has been composed by the author and has not been previously submitted for examination, which has led to the award of a degree.

The copyright of this thesis belongs to the author under the terms of the United Kingdom Copyright Acts as qualified by University of Strathclyde Regulation 3.50. Due acknowledgement must always be made of the use of any material contained in, or derived from, this thesis.

Signed: Konstantinos - Marios Tsitsilonis



Date: 11th May, 2023

Acknowledgements

I would like to thank my highschool Physics and Mathematics teachers, Dr. L. Hristakos and Dr. K.A. Tsokos respectively, whose passion and dedication to science and education, continually inspired me throughout my academic journey. Furthermore, I would like to express my deepest gratitude to my supervisor, Prof. G. Theotokatos, for going above and beyond to support me in my academic as well as professional endeavours. Finally, I dedicate this thesis to both my parents, for their vision and perseverance enabled me to follow my dreams from a very young age.

Abstract

The maritime industry faces significant challenges due to its dependence on the global economy, stringent regulations, and harsh operating environment of ships. Inevitably, motivated by the advent of digitalisation, the ship's engines play a prominent role in addressing such challenges, considering that they are the largest energy consumer on board. Therefore, this drives the need for a systematic methodology incorporating digital twins, to enable the health assessment of marine engines.

This is achieved via a five stage systematic methodology, in which the first stage involves the setup and formulation of a thermodynamics model. In the second stage, this model is utilised in a rigorous calibration process along with minimal shop test data to develop the healthy conditions digital twin. In the third stage a novel approach considers an inverse crankshaft dynamics model to reconstruct the in-cylinder pressure curves employing Instantaneous Crankshaft Torque (ICT) measurements. In the fourth stage the inverse crankshaft dynamics model is employed in tandem with the thermodynamics model to configure the current engine conditions digital twin. In the fifth and final stage, the healthy and current conditions digital twins are utilised to benchmark the engine performance and assess the engine health.

The healthy conditions digital twin provides results of sufficient accuracy with less than 3% maximum error in the BSFC and peak in-cylinder pressure, considering a 4-stroke W9L46C and 2-stroke 6RTflex50 engines. Furthermore, the inverse crankshaft dynamics model reconstructs the in-cylinder pressures with errors just exceeding 5% for the W9L46C engine. Finally, the health assessment reveals a 2.1% average increase in BSFC, as well as 6.1% increase and 6.8% reduction in Exhaust Gas Temperatures (EGTs) and Indicated Mean Effective Pressures (IMEP) respectively, for the under-performing cylinders of the W9L46C engine.

The systematic methodology proposed successfully develops both healthy and current engine conditions digital twins, making novel use of ICT measurements as well as first-principles models for any engine type (4-stroke, 2-stroke) and configuration. Therefore a systematic approach which leads to quantified benchmarking is established, enabling effective health assessment of marine engines.

Research Output

Journal Papers

Tsitsilonis, K-M., Theotokatos, G., Patil, C., Coraddu, A. (2023). Health Assessment Framework of Marine Engines Enabled by Digital Twins. *International Journal of Engine Research*. <https://doi.org/10.1177/14680874221146835>

Tsitsilonis, K-M., & Theotokatos, G. (2021). A novel method for in-cylinder pressure prediction using the engine instantaneous crankshaft torque. *Proceedings of the Institution of Mechanical Engineers, Part M: Journal of Engineering for the Maritime Environment*, 236(1), 131-149. <https://doi.org/10.1177/14750902211028419>

Tsitsilonis, K-M., & Theotokatos, G. (2021). Engine malfunctioning conditions identification through instantaneous crankshaft torque measurement analysis. *Applied Sciences*, 11(8), [3522]. <https://doi.org/10.3390/app11083522>

Tsitsilonis, K-M., Theotokatos, G., Xiros, N., & Habens, M. (2020). Systematic investigation of a large two-stroke engine crankshaft dynamics model. *Energies*, 13(10), [2486]. <https://doi.org/10.3390/en13102486>

Conference Papers

Tsitsilonis, K-M., Theotokatos, G., & Coventry, A. (2021). Development of an intelligent marine engines health assessment system based on digital twins and data driven models. 33-46. Paper presented at *Annual Conference of Marine Technology 2021*, Athens, Greece.

Tsitsilonis, K-M., Theotokatos, G., & Habens, M. (2020). A modelling approach for predicting marine engines shaft dynamics. *In Proceedings of the International Naval Engineering Conference & Exhibition 2020 (Proceedings of the International Naval Engineering Conference & Exhibition; Vol. 2020)*. Institute of Marine Engineering, Science and Technology. <https://doi.org/10.24868/issn.2515-818X.2020.033>

Contents

List of Figures	vii
List of Tables	ix
Abbreviations & Nomenclature	xiii
1 Introduction	1
1.1 Maritime Industry Challenges & Outlook	1
1.1.1 Environmental Sustainability	1
1.1.2 Global Governance & Compliance	2
1.1.3 Technological Innovation	4
1.1.3.1 Technologies Availability in Other Industries	4
1.1.3.2 Barriers to Technological Innovation in Shipping	5
1.1.4 Maritime Industry Outlook	6
1.2 Aim & Objectives	7
1.3 Dissertation Layout	8
2 Literature Review	10
2.1 Machinery Insight & Management	11
2.1.1 Data & Energy Monitoring	11
2.1.2 Condition-Based Maintenance	12
2.1.3 Digital Twin Enabled Machinery Health Assessment	13
2.1.3.1 Critical Engine Measurements	14
2.1.3.2 Thermodynamics Models	16
2.1.3.3 Crankshaft Dynamics Models	17
2.1.3.4 Parameter Estimation Techniques	19
2.2 Research Gaps	21

3	Research Methodology	23
3.1	Thermodynamics Model	23
3.2	Healthy Conditions Digital Twin	24
3.3	Crankshaft Dynamics Models	25
3.4	Current Conditions Digital Twin	26
3.5	Engine Health Assessment	27
4	Thermodynamics Model	29
4.1	Thermodynamics Model Overview	29
4.2	System of Governing Equations	31
4.2.1	Single-Zone & Two-Zone Cylinder Models	31
4.2.1.1	Formulation	31
4.2.1.2	Description of Terms	35
4.2.1.3	Combustion Model	37
4.2.2	Turbocharger Model	38
4.2.3	Manifolds Model	41
4.2.4	Complete Formulation	43
4.3	Solution Method & Model Convergence	44
4.4	Model Input, Output & Assumptions	47
4.5	Calibration of Thermodynamics Model	49
4.6	Configuration of Current Conditions Digital Twin	52
4.7	Engine Health Assessment	53
5	Crankshaft Dynamics Models	57
5.1	Direct Crankshaft Dynamics Model	58
5.1.1	Lumped Mass Model Overview	58
5.1.2	System of Governing Equations	58
5.1.3	Engine Crankshaft Excitation Torques	61
5.1.4	Solution Methods for the Direct Crankshaft Dynamics Model	63
5.1.4.1	TR-BDF2 Numerical Scheme	64
5.1.4.2	Piecewise LTI Numerical Scheme	66
5.1.4.3	Harmonic Balancing Numerical Scheme	67
5.1.5	Model Convergence	69

5.1.6	Numerical Scheme Performance Quantification	71
5.1.7	Model Input, Output & Assumptions	73
5.1.8	Calibration of Direct Crankshaft Dynamics Model	75
5.2	Inverse Crankshaft Dynamics Model	77
5.2.1	Inverse Model Overview	77
5.2.2	In-cylinder Pressure Parametrisation	78
5.2.3	Sensitivity Equations & Extended Crankshaft Dynamics Model	82
5.2.4	Stability Analysis	84
5.2.5	Inverse Model Development	85
5.2.6	Inverse Model Verification Procedure	90
6	Reference System, Available Data, and Case Studies	93
6.1	Reference Systems & Available Data	93
6.2	Case Studies	96
7	Results & Discussion	98
7.1	Case Study 2(a): Healthy Conditions Digital Twin Calibration	98
7.2	Case Study 2(b): Healthy Conditions Performance Maps	101
7.3	Case Study 3(a): Direct Crankshaft Dynamics Model Solution Method Determination	103
7.4	Case Study 4(a): Direct Crankshaft Dynamics Model Calibration	107
7.5	Case Study 4(b): Inverse Crankshaft Dynamics Model Verification	109
7.5.1	Determination of Optimal Settings	110
7.5.2	Torsional Vibration Damper Coefficient Discrepancies	112
7.5.3	Noise in the Instantaneous Crankshaft Torque Measurements	114
7.5.4	Validation Utilising Instantaneous Crankshaft Torque Mea- surements	116
7.6	Case Study 4(c): Current Conditions Digital Twin Configuration & Performance Maps	118
7.7	Case Study 5(a): Derivation of Health Assessment KPIs & Maps	121
8	Final Remarks & Future Work	125
8.1	Case Studies Findings	125
8.2	Research Methodology Remarks	127

8.3	Novelty & Implications	128
8.4	Achievement of Aims & Objectives	130
8.5	Future Work	131
A	Derivation of Equations	154
A.1	Direct Crankshaft Dynamics Model	154
B	Reference Systems Data & Layout	157
B.1	W9L46C Reference System	158
B.2	1067LGBE Reference System	162
C	Measuring Equipment	164
C.1	In-cylinder Pressure Sensor & Analyser	164
C.2	Prototype High-Sample Rate Torquemeter	165
D	Experimental Measurements Rectification & Processing	167
D.1	In-Cylinder Pressure Rectification	167
D.2	Heat Release Curves	170
D.3	Instantaneous Crankshaft Torque	172
E	Optimisation Algorithms Results & Performance	173
E.1	Healthy Conditions Digital Twin Calibration	173
E.2	Direct Crankshaft Dynamics Model Calibration	175
E.3	Inverse Crankshaft Dynamics Model	177

List of Figures

1.1	GHG reduction pathway to achieve the Initial IMO Strategy.	2
2.1	Direct vs. inverse crankshaft dynamics models input/output.	18
3.1	Intelligent engine health assessment framework utilising digital twins.	28
4.1	Overview of the thermodynamics model.	30
4.2	Thermodynamics model convergence algorithm.	45
4.3	Thermodynamics model input and output.	47
4.4	Thermodynamics model calibration procedure.	50
4.5	Thermodynamics model configuration to current engine conditions. .	54
5.1	Overview of lumped mass model of typical marine shafting system. .	59
5.2	Direct crankshaft dynamics model convergence algorithm for time domain simulation.	70
5.3	Direct crankshaft dynamics model detailed input and output.	74
5.4	Overview of the inverse crankshaft dynamics model.	78
5.5	Inverse crankshaft dynamics model algorithm, used to reconstruct the in-cylinder pressure curves.	87
6.1	Measurement samples of the W9L46C reference system.	95
6.2	Measurement samples of the 10L67GBE reference system.	95
7.1	Performance maps of the W9L46C digital twin in healthy conditions.	101
7.2	Numerical schemes performance KPI for TR-BDF2 and piecewise LTI, with weight $w_{sol} = 10$	103
7.3	Numerical scheme performance KPI for Harmonic Balancing, with weight $w_{sol} = 10$	104

7.4	Comparison of 10L67GBE engine measured and simulated ICT at the flywheel	106
7.5	Direct crankshaft dynamics model calibration of W9L46C reference system for 2,949 kW at 401 RPM.	108
7.6	FRF for W9L46C reference system of flywheel response per unit of excitation force in the cylinders.	109
7.7	Sample operating points of simulated measurements utilised for the verification of the inverse crankshaft dynamics model for the W9L46C engine.	110
7.8	Inverse crankshaft dynamics model KPI for the first part of the verification procedure.	111
7.9	Inverse crankshaft dynamics model convergence utilising the optimal settings.	112
7.10	Inverse crankshaft dynamics model performance with torsional vibration damper coefficient discrepancies.	113
7.11	Inverse crankshaft dynamics model performance with noise in the input ICT.	115
7.12	Inverse crankshaft dynamics model performance using measured ICT for 2,949 kW at 401 RPM.	117
7.13	Measured and reconstructed in-cylinder pressures by the inverse crankshaft dynamics model for validation of the inverse crankshaft dynamics model, at operating point of 5,491 kW at 450 RPM.	118
7.14	Performance maps of W9L46C engine current conditions digital twin.	120
7.15	BSFC percentage difference of current engine conditions with reference to healthy conditions of W9L46C engine.	121
7.16	Cylinder EGT percentage difference of current engine conditions with reference to healthy conditions of W9L46C engine.	122
7.17	Cylinder IMEP percentage difference of current engine conditions with reference to healthy conditions of W9L46C engine.	123
B.1	Lumped mass model layout of W9L46C reference system.	161
B.2	Lumped mass model layout of 10L67GBE reference system.	163

C.1	Kistler 6619AP35 in-cylinder pressure sensor with a 6513AK Thompson adapter.	164
C.2	Schematic of prototype high-sample rate torquemeter.	166
C.3	Prototype high-sample rate torquemeter installation for W9L46C referene system.	166
D.1	Start of combustion identification in measured in-cylinder pressure diagram.	167
D.2	Corrected in-cylinder pressure measurements for W9L46C engine. . .	169
D.3	Heat release analysis curves for W9L46C engine	170
D.4	Heat release analysis curves for W9L46C engine	171
D.5	Measured ICT SNR for raw and smoothed data using Gaussian-weighted moving average with 20 samples window.	172
E.1	Direct crankshaft dynamics model calibration of W9L46C reference system for 2,949 kW at 401 RPM.	175
E.2	Direct crankshaft dynamics model calibration of W9L46C reference system for 5,491 kW at 450 RPM.	175
E.3	Inverse crankshaft dynamics model performance using measured ICT for 2,949 kW at 401 RPM.	177
E.4	Inverse crankshaft dynamics model performance using measured ICT for 5,491 kW at 450 RPM.	178

List of Tables

4.1	Thermodynamics model input	49
5.1	Numerical schemes user-defined settings investigation.	72
5.2	In-cylinder pressure curve parameters classification.	80
5.3	Four part verification procedure of inverse crankshaft dynamics model.	91
6.1	Reference systems overview.	93
6.2	Overview of reference systems available data and case studies deployment.	94
6.3	Case studies pertaining to each stage of the methodology.	96
7.1	Healthy conditions digital twin calibrated values for W9L46C and 6RTflex50 reference systems.	99
7.2	Digital twin validation results at healthy conditions following calibration, for W9L46C and 6RTflex50 reference systems.	100
7.3	Numerical scheme user-defined settings to achieve best performance.	105
7.4	Numerical schemes selection, considering NRME and execution time.	105
7.5	Direct crankshaft dynamics model calibration results for W9L46C reference system.	107
7.6	Heat release analysis results for operating point of 5,491 kW at 450 RPM for W9L46C reference system, with underperforming cylinders highlighted.	119
8.1	Addressed literature review gaps.	129
B.1	Reference system data of W9L46C engine.	158
B.2	Port engine shaft uncalibrated DOF coefficients for W9L46C reference system.	159

B.3	Starboard engine, propeller and generator shaft uncalibrated DOF coefficients for W9L46C reference system.	160
B.4	Reference system data of 10L67GBE engine.	162
B.5	Calibrated DOF coefficients for 10L67GBE reference system.	162
C.1	Specifications of Kistler 6619AP35 pressure sensor.	164
C.2	Specifications of Doctor Diesel DK-20 in-cylinder pressure analyser. .	165
D.1	In-cylinder pressure measurement correction for W9L46C engine. . .	168
D.2	Heat release analysis results for operating point of 5,491 kW at 450 RPM for W9L46C reference system.	170
D.3	Heat release analysis results for operating point of 2,949 kW at 401 RPM for W9L46C reference system.	171
E.1	Step 1 of thermodynamics model calibration using particle swarm optimisation algorithm; Wiebe function and FMEP constants.	173
E.2	Step 2 of thermodynamics model calibration using particle swarm optimisation algorithm; Woschni-Anisits model constants.	174
E.3	Direct crankshaft dynamics model calibration algorithm performance for W9L46C reference system, for 2,949 kW at 401 RPM.	176
E.4	Direct crankshaft dynamics model calibration algorithm performance for W9L46C reference system, for 5,491 kW at 450 RPM	176

Acronyms & List of Symbols

Acronyms

AER	Annual Efficiency Ratio	ICS	Instantaneous Crankshaft Speed
ANN	Artificial Neural Network	ICT	Instantaneous Crankshaft Torque
BSFC	Brake Specific Fuel Oil Consumption	IMEP	Indicated Mean Effective Pressure
CBM	Condition Based Maintenance	IMO	International Maritime Organisation
CCS	Carbon Capture and Storage	IN4.0	Industry 4.0
CFD	Computational Fluid Dynamics	IVC	Inlet Valve Close
CII	Carbon Intensity Indicator	KPI	Key Performance Indicator
CNN	Convolutional Neural Network	LE	Lyapunov Exponent
DBN	Deep Belief Network	LM	Levenberg-Marquardt algorithm
DCS	Data Collection System	LNG	Liquefied Natural Gas
DOF	Degree of Freedom	LPG	Liquefied Petroleum Gas
DSS	Decision Support Systems	LSTM	Long-Short Term Memory
ECA	Emission Control Area	LTI	Piecewise Linear Time Invariant
EEDI	Energy Efficiency Design Index	MARPOL	International Convention for the Prevention of Pollution from Ships
EEOI	Energy Efficiency Operational Indicator	MCR	Maximum Continuous Rating
EEXI	Energy Efficiency eXisting ship Index	MRV	Monitoring Verification and Reporting
EGT	Exhaust Gas Temperature	MVEM	Mean Value Engine Models
ETS	Emissions Trading Scheme	NRME	Normalised Root Mean Error
EU	European Union	NSALMN	Nonmonotone Self-Adaptive Levenberg-Marquardt algorithm
EVC	Exhaust Valve Close	PM _{2.5}	Particulate Matter
FEM	Finite Element Models	SEEMP	Ship Energy Efficiency Management Plan
FMEP	Friction mean effective pressure	SNR	Signal-to-Noise Ratio
FRF	Frequency Response Function		
GHG	Greenhouse Gas		

TDC	Top Dead Center	d	Compressor isentropic efficiency map coefficients
TR-BDF2	Trapezoidal Rule with 2 nd Order Backwards Differentiation	FA	Fuel-air ratio
TVD	Torsional Vibration Damper	f _{mep}	Friction mean effective pressure
WHO	World Health Organisation	g	Woschni-Anisits model constants
Symbols		k	Compressor mass flowrate map coefficients
<i>B</i>	In-cylinder pressure parameter vector for all cylinders	m	Chen-Flynn model coefficients
<i>I</i>	Identity matrix	p	Air cooler effectiveness constants
<i>u</i>	LTI system input vector	r	Turbocharger correction factor
τ	Excitation torque Fourier magnitude	w	Optimisation weights
<i>C</i>	Relative viscous damping matrix	x	Direct crankshaft dynamics model calibration factor
<i>D</i>	Absolute viscous damping matrix	<i>A</i>	Area
<i>H</i>	Structural damping matrix	<i>a</i>	Wiebe constant
<i>J</i>	Inertia matrix	<i>b</i>	Engine bore
<i>K</i>	Stiffness matrix	<i>c</i>	Relative viscous damping
<i>M</i>	Generic mass matrix	<i>D</i>	Diameter
\hat{c}	Specific heat capacity at constant pressure	<i>d</i>	Absolute viscous damping
<i>j</i>	Inertia Fourier magnitude	<i>F</i>	Force
<i>A</i>	LTI system dynamics matrix	<i>f</i>	Generic function
<i>B</i>	LTI system input matrix	<i>G</i>	Thermal conductivity coefficient
\mathcal{H}	Hysteretic damping energy	<i>H</i>	Enthalpy
\mathcal{K}	Kinetic energy	<i>h</i>	Specific enthalpy
\mathcal{L}	The Lagrangian	<i>i</i>	Imaginary unit
\mathcal{R}	Rayleigh dissipation function	<i>J</i>	Polar moment of inertia
\mathcal{T}	Torque	<i>k</i>	Stiffness
\mathcal{V}	Potential energy	<i>M</i>	Inlet Mach number
a	Propeller excitation torque coefficients	<i>m</i>	Mass
b	Turbine mass flowrate map coefficients	<i>N</i>	Number of DOFs or cylinders
c	Turbine isentropic efficiency map coefficients	<i>O</i>	Objective function
		<i>P</i>	Power

p	Pressure	Φ	Non-dimensional flow rate coefficient
Q	Energy supplied to the system	ϕ	Equivalence ratio
s	Piston distance from TDC	Π	Pressure ratio
T	Temperature	Ψ	Non-dimensional head coefficient
t	Time	ψ	Lyapunov exponent
U	Blade tip speed	ρ	Density
U	Internal energy	σ	Structural damping coefficient
u	Specific internal energy	θ	Angle
V	Volume	ε	Algorithm or solver tolerance
W	Thermodynamic work	ξ	Burnt fuel fraction
w	Wiebe exponent		
x	Generic variable		

Greek Symbols

α	Propeller phase angle
β	In-cylinder pressure parameter vector for a single cylinder
θ	Angular displacement Fourier magnitude
χ	Scavenging mixing factor
Δ	Macroscopic difference
δ	Infinitesimal difference
ϵ	Local pointwise error fraction
η	Efficiency
γ	Ratio of specific heats
$\hat{\rho}$	NSALMN algorithm Levenberg-Marquardt ratio
κ	ODE23tb solver constant
μ	NSALMN algorithm step acceptance criterion
ν	Levenberg-Marquardt damping parameter
ω	Average angular velocity

Subscripts

Ω	Harmonic balance
abs	Absolute
amb	Ambient
back	Back-pressure
com	Compressor
CW	Cooling Water
cyl	Cylinder
damp	Vibration damper
DOC	Duration of Combustion
D	Direct crankshaft dynamics model
EVC	Exhaust Valve Close
EVO	Exhaust Valve Open
EV	Exhaust valve
filt	Filter
fly	Flywheel
IVC	Inlet Valve Close
IV	Inlet valve or port
I	Inverse crankshaft dynamics model
lin	Cylinder liner
loc	Local
mea	Measured

prop	Propeller	d	Downstream
rec	Reciprocating	e	Exhaust
ref	Reference	ex	Expansion
rel	Relative	f	Fuel
sim	Simulated	i	Generic counter
SOC	Start of Combustion	J	Inertia
TC	Turbocharger	j	DOF counter
TDC	Top Dead Center	k	Algorithm, step or timeseries counter
tur	Turbine	L	Load
T	Thermodynamics model	me	Maximum isentropic expansion
Wos	Woschni	n	Cylinder counter
a	Air	p	Piston
b	Brake	p or q	Fourier order counter
C	Combustion	s	Stoichiometric
c	Clearance	u	Upstream
co	Compression	V	Variable inertia

Chapter 1

Introduction

1.1 Maritime Industry Challenges & Outlook

Shipping is responsible for the transport of over 80% of the global goods by volume and over 70% of the global trade by value, therefore acting as a vital backbone to the global economy [1]. As a result, the maritime industry is linking several major sectors of the world economy including agriculture and energy, heavy industries and manufacturing, insurance and banking, as well as retail and tourism [2]. Therefore, by supporting international trade and facilitating the world economy, the maritime industry stands exposed to significant global challenges of environmental sustainability, global governance and compliance, as well as technological innovation.

1.1.1 Environmental Sustainability

Climate change due to atmospheric pollution and Green-House Gas (GHG) emissions is identified as the greatest threat to environmental sustainability [3]. Therefore the challenge facing the maritime industry becomes apparent due to the comparatively large share of atmospheric pollution that the industry is responsible for. In specific, the internal combustion engines and oil-fired boilers on ships emit various GHG gases including CO₂, CH₄ and N₂O which account for 2.89% of all anthropogenic GHG emissions [3]. Hence, if the maritime industry were a country, it would be the world's sixth largest GHG emitter [4]. In addition, other harmful emissions produced by shipping including SO_x, NO_x account for 13.0% and 9.0% of the global emissions respectively as well as fine Particulate Matter (PM_{2.5}), which results to harmful

effects to land-based ecosystems and human health [5].

Therefore, as demand for global trade increases, shipping emissions are projected to increase for scenarios of business-as-usual from 90-130% by 2050 compared to 2008, with higher levels of emissions being more likely due to increased global growth rates [3]. Considering the above, the majority of emissions reductions potential in the short term can be attributed to operational measures, and the absolute reduction in emissions is maintained in the long term as well, indicating the enduring contribution of operational measures to emission savings, as shown in Figure 1.1 [6, 7].

The focus of such operational measures can be considered to be the ship’s main engine, which is the largest fuel consumer on board the vessel. Therefore this presents significant potential in operational performance improvement, particularly since the ship’s engine is often operating in sub-optimal or degraded conditions as a result of the harsh marine environment and demanding operational profiles [6, 8]. Consequently, the atmospheric pollution is a significant challenge faced by the maritime industry which is bound to persist in the future, and can be addressed in large, by focusing on improving the engine’s health during ship technical operations.

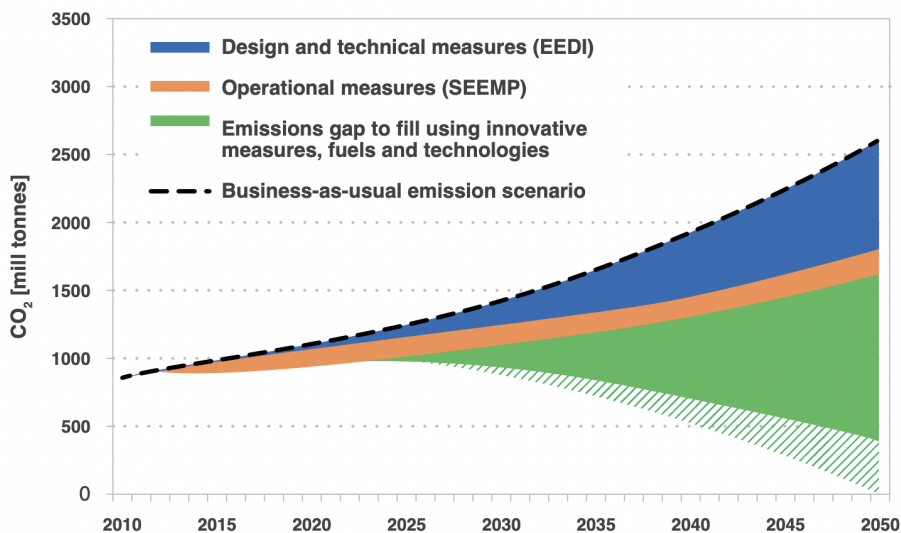


Figure 1.1: GHG reduction pathway to achieve the Initial IMO Strategy [7].

1.1.2 Global Governance & Compliance

The global community has realised the inherent potential to improve the shipping industry’s environmental footprint by focusing on operational measures. Therefore, an appropriate framework of global governance and compliance has been enacted to

ensure that the maritime industry is heading towards a sustainable future.

In specific, the main governing body of the maritime industry is the International Maritime Organisation (IMO) with 175 member states [9] and the most prominent regulations for the near and long-term future include the Prevention of Pollution from Ships (MARPOL) Annex VI. Among other things, regulations contained within MARPOL ensure that ships maintain their efficiency using the Ship Energy Efficiency Management Plan (SEEMP) [10]. Within the SEEMP, plans to enhance and maintain operational energy efficiency need to be defined, and the mandatory IMO Data Collection System (DCS) needs to be adhered to. Moreover the SEEMP establishes the Carbon Intensity Indicator (CII) rating starting on 2023, which measures the operational efficiency of the ship and assigns each vessel with a rating. The thresholds to maintain each rating decrease steadily with time, thus eventually phasing out old and operationally inefficient vessels from trading.

In addition to the IMO, the European Union (EU) imposes additional regulations such as the EU Emissions Trading Scheme (ETS) which will be implemented in 2023. This is predicted to have a considerable impact in freight rates and particularly ship operations, effecting more than 38% of the world fleet [11]. Furthermore, financial institutions including lenders, lessors, and financial guarantors impose further requirements to shipowners, the most influential of which are the Poseidon Principles. These interface with the IMO DCS to collect data, and similar to the IMO CII, they quantify ship operational efficiency, with the aim to achieve 80% improvement in 2050 as compared to 2019 [12].

It is therefore apparent that the maritime industry is regulated by a number of entities, including the IMO, EU, individual governments, as well as financial institutions. The varying scope of each entity and potential competing interests result to a complicated regulatory framework that is not controlled by a single overarching authority, making it challenging for shipping companies to comply with. However, common elements of the global regulatory frameworks in shipping include significant emphasis on improving technical aspects of the ships' operational efficiency. Consequently, approaches and methods to upkeep the engine operational efficiency are not just optional, but are considered necessary as a matter of regulatory compliance.

1.1.3 Technological Innovation

Technological innovation poses a challenge to the shipping industry as it has to deliver improvements in accordance to the strict time frame imposed by the regulations, however at an appropriate cost to ensure commercial viability. The majority of current practices focused on upkeeping the efficiency of the ship's engine are primarily manual or semi-manual methods of collecting data and performing basic analysis based on expert knowledge and past experience [13, 14]. Therefore, existing approaches lack consistency, scientific rigor, and scalability to address the increasingly complex modern machinery. Consequently, there are significant advantages of implementing a systematic approach to machinery health assessment which incorporates digital twins, as also demonstrated in other more more technology-intensive industries.

1.1.3.1 Technologies Availability in Other Industries

Health assessment by means of digital twins is made possible by Industry 4.0 (IN4.0) technologies which include connectivity, real time data collection, machine learning and systems modelling [14]. This primarily enables data-driven diagnostics techniques which rely on models of the subject machine, that utilise high frequency measurements including sound, acceleration, torquemeter and pressure sensors. These can be used to diagnose blade cracks, cavitation and bearing faults in hydroelectric turbines [15, 16], electrical erosion, bearings and gearbox degradation for wind turbines [17, 18], as well as bearing condition and imbalances in large hydraulic and centrifugal pumps [19]. The advantages of such state-of-the-art approaches for stationary land based applications are that no a-priory physical knowledge is required and transferable techniques can be employed regardless of the machinery studied, such as Artificial Neural Networks (ANNs), Convolutional Neural Networks (CNNs), Deep Belief Networks (DBNs) and Long-Short Term Memory (LSTM) networks [19].

However, the large volumes of data generated require good connectivity, expensive infrastructure to collect, store and process, whilst lacking insight on the physical processes undergone by the machinery. This hampers the accuracy of the diagnostics process, consequently for mobile assets such as the automotive industry, the main challenge lies in developing diagnostic methods which employ digital twins requiring a minimal number of input data from sensors [20, 21]. The same trend exists for the

aerospace industry, where well established physical approaches for turbine health assessment such as gas path analysis, are combined with critical measured parameters to perform baseline establishment, pattern recognition and even sensor validation [22].

The good connectivity and higher levels of machinery integration from manufacturers present in other industries, create a suitable environment for the adoption of computationally-intensive and data-intensive approaches that address machinery health assessment in an intelligent manner. However, the shipping industry operates in a different context, specifically due to financial and corporate barriers, as well as technological challenges stemming from lack of systems integration and connectivity.

1.1.3.2 Barriers to Technological Innovation in Shipping

Financial and corporate barriers in the shipping industry such as split incentives present challenges in the adoption of IN4.0 technologies, and subsequently in health assessment approaches enabled by digital twins. In specific, for the case of a typical time charter, fuel costs are covered by the charterer who would benefit from reduced fuel consumption, however the capital expenditure of fuel saving technologies is incurred by the owner [23]. Furthermore, even for the case of a typical voyage charter where operational costs are incurred by the owner, fuel saving measures such as speed optimisation are not able to take place due to contractual clauses including demurrage, laycan, and speed restrictions [24].

However, as also encouraged by the regulatory framework such as the IMO DCS, IN4.0 technologies particularly concerning ship connectivity have seen a significant uptake in shipping recently, with large data sets being made available onboard as well as onshore [14]. Nevertheless, the involvement of such data in critical decision making processes is quite limited [25], primarily due to lack of industry-wide standard protocols and approaches, as well as large expenses in transmitting data from the ship to shore [26].

As also observed from other industries, a key aspect of machinery health monitoring is the digital twins, however marine engine models development is particularly challenging. In specific, the multitude subsystems involved such as turbochargers, air coolers, injectors, etc., are designed by different manufacturers than those of

the main engine, erecting barriers regarding access to proprietary data and overall integration [25]. In addition, the time and costs involved in physical tests used to validate digital twins of marine engines becomes prohibitive, due to the size and inherently challenging to replicate operating profiles.

Overall, the rapid uptake of IN4.0 tools and digitalisation, in addition to the current state of the shipping industry which relies on more conservative methods and approaches, presents significant opportunities. However, important challenges persist, which have to be addressed particularly regarding marine engines health assessment.

1.1.4 Maritime Industry Outlook

Despite the comparatively large share in GHG emissions, shipping is and will continue to be by far the most efficient mode of cargo transport [3], which is a noteworthy fact for an industry that plays such a major role in the global economy. As a result, in the future the maritime industry will be an important enabler of sustainable development. However, the international reach of the shipping industry is mobilising the global community to focus and act on making ships ever more efficient.

Consequently, the long term outlook of the maritime industry, even though uncertain in terms of the ways and means used to ensure compliance, will certainly be a green one. The global community is acting fast to set ambitious targets through various roadmaps and future strategies for the long term outlook of this industry. These include the European Green Deal [27], the Industry Roadmap for Zero-Emission Shipping led by various Group of Twenty (G20) countries and large organisations [28], as well as over seven national action plans from countries with a large stake in shipping [29].

In the short term, the maritime industry will have to employ state-of-the-art technologies and approaches to ensure compliance and maximise profitability. Despite the challenges presented in this task, there are significant opportunities which can be exploited as follows:

1. A large potential in operational performance improvement has been identified by the regulatory authorities which are introducing stringent measures to encourage operational efficiency improvements, such as the SEEMP, CII and

AER. This is particularly true for the ship's engines as they are amongst the most critical machinery, and are the largest energy consumers onboard.

2. The recent uptake of digitalisation is providing improved access larger data sets and enhanced computational capabilities. As a result, digital twins enabling the condition assessment of critical machinery such as the main engine can be developed. This provides deeper insight into the engine's efficiency, health status, including imminent failures which can lead to costly down time.
3. The capabilities of digital twins of critical machinery including engines is being demonstrated comprehensively in other industries employing mobile assets such as aircraft and automobiles. Therefore machinery models can be deployed to offer the required insight and intelligence in approaches used to conduct health assessment.

1.2 Aim & Objectives

The urgency of environmental sustainability in the shipping industry has motivated the commercial and regulatory environment, with particular emphasis being placed on the main engine of the vessel. Therefore, it is anticipated that a systematic and scientific methodology incorporating digital twins will enable the health assessment of marine engines. Consequently, this research aims to develop a systematic methodology enabling marine engine health assessment by employing first-principles digital twins.

The high-level objectives of this research are as follows.

1. Develop a systematic methodology to benchmark, quantify and assess the marine engine health.
2. Develop modelling tools based on first-principles and digital twins, which utilise critical measurements to accurately simulate the mechanical and thermodynamic performance of marine engines.
3. To demonstrate the application of the methodology and developed tools, for several representative case studies including marine engines of any type (4-stroke, 2-stroke) and configuration.

1.3 Dissertation Layout

The layout of the dissertation is structured in eight chapters, an overview of which is provided as follows.

Chapter 1: Introduction to the shipping industry challenges, outlook as well as aims and objectives of the dissertation.

Chapter 2: The literature review is contained in this chapter, the outcome of which includes the research gaps.

Chapter 3: The research methodology is contained in this chapter, inclusive of brief descriptions of its five distinct stages as well as the figure demonstrating the input, output and relationships between the respective steps contained within the stages.

Chapter 4: The descriptions and procedures related to the thermodynamics model are contained in this chapter. This firstly includes the formulation of the thermodynamics model, solution method and model convergence, as well as an overall description of the input and output. Furthermore, the systematic calibration process of the thermodynamics model for the healthy conditions digital twin is described, and the configuration for the current engine conditions. Last, the engine health assessment process is presented within this chapter.

Chapter 5: The descriptions and procedures related to the crankshaft dynamics models are contained in this chapter. This includes the formulation of the direct crankshaft dynamics model, solution methods and model convergence, as well as the description of the input and output and the direct crankshaft dynamics model calibration to the current engine conditions. Furthermore, this chapter contains the inverse crankshaft dynamics model development which includes the in-cylinder pressure parametrisation, the necessary preparation, concepts and description of the inverse crankshaft dynamics model development, as well as the involved verification process of said model.

Chapter 6: This chapter contains a description of the three distinct reference systems employed and the measurements available for each, as well as the description of the case studies which showcase the different stages of the research methodology from Chapter 3.

Chapter 7: In this chapter the results and discussion for each respective case study are presented for the applicable reference systems.

Chapter 8: The final remarks and conclusions on the research methodology, case studies as well as the digital twins are discussed. Furthermore, the achievement of the aims and objectives is discussed, as well as the future work potential.

Chapter 2

Literature Review

In light of the maritime industry challenges, considerable benefits have been demonstrated in addressing ship operations and their various technical aspects, as discussed in Chapter 1. Therefore, aiming to improve ship systems operational savings and efficiency is instrumental in achieving reduced costs to stakeholders, as well as the ambitious emission targets of the coming decades. In specific, ship systems operational savings and efficiency can be categorised into; hull and propeller condition management, voyage monitoring and optimisation, as well as machinery operational insight and management.

Hull and propeller condition monitoring and management is critical for ship owners and charterers alike as it correlates directly with increases in the fuel consumption. Specifically, by monitoring and analysing a multitude of variables including wind and sea state, as well as ship trim and draft, critical decisions can be made effectively. These include the determination of the optimal timing for hull inspections and cleaning, verification of the anti-fouling paint performance against manufacturer claims, as well as verification of the vessel overall performance against the charterer requirements [30–32]. Furthermore, voyage monitoring and optimisation is vital in optimising the ship’s routing and minimising fuel consumption, which is performed by taking into account additional data including weather forecasts and navigational parameters [33, 34]. However, to evaluate the performance and conduct decision making for the above two cases, there is a significant number of uncertain and hard to measure variables involved (e.g. wave height, current speed, ship speed through water, etc.), which increases the complexity and thus compromises the accuracy of

the analysis [6].

Machinery operational insight and management is utilised to determine and predict the performance of the ship's critical machinery, and subsequently exercise effective decisions to prevent degradation and failures, as well as upkeep efficiency. As a result, this process carries a substantial impact on operational savings, which includes fuel savings and spare parts [35], extension of overhaul periods [36], as well as avoidance of large off-hire costs and performance claims [37]. However, as a result of the very recent advent of digitalisation and improved monitoring and modelling techniques, engine operational insight and management practices remain largely unexplored due to persisting data collection challenges, data analysis problems and lack of testing in state-of-the-art technologies [14, 38]. Thus, the shipping industry still lacks understanding on the operation of ship machinery such as the main engine, which has a cascading effect on their efficiency.

2.1 Machinery Insight & Management

Following the above, it is prudent to address the topic of machinery insight and management during vessel operation, since it improves both operational expenditure and the environmental sustainability. This has been addressed in the literature by predominantly utilising three basic approaches; data and energy monitoring, Condition-Based Maintenance (CBM), as well as machinery health assessment and management.

2.1.1 Data & Energy Monitoring

Data and energy monitoring consists of monitoring machinery parameters to extract information on the energy (and exergy) consumption and conversion processes, in order to identify potential inefficiencies [6], and this approach can be further subdivided into engine operating profile and performance monitoring, ship systems energy and exergy monitoring, as well as thermo-economic analysis.

Engine operating profile and performance monitoring, employs basic and peripheral engine data such as shaft power, vessel speed, distance travelled and loading condition, to monitor the ship's Energy Efficiency Operational Indicator (EEOI)

[39–41], as well as other custom indices and Key Performance Indicators (KPIs) for benchmark setting and comparison standards [42, 43], as well as improving the load allocation of prime movers [44]. Ship systems energy and exergy monitoring tracks the energy and exergy flows which are used as indicators of the machinery performance. This is accomplished by first principles modelling [45, 46], or by using operational data [6, 8, 47]. Ship systems thermo-economic analysis performs an exergy analysis in addition to an economic analysis which associates monetary value to the calculated energy and exergy flows, thus making the results more relatable to the wider industry stakeholders [48–50].

Data and energy monitoring techniques provide a deeper insight into ship operational efficiency, and are particularly useful for large fleet performance overviews which is why they are also exploited by regulatory authorities (e.g. EEOI from IMO). However such approaches are not able to offer direct operational suggestions such as spare parts replacement or machinery overhaul actions, therefore an approach with a more direct path to actionable information is needed.

2.1.2 Condition-Based Maintenance

Condition-based maintenance (CBM) tends to offer a direct approach specifically in regards to critical machinery management, as it consists of monitoring the diesel engine condition and subsequently diagnosing degradation and failures which lead to precise maintenance actions [51].

In specific, the condition of the engine mechanical parts can be monitored using lubrication oil monitoring. This includes off-line and in some advanced applications on-line sampling, which relies on statistical trends and predefined limits to diagnose excessive wear and tear in engine bearings and liner [52, 53]. Furthermore, vibration monitoring can also be employed to perform CBM on mechanical parts, typically by using order tracking [54], and most recently by employing advanced statistical techniques incorporating machine learning, to correlate abnormal vibration characteristics to specific component failures [55, 56].

Regarding the thermodynamic performance of machinery and particularly the engine, critical measurements such as exhaust temperatures, cooling oil temperatures, jacket water temperatures, etc. are analysed statistically using Artificial Neural

Networks (ANNs) [57, 58], support vector machines [59], and various unsupervised learning techniques [60, 61], to detect abnormal deviations in time-series measurements. More elaborate CBM approaches include condition prediction and prognostics, such as predictions of changes in the Indicated Mean Effective Pressure (IMEP) using Deep Belief Networks (DBNs) [62], prognostics of turbocharger condition using Long-Short Term Memory (LSTM) networks [63], and prediction of the remaining useful life of critical machinery using Convolutional Neural Network (CNNs) [64, 65].

Furthermore, a more holistic approach for CBM includes Decision Support Systems (DSS), which recommend specific maintenance actions in addition to diagnostics and/or prognostics. In specific, such DSS systems analyse past and current data using pattern recognition and ANNs to calculate metrics such as failure rates, probability of failures and mean time between failure, which are used to present KPIs on a component level in a graphical interface [66]. Similarly, holistic DSS systems integrate voyage management with fault diagnostics using multi-criteria decision aid techniques to optimise maintenance tasks and planning [67].

CBM is a relatively recent and pragmatic approach in addressing operational insight and management. However, it includes extensive (if not exclusive) use of black-box models, which do not offer physical insight into the machinery condition, and requires large data sets obtained from sophisticated monitoring systems which are not available for most vessels [13]. In addition CBM requires input assumptions such as mean time between failures and mean time to failure, which is hard to obtain due to the mostly manual failure identification approaches that are used, as well as the long monitoring period required to ensure statistical significance [51].

2.1.3 Digital Twin Enabled Machinery Health Assessment

There is an important distinction between a model and a digital twin. The model of a marine engine (or any physical system) refers to a mathematical description of the system which can be deployed to simulate various facets of said system's operation. The digital twin is the process by which the model is utilised in combination with measured data sets, in order to simulate the various realistic states of the system's behaviour [68].

Considering the above distinction, digital twin enabled machinery health assess-

ment plays a major role in reducing operating costs as well as down time. However, the fundamental difference compared to CBM is the primary use (though not exclusive) of first-principles model-based approaches in order to assess and manage the health of machinery. There are several critical machinery types where digital twins have been developed and implemented for health assessment including electric motors, pumps, boilers, and purifiers [69]. However, largest energy consumers on-board for the great majority of the vessels in the world fleet are the internal combustion engines, which convert the fuel chemical energy to propulsion, and to all other ship functions [6]. As a result, emphasis has been placed in the literature at developing digital twins for the ship's engines due to their criticality [70], and their large share of operational expenditures (e.g. fuel consumption, spare parts, etc.) [71].

2.1.3.1 Critical Engine Measurements

Digital twin enabled engine health assessment relies on utilising critical engine measurements which contain useful information regarding the engine performance, and can thus be employed to compare with simulation results or even be incorporated into the digital twin itself in order to enhance accuracy and health assessment capabilities [72]. Amongst the most prominent measurements for the engine condition is the in-cylinder pressure measurement. This measurement, particularly when analysed using approaches involving digital twins, provides information to examine the combustion process quality [73], blowby [74], cylinder misfire and knock [75], cylinder compression ratio and injection timing [76, 77], as well as injector degradation and failures [78]. However, the methods currently employed in determining all of the above, rely on direct measurements of the in-cylinder pressure by deploying pressure sensors to either one or multiple cylinders, which can be expensive, suffer from poor durability [79–81], exhibit synchronisation issues [82] and most often do not allow for continuous monitoring. Furthermore, the inherited technicalities of piezoelectric sensors utilised to perform such measurements require extensive corrections and rectifications to be made on the in-cylinder pressure diagrams [83].

Nonetheless, recent technological improvements have led to the development of continuous pressure monitoring systems which are primarily utilised in high-value power plants, such as those with dual-fuel engines [84]. However, for the majority of

typical large internal combustion engines employed in the thousands of ocean-going vessels world wide, the costs involved with such monitoring systems remain outside the reach of most shipowners and operators [13, 14]. Moreover, having measured the in-cylinder pressure, the non-trivial task of signal correction is required, in order to remove the noise and perform averaging over several cycles, and most importantly to remove offsets by calibrating the acquired signal with respect to the engine crank angle and the cylinder pressure [85, 86].

As a result, alternative measurements have been utilised to extract important features that belong to, or can be directly derived from the in-cylinder pressure diagram, in a reliable and low-cost manner. In specific, for automotive industry applications, the peak pressure position [87, 88], and part of the in-cylinder pressure diagram was reconstructed [89–91], utilising vibration measurements by deploying accelerometers on the cylinder heads and engine block respectively. However, signal quality is sensitive to the sensor’s placement which is determined arbitrarily [90], and vibration measurements record the effects from additional phenomena not related to combustion, which significantly complicates the analysis [91].

Furthermore, the engine Instantaneous Crankshaft Speed (ICS) and Instantaneous Crankshaft Torque (ICT) have been utilised with a similar scope as the vibration measurements, and information regarding the thermodynamic performance of the cylinders has been successfully extracted, which is discussed with greater detail in Section 2.1.3.3 below. Consequently, the ICS and ICT are critical measurements which can be cheaply and accurately obtained to perform continuous monitoring, using only a single speed sensor or a torquemeter respectively [92]. Furthermore, when comparing the ICS and ICT, the former exhibits a high noise to signal ratio, and therefore requires more involved post-processing [93]. Additionally, the ICS requires higher sample rates compared to the ICT to capture the rapid fluctuations, and finally the ICT has a linear relationship with the load for the case of marine engines operating on propeller or combinator curves [92, 94]. As a result, it is preferable to obtain the ICT instead of the ICS measurement.

To gain a deeper insight on the engine health, the in-cylinder pressure and the ICT measurements can be analysed in detail using model-based approaches involving thermodynamics and crankshaft dynamics models respectively. Such models are

able to act as baselines, as well as establish robust relationships demonstrating the effect of specific component faults on the in-cylinder pressure or the engine ICT for a multitude of engine operating points and ambient conditions [95]. Consequently model-based approaches combining measurements as well as thermodynamics and crankshaft dynamics models are an integral part of engine health assessment.

2.1.3.2 Thermodynamics Models

Thermodynamic models are employed to simulate the marine engine performance under a variety of operating conditions, including healthy, degraded or faulty. Consequently, they offer a cost effective alternative to full scale testing, by diagnosing the engine health status and minimising machinery downtime for preventative disassembly and inspection. Depending on specific requirements, thermodynamics models can be either data-driven or first-principles.

Data-driven thermodynamics models are mainly utilised for to perform engine health assessment particularly due to their small computational requirements and their ability to effectively capture the realism and complexities of the engine processes. In specific, such models are utilised for fault detection and diagnostics [96–98], as well as condition monitoring [99, 100] by identifying features and abnormal patterns in the data. However, data-driven models lack the physical insight of the engine processes, and pose difficulties in obtaining training data sets for healthy, but most importantly for faulty conditions which may be extremely challenging to identify during actual operation.

Therefore, for improved physical insight, first-principles models are utilised which employ a-priori knowledge of the physical processes taking place within the engine, however their lack of combination with operational data has resulted to limited use for engine health assessment applications in operational level. Such thermodynamics models can be categorised as Mean Value Engine Models (MVEM) and zero and multi-dimensional models [72]. The MVEMs are computationally simple models, however they provide limited insight. Hence MVEMs are primarily used for control applications in emissions [101, 102] and variable pitch propellers [103], prediction of various aspects of the engine performance under different settings [95, 104], as well as engine monitoring and management [6].

Zero and multi-dimensional models are more computationally complex, and as a result they can allow for greater accuracy and deeper insight into the engine health status, since they are able to predict the instantaneous in-cylinder processes. Applications of such models include investigations in engine design [105, 106], settings [107], and failure simulators [108], as well as virtual test-beds to generate data for the implementation of data-driven approaches [109–111]. However, there are sparse instances in the literature where such models have successfully performed engine health assessment, which include combinations with operational data, to identify main and auxiliary engine degradation as well as potential faults [76].

Zero-dimensional models in particular, are demonstrating good computational performance with enhanced predictive capabilities particularly when the in-cylinder processes are subdivided to an appropriate number of zones [72]. A zone corresponds to a discrete cylinder volume, and zero-dimensional multi-zonal models have successfully predicted emissions [112] as well as complex phenomena such as scavenging for the case of two-stroke engines [113, 114].

Despite the advantages of zero-dimensional multi-zonal models, there are limited applications in the literature regarding engine health assessment. This is primarily owing to the challenges that arise during the model calibration process which is an important requirement for capturing the engine’s current health status [76].

2.1.3.3 Crankshaft Dynamics Models

Crankshaft dynamics models can be categorised as direct or inverse crankshaft dynamics models, and the latter has demonstrated engine health assessment capabilities by utilising the ICS and ICT measurements. The inverse crankshaft dynamics model can be formally considered as a parameter estimation problem, which utilises measured data (i.e. the ICS or ICT) and a physical model of the dynamic system (i.e. the direct crankshaft dynamics model), to identify critical parameters of said dynamic system [115].

In specific as shown in Figure 2.1, the direct crankshaft dynamics model utilises as input the engine excitation forces which are induced by the cylinder combustion phenomena, and provides as output the torsional vibration response, shaft stresses, deformation, and most importantly in this case the engine ICS and ICT [116]. This

is accomplished by a computationally efficient method of discretising the crankshaft into a series of a few large masses, referred to as lumped mass model [117, 118]. The solution of the system of non-linear differential equations developed for the lumped mass model is critical to the performance of the crankshaft dynamics model, and has been presented in the literature however with limited discussion on solution methods and numerical schemes on small and large engines alike [94, 119].

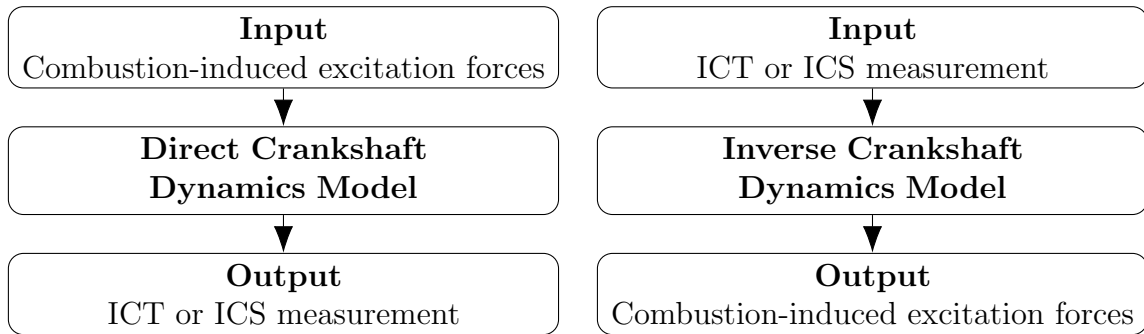


Figure 2.1: Direct vs. inverse crankshaft dynamics models input/output.

The inverse crankshaft dynamics model utilises the ICS and ICT measurements to obtain insight on the cylinder combustion phenomena. The advantage for this model is that a single and relatively low cost speed or torque sensor can be used to obtain deep insight regarding the thermodynamic performance of individual engine cylinders, which would be otherwise obtained using multiple temperature and pressure sensors with inherently large uncertainties and data synchronisation issues [94]. Inverse crankshaft dynamics models have been successfully deployed for larger engines, using various parameter estimation techniques, more details of which are provided in Section 2.1.3.4. The applications of such parameter estimation techniques include balancing the torque output of cylinders on a large 4-stroke diesel generator by employing the engine ICT measurement and a constrained optimisation algorithm to adjust the quantity and timing of the fuel injected [77, 120]. Furthermore, on similar 4-stroke generator sets, faulty fuel pumps were diagnosed [93] as well as large variations in the peak in-cylinder pressure [121] by utilising feature extraction ANN algorithms which employ the ICS measurement. Regarding large 2-stroke generator sets, under-performing cylinders were identified utilising ANN algorithms which employ the ICT measurement to obtain the indicated mean power of each cylinder [94].

The abilities of inverse crankshaft dynamics models to obtain critical information regarding the cylinders performance are further showcased in automotive applications. In specific, a windowing approach has been employed to obtain accurately the the peak in-cylinder pressure for a small five-cylinder engine at specific operating points [79]. Furthermore the burnt mass fraction and combustion phasing where successfully estimated utilising the engine ICS and a non-linear mapping algorithm [122].

Consequently, inverse crankshaft dynamics models employing the ICT measurement are able to cost-effectively and accurately perform engine health assessment. However, the application of such models in the literature remains focused to only generator sets of larger engines, whilst not including marine engines with more complex shafting systems, as well as additional dynamics introduced by the propeller. Furthermore, inverse crankshaft dynamics models have been utilised to determine various parameters describing the individual cylinders performance as mentioned above, however they have not succeeded in reconstructing the entire in-cylinder pressure diagram, which is arguably the most vital indicator for the engine health [86]. Finally, integration of crankshaft dynamics models with thermodynamics models as part of a unified approach has not been exploited to provide further insight into engine health assessment and management.

2.1.3.4 Parameter Estimation Techniques

Parameter estimation techniques are robust methods to employ in developing inverse models such as the inverse crankshaft dynamics models discussed in the Section above. In specific, parameter estimation techniques have vast applications in the field of engineering such as automation and control [123], aerospace [124], chemical [125], structural [126], hydraulic [127], as well as medical engineering [128]. Alternative terminologies found in the literature for parameter estimation include system identification, which primarily alludes to control and automation [129], and inverse problem techniques which primarily alludes to broader theoretical applications of primarily mathematical nature [130].

There are several techniques used for parameter estimation, the first of which is the Initial Value Problem (IVP) numerical approximation [131], otherwise known as the single shooting method [132]. In this technique, a model of the system is

used as part of an optimisation algorithm to perform simulations, whilst varying the values of its parameters appropriately, such that the simulated result matches the measured data [131]. The advantages include its computational simplicity [133, 134], and that the highly complex inverse structure of the problem (which may often be ill-posed) is completely bypassed [135]. However, a very good estimate of the initial parameters needs to be obtained, and the differential equations should have small sensitivity with respect to changes in the initial conditions, thereby demonstrating good stability characteristics [136].

To address the above shortcomings, a technique referred to as multiple shooting was developed [136]. In this case, the measured data set is split into several subsets, and the optimisation algorithm is deployed for each subset to match the modelled system response with the measured data. Therefore, to ensure continuity, a constrained optimisation Boundary Value Problem (BVP) is solved. The advantage in this technique is that the objective function is greatly simplified and any instability issues arising from the previous technique are significantly reduced [137], however at the cost of increased computational complexity [132].

Furthermore, to address the larger computational requirements of the above, collocation parameter estimation techniques have been developed [138] and formally formulated [139]. These methods smooth the measured data by basis functions such as polynomials or splines [140], and optimise the system's governing equations without integrating them, to match the derivative of the basis functions. Consequently, these methods have considerably reduced computational requirements, however introduce large uncertainties in the parameters estimated, especially in the case where a small signal to noise ratio is exhibited in the measurements [141].

Finally, to estimate parameters of differential equations ANNs have been extensively used in the past [142–144]. The advantages of using ANNs include their effectiveness in highly non-linear models, and explicit relationships between the input and measured output of the system do not have to be known a-priori (i.e. a black box approach). However, large data training sets are required for system conditions that may not be easily measured (e.g. faulty conditions), and the black box approach does not provide any physical insight on the system and its processes [144].

2.2 Research Gaps

Overall, first-principles digital twins are critical in offering physical insight into the engine processes, and subsequently enable the engine's health assessment. As a result they have been extensively discussed in the pertinent literature review, however the following research gaps have been identified:

1. Engine health assessment procedures involving diagnostics have demonstrated their benefits in the literature in other industries. However, regarding the shipping industry, the literature is lacking systematic approaches incorporating state-of-the-art data collection and processing methods, as well as first-principles digital twins which benchmark and baseline the engine, and provide actionable diagnostics information.
2. Continuous and instantaneous engine measurements are a critical enabler in performing engine health assessment since they allow for early identification of failures and degradation, as well as provide insight into important engine processes which change from cycle to cycle. However due to the large data sets required and the remote operation of ships, the current literature lacks the techniques and methodologies exploiting such measurements.
3. First-principles digital twins provide deeper insight into the engine processes, and their current use in the literature primarily includes either thermodynamics or crankshaft dynamics models for specific types and engine configurations. However, such models are employed as part of disparate approaches, lacking a unified systematic methodology which incorporates configurable thermodynamics and crankshaft dynamics models for various marine engines to enable health assessment.
4. The thermodynamic model formulation requires a number of model constants and inputs, to ensure that the healthy as well as current engine operating conditions are captured effectively. However, the literature lacks a systematic approach for the determination of such unknown model constants and inputs, to underpin the rigor and detail of the calibration procedures and algorithms used.

5. Inverse crankshaft dynamics models provide a vital link between the mechanical and thermodynamic performance of the engine, particularly when considering critical and easy to obtain measurements such as the ICT can be utilised to provide vital information for the performance each cylinder. This however, has not not been demonstrated for marine applications which include added complexities in operating profiles, shafting system design, and excitation forces.
6. The direct crankshaft dynamics model is deployed as part of the inverse crankshaft dynamics model, and therefore plays a vital part when trying to predict the performance of individual cylinders. However, the literature contains limited discussion on the effect of the solution methods and numerical schemes of the non-linear differential equations on the direct crankshaft dynamics model performance.

Chapter 3

Research Methodology

To address the aim of this research, a model-based approach is employed with digital twins utilising a state-of-the-art torque sensor to obtain critical measurements, as part of a systematic framework. This framework is consistent of five stages as shown in Figure 3.1 which include:

1. Thermodynamics model
2. Healthy conditions digital twin
3. Crankshaft dynamics models
4. Current conditions digital twin
5. Engine health assessment

3.1 Thermodynamics Model

The thermodynamics model is a zero-dimensional engine model, which is configurable to four and two-stroke engines with any number of cylinders and turbochargers. The selection and formulation of said model is further described Chapter 4. In step 1.1 the various input data required are obtained and in step 1.2 the formulation for the single-cylinder engine model is setup. This formulation can be utilised for the combustion model calibration as described in stage 2 of the methodology, further details of which are given in Section 3.2 below.

Following the single-cylinder engine model setup, in step 1.3 the baseline turbocharger maps are utilised as input to the scaling methodology proposed in [145], and the turbocharger model governing equations are setup. In steps 1.4 and 1.5, the

engine manifolds model, followed by the multi-cylinder turbocharged engine model are setup respectively. The latter is accomplished by expanding the formulation of the single-cylinder model, and combining the turbocharger and manifolds models as described.

The thermodynamics model governing equations and setup in steps 1.1–1.5 described in Sections 4.2, whilst the solution method and model convergence of these equations are presented in Section 4.3

3.2 Healthy Conditions Digital Twin

To develop the healthy conditions digital twin, step 2.1 involves the shop test data collection from the respective shop test reports. Step 2.2 involves extraction of the initial and boundary conditions from the shop test reports, including the pressures and temperatures of the inlet and exhaust receivers/manifolds.

Step 2.3 takes advantage of the mathematical and computational simplicity of the single-cylinder engine model to perform the combustion model calibration as described in Section 4.5. Specifically, the shop test data is used to obtain the Brake Specific Fuel Consumption (BSFC), and peak in-cylinder pressures which are utilised as part of the objective function for this calibration step. The calibration process itself takes place in 2 parts. In the first part the Wiebe function and FMEP are calibrated to determine the duration of combustion, Wiebe exponent, and FMEP factor. The Wiebe function and FMEP calibration is performed at a single engine operating point referred to as the reference operating point. This is chosen from the shop tests to lie within the engine’s most frequent operational envelope. In the second stage, the Woschni-Anisits model calibration takes place to find the values of its respective constants. This takes place at all shop test loads.

Both parts of the calibration process use a particle swarm optimisation algorithm which is most effective in determining a global minimum particularly since the single Wiebe function utilised to simulate is known to yield similar results for widely different combinations of its parameters [72]. Subsequently a gradient-free algorithm such as the one employed in this case is suitable in overcoming local minima.

Following the two part calibration process, the step 2.4 involves deploying the

calibrated parameters of the combustion model in the multi-cylinder turbocharged engine model, thus setting up the digital twin for healthy engine conditions.

Two case studies are dedicated to this stage as described in Section 6.2 which firstly demonstrate the 2-part healthy conditions digital twin calibration process, and secondly the healthy conditions digital twin, by deriving performance maps of key parameters including BSFC, boost pressure, peak pressure, Indicated Mean Effective Pressure (IMEP), Exhaust Gas Temperature (EGT) and equivalence ratio. Furthermore the first case study is implemented for 2 and 4-stroke propulsion engines to demonstrate the versatility of the thermodynamics model.

3.3 Crankshaft Dynamics Models

The crankshaft dynamics models play a vital role in the setup of the current conditions digital twin. In step 3.1, the necessary input is provided which includes DOF coefficients, load torque data, solver settings and engine geometric data. Utilising the input, in step 3.2 the direct crankshaft dynamics model is setup as described in Sections 5.1.1–5.1.3 which is calibrated for the current engine conditions as part of stage 4 below.

The direct crankshaft dynamics model is employed in the step 3.3 in order to setup the inverse crankshaft dynamics model. In specific, the inverse crankshaft dynamics model is able to reconstruct the in-cylinder pressure curves utilising the measured engine ICT, and a parameter estimation technique as described in Section 5.2.5. As a result, by nature of this technique the direct crankshaft dynamics model becomes an essential part of the inverse crankshaft dynamics model.

Due to the criticality of the direct crankshaft dynamics model in the overall research methodology, a case study is dedicated to this stage, to determine the solution method of said model as discussed in Section 6.2. In specific, by investigating three alternative solution methods and combinations of their respective user-defined settings for a 2-stroke generator engine as described in Sections 5.1.4–5.1.6, the best performing solution method is determined by considering criteria of accuracy and execution time.

3.4 Current Conditions Digital Twin

The current conditions digital twins capitalises on all of the above stages of the framework, by combining measured data, the thermodynamics model, as well as the crankshaft dynamics models. In specific, in steps 4.1 and 4.2 the measured in-cylinder pressure and engine ICT are collected, corrected and processed respectively, using a pressure sensor and a high-sample rate prototype torque meter, more details of which are provided in Appendix D–C.

The in-cylinder pressure measurement is utilised for the calibration of specific DOF coefficients from the direct crankshaft dynamics model in step 4.3 as discussed in Section 5.1.8, and can be obtained by the user at at only a few engine operating points, preferably at least two. The measurement of ICT is performed continuously by the torque meter during normal engine operation, and is eventually deployed in the inverse crankshaft dynamics model in step 4.4. In step 4.4, the calibrated DOF coefficients are deployed in the inverse crankshaft dynamics model together with the ICT measurements, to obtain the reconstructed in-cylinder pressure curves as described in Section 5.2. Even though the in-cylinder pressure measurements are available in this study, the above demonstrates a novel method by which the measured ICT can be utilised to monitor continuously and thereby obtain the in-cylinder pressures of the engine at any engine operating point. The critical information obtained can be subsequently employed straight away for diagnostics, or further processing in the current conditions digital twin such as in this case.

Steps 4.5 and 4.6 extract the parameters of the in-cylinder pressure curves which include the start of combustion, duration of combustion, Wiebe exponent, and mass of fuel injected in each cylinder, and are then deployed in the thermodynamics model to configure it for the current engine conditions as described in Section 4.6. In short, depending on the number of operating points where the in-cylinder pressure parameters are available, intermediate operating points can be interpolated to be able to run the current conditions digital twin for a sufficiently wide operating envelope. Otherwise, the parameters for a single operating point can be chosen and the thermodynamics model can be deployed along with semi-empirical combustion models which predict how the in-cylinder pressure parameters change within a sufficiently large operating envelope.

Four case studies are designed to demonstrate this stage of the research methodology as described in Section 6.2. Firstly the direct crankshaft dynamics model is calibrated, secondly the inverse crankshaft dynamics is verified, thirdly the current conditions digital twin is calibrated, and lastly the current conditions performance maps are generated. All of the above take place for a 4-stroke propulsion engine.

3.5 Engine Health Assessment

The health assessment is the last stage of the framework for engine health diagnostics and is presented in greater detail in Section 4.7. In step 5.1, engine performance maps of critical parameters are derived by performing parametric runs for both digital twins for a wide engine operating envelope. These parameters include BSFC, peak in-cylinder pressure, IMEP, equivalence ratio, boost pressure, and EGT after the exhaust valve.

Subsequently in step 5.2 KPIs are derived which involve the parameter maps derived in the previous step. These KPIs include:

1. BSFC percentage difference between healthy and current engine conditions.
2. Peak in-cylinder pressure percentage difference between healthy and current engine conditions.
3. IMEP percentage difference between healthy and current engine conditions.
4. Cylinder EGT at the exhaust valve percentage difference between healthy and current engine conditions.

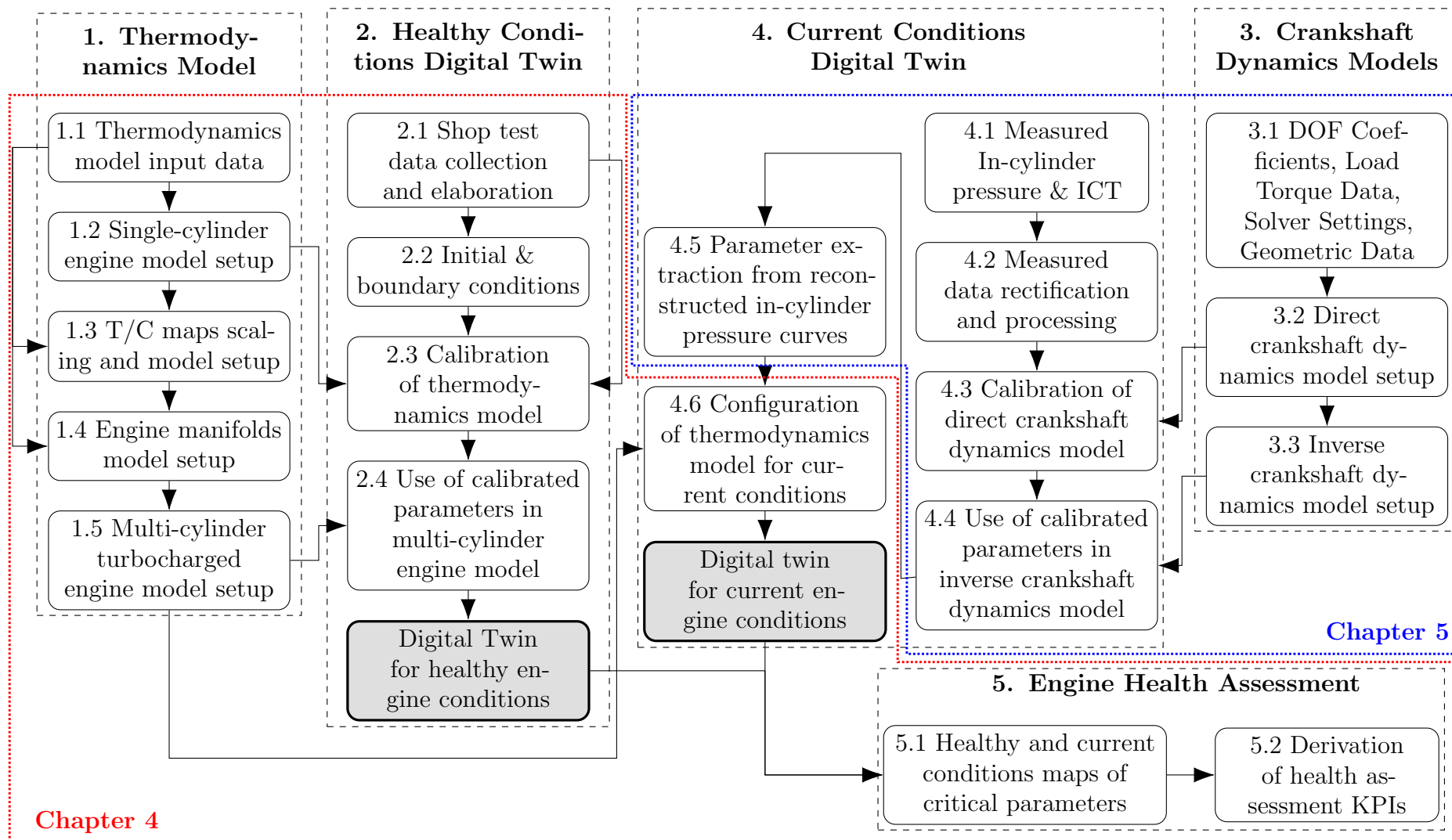


Figure 3.1: Intelligent engine health assessment framework utilising digital twins.

Chapter 4

Thermodynamics Model

The aim of this chapter is to describe the process of setting up and calibrating the thermodynamics model. Firstly the system of governing equations is derived in Section 4.2 which include the cylinders, turbochargers and manifolds models formulations. Subsequently, the solution method (i.e. the numerical scheme employed) is described in addition to the model convergence algorithm in Section 4.3. This is followed by the description of the calibration procedure in Section 4.5 that concludes the setup of the healthy conditions digital twin, as well as the configuration of the current condition digital twin using the appropriate input data in Section 4.6. Last, the engine health assessment procedure is described in Section 4.7.

4.1 Thermodynamics Model Overview

The thermodynamics model is utilised to simulate the operation of either a two or a four-stroke diesel engine with any number of cylinders and turbochargers, by employing as a configurable user input the engine operating point (i.e. the shaft power and speed), in addition to other various engine specific data as detailed in Section 4.4. The four-stroke variant of the thermodynamics model employs a single-zone formulation due to its proven in-cylinder pressure prediction capabilities, whilst for the two-stroke variant employs a two-zone formulation as it is able to accurately capture the complexities of scavenging as discussed in Chapter 2.

The thermodynamics model, as shown in Figure 4.1 is comprised by three models including the turbocharger, manifolds (inclusive of the air cooler), and the cylinders,

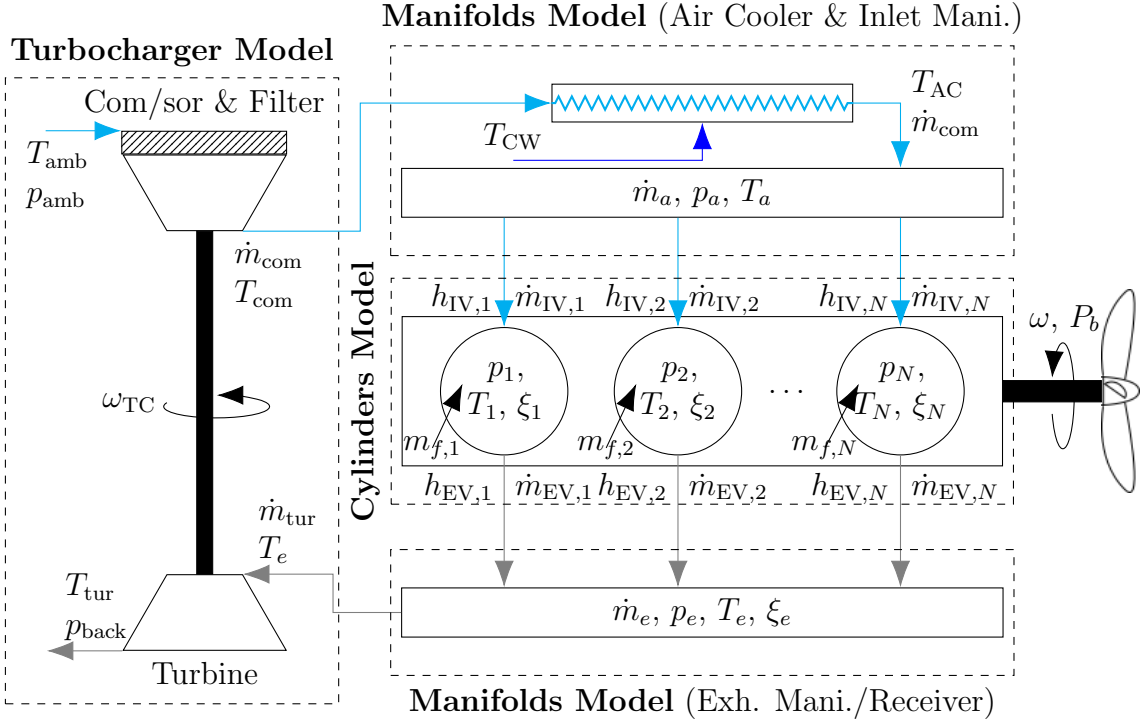


Figure 4.1: Overview of the thermodynamics model.

where for the sake of brevity only a single turbocharger is shown in the respective figure. Following the air path, the engine room air with ambient temperature and pressure T_{amb} and p_{amb} respectively, is compressed by the turbocharger compressor which induces a mass flow rate \dot{m}_{com} and increases the air temperature to T_{com} . Subsequently, considering the air cooler effectiveness and the cooling water temperature T_{CW} , the air thermodynamic properties at the air cooler outlet can be simulated, most notably including the temperature T_{AC} . The thermodynamic properties within the inlet manifold can be simulated which include the air mass flow \dot{m}_a , inlet/scavenge air pressure p_a and temperature T_a .

The cylinders model takes as boundary conditions the simulated thermodynamic properties of the inlet and exhaust manifolds, which include the pressure, temperature and burnt fuel fraction (where applicable). In specific, the boundary conditions from the inlet manifold of air pressure and temperature are employed by the inlet valve/scavenge port isentropic flow model, and the cylinder inlet mass flow rate \dot{m}_{IV} is simulated. Subsequently, by considering a single or two-zone thermodynamics formulation the in-cylinder state variables of pressure p , temperature T and burnt fuel fraction ξ are simulated, by also providing as input the mass of fuel injected

per cycle m_f . The cylinder exhaust valve mass flow rate \dot{m}_{EV} is simulated using the same isentropic flow model as for the inlet valves, and the outlet boundary conditions are the simulated thermodynamic properties of the exhaust manifold.

Therefore, the thermodynamic properties of exhaust gas in the exhaust manifold/receiver of mass flow rate \dot{m}_e , pressure p_e , temperature T_e , and burnt fuel fraction are simulated. Subsequently, by considering primarily the turbine map and exhaust system back pressure p_{back} , the turbine mass flow rate \dot{m}_{tur} and outlet temperature T_{tur} can be simulated.

4.2 System of Governing Equations

4.2.1 Single-Zone & Two-Zone Cylinder Models

4.2.1.1 Formulation

The single-zone formulation considers the cylinder as one uniform volume, and therefore stems from the application of the first law of thermodynamics in differential form:

$$\dot{U} = \dot{Q} - \dot{W} + \dot{H} \quad (4.1)$$

$$\Rightarrow m\dot{u} + \dot{m}u = \dot{Q} - p\dot{V} + \dot{H} \quad (4.2)$$

where the specific internal energy is a function of temperature, pressure and equivalence ratio such that $u(T, p, \phi)$. Consequently, by firstly taking the internal energy derivative and substituting it in Equation 4.2, and secondly rearranging the same equation such that the terms involving the state variable derivatives of temperature and pressure are kept on the right hand side, the following equations can be derived:

$$m \left(\frac{\partial u}{\partial T} \dot{T} + \frac{\partial u}{\partial p} \dot{p} + \frac{\partial u}{\partial \phi} \dot{\phi} \right) + \dot{m}u = \dot{Q} - p\dot{V} + \dot{H} \quad (4.3)$$

$$\Rightarrow m \frac{\partial u}{\partial T} \dot{T} + m \frac{\partial u}{\partial p} \dot{p} = \dot{Q} - p\dot{V} + \dot{H} - \dot{m}u - m \frac{\partial u}{\partial \phi} \dot{\phi} \quad (4.4)$$

Considering that Equation 4.4 contains three unknowns of pressure, temperature, and equivalence ratio, two additional differential equations are required to form a

solvable system. Firstly, this can be accomplished by differentiating the ideal gas law $pV = mRT$. Furthermore, by considering that the ideal gas constant R is a function of temperature, pressure and equivalence ratio, the ideal gas law can be differentiated according to the following equations:

$$\dot{p}V = \dot{m}RT + m \left(\frac{\partial R}{\partial T} \dot{T} + \frac{\partial R}{\partial p} \dot{p} + \frac{\partial R}{\partial \phi} \dot{\phi} \right) T + mR\dot{T} - p\dot{V} \quad (4.5)$$

$$\Rightarrow - \left(mT \frac{\partial R}{\partial T} + mR \right) \dot{T} + \left(V - mT \frac{\partial R}{\partial p} \right) \dot{p} = \dot{m}RT + mT \frac{\partial R}{\partial \phi} \dot{\phi} - p\dot{V} \quad (4.6)$$

Secondly, by considering the definition of the equivalence ratio as shown in Equation 4.7 [146], the third equation can be formulated by introducing a third state variable of the burnt fuel fraction. Subsequently, Equation 4.7 can be differentiated and rearranged such that the derivative of the burnt fuel fraction is on the left hand side, as shown in Equation 4.8:

$$\phi = \text{FA}_s \frac{\xi}{(1 - \xi)} \quad (4.7)$$

$$\Rightarrow \dot{\xi} = \dot{\phi} \text{FA}_s (1 - \xi)^2 \quad (4.8)$$

Finally, the energy conservation, ideal gas law, and burnt fuel fraction differential equations derived above according to Equations 4.2, 4.6 and 4.8 respectively, can be gathered within a matrix system, to be solved for the unknown state variable derivatives of temperature, pressure and burnt fuel fraction:

$$\underbrace{\begin{bmatrix} m \frac{\partial u}{\partial p} & m \frac{\partial u}{\partial T} & 0 \\ V - mT \frac{\partial R}{\partial p} & -m \left(R + T \frac{\partial R}{\partial T} \right) & 0 \\ 0 & 0 & 1 \end{bmatrix}}_{\mathbf{L}^{(1)}} \underbrace{\begin{bmatrix} \dot{p} \\ \dot{T} \\ \dot{\xi} \end{bmatrix}}_{\mathbf{X}^{(1)}} = \underbrace{\begin{bmatrix} \dot{Q} - p\dot{V} + \dot{H} - u\dot{m} - \frac{\partial u}{\partial \phi} m\dot{\phi} \\ T \left(\frac{\partial R}{\partial \phi} m\dot{\phi} + R\dot{m} \right) - p\dot{V} \\ \dot{\phi} \text{FA}_s (1 - \xi)^2 \end{bmatrix}}_{\mathbf{R}^{(1)}} \quad (4.9)$$

$$\Rightarrow \mathbf{L}^{(1)} \mathbf{X}^{(1)} = \mathbf{R}^{(1)} \quad (4.10)$$

where the superscript $\cdot^{(1)}$ refers to the single-zone formulation.

The two-zone model deployed for two-stroke engines splits the cylinder volume in two separate volumes or zones, the first containing charge air, and the second containing a mixture of charge air and exhaust. Therefore, similar to the one-zone

formulation, the first law of thermodynamics and the ideal gas law can be considered to develop the formulation of the two-zone model. For the first zone, Equations 4.4 and 4.6 will be utilised, where all partial derivatives except that of internal energy with respect to temperature will be set to zero, due to the low temperatures of charge air. Moreover, any terms involving the equivalence ratio can be set to zero since there is no mixing of charge air with exhaust in the first zone. Furthermore, an additional differential equation of the volume balance needs to be included. Consequently, the following additional governing equations are formulated for the two-zone model:

$$m_1 \frac{\partial u_1}{\partial T_1} \dot{T}_1 = \dot{Q}_1 - p\dot{V}_1 + \dot{H}_1 - \dot{m}_1 u_1 \quad (4.11)$$

$$m_1 R_1 \dot{T}_1 + V_1 \dot{p} = \dot{m}_1 R_1 T_1 - p\dot{V}_1 \quad (4.12)$$

$$\dot{V} = \dot{V}_1 + \dot{V}_2 \quad (4.13)$$

Regarding the second zone, the formulation will be identical to Equations 4.4 and 4.6, with the only difference being that the relevant mass, temperature, volume and partial derivative variables will be subscripted with the number 2, as reference to the second zone. As a result, the second zone governing equations are formulated below respectively:

$$m_2 \frac{\partial u_2}{\partial T_2} \dot{T}_2 + m_2 \frac{\partial u_2}{\partial p} \dot{p} = \dot{Q}_2 - p\dot{V}_2 + \dot{H}_2 - \dot{m}_2 u_2 - m_2 \frac{\partial u_2}{\partial \phi} \dot{\phi} \quad (4.14)$$

$$\begin{aligned} - \left(m_2 T_2 \frac{\partial R_2}{\partial T_2} + m_2 R_2 \right) \dot{T}_2 + \left(V_2 - m_2 T_2 \frac{\partial R_2}{\partial p} \right) \dot{p} = \dot{m}_2 R_2 T_2 \\ + m_2 T_2 \frac{\partial R_2}{\partial \phi} \dot{\phi} - p\dot{V}_2 \end{aligned} \quad (4.15)$$

Therefore, to provide the complete formulation of the two-zone model, Equa-

tions 4.8, 4.14–4.13 are combined, in accordance to the following matrix system:

$$\underbrace{\begin{bmatrix} 0 & 1 & 0 & 1 & 0 & 0 \\ B_L & p & -m_1 R_1 & 0 & 0 & 0 \\ 0 & p & m_1 \frac{\partial u_1}{\partial T_1} & 0 & 0 & 0 \\ V_2 - m_2 T_2 \frac{\partial R_2}{\partial p} & 0 & 0 & p & -m_2 R_2 - m_2 T_2 \frac{\partial R_2}{\partial T_2} & 0 \\ m_2 \frac{\partial u_2}{\partial p} & 0 & 0 & p & m_2 \frac{\partial u_2}{\partial T_2} & 0 \\ 0 & 0 & 0 & 0 & 0 & 1 \end{bmatrix}}_{\mathbf{L}^{(2)}} \underbrace{\begin{bmatrix} \dot{p} \\ \dot{V}_1 \\ \dot{T}_1 \\ \dot{V}_2 \\ \dot{T}_2 \\ \dot{\xi}_2 \end{bmatrix}}_{\mathbf{X}^{(2)}} \quad (4.16)$$

$$= \underbrace{\begin{bmatrix} \dot{V} \\ \dot{m}_1 R_1 T_1 \\ B_R \\ T_2 \left(\dot{m}_2 R_2 + \frac{\partial R_2}{\partial \phi} m_2 \dot{\phi} \right) \\ \dot{Q}_2 + \dot{H}_2 - \dot{m}_2 u_2 - \frac{\partial u_2}{\partial \phi} m_2 \dot{\phi} \\ \dot{\phi} \text{FA}_s (1 - \xi)^2 \end{bmatrix}}_{\mathbf{R}^{(2)}}$$

$$\Rightarrow \mathbf{L}^{(2)} \mathbf{X}^{(2)} = \mathbf{R}^{(2)} \quad (4.17)$$

where:

$$B_L = \begin{cases} V_1 & \text{if } v_1/V > 1 \times 10^{-3} \\ 1 & \text{else} \end{cases}, \quad B_R = \begin{cases} \dot{Q}_1 + \dot{H}_1 - \dot{m}_1 u_1 & \text{if } v_1/V > 1 \times 10^{-3} \\ 0 & \text{else} \end{cases}$$

The variables B_L and B_R take the values of 1 and 0 respectively when the volume of the first zone has not been formed adequately such that matrix $\mathbf{L}^{(2)}$ can remain invertible and the solution of the differential equations can continue without singularities. This occurs during the closed part of the thermodynamic cycle, and at the beginning of the scavenging process. Subsequently, provided that the first zone has formed appropriately as decided by the criterion $v_1/V > 1 \times 10^{-3}$, the values of B_L and B_R change as indicated above, to incorporate the second zone formulation and the effects of scavenging into the thermodynamics model.

4.2.1.2 Description of Terms

In the single and two-zone formulations shown in Equations 4.9 and 4.16 respectively, the the internal energy u and ideal gas constant R , as well as all of their respective partial derivatives with respect to pressure, temperature and equivalence ratio, in addition to the ratio of specific heats γ and enthalpy h , are calculated using known properties of combustion gas properties [147]. In addition, the stoichiometric fuel-air ratio FA_s is taken as 0.0694 for marine diesel fuel [148].

For the case of the single-zone formulation, the cylinder mass is obtained through the following mass balance equation:

$$\dot{m} = \dot{m}_{IV} - \dot{m}_{EV} + \dot{m}_{fb} \quad (4.18)$$

For the case of the two-zone formulation, the mass of each zone is obtained through the following three mass balance equations which denote; the mass flow rates in the charge air and the exhaust gas zones, as well as the flow rate from the charge air zone to the exhaust gas zone respectively:

$$\dot{m}_1 = (1 - \chi) \dot{m}_{IV} \quad (4.19)$$

$$\dot{m}_2 = \chi \dot{m}_{IV} - \dot{m}_{EV} + \dot{m}_{fb} \quad (4.20)$$

$$\dot{m}_{1,2} = \chi \dot{m}_{IV} \quad (4.21)$$

where subscripts IV and EV refer to the inlet valve/scavenge port and exhaust mass flow rates valves respectively, χ denotes the scavenging mixing factor which takes known values for certain engine types and operating points [105], and \dot{m}_{fb} denotes the fuel burnt mass flow rate which is obtained in accordance to the combustion model described in Section 4.2.1.3.

Furthermore, the valve or scavenge port mass flow rates are obtained by using the isentropic flow equations of the exhaust and inlet valves or ports respectively [146]:

$$\dot{m}_{\text{valve}} = A_{\text{valve}} \frac{p_u}{\sqrt{RT_u}} \Gamma(p_d/p_u) \quad (4.22)$$

and

$$\Gamma(\Pi) = \begin{cases} \sqrt{\gamma \left(\frac{2}{\gamma+1}\right)^{\frac{\gamma+1}{\gamma-1}}} & \text{if } \Pi < \frac{2}{\gamma+1} \gamma^{-1} \\ \sqrt{\frac{2\gamma}{\gamma-1} \left(\left(\frac{2}{\gamma+1}\right)^{\frac{2(\gamma-1)}{\gamma}} - \left(\frac{2}{\gamma+1}\right)^{\frac{\gamma^2-1}{\gamma}} \right)} & \text{else} \end{cases} \quad (4.23)$$

where A_{valve} is the valve effective area as a function of crank angle and subscripts u and d refer to the upstream and downstream variables respectively. Therefore, the inlet and outlet valve mass flow rates are functions of the upstream and downstream pressures, upstream temperature, ideal gas constant and ratio of specific heats, as well as the valve effective area.

The heat release rates denoted by \dot{Q} for the single and two-zone formulations can be calculated by considering the heat transfer rate according to the Woschni model [149], and the heat released during fuel combustion. The latter of which is not included in first zone of the two-zone formulation, since no combustion phenomena take place there. As a result, the heat release rates can be formulated according to the following equations respectively:

$$\dot{Q} = \dot{m}_{fb} h_f - G_{\text{Wos}} \sum_i A_i (T - T_i) \quad (4.24)$$

$$\dot{Q}_1 = -G_{\text{Wos}} \left(A_p (T - T_p) + A_{\text{lin}} \frac{V_1}{V} (T - T_{\text{lin}}) \right) \quad (4.25)$$

$$\dot{Q}_2 = \dot{m}_{fb} h_f - G_{\text{Wos}} \left(\sum_{i, i \neq \text{lin}} A_i (T - T_i) + A_{\text{lin}} \frac{V_2}{V} (T - T_{\text{lin}}) \right) \quad (4.26)$$

where the subscript lin refers to the cylinder liner, h_f denotes the fuel enthalpy of formation, G_{Wos} is the Woschni heat transfer coefficient, and A_i , T_i are the heat transfer areas and surface temperatures respectively for the piston, cylinder head, liner and exhaust valve.

The heat transfer rates denoted by \dot{H} for the single and two-zone formulations, include the enthalpy balance across the entire cylinder for the case of the single-zone formulation, or across each zone for the case of the two-zone formulation according

to the equations below respectively:

$$\dot{H} = \dot{m}_{IV} h_a - \dot{m}_{EV} h_e \quad (4.27)$$

$$\dot{H}_1 = \dot{m}_{IV} h_a - \dot{m}_{1,2} h_1 \quad (4.28)$$

$$\dot{H}_2 = \dot{m}_{1,2} h_1 - \dot{m}_{EV} h_e \quad (4.29)$$

where subscripts a and e denote the air and exhaust respectively, and the specific enthalpies can be calculated using known gas properties [147].

A critical output of the cylinder model besides the values of the state variables provided in Equations 4.10 and 4.17, would be the brake power of the engine. This can be calculated following the integration of the complete formulation equations, and utilising the value obtained for the in-cylinder pressure state variable p , according to the equation below:

$$P_b = 4 \frac{\pi}{\omega} \left(\oint p dV - \text{fmep} V_d \right) \quad (4.30)$$

where fmep is the friction mean effective pressure given by the Chen-Flynn model [150] according to the following equation:

$$\text{fmep} = \text{fmep}_0 (m_1 + m_2 \max\{p\} + m_3 r \omega) \quad (4.31)$$

and the model constants m are known from parent engines [105, 151], with fmep_0 being used as a calibration factor further described in Section 4.5.

4.2.1.3 Combustion Model

The combustion model is utilised to calculate the fuel burnt mass flow rate \dot{m}_{fb} , according to the single Wiebe function and in accordance to the following equation:

$$\dot{m}_{fb} = m_f \omega \frac{a(w+1)}{\theta_{\text{DOC}}} \left(\frac{\theta - \theta_{\text{SOC}}}{\theta_{\text{DOC}}} \right)^w \exp \left\{ -a \left(\frac{\theta - \theta_{\text{SOC}}}{\theta_{\text{DOC}}} \right)^{w+1} \right\} \quad (4.32)$$

where m_f is the total fuel injected in the cylinder per cycle, and a is set to 6.9078 to maintain a combustion efficiency of 99.9% [152]. In addition, θ_{SOC} denotes the start of combustion crank angle, which is calculated in accordance to the following

equation:

$$\theta_{\text{SOC}} = \theta_{\text{SOI}} + \theta_{\text{IGD}} \quad (4.33)$$

and the start of injection θ_{SOI} is known and the ignition delay θ_{IGD} is calculated in accordance to the Sitkey model [149].

Furthermore, the variation of the duration of combustion θ_{DOC} , and Wiebe exponent w , in response to a change in the engine operating point can be accounted for using the Woschni-Anisits model:

$$\theta_{\text{DOC}} = \theta_{\text{DOC,ref}} \left(\frac{\omega}{\omega_{\text{ref}}} \right)^{g_1} \left(\frac{\phi_{\text{IVC}}}{\phi_{\text{IVC,ref}}} \right)^{g_2} \quad (4.34)$$

$$w = w_{\text{ref}} \left(\frac{\omega_{\text{ref}}}{\omega} \right)^{g_3} \left(\frac{p_{\text{IVC}} V_{\text{IVC}} T_{\text{IVC,ref}}}{p_{\text{IVC,ref}} V_{\text{IVC,ref}} T_{\text{IVC}}} \right)^{g_4} + \Delta w \quad (4.35)$$

where constants g and Δw are treated as calibration parameters of the Woschni-Anisits model, and the subscript ref refers to the engine reference operating point at which the respective variables are either calibrated (for the case of θ_{DOC} and w) or obtained by calibration (for the case of the rest), as described further in Section 4.5.

4.2.2 Turbocharger Model

The turbocharger model is utilised to calculate mass flow rates and outlet temperatures of the compressor and turbine, which are employed by the manifolds model in Section 4.2.3. The only differential equation of the turbocharger model involves its speed as the state variable, which can be derived considering the turbocharger torque balance and the power of the turbine and compressor:

$$\dot{\omega}_{\text{TC}} = \frac{P_{\text{tur}} - P_{\text{com}}}{J_{\text{TC}} \omega_{\text{TC}}} \quad (4.36)$$

where P_{tur} and P_{com} refer to the turbine and compressor power, and J_{TC} refers to the turbocharger impeller, shaft and turbine blades inertia. The turbocharger compressor and turbine power used in Equation (4.36) can be calculated using the following

equations respectively [153]:

$$P_{\text{tur}} = \dot{m}_{\text{tur}} \hat{c}_e T_e \left(1 - \Pi_{\text{tur}}^{\frac{1-\gamma_e}{\gamma_e}} \right) \eta_{\text{tur}} \quad (4.37)$$

$$P_{\text{com}} = \dot{m}_{\text{com}} \hat{c}_a T_{\text{amb}} \left(\Pi_{\text{com}}^{\frac{\gamma_a-1}{\gamma_a}} - 1 \right) \eta_{\text{com}}^{-1} \quad (4.38)$$

where \hat{c} denotes the specific heat capacity at constant pressure, η_{tur} denotes the combined isentropic and mechanical efficiency of the turbine, and η_{com} is the compressor isentropic efficiency. The expansion and compression ratios from Equations (4.37)–(4.38) can be calculated according to the following formulas respectively:

$$\Pi_{\text{tur}} = \frac{p_e}{p_{\text{back}} + p_{\text{amb}}} \quad (4.39)$$

$$\Pi_{\text{com}} = \frac{p_a - \Delta p_{\text{AC}}}{p_{\text{amb}} + \Delta p_{\text{filt}}} \quad (4.40)$$

where Δp_{AC} and Δp_{filt} denote the pressure drop in the compressor filter and air cooler respectively, which are proportional the square of the compressor mass flow rate according to the following equations [154]:

$$\Delta p_{\text{AC}} = f_{\text{AC}} \frac{1}{2\rho_a} \dot{m}_{\text{com}}^2 \quad (4.41)$$

$$\Delta p_{\text{filt}} = f_{\text{filt}} \frac{1}{2\rho_a} \dot{m}_{\text{com}}^2 \quad (4.42)$$

where the pressure drop coefficients are $f_{\text{AC}} \approx 0.5$ [155], and $f_{\text{filt}} \approx 2 \times 10^{-4}$ [95]. Furthermore, the pressure within the inlet and exhaust manifolds p_a and p_e respectively are calculated by the manifolds model described in Section 4.2.3.

The turbine mass flow rate and isentropic efficiency utilised in Equations (4.54), (4.58) and (4.37) can be calculated using the turbine expansion ratio according to the following equations:

$$\dot{m}_{\text{tur}} = \frac{b_1 + b_2 \Pi_{\text{tur}}}{b_3 + b_4 \Pi_{\text{tur}}} p_e \frac{1}{\sqrt{T_e}} \quad (4.43)$$

$$\eta_{\text{tur}} = c_1 + c_2 \Pi_{\text{tur}} + c_3 \Pi_{\text{tur}}^2 \quad (4.44)$$

where the constants b_1 to b_4 and c_1 to c_3 are determined via non-linear regression using the turbine map data obtained from the turbocharger manufacturer.

The compressor mass flow rate utilised in the manifolds model described in Section 4.2.3, can be determined by firstly utilising the turbocharger speed and compressor pressure ratio to calculate the blade tip speed, non-dimensional head, and inlet Mach number respectively:

$$U = \frac{1}{2} D_{\text{com}} \omega_{\text{TC}} r_{\omega} \quad (4.45)$$

$$\Psi = 2 \hat{c}_{\text{ISO}} T_{\text{ISO}} \left(\Pi_{\text{com}}^{\frac{\gamma_{\text{ISO}}-1}{\gamma_{\text{ISO}}}} - 1 \right) U^{-2} \quad (4.46)$$

$$M = \frac{U}{\sqrt{\gamma_{\text{ISO}} R_{\text{ISO}} T_{\text{ISO}}}} \quad (4.47)$$

where D_{com} is the compressor impeller diameter, and $r_{\omega} = \sqrt{T_{\text{amb}}/T_{\text{ISO}}}$ is the turbocharger speed correction factor. The compressor mass flow rate can subsequently be calculated according to the following equation:

$$\dot{m}_{\text{com}} = \rho_{\text{ISO}} \alpha (1 - \exp \{ \Psi^{\beta} - \mu \}) r_m^{-1} \quad (4.48)$$

where $r_m = (p_{\text{amb}}/p_{\text{ISO}}) / \sqrt{T_{\text{amb}}/T_{\text{ISO}}}$ is the flow rate correction factor and:

$$\alpha = k_1 + k_2 M + k_3 M^2 + k_4 M^3$$

$$\beta = k_5 + k_6 M + k_7 M^2$$

$$\mu = k_8 + k_9 M + k_{10} M^2$$

with constants k_1 to k_{10} determined via non-linear regression using the compressor map data obtained from the turbocharger manufacturer.

The compressor isentropic efficiency utilised in Equations (4.37)–(4.38) is calculated according to the following equation:

$$\eta_{\text{com}} = \sum_{j=1}^4 \sum_{k=1}^{4-(j-2)} d_{j,k} \Phi^{j-1} \Pi_{\text{com}}^{k-1} \quad (4.49)$$

where constants $d_{j,k}$ are determined via non-linear regression using the compressor map data, and Φ is the non-dimensional flow rate calculated in accordance to the following equation:

$$\Phi = \frac{\dot{m}_{\text{com}} r_m}{\rho_{\text{ISO}} \frac{\pi}{4} D_{\text{com}}^2 U} \quad (4.50)$$

Considering all the equations pertaining to turbocharger compressor, it is apparent that the mass flow rate and isentropic efficiencies can be both expressed as functions of the pressure ratio and turbocharger speed. Furthermore, considering Equations (4.40) and (4.41)–(4.42) the pressure ratio is also a function of the mass flow rate as well. Therefore, the above can be expressed in functional form by the following two equations:

$$\dot{m}_{\text{com}} = f_{\dot{m}_{\text{com}}}(\Pi_{\text{com}}(\dot{m}_{\text{com}}), \omega_{\text{TC}}) \quad (4.51)$$

$$\eta_{\text{com}} = f_{\eta_{\text{com}}}(\Pi_{\text{com}}(\dot{m}_{\text{com}}), \omega_{\text{TC}}) \quad (4.52)$$

Hence, since the term \dot{m}_{com} appears in both sides of Equation (4.51), a non-linear equation needs to be solved which can be achieved using a simple fixed-point iteration algorithm as described in Section 4.2.4.

4.2.3 Manifolds Model

To model the engine manifolds, four differential equations are needed that calculate the thermodynamic properties of the gases contained within the manifolds which can be derived by either the mass or the energy balance. Firstly, the inlet manifold or scavenge air receiver differential equations involve the mass and temperature state variables:

$$\dot{m}_a = \dot{m}_{\text{com}} - \sum_n^N \dot{m}_{\text{IV},n} \quad (4.53)$$

$$\dot{T}_a = \left(\dot{m}_{\text{com}} h_{\text{AC}} - \sum_n^N \dot{m}_{\text{IV},n} h_{\text{IV},n} - u_{\text{AC}} \dot{m}_a \right) \left(m_a \frac{\partial u_{\text{AC}}}{\partial T_{\text{AC}}} \right)^{-1} \quad (4.54)$$

where the subscript AC refers to the air cooler, and N is the total number of cylinders. Furthermore, the air cooler specific enthalpy h_{AC} can be calculated by considering the air as an ideal gas. Specifically, it is a function of the temperature of the air exiting the air cooler T_{AC} , which can be calculated according to the following equation:

$$T_{\text{AC}} = T_{\text{com}} - \eta_{\text{AC}}(T_{\text{com}} - T_{\text{CW}}) \quad (4.55)$$

where the subscript CW refers to the cooling water, and η_{AC} is the air cooler effectiveness which is calculated as a function of the compressor mass flow rate using known coefficients from parent engines [154, 156]:

$$\eta_{AC} = p_1 \dot{m}_{com}^2 + p_2 \dot{m}_{com} + p_3 \quad (4.56)$$

The exhaust manifold or receiver differential equations involve the mass, temperature and burnt fuel fraction:

$$\dot{m}_e = \sum_n^N \dot{m}_{EV,n} - \dot{m}_{tur} \quad (4.57)$$

$$\dot{T}_e = \left(\sum_n^N \dot{m}_{EV,n} h_{EV,n} - \dot{m}_{tur} h_e - u_e \dot{m}_e - \dot{Q}_{loss} \right) \left(m_e \frac{\partial u_e}{\partial T_e} \right)^{-1} \quad (4.58)$$

$$\dot{\xi}_e = \left(\sum_n^N \dot{m}_{EV,n} \xi_{e,n} - \dot{m}_{tur} \xi_e - \dot{m}_e \xi_e \right) m_e^{-1} \quad (4.59)$$

where \dot{Q}_{loss} stands for the heat loss of the exhaust manifold or receiver, and can be calculated in accordance to the following equation:

$$\dot{Q}_{loss} = G_e A_e (T_e - T_{amb}) \quad (4.60)$$

and $G_e = 10.8 \text{ W/m}^2\text{K}$ is the thermal conductivity of the exhaust manifold insulation [157], and A_e is the surface area of the exhaust manifold or receiver.

In addition, the pressure within the manifolds which is utilised by the turbocharger model can be calculated utilising the ideal gas law, according to the below equations:

$$p_a = \frac{m_a R_a T_a}{V_a} \quad (4.61)$$

$$p_e = \frac{m_e R_e T_e}{V_e} \quad (4.62)$$

where V_a and V_e are the volumes of the inlet and exhaust manifolds respectively (or scavenge air and exhaust receivers for the case of two-stroke engines).

4.2.4 Complete Formulation

The complete formulation of the thermodynamics model commences by combining the turbocharger and manifold governing equations as derived in Sections 4.2.2–4.2.3 above. In specific Equations 4.36, 4.53–4.54, 4.57–4.59 can be combined in the following matrix system of equations:

$$\begin{array}{c}
 \begin{array}{c} \mathbf{T} \\ \hline \left[\begin{array}{cccc} J_{TC}\omega_{TC} & & & \\ & 1 & & \\ & & m_a \frac{\partial u_{AC}}{\partial T_{AC}} & \\ & & & 1 \\ & & & & m_e \frac{\partial u_e}{\partial T_e} \\ & & & & & m_e \end{array} \right] \end{array} \\
 \begin{array}{c} \mathbf{Y} \\ \hline \left[\begin{array}{c} \dot{\omega}_{TC} \\ \dot{m}_a \\ \dot{T}_a \\ \dot{m}_e \\ \dot{T}_e \\ \dot{\xi}_e \end{array} \right] \end{array} \\
 \\
 = \begin{array}{c} \left[\begin{array}{c} P_{tur} - P_{com} \\ \dot{m}_{com} - \sum_n^N \dot{m}_{IV,n} \\ \dot{m}_{com} h_{AC} - \sum_n^N m_{IV,n} h_{IV,n} - u_{AC} \dot{m}_a \\ \sum_n^N \dot{m}_{EV,n} - \dot{m}_{tur} \\ \sum_n^N m_{EV,n} h_{EV,n} - \dot{m}_{tur} h_e - u_e \dot{m}_e - \dot{Q}_{loss} \\ \sum_n^N \dot{m}_{EV,n} \xi_{e,n} - \dot{m}_{tur} \xi_e - \dot{m}_e \xi_e \end{array} \right] \\ \mathbf{S} \end{array} \\
 \Rightarrow \mathbf{TY} = \mathbf{S} \tag{4.63}
 \end{array}$$

To derive the complete formulation of the thermodynamics model, the turbocharger and manifolds, as well as the cylinder models (derived in Section 4.2.1) need to be considered. In specific, the cylinder model in matrix format provided by Equations 4.10 and 4.17 refer to only a single cylinder. Consequently, by replicating the same formulation for all engine cylinders, the relevant matrices can be concatenated into a larger system of equations, by also including the turbocharger and manifolds model provided by Equation 4.64. Subsequently, this larger system of equations representing the complete formulation, needs to be solved by using the

appropriate matrix inversions, to provide the following final version of the complete thermodynamics model formulation:

$$\begin{bmatrix} \mathbf{X}_1^{(z)} \\ \mathbf{X}_2^{(z)} \\ \mathbf{X}_3^{(z)} \\ \vdots \\ \mathbf{X}_N^{(z)} \\ \mathbf{Y} \end{bmatrix} = \begin{bmatrix} \mathbf{L}_1^{(z)} & & & & & \\ & \mathbf{L}_2^{(z)} & & & & \\ & & \mathbf{L}_3^{(z)} & & & \\ & & & \ddots & & \\ & & & & \mathbf{L}_N^{(z)} & \\ & & & & & \mathbf{T} \end{bmatrix}^{-1} \begin{bmatrix} \mathbf{R}_1^{(z)} \\ \mathbf{R}_2^{(z)} \\ \mathbf{R}_3^{(z)} \\ \vdots \\ \mathbf{R}_N^{(z)} \\ \mathbf{S} \end{bmatrix} \quad (4.65)$$

where z is either 1 or 2 depending on whether the single or two-zone cylinder models are employed respectively.

The complete formulation shown in Equation 4.65 above, is therefore configurable to either a two or a four-stroke engine by selecting whether a single or a two-zone cylinder model will be utilised respectively. Furthermore, it is also extendable to an engine with any number of cylinders, turbochargers or air coolers.

4.3 Solution Method & Model Convergence

The model convergence introduces additional complexities to the modelling process, as shown in Figure 4.2. In specific, the model convergence algorithm utilises a proportional fuel controller to adjust the total fuel injected once every engine cycle, for a given engine speed and brake power setpoint set by the user. Eventually, the steady state is identified if the difference of the turbocharger(s) speed between subsequent engine cycles is below the user set tolerance, in addition to the difference of the engine brake power as compared to the user setpoint.

The thermodynamics model governing equations are considered mildly stiff nonlinear differential equations when applied to medium and slow speed engines [158], as a result their solution does not pose particular challenges. Consequently, they are solved in MATLAB using the default stiff solver ODE23tb, which can easily handle the mild stiffness as well as the slight non-linearities. Furthermore, its higher order numerical scheme allows for employing larger time steps whilst maintaining

accuracy for this type of equations [159].

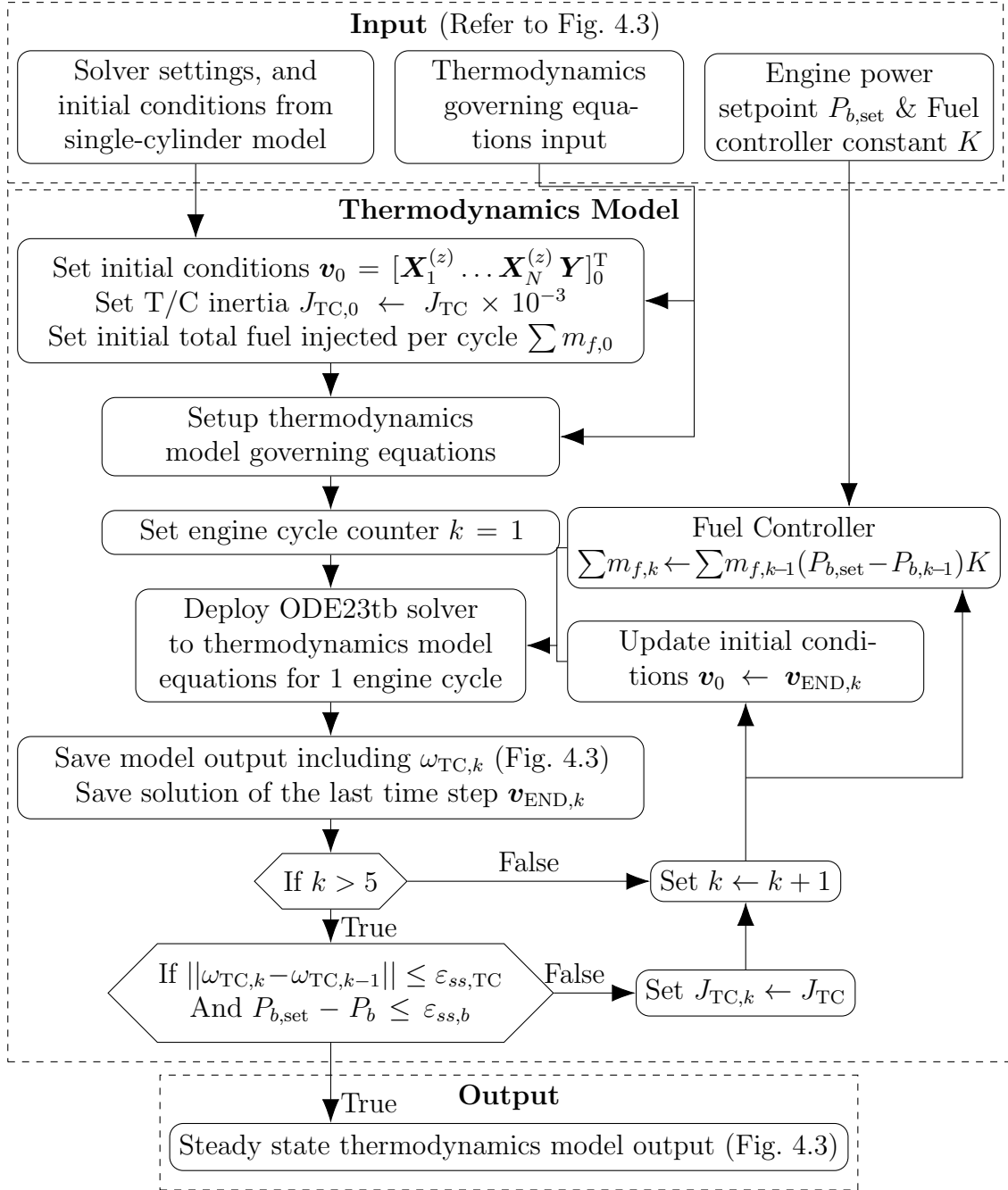


Figure 4.2: Thermodynamics model convergence algorithm.

Firstly, the input includes the solver settings for the ODE23tb which include the absolute and relative error tolerances, as well as the initial conditions estimates of pressure, temperature and burnt fuel fraction. These are obtained from the single cylinder model which is setup using the available shop test data. The estimates of the initial conditions can be obtained near a load of 50% (depending on the shop test data availability), which is close to the most frequently operating point of most

engines. Furthermore, the initial conditions can be approximate, thus they need not be obtained from a calibrated model. Secondly, the thermodynamics governing equations input data as discussed in Section 5.1.7, as well as the engine brake power setpoint and proportional controller constant are utilised as input.

Subsequently, the approximate initial conditions from the single cylinder model are phase-shifted according to the firing order and combined as part of the state variables vector, to be utilised in the differential equations solver. The turbocharger inertia is also reduced by a factor of 10^{-3} (only in the first 5 engine cycles) to accelerate the model's transition to the steady state. Finally, the initial mass of fuel injected is set using the BSFC of the shop tests at the same operating point that the initial conditions were approximated.

Following the above, the setup of the thermodynamics model and governing equations takes place as described in Section 4.2 taking into account the type of the engine (2 or 4 stroke) which affects the cylinders model formulation, as well as the number of turbochargers. The engine cycle counter is set to $k = 1$ and the solver is deployed to solve the thermodynamics model governing equations for one engine cycle. Since the differential equations are considered as stiff, a typical higher order solver is considered adequate. In this case, the ODE23tb from MATLAB's library has demonstrated quick computation and higher accuracy compared to other higher order solvers according to the author's experience.

Considering the thermodynamics model governing equations have been solved successfully for 1 engine cycle, the state variables are all saved (including the turbocharger speed), including their value for the last time step taken by the solver. If the model has been solved for a total of less than 5 engine cycles, then the process is repeated by updating the engine cycle counter, updating the initial conditions by using the ones obtained from the final step taken by the solver, and adjusting the mass of total fuel injected for the k^{th} cycle $\sum m_{f,k}$, according to the proportional fuel controller formula shown in Figure 4.2. If the model has been solved for 5 engine cycles or more, the turbocharger speed can be compared with from the last two cycles as well as the engine brake power compared to the setpoint. If those lie within the user-specified tolerances the model is considered to have reached steady state.

If not, the turbocharger inertia is updated to its actual value by removing the

multiplication factor of 10^{-3} , which was considered for the first 5 engine cycles to accelerate the model's transition to the steady state. Subsequently, the same process is repeated by updating the initial conditions and setting the updated mass of fuel injected according to the proportional controller equation.

4.4 Model Input, Output & Assumptions

The thermodynamics model input can be separated in six categories as detailed in Table 4.1 and demonstrated in Figure 4.3. Each input category relates to the respective part of the thermodynamics model, which comes with inherent assumptions.

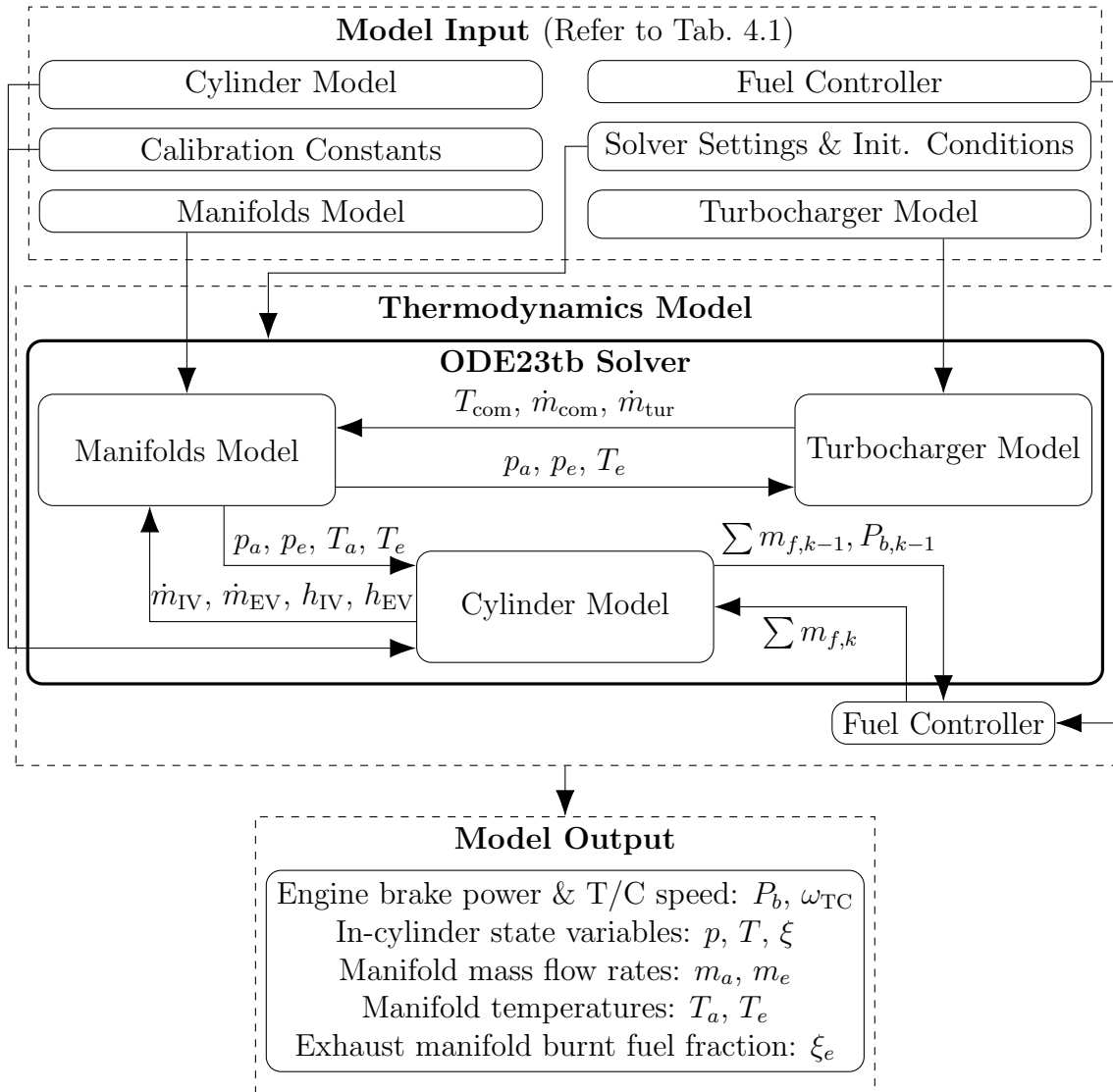


Figure 4.3: Thermodynamics model input and output.

In specific, the first input category is the cylinder model input data. The most

important of which include the average engine speed which is utilised in the Wiebe and Woschni-Anisits combustion models, as well as the engine type and number of cylinders, which dictate the cylinders model formulation. The rest of the input data include various values and constants which serve as input to the combustion models, Woschni heat transfer model, as well as the valve isentropic flow models.

The assumptions made in the cylinder models firstly include the zero-dimensional formulation of the model, which has no spatial resolution thus provide no information on the fluid mechanics. As a result the pressure and temperature values returned as output from the model can be considered as the average of the gases within the cylinder. Furthermore, the Wiebe and Woschni-Anisits combustion models are developed semi-empirically, thus do not entirely capture the physics of the combustion phenomena and rely on the calibration of their various parameters as described in Section 4.5. An assumption of lesser effect also includes the semi-empirical Woschni heat transfer model, the constants of which are selected in accordance to similar studies of large engines [95, 149].

The second input category is the turbocharger model input data, the most important input of which includes the compressor and turbine maps respectively, as listed on Table 4.1. The most significant assumptions of this model are also related to the aforementioned maps, as these are issued by manufacturers to represent steady state operation without including transients [153].

The third input category is the manifolds model input data, which includes geometrical data such as the manifolds volumes, and the cooling water inlet temperature, which is employed in the air cooler effectiveness model. The remaining input data including the manifold surface area, thermal conductivity and ambient temperature are utilised to calculate the exhaust manifold heat loss by employing Newton's law of cooling. The two inherit assumptions included there are that the temperature difference between the object and surroundings is small, and that the nature of the radiating surface remains the same [146]. Finally, the manifolds model is also zero dimensional, thus the same assumptions as for the cylinder model hold.

The fourth and fifth input categories are the calibration constants and fuel controller input data respectively. In specific, the calibration input data, they are deployed in the cylinders model, and the fuel controller input data include the engine

Table 4.1: Thermodynamics model input

Cylinder Model	Average engine speed: ω Type of engine (2 or 4-stroke) & no. of cylinders Firing order Initial fuel injected per cylinder per cycle: $m_{f,0}$ Stoichiometric fuel-air ratio: FA_s Scavenging mixing factor: χ Woschni-Anisits reference values: Eq. 4.34–4.35 Woschni heat transfer constants: Eq. 4.24–4.26 Geometric data: bore, con. rod length, stroke Valve profiles: A_{valve} Start of injection: θ_{SOI} Wiebe constant: a
Turbocharger Model	Compressor maps constants: Eq. 4.48–4.49 Turbine maps constants: Eq. 4.43–4.44 Ambient & ISO pressures and temperatures Impeller diameter: D_{com} Turbocharger inertia: J_{TC}
Manifolds Model	Manifold volumes: V_a, V_e Air cooler effectiveness constants: Eq. 4.55 Cooling water inlet temperature: T_{CW} Exhaust manifold surface area: A_e Exhaust manifold thermal conductivity: G_e Ambient temperature T_{amb}
Calibration Constants	Wiebe function: θ_{DOC}, w Woschni-Anisits: $g, \Delta w$ FMEP factor: fmep_0
Fuel Controller	Brake power setpoint: $P_{b,\text{set}}$ Controller constant: K

brake power set point as well as the controller constant. This is a proportional controller which re-adjusts the fuel injected per cylinder once every cycle as shown in Figure 4.2. Therefore, this does not reflect the behaviour of a realistic fuel controller, and is therefore simply utilised as a mathematical tool to help the model achieve steady state faster.

4.5 Calibration of Thermodynamics Model

The thermodynamics model calibration takes place in two parts as described in Section 3.2, by employing the single-cylinder model without a turbocharger, and a particle-swarm optimisation algorithm. In specific, in the first part of the cali-

bration, the the duration of combustion and Wiebe exponent as well as the FMEP factor are calibrated at the reference operating point. At this operating point, the reference values for the Woschni-Anisits model are obtained as well, to be utilised in Equations 4.34–4.35, and the second part of the calibration follows where the Woschni-Anisits model constants are calibrated for all operating points available in the shop tests.

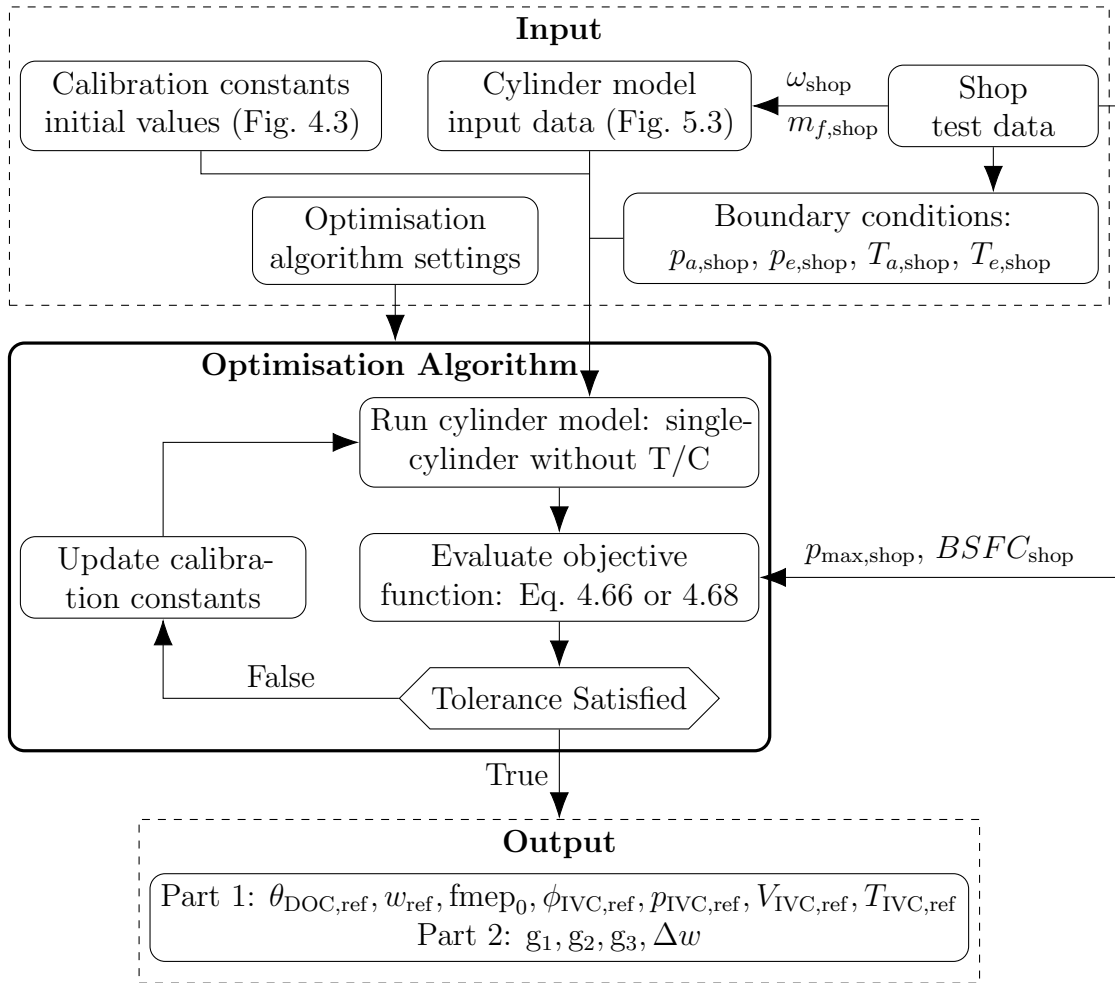


Figure 4.4: Thermodynamics model calibration procedure.

For both the first and second parts of the thermodynamics model calibration, the process employed is depicted in Figure 4.4. For the first part, the initial values of the calibration constants of θ_{DOC} , w and fmep_0 are estimated as input from the literature [151, 154], and the Woschni-Anisits constants (g and Δw) are all set to zero. Furthermore, a single operating point from the shop test data is chosen which lies within the engine’s most frequent operating envelope, referred to as the reference operating point. For the reference operating point, the engine average

speed is utilised, and mass of fuel injected per cylinder per cycle is calculated using the available BSFC measurements from the shop tests, and is provided as input to the cylinder model input data. In addition, the pressures and temperatures at the exhaust and inlet manifolds are obtained, which are utilised as the boundary conditions. Finally, the particle-swarm optimisation algorithm settings are provided, which primarily include the termination tolerance.

Subsequently, the objective function can be formulated by comparing the simulated BSFC and the maximum in-cylinder pressure (which are functions of the appropriate calibration constants), to the same values made available from the shop tests. To improve performance of the calibration, weights are also included in the objective function which are set to favour the BSFC term, as it encompasses the f_{mep_0} calibration factor, which the maximum in-cylinder pressure does not. Boundaries are also provided for the calibrated values, which are obtained in accordance to literature [149, 151, 156]. The formulation of the objective function and optimisation problem are shown in Equations 4.66–4.67 respectively:

$$O_{T,1} = w_{T,1} \left(\frac{BSFC_{sim,ref}(\theta_{DOC}, w, f_{mep_0}) - BSFC_{shop,ref}}{BSFC_{shop,ref}} \right) + w_{T,2} \left(\frac{p_{max,sim,ref}(\theta_{DOC}, w) - p_{max,shop,ref}}{p_{max,shop,ref}} \right) \quad (4.66)$$

$$\Rightarrow \min_{\theta_{DOC}, w, f_{mep_0}} \{O_{T,1}(\theta_{DOC}, w, f_{mep_0})\} \quad \text{subject to: } \begin{aligned} 40^\circ &\leq \theta_{DOC} \leq 110^\circ \\ 0.2 &\leq w \leq 2.0 \\ 0.6 &\leq f_{mep_0} \leq 1.4 \end{aligned} \quad (4.67)$$

where subscripts sim and ref denote the simulated values from the model and the reference operating point respectively, $w_{T,1}$ and $w_{T,2}$ are the weights set to 1 and 0.5 respectively, and $p_{max,shop}$ is the average of all maximum pressures obtained from the shop tests. Following the successful termination of the algorithm, the output includes the calibrated values of $\theta_{SOC,ref}$, w_{ref} and f_{mep_0} , which correspond to the reference operating point. Furthermore, the output also includes additional reference values such as the equivalence ratio at inlet valve close $\phi_{IVC,ref}$, as well as the pressure, volume and temperature at inlet valve close, $p_{IVC,ref}$, $V_{IVC,ref}$, $T_{IVC,ref}$. These will be deployed in the Woschni-Anisits model on the second part of the calibration.

The second part of the calibration uses the calibrated and reference values from the first part as described above, as well as initial values for the Woschni-Anisits model constants $g_{1,\dots,3}$ and Δw which are obtained from the literature [149, 151], and g_4 is set to 1. The same particle-swarm optimisation algorithm is utilised, however this time the objective function is formulated considering all the shop test operating points. The objective function formulation and optimisation problem are shown in Equations 4.68–4.69 respectively:

$$O_{T,2} = \sum_{i=1}^{\text{all shop test loads}} \left(w_{T,1} \frac{BSFC_{\text{sim},i}(g_{1,\dots,3}, \Delta w) - BSFC_{\text{shop},i}}{BSFC_{\text{shop},i}} + w_{T,2} \frac{p_{\text{max},\text{sim},i}(g_{1,\dots,3}, \Delta w) - p_{\text{max},\text{shop},i}}{p_{\text{max},\text{shop},i}} \right) \quad (4.68)$$

$$\begin{aligned} \Rightarrow \min_{g_{1,\dots,3}, \Delta w} \{O_{T,2}(g_{1,\dots,3}, \Delta w)\} \quad \text{subject to:} \quad & -0.30 \leq g_1 \leq 0.60 \\ & -0.65 \leq g_2 \leq 0.5 \\ & -0.80 \leq g_3 \leq 0.3 \\ & 0.10 \leq \Delta w \leq 0.80 \end{aligned} \quad (4.69)$$

Following the termination of the particle-swarm optimisation algorithm, the calibrated values of the Woschni-Anisits model constants are obtained as output from the second part of the calibration procedure.

4.6 Configuration of Current Conditions Digital Twin

The configuration of the current conditions digital twin takes place as shown in Figure 4.5. In specific, the first step is to obtain the in-cylinder pressure unknown parameters for every cylinder at all operating points where ICT measurements are available, using the inverse crankshaft dynamics model. Then, the analytic equation from Erikson and Anderson [160] is utilised to calculate the mass of fuel injected in each cylinder, using as input the p_{me} parameter which has been identified by the inverse crankshaft dynamics model.

Subsequently, if the in-cylinder pressure parameters have been obtained for

more than 10 operating points and cover more than 50% of the engine operating envelope, the parameters maps (including the mass of fuel injected) can be created by interpolation at any operating point within the limits of the measured engine operating envelope. For limits exceeding the measured operating envelope, the Woschni-Anisits model is used to extrapolate the aforementioned parameters maps. In the next step, these maps can be deployed to the Wiebe combustion model since they include all the required input parameters of mass fuel injected per cycle per cylinder, SOC, DOC, and Wiebe exponent. At this point the current conditions digital twin can be considered as configured.

If the in-cylinder pressure parameters are obtained for less than 10 operating points or less than 50% of the engine operating envelope, the parameter map is not able to be interpolated with sufficient accuracy. Consequently, the in-cylinder pressure parameters have to be obtained closest to the Woschni-Anisits reference point as mentioned in Section 4.2.1.3. The DOC, and Wiebe exponent parameters can then be deployed to the Woschni-Anisits model, whilst the SOC can be assumed to remain the same for the entire operating envelope (unless variable injection timing is employed). The percentage of the mass of fuel injected per cylinder can then be calculated and deployed to the Wiebe combustion model in Section 4.2.1.3 for the entire operating envelope, whilst the total mass of fuel injected for all cylinders at every operating point is calculated by the fuel controller. At this point the current digital twin can be considered as configured.

It should be noted that the criterion on the third step of Figure 4.5 has been decided based on the fact that marine engines on commercial applications will most frequently use approximately 50% of their entire operating envelope, exceeding this in only exceptional circumstances [6]. As a result, this is considered an adequate criterion to setup the current conditions digital twin by capturing the most frequent operating area of the engine.

4.7 Engine Health Assessment

The engine health assessment takes place by means of comparison of the healthy and current conditions digital twin. In specific, the healthy conditions digital twin

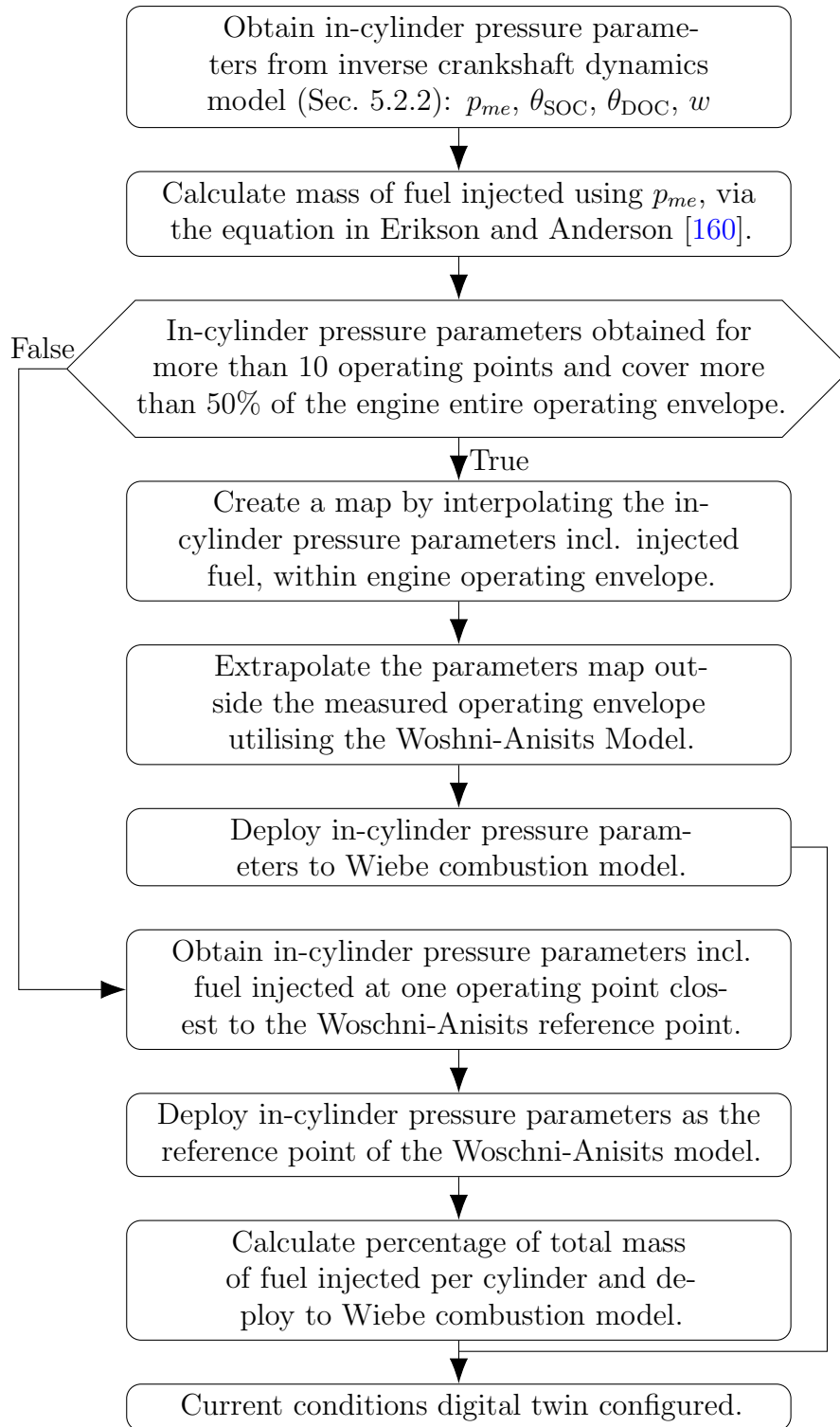


Figure 4.5: Thermodynamics model configuration to current engine conditions.

is setup by the calibrated thermodynamics model based on the engine shop tests as described in Section 4.5, and the current conditions digital twin is configured by utilising the current engine thermodynamic performance which is obtained from the measured ICT, as described in Section 4.6. Both of the above digital twins are

utilised to perform parametric runs in order to map the engine performance for the entire operating envelope. These parametric runs are performed from 20% load and engine speed, to 100% load and engine speed, for every 2.5% increments, below the torque limiter.

Subsequently, critical parameters are extracted from the aforementioned parametric runs, and the percentage difference of the current conditions with the healthy conditions digital twins is determined. In specific, the percentage difference of the following parameters is investigated

- Brake Specific Fuel Consumption (BSFC): This quantity directly relates to how much fuel the engine consumes per unit of energy produced on the shaft, which is a direct measure of the engine efficiency. As a result it is a vital metric that indicates the health status of the engine, and deviations in which have significant monetary as well as technical implications in the plant operation. Furthermore, this metric can be utilised most effectively to assess lifecycle costs of the engine by considering the effect of potential degradation and faults to the overall current and future performance.
- Peak in-cylinder pressure: This is a critical metric that summarises the in-cylinder combustion which becomes particularly useful when compared with the healthy conditions. Substantial differences upon such comparison may indicate abnormal changes in the start of injection, pre-ignition, faulty injections, in addition to extreme mechanical stresses in the engine.
- Indicated Mean Effective Pressure (IMEP): This metric is directly related to the work performed by each cylinder by encompassing the area of the entire in-cylinder pressure diagram. Therefore, it can be readily utilised to identify under-performing cylinders, particularly when considering that many modern engines employ peak in-cylinder pressure control. As a result, an additional indicator considering the in-cylinder pressure such as the IMEP needs to be employed, which can determine unhealthy cylinders.
- Cylinder Exhaust Gas Temperature (EGT) at exhaust valve: The exhaust gas temperature is a fundamental indicator of cylinder health and its comparison against tables and basic values is even encouraged by engine manufacturers.

As a result, comparing the EGT at the exhaust valve between healthy and current conditions can identify cylinders with inefficient combustion, cooling issues or even alarming changes in the duration of combustion caused by faulty injectors or pre-ignition.

Chapter 5

Crankshaft Dynamics Models

The aim of this chapter is to describe the process used to setup, solve as well as calibrate and validate (where applicable) the crankshaft dynamics models. Firstly, the direct crankshaft dynamics model governing equations presented in Sections 5.1.1–5.1.3 which utilise the in-cylinder pressure and other excitation forces to simulate the engine ICT. This is followed by the description of the solution methods and model convergence algorithm in Sections 5.1.4 and 5.1.5 respectively, in addition to the numerical schemes performance quantification KPI in Section 5.1.6, which greatly contributes to the overall accuracy and computational efficiency of the engine health assessment framework proposed. Finally, the calibration process of the direct crankshaft dynamics model is presented in Section 5.1.8, which calibrates the values of the stiffness and damping coefficients of the engine Torsional Vibration Damper (TVD).

Secondly, the inverse crankshaft dynamics model setup is presented which utilises the measured engine ICT to reconstruct the in-cylinder pressure curves by calculating their respective parameters. This commences by an overview of the model in Section 5.2.1, followed by the parametrisation of the in-cylinder pressure curves in Section 5.2.2 which renders them suitable for deployment within the inverse crankshaft dynamics model. Subsequently, the sensitivity equations and extended crankshaft dynamics model formulations are presented, through which the stability analysis and gradient of the objective function within the inverse crankshaft dynamics model algorithm can be obtained, as described in Sections 5.2.3–5.2.4. Finally, the inverse crankshaft dynamics model is developed, and its verification procedure is

described in Sections 5.2.5 and 5.2.6 respectively.

5.1 Direct Crankshaft Dynamics Model

5.1.1 Lumped Mass Model Overview

The direct crankshaft dynamics model utilises the lumped mass model approach as mentioned in Chapter 2, to simulate the engine torsional vibration response, shaft stresses, and deformation, which also includes the engine ICS and ICT. In addition, it is an integral part of the inverse crankshaft dynamics model as described in Section 5.2.1.

The lumped mass model approach approximates the continuous crankshaft as a series of lumped masses, or Degrees of Freedom (DOFs) as shown in Figure 5.1. Each of these DOFs has an associated inertia, and is connected to the next DOF with spring and damper elements, which represent the shafting material stiffness and inherit damping properties. In addition, DOFs are connected to the ground with a damper element to represent the viscous friction induced by the bearing oil film, the piston rings friction with the line, and the viscous friction for the case of the propeller.

The most prominent input to such models is the in-cylinder pressure which induces excitation torques, which are applied appropriately to each DOF as shown in Figure 5.1. Any changes to the excitation torques induced by the in-cylinder pressure indicate a change in the engine performance or health status, that is directly reflected to the model output which is chosen to be the ICT between DOFs in this case [119]. A more detailed overview of the model input and output is provided in Section 5.1.7.

5.1.2 System of Governing Equations

The equations that describe the motion of each DOF on the shafting system can be derived either using the torque balance, or using the Lagrange equations. The latter has the advantage that the equations of motion for any shafting system can be derived easier, independent of the coordinate system or the shafting system complexity [161].

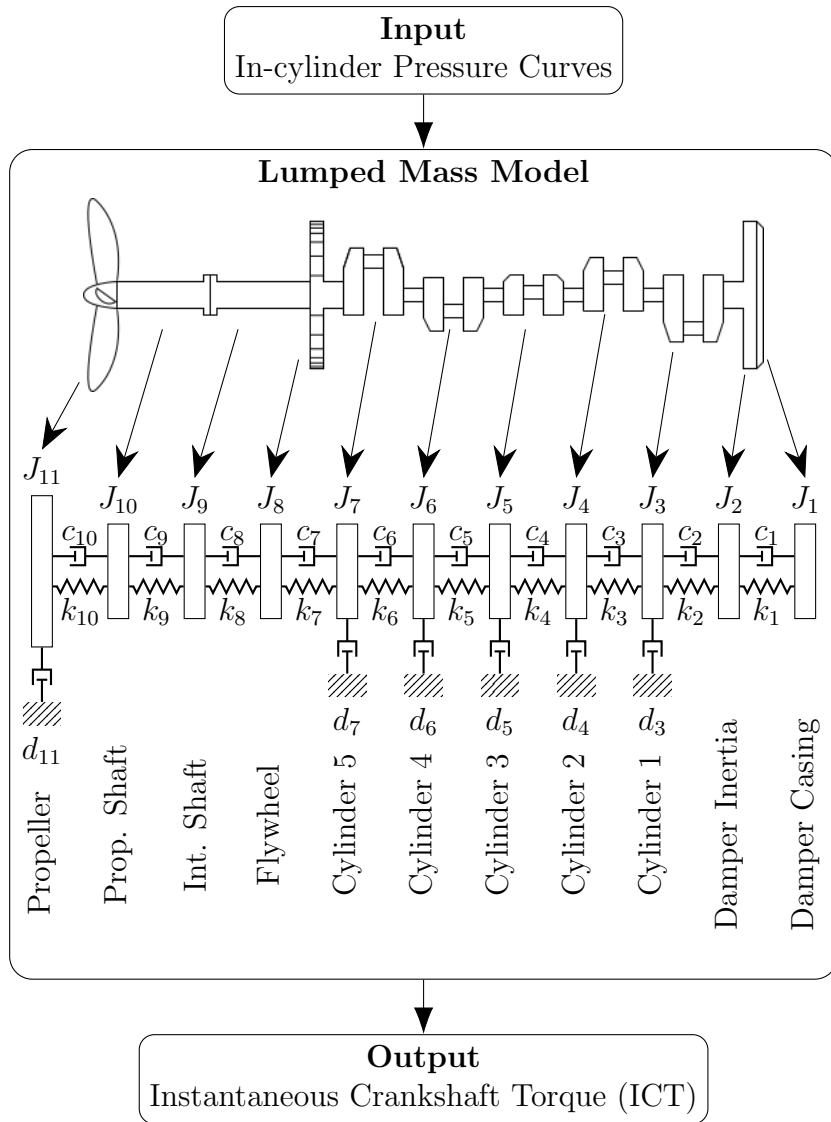


Figure 5.1: Overview of lumped mass model of typical marine shafting system.

Therefore, for a non-conservative system such as the marine engine shafting system, the Lagrange equations are expressed as follows:

$$\frac{d}{dt} \left(\frac{\partial \mathcal{L}}{\partial \dot{\theta}} \right) - \frac{\partial \mathcal{L}}{\partial \theta} = \mathcal{T} - \frac{\partial \mathcal{R}}{\partial \dot{\theta}} - \frac{\partial \mathcal{H}}{\partial \theta} \quad (5.1)$$

and $\mathcal{L} \equiv \mathcal{K} - \mathcal{V}$

where the Lagrangian \mathcal{L} consists of \mathcal{K} and \mathcal{V} which the system's total kinetic and potential energy respectively, \mathcal{T} is the excitation torque, and \mathcal{R} with \mathcal{H} denote the energy dissipated due to viscous and hysteretic damping effects.

The viscous damping results from bearing oil friction, oil-filled engine vibration dampers, and propellers rotating in water. It can be separated in absolute or relative

viscous damping, where the former takes effect between DOFs, whilst the latter takes place between a stationary point and a DOF, such as viscous friction or propeller damping [116]. Absolute and relative viscous damping is independent of the vibration frequency, and is proportional to the angular velocity squared as demonstrated in Equation 5.2. Hysteretic damping stems from molecular forces within the shaft steel or rubber couplings material, which results in energy dissipation during vibrations [116]. Furthermore, the energy dissipated is proportional to the angular displacement squared and dependent on the vibration frequency which is implied by the imaginary unit i as demonstrated by Equation 5.3 below:

$$\mathcal{R} = \frac{1}{2} \sum_{j=1}^{N-1} c_j (\dot{\theta}_{j+1} - \dot{\theta}_j)^2 + d_j \dot{\theta}_j^2 \quad (5.2)$$

$$\mathcal{H} = \frac{1}{2} \sum_{j=1}^{N-1} i k_j \sigma_j (\theta_{j+1} - \theta_j)^2 \quad (5.3)$$

where c with d are the relative and absolute viscous damping coefficients respectively, k is the shaft stiffness coefficient, and σ is the hysteretic damping coefficient, also mentioned as structural damping or loss factor [162].

Considering the right hand side of Equation 5.1, \mathcal{R} and \mathcal{H} can be differentiated appropriately as shown in Appendix A for each DOF, to obtain a system of equations which can be placed in a matrix format as shown below:

$$\frac{\partial \mathcal{R}}{\partial \dot{\Theta}} = -(\mathbf{D} + \mathbf{C})\dot{\Theta} \quad (5.4)$$

$$\frac{\partial \mathcal{H}}{\partial \Theta} = -i\mathbf{H}\Theta \quad (5.5)$$

where N is the total number of DOFs, \mathbf{D} with \mathbf{C} are the absolute and relative viscous damping matrices, \mathbf{H} is the structural damping matrix, and Θ with $\dot{\Theta}$ are the angular velocity vector and its time derivative respectively.

Similarly, by considering the left hand side of Equation 5.1, the Lagrangian \mathcal{L} of the shafting system can be formulated utilising the difference between the total kinetic and potential energy:

$$\mathcal{L} = \frac{1}{2} \sum_{j=1}^N J_j \ddot{\theta}_j^2 - \frac{1}{2} \sum_{j=1}^{N-1} k_j (\theta_{j+1} - \theta_j)^2 \quad (5.6)$$

where J is the DOF moment of inertia. Subsequently, by differentiating the Lagrangian as shown in Appendix A for each DOF, a system of equations is obtained in matrix format as shown below:

$$\frac{d}{dt} \left(\frac{\partial \mathcal{L}}{\partial \dot{\Theta}} \right) - \frac{d\mathcal{L}}{d\Theta} = \mathbf{J}\ddot{\Theta} + \mathbf{K}\Theta \quad (5.7)$$

Therefore, by combining Equations 5.2–5.7 in accordance to the Lagrange equations (Eq. 5.1) and rearranging the terms such that only the excitation torques are in the right hand side, the following system of governing equations is obtained:

$$\mathbf{J}\ddot{\Theta} + (\mathbf{D} + \mathbf{C})\dot{\Theta} + (\mathbf{K} + i\mathbf{H})\Theta = \mathcal{T} \quad (5.8)$$

The imaginary numbers introduced by the hysteretic damping in Equation 5.8 pose no problem if the governing equations are solved in the frequency domain, however when solved in the time domain, their solution becomes physically meaningless. As a result, hysteretic damping can be adequately approximated with viscous damping using numerous techniques or simplistic conversions found in the literature [116, 162, 163]. Consequently, henceforward the direct crankshaft dynamics model governing equations will be presented without hysteretic damping, implying that its effect has been accounted for already within the relevant viscous damping matrices using any of the standard techniques found in the literature. An exception to this will be made when solving the governing equations using the harmonic balancing numerical scheme, since in this case the equations are solved in the frequency domain and the hysteretic damping matrix can be employed appropriately as discussed in Section 5.1.4.3.

5.1.3 Engine Crankshaft Excitation Torques

The total excitation forces on an engine shaft include the torque exerted due to combustion gases, the propeller or generic engine load torque, and the reciprocating piston inertial torque. Therefore, the right hand side of Equation 5.8 can be expanded to represent the above torques explicitly:

$$\mathbf{J}\ddot{\Theta} + (\mathbf{D} + \mathbf{C})\dot{\Theta} + \mathbf{K}\Theta = \mathcal{T}_C - \mathcal{T}_L + \mathcal{T}_J \quad (5.9)$$

The combustion gases torque can be calculated by considering the power balance on the piston and crankshaft assembly. In specific, the product of the torque exerted on the crankshaft with its angular speed, should be equivalent to the product of the combustion gases force with the piston instantaneous velocity, as demonstrated by Equation 5.10. By considering that the combustion force exerted on the piston is equivalent to the in-cylinder pressure multiplied by the piston area, the torque due to combustion gases can be obtained in accordance to Equation 5.12:

$$\mathcal{T}_C \frac{d\theta}{dt} = F_C \frac{ds}{dt} \quad (5.10)$$

$$\Rightarrow \mathcal{T}_C = p(\theta) A_p \frac{ds}{d\theta} \quad (5.11)$$

$$\Rightarrow \mathcal{T}_C = p(\theta) \frac{\pi}{4} b^2 \frac{ds}{d\theta} \quad (5.12)$$

where $p(\theta)$ is the in-cylinder pressure as a function of crank angle, and b is the cylinder bore. Furthermore, the instantaneous position of the piston relative to TDC is $s = r \cos \theta - \sqrt{l^2 - r^2 \sin^2 \theta}$, which when differentiated with respect to crank angle is equivalent to the following equation [164]:

$$\frac{ds}{d\theta} = r \sin \theta \left(1 + \frac{r \cos \theta}{\sqrt{l^2 - r^2 \sin^2 \theta}} \right) \quad (5.13)$$

where r is the crank radius and l is the connecting rod length.

The propeller torque load can be calculated semi-empirically using the formulations obtained from Classification societies [165], in accordance to the following equation:

$$\mathcal{T}_L = \mathcal{T}_{\text{prop}} (a_1 \sin(Z(\theta + \alpha)) + a_2 \sin(2Z(\theta + \alpha))) \quad (5.14)$$

where $\mathcal{T}_{\text{prop}}$ is the steady-state propeller torque calculated using the propeller law [166], excitation coefficients a_1 and a_2 are obtained from the relevant Classification society regulations, Z is the number of propeller blades, and α is the phase angle of the first propeller blade relative to the engine TDC. For the case where the engine is driving the generator, the generator load can be taken as constant.

The reciprocating pistons inertia torque is induced by the vertical motion of the piston which causes the crankshaft polar moment of inertia to change continuously about its axis of rotation. Therefore, this phenomenon is frequently referred to as

variable inertia torque in the literature, and has significant effects in the dynamic response of the shafting system, particularly for the larger reciprocating piston masses of the marine engines. The variable inertia is therefore modelled in accordance to the following equations [164]:

$$\mathcal{T}_J = -J_V(\theta)\ddot{\theta} + \frac{1}{2} \frac{\partial J_V(\theta)}{\partial \theta} \dot{\theta}^2 \quad (5.15)$$

where $J_V(\theta)$ is the variable inertia as a function of crank angle which is equivalent to the following equation:

$$J_V(\theta) = m_{\text{rec}} \left(\frac{ds}{d\theta} \right)^2 \quad (5.16)$$

The formulation from Equation 5.9 can be expanded to include the variable inertia equations more descriptively according to Equation 5.17 below. This aids in the easier identification of the nonlinearities of the crankshaft dynamics governing equations as well as the mass matrix state variability, which are important features that determine an effective approach to the equations solution, as demonstrated by the equation below:

$$(\mathbf{J} - \mathbf{J}_V) \ddot{\Theta} + \frac{1}{2} \frac{\partial \mathbf{J}_V}{\partial \Theta} \dot{\Theta}^2 + (\mathbf{D} + \mathbf{C}) \dot{\Theta} + \mathbf{K} \Theta = \mathcal{T}_C - \mathcal{T}_L \quad (5.17)$$

Therefore, the crankshaft dynamics governing equations in Equation 5.17 when solved provides the angular displacement and speed of each DOF. Subsequently, the angular displacement solution can be used to calculate the ICT between the j^{th} and $j^{\text{th}} + 1$ DOFs:

$$\mathcal{T}_j = k_j(\theta_j - \theta_{j+1}) \quad (5.18)$$

5.1.4 Solution Methods for the Direct Crankshaft Dynamics Model

The crankshaft dynamics equation is a nonlinear non-homogeneous second order differential equation. The nonlinearities stem from the squared angular speed term introduced by the variable inertia of the reciprocating pistons, and the non-homogeneity is induced by the nonzero combustion gases and engine load torques. However, considering similar applications of crankshaft dynamics models in the

literature particularly for smaller engines, the nonlinearities do not cause instability in the solution of the equation, and have a reasonably small effect in the solution of the equation [119].

Furthermore, the crankshaft dynamics governing equations tend to exhibit variations in the solution over a large spectrum of different time scales which indicates they are either moderately or highly stiff [79, 119, 162]. The stiffness of the governing equations, is an important feature that dictates the numerical approach which has to be employed. This is because stiff differential equations exhibit challenging behaviour and thus more complex numerical schemes and approaches need to be employed to obtain an accurate solution [167]. Considering the already known features and behaviour of the governing equations, three types of numerical schemes or techniques can be introduced to obtain the solution.

The trapezoidal rule with backwards differentiation numerical scheme (TR-BDF2) has proven effectiveness in solving stiff nonlinear differential equations, and is utilised by the ODE23tb solver in MATLAB [168]. The disadvantage of the TR-BDF2 numerical scheme is its computational complexity as well as its unavailability, since it is used in the proprietary programming language of MATLAB. The second approach to solve the governing equations is by a piecewise Linear Time Invariant (LTI) numerical scheme which is computationally simple, easy to setup and has been successfully utilised to solve crankshaft dynamics governing equations [119]. However, the simplicity of the LTI numerical scheme might inhibit its accuracy, therefore the third approach of harmonic balancing can be employed which is suitable for this case, since the expected solution will be sinusoidal and periodic [94]. Furthermore harmonic balancing can solve the governing equations straight into the steady state bypassing undesirable transients, however depending on the user case that may be its disadvantage as well since this implies it cannot be used for transient analysis.

5.1.4.1 TR-BDF2 Numerical Scheme

To address the stiffness and nonlinearities of the governing equations, a higher order implicit numerical scheme is necessary. Therefore, the Trapezoidal Rule with 2nd order Backwards Differentiation (TR-BDF2) numerical scheme can be utilised which implements an implicit Runge-Kutta method with the trapezoidal rule for its first

stage, and a second order backward differentiation formula as its second stage [168]. The TR-BDF2 numerical scheme is available in MATLAB through the ODE23tb solver. Therefore, to integrate a differential equation in the form $\dot{x} = f(t, x)$, the solution is firstly advanced from t_k to $t_k + \kappa\Delta t_k$ using the trapezoidal rule according to Equation 5.19, and secondly advanced from $t_k + \kappa\Delta t_k$ to $t_k + \Delta t_k$ using a backward differentiation formula according to Equation 5.20.

$$x_{k+\kappa} - \kappa \frac{\Delta t_k}{2} f(t_k + \kappa\Delta t_k, x_{k+\kappa}) = x_k + \kappa \frac{\Delta t_k}{2} f(t_k, x_k) \quad (5.19)$$

$$x_{k+1} - \frac{1 - \kappa}{2 - \kappa} \Delta t_k f(t_k + \Delta t_k, x_{k+1}) = \frac{1}{\kappa(2 - \kappa)} x_{k+\kappa} - \frac{(1 - \kappa)^2}{\kappa(2 - \kappa)} x_k \quad (5.20)$$

The value of κ is chosen to be $\kappa = 2 - \sqrt{2}$, such that the local truncation error is minimised [168]. The trapezoidal and backward differentiation formulae are implicit equations of the variables $x_{k+\kappa}$ and x_{k+1} respectively, so they are solved using an iterative method, most commonly the Newton-Raphson approach.

The time step is dynamically adjusted by monitoring the pointwise normalised error fraction ϵ , which is calculated according to the following equation:

$$\epsilon = \frac{\|e_{\text{loc}}\|}{\varepsilon_{\text{abs}}\|x_k\| + \varepsilon_{\text{rel}}} \quad (5.21)$$

where e_{loc} is the local truncation error and ε_{abs} , ε_{rel} are the absolute and relative tolerances respectively set by the user. If $\epsilon < 2$ the candidate time step for the next iteration is chosen as $\Delta t_{i+1} = \min\{\Delta t_k \epsilon^{-1/2}, 2\Delta t_k\}$, whilst if $\epsilon \geq 2$ the candidate step becomes $\Delta t_{i+1} = 0.7\Delta t_k \epsilon^{-1/2}$.

The governing equations of the crankshaft dynamics model have an additional peculiarity, which is a state-dependent mass matrix that results from the variable inertia of the reciprocating pistons. The ODE23tb solver is designed to handle efficiently state-dependent mass matrices within the implementation of the Newton-Raphson approach, without requiring time consuming matrix inversions at every step [168]. In specific, the system of equations which can be solved by ODE23tb has the following standard format: $\mathbf{M}(\mathbf{x})\dot{\mathbf{x}} = \mathbf{f}(t, \mathbf{x})$, where $\mathbf{M}(\mathbf{x})$ is the mass matrix, and quantities in bold represent matrices or vectors as applicable.

Therefore, the equation below relates the above standard format employed by the ODE23tb solver, to the crankshaft dynamics governing formulation in Equation 5.17:

$$\underbrace{\begin{bmatrix} \mathbf{I} & \mathbf{0} \\ \mathbf{0} & \mathbf{J} - \mathbf{J}_V(\Theta) \end{bmatrix}}_{\mathbf{M}(\mathbf{x})} \underbrace{\begin{bmatrix} \dot{\Theta} \\ \ddot{\Theta} \end{bmatrix}}_{\dot{\mathbf{x}}} = \underbrace{\begin{bmatrix} \dot{\Theta} \\ \mathcal{T}_C - \mathcal{T}_L - \frac{1}{2} \frac{\partial \mathbf{J}_V}{\partial \Theta} \dot{\Theta}^2 - (\mathbf{D} + \mathbf{C}) \dot{\Theta} - \mathbf{K} \Theta \end{bmatrix}}_{\mathbf{f}(t, \mathbf{x})} \quad (5.22)$$

5.1.4.2 Piecewise LTI Numerical Scheme

The piecewise Linear Time Invariant (LTI) numerical scheme can be used to setup an LTI solver. This solver exhibits computational simplicity by approximating the nonlinear governing equations as a first order linear differential equation for a small enough time step, for which the analytical solution is already known. Therefore the crankshaft dynamics equation can be approximated using the LTI system equation:

$$\dot{\mathbf{x}} = \mathcal{A}\mathbf{x} + \mathcal{B}\mathbf{u} \quad (5.23)$$

where \mathcal{A} and \mathcal{B} are the dynamics and input matrices respectively, and \mathbf{u} is the input vector. The analytical solution of the above equation is known, and is provided by the following formula [169]:

$$\mathbf{x}(t) = e^{\mathcal{A}t} \mathbf{x}(0) + \int_0^t e^{\mathcal{A}(t-\tau)} \mathcal{B} \mathbf{u}(\tau) d\tau \quad (5.24)$$

The piecewise LTI numerical scheme can therefore be derived by discretising the above equation for the k^{th} time step, where it is assumed that the value of \mathbf{u} remains constant within each time step so it can be considered to be independent of time, and the integral of the exponential function is approximated using the trapezoidal rule:

$$\mathbf{x}(t_{i+1}) = e^{\mathcal{A}\Delta t} \mathbf{x}(t_k) + \frac{1}{2} (\mathbf{I} + e^{\mathcal{A}\Delta t}) \mathcal{B} \Delta t \mathbf{u}(t_k) \quad (5.25)$$

To determine the dynamics and input matrices of the crankshaft dynamics governing equations, Equation 5.17 needs to be reformulated in the state-space form

which resembles the LTI system equation from Equation 5.23:

$$\begin{aligned}
 \dot{\mathbf{x}} = & \underbrace{\begin{bmatrix} \mathbf{0} & \mathbf{I} \\ -(\mathbf{J} - \mathbf{J}_V)^{-1}\mathbf{K} & -(\mathbf{J} - \mathbf{J}_V)^{-1}(\mathbf{C} + \mathbf{D}) \end{bmatrix}}_{\mathcal{A}} \underbrace{\begin{bmatrix} \Theta \\ \dot{\Theta} \end{bmatrix}}_{\mathbf{x}} \\
 + & \underbrace{\begin{bmatrix} \mathbf{I} & \mathbf{0} \\ \mathbf{0} & -(\mathbf{J} - \mathbf{J}_V)^{-1} \end{bmatrix}}_{\mathcal{B}} \underbrace{\begin{bmatrix} \mathbf{0} \\ \frac{1}{2} \frac{\partial \mathbf{J}_V}{\partial \Theta} \dot{\Theta}^2 + \mathcal{T}_C - \mathcal{T}_L \end{bmatrix}}_{\mathbf{u}}
 \end{aligned} \tag{5.26}$$

5.1.4.3 Harmonic Balancing Numerical Scheme

The harmonic balancing numerical scheme employs Fourier series to approximate the solution of the crankshaft dynamics governing equations in the frequency domain, and subsequently the solution is converted to the time domain. For this to take place, the governing equations need to be solved considering the angular speed from the shaft's frame of reference. This implies that the nonlinear angular speed term from Equation 5.17 should be set equal to the following sum:

$$\frac{1}{2} \frac{\partial \mathbf{J}_V}{\partial \Theta} \dot{\Theta}^2 = \frac{1}{2} \frac{\partial \mathbf{J}_V}{\partial \Theta} (\omega + \Omega)^2 \tag{5.27}$$

where the instantaneous angular speed $\dot{\Theta}$ is set equal to the sum of the average angular speed within one engine cycle ω , and the instantaneous angular speed fluctuations Ω .

Furthermore, the linear angular speed term which is multiplied by the damping matrices is set to the instantaneous angular speed fluctuations. This implies that the absolute viscous damping matrix provided by the manufacturer when solving the governing equations using harmonic balance, has larger values than the one utilised when solving the governing equations with any of the other two methods mentioned. Therefore the torque due to damping becomes as follows:

$$(\mathbf{D} + \mathbf{C})\dot{\Theta} = (\mathbf{D}_\Omega + \mathbf{C})\Omega \tag{5.28}$$

where \mathbf{D}_Ω is the absolute damping matrix employed when solving the governing equations utilising harmonic balance.

In addition, it should be noted that as mentioned in Section 5.1.2, this numerical scheme solves the governing equations in the frequency domain, hence the imaginary hysteretic damping matrix $i\mathbf{H}$ can be re-introduced into the governing equations.

As a result, Equation 5.17 is reformulated as follows:

$$(\mathbf{J} - \mathbf{J}_V)\ddot{\Theta} + \frac{1}{2} \frac{\partial \mathbf{J}_V}{\partial \Theta} (\omega + \Omega)^2 + (\mathbf{D}_\Omega + \mathbf{C})\Omega + (\mathbf{K} + i\mathbf{H})\Theta = \mathcal{T}_C - \mathcal{T}_L \quad (5.29)$$

$$\Rightarrow (\mathbf{J} - \mathbf{J}_V)\ddot{\Theta} + \frac{1}{2} \frac{\partial \mathbf{J}_V}{\partial \Theta} \omega^2 + \left(\mathbf{D}_\Omega + \mathbf{C} + \frac{\partial \mathbf{J}_V}{\partial \Theta} \right) \Omega + (\mathbf{K} + i\mathbf{H})\Theta = \mathcal{T}_C - \mathcal{T}_L \quad (5.30)$$

where the term consisting of Ω^2 has been neglected from Equation 5.30 as the angular speed fluctuations are deemed to small to affect the solution [170].

To solve Equation 5.30, the exponential form of the Fourier series can be utilised to approximate the variable inertia function, the combustion and load torques, as well as the angular displacement:

$$\mathbf{J}_V = \sum_{p=-\infty}^{+\infty} \mathbf{j}_p e^{ip\omega t}, \quad \mathcal{T}_C - \mathcal{T}_L = \sum_{q=-\infty}^{+\infty} \tau_q e^{iq\omega t}, \quad \Theta = \sum_{q=-\infty}^{+\infty} \theta_q e^{iq\omega t}$$

By substituting the above Fourier series into Equation 5.30 and simplifying the terms accordingly, the following equation can be obtained:

$$\begin{aligned} & \sum_{q=-\infty}^{+\infty} (iq\omega(\mathbf{D}_\Omega + \mathbf{C}) - (q\omega)^2 \mathbf{J} + \mathbf{K} + i\mathbf{H}) \theta_q e^{iq\omega t} \\ & - \sum_{q=-\infty}^{+\infty} \sum_{p=-\infty}^{+\infty} q\omega(p + q\omega) \mathbf{j}_p \theta_q e^{i(p+q)\omega t} = \sum_{q=-\infty}^{+\infty} \left(\tau_q - \frac{iq\omega^2}{2} \mathbf{j}_q \right) e^{iq\omega t} \end{aligned} \quad (5.31)$$

In Equation 5.31 the unknown variable is θ_q . Consequently, for identical sum indices the exponential functions cancel out and a linear equation can be solved for the unknown variable. This is performed for all sum indices such that the following

system of equations can be solved:

$$\begin{aligned}
 (i\omega(\mathbf{D}_\Omega + \mathbf{C}) - (\omega)^2\mathbf{J} + \mathbf{K} + i\mathbf{H})\boldsymbol{\theta}_1 &= \boldsymbol{\tau}_1 - \frac{i\omega^2}{2}\mathbf{j}_1 \\
 (i2\omega(\mathbf{D}_\Omega + \mathbf{C}) - (2\omega)^2\mathbf{J} + \mathbf{K} + i\mathbf{H})\boldsymbol{\theta}_2 - \omega(1 + \omega)\mathbf{j}_1\boldsymbol{\theta}_1 &= \boldsymbol{\tau}_2 - \frac{i2\omega^2}{2}\mathbf{j}_2 \\
 (i3\omega(\mathbf{D}_\Omega + \mathbf{C}) - (3\omega)^2\mathbf{J} + \mathbf{K} + i\mathbf{H})\boldsymbol{\theta}_3 - 2\omega(1 + 2\omega)\mathbf{j}_1\boldsymbol{\theta}_2 - \omega(2 + \omega)\mathbf{j}_2\boldsymbol{\theta}_1 &= \boldsymbol{\tau}_3 - \frac{i3\omega^2}{2}\mathbf{j}_3 \\
 \vdots &
 \end{aligned}$$

The system of equations above can be subsequently reformulated in a more compact matrix format according to the below equation, which can be solved using a linear solver for the unknown vector containing $\boldsymbol{\theta}$ variables:

$$\begin{bmatrix} \mathbf{A}_1 & & & \\ \mathbf{A}_{2,1} & \mathbf{A}_2 & & \\ \mathbf{A}_{3,1} & \mathbf{A}_{3,2} & \mathbf{A}_3 & \\ & & & \ddots \end{bmatrix} \begin{bmatrix} \boldsymbol{\theta}_1 \\ \boldsymbol{\theta}_2 \\ \boldsymbol{\theta}_3 \\ \vdots \end{bmatrix} = \begin{bmatrix} \boldsymbol{\tau}_1 - i\omega/2\mathbf{j}_1 \\ \boldsymbol{\tau}_2 - i2\omega/2\mathbf{j}_2 \\ \boldsymbol{\tau}_3 - i3\omega/2\mathbf{j}_3 \\ \vdots \end{bmatrix} \quad (5.32)$$

where on the diagonal:

$$\mathbf{A}_n = iq\omega(\mathbf{D}_\Omega + \mathbf{C}) - (q\omega)^2\mathbf{J} + \mathbf{K} + i\mathbf{H}$$

and on the remaining elements:

$$\mathbf{A}_{q,p} = -p\omega(q - p + q\omega)\mathbf{j}_{q-p}$$

5.1.5 Model Convergence

The TR-BDF2 and piecewise LTI numerical schemes rely on user-defined initial conditions to initiate the integration. Therefore, the integration should stop at the point in time where the crankshaft dynamics model has reached steady state according to the algorithm in Figure 5.2. This is not required for the case where harmonic balancing is employed, since as explained in the beginning of this Section, this method solves the governing equations directly in steady state.

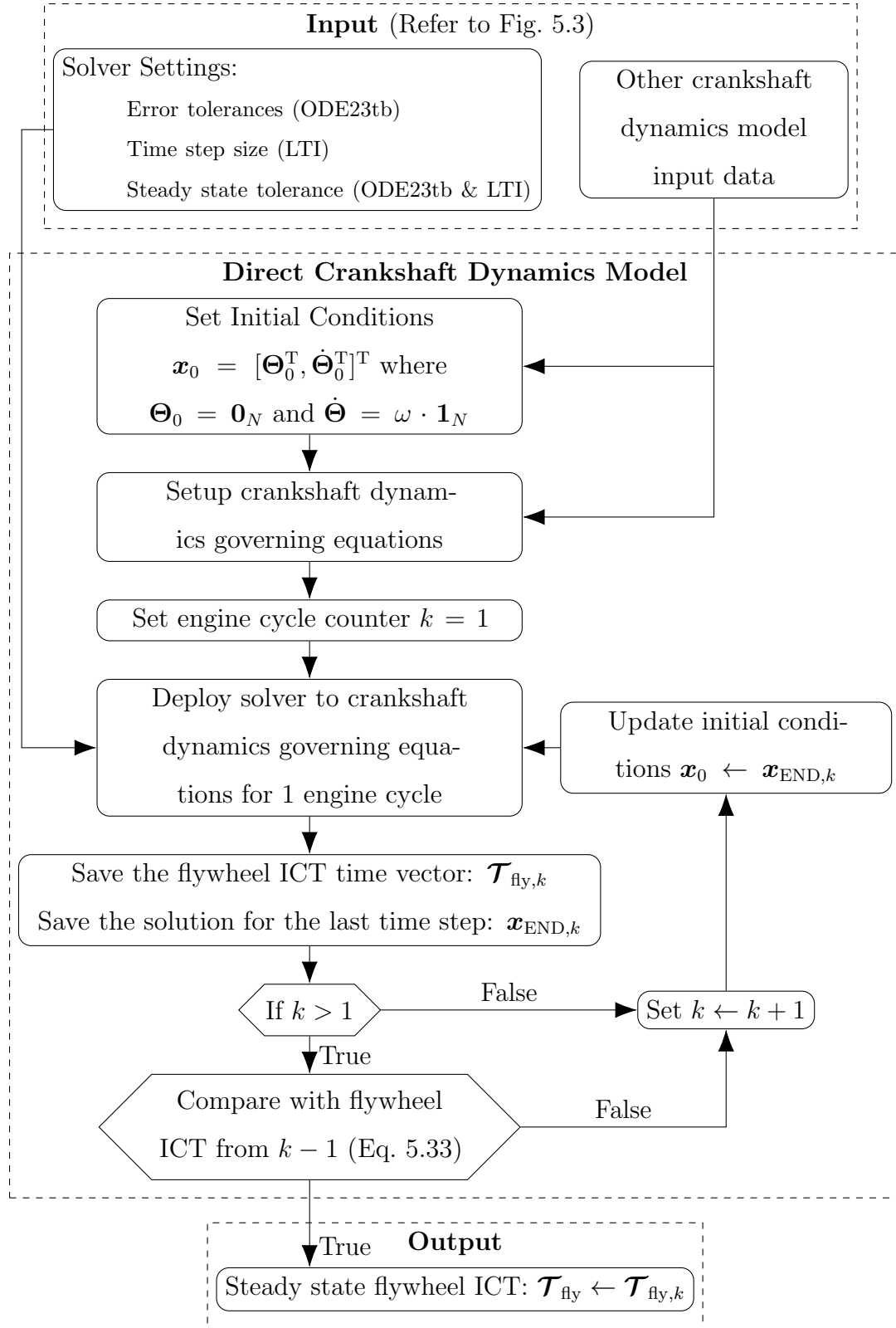


Figure 5.2: Direct crankshaft dynamics model convergence algorithm for time domain simulation.

In specific, the input data is utilised first to set the initial conditions by employing the average engine speed ω , setup the matrices and excitation vectors of the crankshaft

dynamics governing equations, set the appropriate solver settings, as well as the user-defined steady state tolerance ε_{ss} . Further detail regarding the input data is provided in Section 5.1.7.

Subsequently, after setting the initial conditions and the governing equations, the engine cycle counter is set to $k = 1$, and the ODE23tb or LTI solvers can be utilised to solve the respective equations for 1 cycle. Following the solution of the equations, the ICT at the engine flywheel $\mathcal{T}_{\text{fly},k}$ is calculated and saved, as well as the governing equations state variables for the last time step, $\mathbf{x}_{\text{END},k}$. If this is the first engine cycle, the engine cycle counter is advanced by setting $k \leftarrow k + 1$ and the initial conditions are updated appropriately so that the crankshaft dynamics equation integration can take place for the 2nd cycle. If the engine cycle counter is larger than 1, then the flywheel torque of the last two engine cycles is compared. Provided that the comparison lies within the steady state tolerance, the crankshaft dynamics model is deemed to have reached steady state and the flywheel ICT is provided from the last engine cycle as output. The comparison of the flywheel ICT between the last two engine cycles takes place according to the Normalised Root Mean Error (NRME) which is obtained using the following equation:

$$\frac{\|\mathcal{T}_{\text{fly},k} - \mathcal{T}_{\text{fly},k-1}\|_2}{\text{mean}(\mathcal{T}_{\text{fly},k})} \leq \varepsilon_{ss} \quad (5.33)$$

where $\|\cdot\|_2$ is the Euclidean norm and ε_{ss} is the user-defined steady state tolerance.

5.1.6 Numerical Scheme Performance Quantification

Following the three numerical schemes of TR-BDF2, piecewise LTI, and harmonic balancing presented above, their performance is evaluated and quantified in as part of case study 3(a) presented in Section 6.2. This takes place through the respective KPI, which takes into account the accuracy as compared to measured data, as well as the numerical scheme execution time. The numerical scheme KPI is formulated in accordance to the equation below, such that a small value indicates a good compromise between fast execution time and reduced error as compared to the measured data:

$$\text{KPI}_{\text{sol}} = \tilde{\varepsilon}_{\mathcal{T}} + w_{\text{sol}} t_{\text{exec}} \quad (5.34)$$

where t_{exec} is the execution time the numerical scheme requires to reach steady state, w_{sol} is a user defined weight, and $\tilde{\varepsilon}$ is the NRME of the simulated flywheel ICT with respect to the measured data which is calculated in accordance to the equation below:

$$\tilde{\varepsilon}_{\mathcal{T}} = \frac{\|\mathcal{T}_{\text{fly,sim}} - \tilde{\mathcal{T}}_{\text{fly}}\|_2}{\text{mean}(\mathcal{T}_{\text{fly,sim}})} \quad (5.35)$$

To evaluate the optimum (i.e. the minimum) numerical schemes KPI, parametric runs are performed by systematically varying the user settings of each numerical scheme. In specific, the available user-defined settings, in addition to the adjustable range within which the parametric runs are performed are listed in Table 5.1. Regarding the TR-BDF2 and piecewise LTI numerical schemes, 10 equally spaced points are obtained for each user-defined setting, extending from the minimum to the maximum of the corresponding range. Since two user-defined settings are available for the two aforementioned numerical schemes, all possible combinations between the values of each setting are deployed, thereby resulting to $10^2 = 100$ parametric runs. The results of both user-defined settings and the attained KPI can be subsequently plotted in a contour plot to find its minimum. For the case of the harmonic balancing numerical scheme, since there is only one user setting its values are varied incrementally in units of 5 within the respective range, to determine the minimum KPI. The results of the above are presented in Section 7.3.

Table 5.1: Numerical schemes user-defined settings investigation.

Numerical Scheme	User Settings	Range	Runs*
TR-BDF2	Abs. & Rel. Tolerance	$1 \times 10^{-4} \sim 6 \times 10^{-3}$	100
	Steady State Tolerance	$5 \times 10^{-4} \sim 5 \times 10^{-2}$	
Piecewise LTI	Time Step (s)	$1 \times 10^{-5} \sim 1 \times 10^{-2}$	100
	Steady State Tolerance	$5 \times 10^{-4} \sim 5 \times 10^{-2}$	
Harmonic Balancing	Number of Fourier Terms	$5 \sim 50$	10

*Number of parametric runs

Regarding the TR-BDF2 numerical scheme, the relative and absolute tolerances as discussed in Section 5.1.4.1 are utilised by the numerical scheme algorithm to determine a suitable time step. Therefore, this numerical scheme employs an internally derived time step, thus not requiring this as an additional user input. A commonly accepted strategy is to set the absolute and relative tolerances to the same value [159], which what is also practiced in this case. Furthermore, the steady state

tolerance needs to be defined as a user-defined setting since this numerical scheme solves the direct crankshaft dynamics model governing equations directly the time domain. Thus the instant when the system has reached steady state needs to be identified as discussed in Section 5.1.5.

The piecewise LTI numerical scheme employs a user defined time step as discussed in Section 5.1.4.2, which remains constant throughout the integration, in contrast to the TR-BDF2 numerical scheme. Since this is also a time domain simulation, the steady state tolerance is also required as a user-defined setting.

The harmonic balancing numerical scheme solves the direct crankshaft dynamics model governing equations firstly in the frequency domain, and subsequently converts that to the time domain straight into the steady state as demonstrated in Section 5.1.4.3. As a result, no time step or steady state criterion are required, however the number of Fourier terms used to compose the final solution is required as user-defined setting.

5.1.7 Model Input, Output & Assumptions

The crankshaft dynamics model input consists five categories of (a) DOF coefficients, (b) in-cylinder pressure curve, (c) engine load torque data, (d) engine geometric data, (e) solver settings. The model output is the ICT between any DOFs selected by the user, as shown in Figure 5.3.

The DOF coefficients are utilised to construct the inertia \mathbf{J} , absolute damping \mathbf{D} , relative damping \mathbf{C} , and stiffness matrices \mathbf{K} . A limitation of these coefficients is that they are obtained from the manufacturer when the engine is in a new condition. Consequently, any subsequent engine degradation that results in changes of these coefficients values is not captured by the model, unless these coefficients are readjusted to reflect on the current engine condition [94].

The in-cylinder pressure diagram is utilised to calculate the combustion gases excitation torque and its accuracy affects significantly the output of the crankshaft dynamics model as also mentioned in Section 5.1.1. Hence, the in-cylinder pressure diagram used as input should be corrected appropriately to account for systemic or other offset errors stemming from the sensor or analyser [86]. Specifics on such measurement correction procedure are mentioned in Appendix D. Furthermore, the

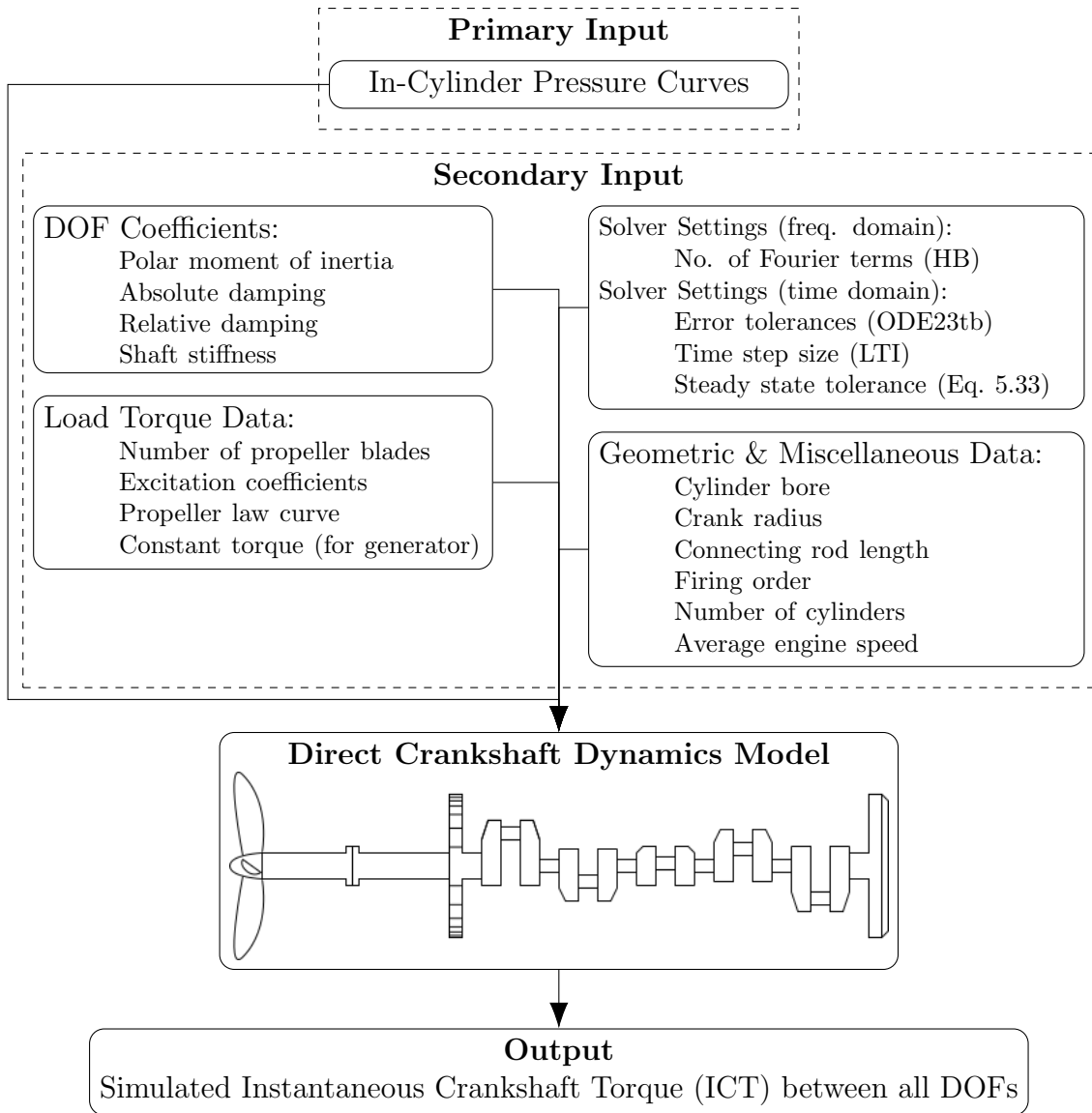


Figure 5.3: Direct crankshaft dynamics model detailed input and output.

appropriate in-cylinder diagram should be utilised for every cylinder which reflects the engine health status which the user aims to simulate, including healthy conditions, degradation, and faults where applicable.

The engine load torque data include the propeller number of blades, excitation coefficients, and the propeller law curve. The propeller excitation coefficients are provided in standard tables from Classification society regulations and depend on the number of propeller blades [165]. However the excitation coefficients are considered the same regardless the type of propeller or its geometry, as they are meant to approximate the physical behaviour of a large range of typical propellers. The crankshaft dynamics model can also be setup with a generator, in which case a

constant engine load is considered neglecting the effects of vibratory torque, since harmonic current disturbances take place at significantly higher orders than those of the crankshaft dynamics [92].

The geometric and miscellaneous data include primarily the reciprocating piston mass, basic crankshaft and engine geometry, and firing order which are all readily available from the manufacturer at high accuracy. Therefore no major assumptions or sources of errors are expected in this case.

The solver settings are a critical user input to ensure optimum model performance as discussed in Section 5.1.6. These depend on the numerical scheme employed by the user and include solver error and steady state tolerances for the case of the TR-BDF2, size of time step and steady state tolerance for the case of the piecewise LTI, and number of Fourier terms to approximate the final solution for the case of the harmonic balancing numerical scheme. Selection of appropriate user-defined settings is performed in Section 7.3, to allow for adequate model performance both in terms of accuracy and computational time.

5.1.8 Calibration of Direct Crankshaft Dynamics Model

The direct crankshaft dynamics model needs to be calibrated prior to its deployment as part of the inverse crankshaft dynamics model as discussed in Section 5.2.1. This ensures the accuracy of the direct crankshaft dynamics model, and as a result improves the performances of the inverse crankshaft dynamics model as well. In specific, the DOF coefficients of relative damping and shaft stiffness are calibrated, since they have exhibited large uncertainties in the literature as provided by the manufacturers, primarily due to engine degradation at the time of the measurement [94, 162]. The optimisation algorithm used is the default MATLAB sequential quadratic programming. This is a gradient based algorithm which is chosen since the objective function is well posed, and its assumed that the manufacturer values provided are already close to the actual ones. Thus its performance is significantly quicker than non-gradient based algorithms.

Firstly, the direct crankshaft dynamics model needs to be parametrised appropriately, and the objective function needs to be formulated. For this, to be accomplished calibration factors are introduced as multiples of their respective DOF coefficients. In

specific, these calibration factors are multiplied by the the torsional damper stiffness and viscous damping coefficients, according to the equations below respectively:

$$c_{\text{damp}} = x_1 c_{\text{damp},0} \quad (5.36)$$

$$k_{\text{damp}} = x_2 k_{\text{damp},0} \quad (5.37)$$

where x denotes the dimensionless calibration factor for the respective coefficients, and subscript damp denotes the DOF corresponding to the torsional damper, whilst subscript 0 denotes the values obtained from the manufacturer.

The above coefficients along with the others provided by the manufacturer, can be utilised to construct the relative damping and stiffness matrices \mathbf{C} and \mathbf{K} respectively, as described in Section 5.1.2. Therefore, the direct crankshaft dynamics governing equations in 5.9, and as a consequence the simulated ICT at the flywheel, becomes a function of the calibration factors x_1 and x_2 .

To formulate the objective function, the measured ICT at the flywheel is compared to the simulated ICT at the flywheel from the direct crankshaft dynamics model, which uses as primary input the measured in-cylinder pressure at the instant that the measured torque was recorded. The comparison within the objective function takes place in the frequency domain, since orders with negligible contributions (including noise) can be selectively excluded, thereby improving the performance of the calibration. In specific, the first 24 orders are included in the objective function since these include all the critical information of the excitation forces, as advised by the literature and all manufacturer torsional vibration studies [116, 171].

To further improve performance of the calibration algorithm, dominant orders which include all multiples of the engine number of cylinders are provided with larger weights, and the calibration factors are constrained appropriately according to the author's experience. Thus, the objective function and optimisation problem are

formulated according to Equations 5.38–5.39 respectively:

$$O_D = \frac{1}{2} \frac{\|\boldsymbol{\tau}_{\text{fly}}(\mathbf{x}_1, \mathbf{x}_2) - \tilde{\boldsymbol{\tau}}_{\text{fly}}\|_2^2}{\max\{\tilde{\boldsymbol{\tau}}_{\text{fly}}\}} \quad (5.38)$$

$$\Rightarrow \min_{\mathbf{x}_1, \mathbf{x}_2} \{O_D(\mathbf{x}_1, \mathbf{x}_2)\} \quad \text{subject to:} \quad \begin{aligned} 0.6 &\leq x_1 \leq 1.4 \\ 0.6 &\leq x_2 \leq 1.4 \end{aligned} \quad (5.39)$$

where $\boldsymbol{\tau}_{\text{fly}}(\mathbf{x}_1, \mathbf{x}_2)$ is the vector containing the Fourier magnitudes of the first 24 orders of the flywheel torque as a function of the DOF coefficients calibration factors, the tilde notation $\tilde{\cdot}$ denotes measured values, and $\|\cdot\|_2$ denotes the Euclidean norm.

5.2 Inverse Crankshaft Dynamics Model

5.2.1 Inverse Model Overview

To develop the inverse crankshaft dynamics model, a formalised parameter estimation approach will be implemented. Considering the review in Section 2.1.3.4, an IVP technique could be most suitable to implement if the crankshaft dynamics model governing equations exhibit stability in their solution, or a BVP technique would be most suitable if unstable behaviour is exhibited. For smaller engines in the automotive industry, the direct crankshaft dynamics model governing equations have demonstrated favourable stability characteristics [119], however for the larger engines this will have to be verified by employing formal stability analysis methods as discussed in Section 5.2.4. The parameter estimation technique and the inverse model development is further discussed in detail in Section 5.2.5.

In summary, the inverse crankshaft dynamics model is utilised to reconstruct the in-cylinder pressure diagram using as input the measured ICT. An optimisation algorithm is employed using as input the measured ICT, and returning as output the in-cylinder pressure diagram for every cylinder. This is performed by parametrising the in-cylinder pressure curve, utilising it as input to the direct crankshaft dynamics model, and comparing the output torque from the direct crankshaft dynamics model to the corresponding measurement. This process keeps repeating by updating the in-cylinder pressure curve parameters until the output ICT from the direct crankshaft

dynamics model is the same as the measured torque within tolerance. To enhance the optimisation process robustness and reduce the number of costly objective function evaluations, the objective function gradient will be provided using the sensitivity equations derived in Section 5.2.3. An overview of this process is shown in Figure 5.4, with further details provided in Sections 5.2.2–5.2.5.

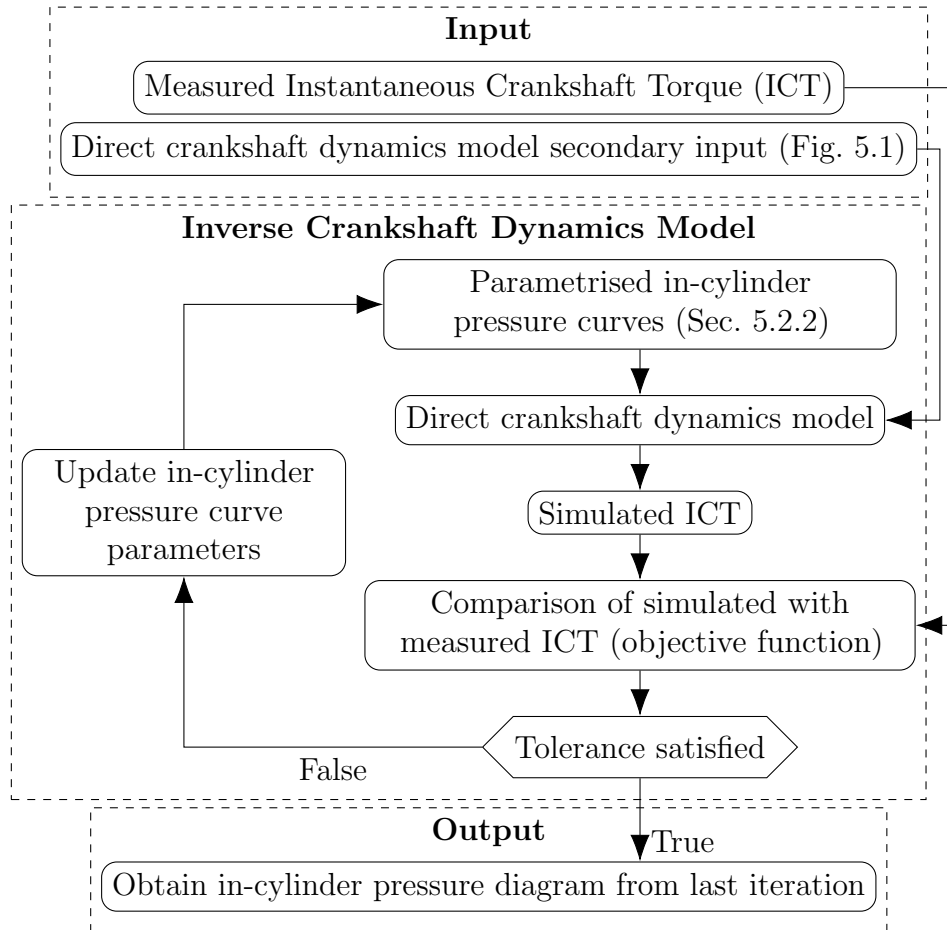


Figure 5.4: Overview of the inverse crankshaft dynamics model.

5.2.2 In-cylinder Pressure Parametrisation

The parametrisation of the in-cylinder pressure curve for the closed part of the diesel cycle is a critical task, since the parametrised in-cylinder pressure function should be able to capture faults or degradation by changing the employed parameters. Moreover, the parametrised in-cylinder pressure function should employ as few parameters as possible, in order to reduce the required mathematical and computational complexity of the optimisation algorithm. Therefore this is accomplished by using different equations to represent the three main in-cylinder processes of compression,

combustion and expansion. The compression and expansion processes are modelled using polytropic relationships according to Equations 5.40 and 5.41. The combustion process can be modelled by using semi-empirical equations which act as interpolating functions between the compression and expansion parts of the cycle, thus the entire in-cylinder pressure curve can be modelled using Equation 5.42.

$$p_{co}(\theta) = p_{EVC} \left(\frac{V(\theta_{EVC})}{V(\theta)} \right)^{\gamma_{co}} \quad (5.40)$$

$$p_{ex}(\theta) = p_{me} \left(\frac{V_c}{V(\theta)} \right)^{\gamma_{ex}} \quad (5.41)$$

$$p(\theta) = (1 - f_C(\theta))p_{co}(\theta) + f_C(\theta)p_{ex}(\theta) \quad (5.42)$$

where p_{EVC} and p_{me} are the in-cylinder pressure at exhaust valve close and the maximum isentropic pressure during expansion respectively, γ is the ratio of specific heats, V_c is the cylinder clearance volume, $V(\theta)$ is the engine cylinder volume as a function of crank angle [164], and $f_C(\theta)$ is the semi-empirical combustion interpolating function.

The interpolating functions used to model combustion include the sigmoid, single Wiebe, or double Wiebe functions in order of increasing mathematical complexity [149]. The sigmoid function is mathematically simple since it depends on only two parameters, however its shape is not always able to capture the shape of the in-cylinder pressure curve during combustion, particularly for varying rates of heat release [172]. The single Wiebe function depends on three parameters and is a very commonly used function to model combustion, as it is able to capture effectively the shape of heat release particularly for the diesel engines considered [152]. The double Wiebe function has various different versions most of which include more than four parameters, and is more aptly used to model the heat release rates for engines using gaseous fuels [173]. As a result, the single Wiebe function is deemed the most suitable for this case, the equation of which is provided below [149]:

$$f_C(\theta) = \begin{cases} 1 - \exp \left\{ -a \left(\frac{\theta - \theta_{SOC}}{\theta_{DOC}} \right)^{w+1} \right\} & \text{for } \theta \geq \theta_{SOC} \\ 0 & \text{for } \theta < \theta_{SOC} \end{cases} \quad (5.43)$$

where θ_{SOC} is the crank angle where the start of combustion takes place, θ_{DOC} is the crank angles corresponding to the duration of combustion, and w is the Wiebe exponent. Furthermore, a is a constant representing the combustion efficiency.

The in-cylinder pressure curve from Equation 5.42 includes several parameters, which can be classified as known and unknown as shown in Table 5.2. Subsequently, the inverse crankshaft dynamics model is utilised to determine the unknown in-cylinder pressure parameters, and use those to reconstruct the in-cylinder pressure curve. In specific, the unknown parameters include the maximum isentropic expansion pressure p_{me} , start of injection θ_{SOI} , duration of combustion θ_{DOC} , and Wiebe exponent w . The maximum isentropic expansion in-cylinder pressure is subsequently utilised by the equation in Erikson and Anderson [160] to calculate the mass of fuel injected in the cylinder, which provides a relationship between p_{me} and m_f .

Table 5.2: In-cylinder pressure curve parameters classification.

Equation	Parameter*	Classification**
Compression (Equation 5.40)	p_{EVC}	K
	γ_{co}	K
	θ_{EVC}	K
Expansion (Equation 5.41)	γ_{ex}	K
	V_c	K
	p_{me}	U
Wiebe function (Equation 5.43)	a	K
	θ_{SOC}	U
	θ_{DOC}	U
	w	U

*EVC for 2-stroke engines and IVC for 4-stroke engines.

**K=Known, U=Unknown

In regards to the parameters classified as known, the in-cylinder pressure at exhaust valve close p_{EVC} can be approximated as equal to the scavenge air pressure, which is monitored for large engines with adequate accuracy [94]. The crank angle at exhaust valve close θ_{EVC} and the clearance volume V_c can be obtained from the manufacturer documentation. The ratio of specific heats γ_{co} and γ_{ex} can be estimated with sufficient accuracy a-priori, by using air ideal gas tables [174], as they do not exhibit significant changes under faulty or degraded engine conditions [175]. Finally, the constant a set to 6.708 which implies a combustion efficiency of 99.9% [152].

Therefore the unknown parameters from Table 5.2 have to be included in Equa-

tion 5.42 such that the parametrised in-cylinder pressure curve can be incorporated in the crankshaft dynamics governing equations. This is firstly performed by grouping the unknown parameters into vector $\boldsymbol{\beta}_n$ for the n^{th} cylinder. Furthermore, from Equations 5.12 and 5.42, it is demonstrated that the combustion gases torque is a function of the crank angle and in-cylinder pressure, and the in-cylinder pressure is a function of the crank-angle and unknown parameters vector respectively. Therefore, the above functional dependencies can be demonstrated by the equations below:

$$\boldsymbol{\beta}_n = [p_{me,n} \quad \theta_{\text{SOC},n} \quad \theta_{\text{DOC},n} \quad w_n]^T \quad (5.44)$$

$$\Rightarrow \mathcal{T}_C(\hat{\boldsymbol{\Theta}}, \mathbf{B}) = [\mathcal{T}_C(\theta_{\text{cyl}1}, p(\theta_{\text{cyl}1}, \boldsymbol{\beta}_1)) \quad \dots \quad \mathcal{T}_C(\theta_{\text{cyl}n}, p(\theta_{\text{cyl}n}, \boldsymbol{\beta}_n)) \quad \dots]^T \quad (5.45)$$

where the angular displacements for the DOFs corresponding to the cylinders are included in the following vector $\hat{\boldsymbol{\Theta}} = [\theta_{\text{cyl}1} \quad \theta_{\text{cyl}2} \quad \dots \quad \theta_{\text{cyl}n} \quad \dots]^T$, and the unknown parameter vectors are concatenated in a larger vector $\mathbf{B} = [\boldsymbol{\beta}_1 \quad \boldsymbol{\beta}_2 \quad \dots \quad \boldsymbol{\beta}_n \quad \dots]^T$.

By establishing the functional dependency of the combustion gas torque with respect to the angular displacement and unknown parameters vector, the same can be done for \mathbf{J}_V which is a function of the angular displacement. As a result, the crankshaft dynamics governing equations can be expressed in the following format:

$$(\mathbf{J} - \mathbf{J}_V(\boldsymbol{\Theta})) \ddot{\boldsymbol{\Theta}} + \frac{1}{2} \frac{\partial \mathbf{J}_V(\boldsymbol{\Theta})}{\partial \boldsymbol{\Theta}} \dot{\boldsymbol{\Theta}}^2 + (\mathbf{D} + \mathbf{C}) \dot{\boldsymbol{\Theta}} + \mathbf{K} \boldsymbol{\Theta} = \mathcal{T}_C(\hat{\boldsymbol{\Theta}}, \mathbf{B}) - \mathcal{T}_L(\boldsymbol{\Theta}) \quad (5.46)$$

where further to the above, the angular displacement, speed and acceleration vectors are functions of time and the unknown parameters vector such that $\ddot{\boldsymbol{\Theta}}(t, \mathbf{B})$, $\dot{\boldsymbol{\Theta}}(t, \mathbf{B})$, and $\boldsymbol{\Theta}(t, \mathbf{B})$. This is due to the fact that the crankshaft dynamics model solution depends on the values of the unknown parameters vector since it greatly effects the excitation torques value. However for notational convenience the functional dependencies of the angular displacement vector and its derivatives will not be explicitly stated.

5.2.3 Sensitivity Equations & Extended Crankshaft Dynamics Model

The sensitivity equations are employed in order to determine the rate of change of a differential equation's solution, with respect to specific parameters contained within that differential equation. In specific, they are employed when a closed form expression of the differential equation solution is not available as its often the case, hence symbolic differentiation cannot be performed directly. The sensitivity equations are used in order to calculate the objective function gradient as described in Section 5.2.5, and to perform the stability analysis which warns the user of chaotic and unstable behaviour in the solution of the governing equations, as described in Section 5.2.4. To derive these equations, the crankshaft dynamics model differential equations are differentiated by considering their functional dependencies provided in Equation 5.46, as shown in the equation below:

$$\begin{aligned}
 (\mathbf{J} - \mathbf{J}_V)\ddot{\mathbf{Q}} + \left(\frac{\partial \mathbf{J}_V}{\partial \Theta} \dot{\Theta} + \mathbf{D} + \mathbf{C} \right) \dot{\mathbf{Q}} + \left(\frac{\partial \mathbf{J}_V}{\partial \Theta} \ddot{\Theta} + \frac{1}{2} \frac{\partial^2 \mathbf{J}_V}{\partial \Theta^2} \dot{\Theta}^2 \right. \\
 \left. + \frac{\partial \mathcal{T}_L}{\partial \Theta} - \frac{\partial \mathcal{T}_C}{\partial \Theta} + \mathbf{K} \right) \mathbf{Q} = \mathbf{E}
 \end{aligned} \tag{5.47}$$

where:

$$\mathbf{Q} = \begin{cases} \frac{\partial \Theta}{\partial \mathbf{B}} & \text{Case 1: objective function gradient calculation, Section 5.2.5} \\ \frac{\partial \Theta}{\partial \mathbf{x}_0} & \text{Case 2: stability analysis in Section 5.2.4} \end{cases}$$

$$\mathbf{E} = \begin{cases} \frac{\partial \mathcal{T}_C}{\partial \mathbf{B}} & \text{Case 1: objective function gradient calculation, Section 5.2.5} \\ \mathbf{0} & \text{Case 2: stability analysis in Section 5.2.4} \end{cases}$$

and $\mathbf{x}_0 = [\Theta_0^T, \dot{\Theta}_0^T]^T$.

The sensitivity equations in Equation 5.47 are a system of linear second order differential equations with variable coefficients, which are solved for state variables \mathbf{Q} for both of the following cases. In the first case, the state variables represent the angular displacement sensitivity with respect to the unknown parameters, and in the second case, the state variables represent the angular displacement sensitivity

with respect to the initial conditions of integration. This depends on whether the objective function gradient needs to be obtained or the stability analysis needs to be performed respectively. For each of the above cases, the sensitivity matrices of the state variables have the following form:

$$\frac{\partial \Theta}{\partial \mathbf{B}} = \begin{bmatrix} \frac{\partial \theta_1}{\partial \mathbf{B}} \\ \vdots \\ \frac{\partial \theta_j}{\partial \mathbf{B}} \end{bmatrix} = \begin{bmatrix} \frac{\partial \theta_1}{\partial \beta_1} & \cdots & \frac{\partial \theta_1}{\partial \beta_n} \\ \vdots & \ddots & \vdots \\ \frac{\partial \theta_j}{\partial \beta_1} & \cdots & \frac{\partial \theta_j}{\partial \beta_n} \end{bmatrix}$$

$$\frac{\partial \Theta}{\partial \mathbf{x}_0} = \begin{bmatrix} \frac{\partial \theta_1}{\partial \mathbf{x}_0} \\ \vdots \\ \frac{\partial \theta_j}{\partial \mathbf{x}_0} \end{bmatrix} = \begin{bmatrix} \frac{\partial \theta_1}{\partial \theta_{0,1}} & \cdots & \frac{\partial \theta_1}{\partial \theta_{0,n}} & \frac{\partial \theta_1}{\partial \theta_{0,1}} & \cdots & \frac{\partial \theta_1}{\partial \theta_{0,n}} \\ \vdots & \ddots & \vdots & \vdots & \ddots & \vdots \\ \frac{\partial \theta_j}{\partial \theta_{0,1}} & \cdots & \frac{\partial \theta_j}{\partial \theta_{0,n}} & \frac{\partial \theta_j}{\partial \theta_{0,1}} & \cdots & \frac{\partial \theta_j}{\partial \theta_{0,n}} \end{bmatrix}$$

As a result, the sensitivity of the torque at the j^{th} DOF with respect to the unknown parameters or the initial conditions can be obtained according to Equations 5.48–5.49. This is accomplished by differentiating Equation 5.18, and utilising the respective elements obtained from the sensitivity matrices above:

$$\frac{\partial \mathcal{T}_j(t, \mathbf{B})}{\partial \mathbf{B}} = k_j \left(\frac{\partial \theta_j}{\partial \mathbf{B}} - \frac{\partial \theta_{j+1}}{\partial \mathbf{B}} \right) \quad (5.48)$$

$$\frac{\partial \mathcal{T}_j(t, \mathbf{x}_0)}{\partial \mathbf{x}_0} = k_j \left(\frac{\partial \theta_j}{\partial \mathbf{x}_0} - \frac{\partial \theta_{j+1}}{\partial \mathbf{x}_0} \right) \quad (5.49)$$

The sensitivity equations have variable coefficients, the values of which depend on the solution of the direct crankshaft dynamics model. However, to improve computational efficiency, the sensitivity equations can be solved simultaneously with the direct crankshaft dynamics model as part of a larger system of equations hereinafter referred to as the extended crankshaft dynamics model.

The extended model is developed by firstly transforming Equations 5.46 and 5.47 into a first order equivalent system, as described in Appendix A. Subsequently, the transformed sensitivity equations are vectorised as indicated by the operator $\text{vec}(\cdot)$, which is a linear operation that converts a matrix into a column vector. Finally, by utilising subscript notation for the partial derivatives, the extended crankshaft

dynamics model can be formulated as follows:

$$\begin{bmatrix} \dot{\Theta} \\ \ddot{\Theta} \\ \text{vec}(\dot{\Theta}_B) \\ \text{vec}(\ddot{\Theta}_B) \\ \text{vec}(\dot{\Theta}_{x_0}) \\ \text{vec}(\ddot{\Theta}_{x_0}) \end{bmatrix} = \begin{bmatrix} G(\dot{\Theta}, \Theta, B) \\ \text{vec} \left(S(\dot{\Theta}_B, \Theta_B, B) \right) \\ \text{vec} \left(S(\dot{\Theta}_{x_0}, \Theta_{x_0}, x_0) \right) \end{bmatrix} \quad (5.50)$$

where G , and S denote the functional form of the first order equivalent systems of Equations 5.46 and 5.47, as presented in Appendix A.

It should be noted that even though the extended crankshaft dynamics model incorporates an additional number of equations, the input remains the same as it was for the direct model shown in Figure 5.3. However, besides the engine torque for the j^{th} DOF according to Equation 5.18, two additional types of output are obtained from the extended model which include the respective sensitivities obtained by Equations 5.48–5.49.

5.2.4 Stability Analysis

The physical stability analysis of differential equations is a prominent issue in determining and predicting the behaviour of the system being modelled [167]. Physical stability analysis should be distinguished from numerical stability analysis, since the latter refers to the numerical scheme employed, and the former refers to the physical characteristics of the modelled system. In specific, the system modelled can be physically stable, however the numerical scheme employed to solve its governing equations may not be. Therefore, numerical stability has been addressed as part of Section 5.1.4. Consequently, the term stability analysis within the context of this research is used to refer to the physical stability.

Stability analysis concerns differential equations with non-linearities in particular, such as the crankshaft dynamics governing equations. Such equations are susceptible chaotic and unstable behaviours due to very small perturbations in the user-set initial conditions. This does not only effect the numerical and mathematical approaches used to solve the equations, but reveals very important dynamics of the physical

system being studied, which is in this case the engine crankshaft dynamics.

As a result, ensuring that the crankshaft dynamics governing equations have good stability characteristics is essential in order to confirm that the direct crankshaft dynamics model will always reach steady state for the given user-defined initial conditions. This can be verified by conducting stability analysis using the concept of Lyapunov Exponents (LEs) [176]. In specific, the LE is a quantity that characterises the rate of separation of two infinitesimally close trajectories in the solution of a system of differential equations, according to the following equation:

$$|\delta\mathbf{Z}(t)| \approx e^{\psi t} |\delta\mathbf{Z}_0| \quad (5.51)$$

where $\delta\mathbf{Z}_0$ is the initial separation vector and ψ is the LE. As a consequence of Equation 5.51, when the value of the LE is negative then the system converges to a steady solution, and when positive chaotic and unstable behaviour is indicated [176]. Provided that there are multiple orientations of the separation vector $\delta\mathbf{Z}_0$, a spectrum of LEs is can be obtained, however to identify if a system is stable only the largest, or the maximal LE is necessary. The maximal LE is defined according to the following equation for the case of the crankshaft dynamics governing equations:

$$\psi = \lim_{n \rightarrow \infty} \frac{1}{n} \sum_{k=0}^{n-1} \ln \left| \frac{\partial \Theta(t_k)}{\partial \mathbf{x}_0} \right| \quad (5.52)$$

where the partial derivative of the crankshaft dynamics governing equation state variable Θ , with respect to the initial conditions vectors \mathbf{x}_0 can be obtained as described in Section 5.2.3.

5.2.5 Inverse Model Development

The inverse crankshaft dynamics model utilises a single-shooting IVP parameter estimation technique in order to determine the unknown parameters of the in-cylinder pressure curve, by utilising the measured engine ICT, as outlined in Section 5.2.1. Amongst the parameter estimation techniques reviewed in Section 2.1.3.4 the IVP technique is chosen due to its computational simplicity, as well as bypassing the complex structure of ill-posed problems. This is advantageous as past attempts to invert direct crankshaft dynamics models have presented an ill-posed problem

since singularities occur near the TDC when attempting to calculate the in-cylinder pressure using the cylinder torque [80].

However, to ensure that the IVP technique performs adequately, the stability of the governing equations from the direct crankshaft dynamics model needs to be verified, and a good estimate of the initial parameters can be obtained. The latter will be ensured by implementing stability analysis within the inverse crankshaft dynamics model, and the former does not pose a challenge, as a relatively accurate estimate for the initial values of the unknown parameters for the in-cylinder pressure curve can be obtained. This is accomplished by means of least squares fitting of Equation 5.42 to in-cylinder pressure diagrams obtained from the thermodynamics model developed in Section 3.1 which are available for a number of engine operating points.

The optimisation algorithm is a basic part of the IVP technique, hence its selection is of critical importance. Overall, optimisation algorithms can be categorised as derivative-free, stochastic and gradient based [177]. Derivative-free algorithms are simplistic, yet their convergence is time consuming as they perform a very large number of objective function evaluations. Stochastic algorithms can handle extremely complex objective functions with multiple minima and discontinuities. However they are computationally complex and require a very large number of function evaluations, which results to an increased execution time. Gradient based algorithms and particularly Levenberg-Marquardt (LM) algorithms, are extensively used for nonlinear parameter identification problems due to their robustness and quick convergence near the minimum. Their application would be especially advantageous for the case of this study, as the analytic gradient of the direct model can be obtained, hence improving the execution time and the solution robustness compared to the use of a numerically estimated gradient. In this respect, this study employs the Nonmonotone Self-Adaptive Levenberg-Marquardt (NSALMN) algorithm [178] which is an especially robust version of the LM algorithm.

The flowchart of the inverse crankshaft dynamics model algorithm is shown in Figure 5.5, and starts by providing the algorithm input. This firstly includes the user-defined settings which comprise of the first-order optimality termination tolerance ε , the initial LM step damping parameter ν_0 which determines the size of the first step,

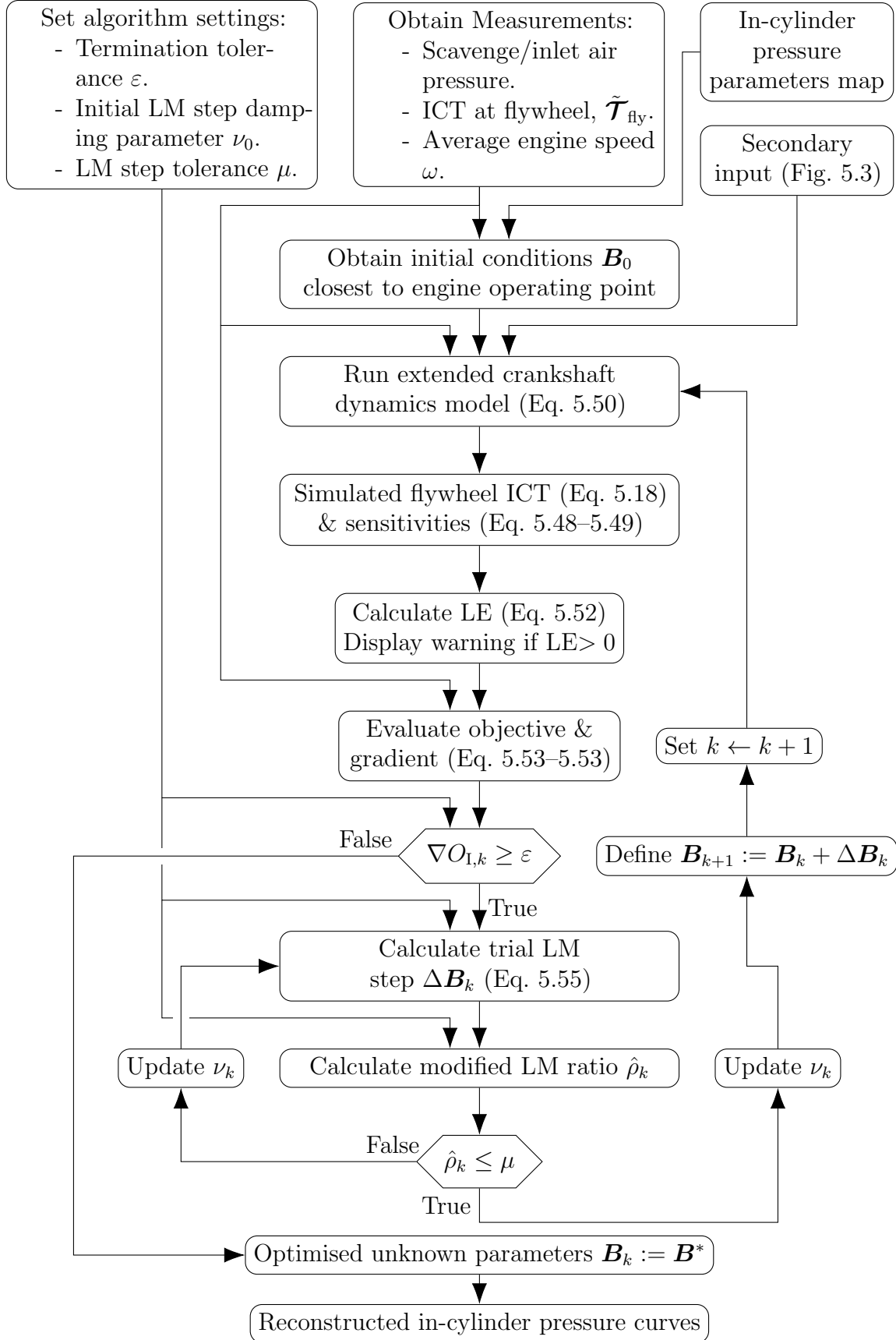


Figure 5.5: Inverse crankshaft dynamics model algorithm, used to reconstruct the in-cylinder pressure curves.

as well as the LM step tolerance μ which determines if the trial step is accepted by the algorithm. Secondly, the measurements included are the scavenge/inlet manifold air pressure and average engine speed utilised in the extended crankshaft dynamics model, as well as the ICT measurement at the flywheel $\tilde{\tau}_{\text{fly}}$ obtained by the high-sample rate torquemeter which is utilised in the objective function formulation. Third, the in-cylinder pressure parameters map is included which contains the values of the unknown parameters vector \mathbf{B} for various engine operating points. In specific, this map is obtained by performing linear-least squares to determine the unknown parameters on the in-cylinder pressure diagrams obtained by the healthy conditions digital twin at 10 engine operating points, covering uniformly the entire operating envelope. Lastly, the secondary input is included as shown in Figure 5.3.

Following the input, the initial conditions of the unknown parameters vector \mathbf{B}_0 are obtained by extracting the parameters within the in-cylinder pressure parameters map which lie closest to the engine's current operating point. The engine's current operating point is obtained from the available measurements, by averaging the measured ICT at the flywheel over one engine cycle, as well as the average engine speed. Subsequently, the extended crankshaft dynamics model from Equation 5.50 is executed, and the simulated flywheel ICT (Eq. 5.18) as well as the related sensitivities (Eq. 5.48–5.49) are obtained as the output. In the next step, the sensitivities with respect to the initial conditions are used to perform the stability analysis by employing the Lyapunov Exponents (LE) as described in Section 5.2.4. A warning is displayed if the LE exponents are negative, thus indicating the possibility of unstable behaviour in the extended crankshaft dynamics model governing equations.

Having completed the stability analysis, the objective function and its gradient can be evaluated in Equations 5.53–5.54 below respectively. This is performed in the frequency domain as it drastically improves algorithm performance since it reduces the effect of noise, and simplifies the objective function by considering the effect of the more dominant dynamics:

$$O_{1,k} = \frac{1}{2} \frac{\|\tau_{\text{fly}}(\mathbf{B}_k) - \tilde{\tau}_{\text{fly}}\|_2^2}{\max\{\tilde{\tau}_{\text{fly}}\}} \quad (5.53)$$

$$\nabla O_{1,k} = \frac{\partial \tau_{\text{fly}}}{\partial \mathbf{B}_k}^T \left(\frac{\tau_{\text{fly}}(\mathbf{B}_k) - \tilde{\tau}_{\text{fly}}}{\max\{\tilde{\tau}_{\text{fly}}\}} \right) \quad (5.54)$$

where $\|\cdot\|_2$ is the Euclidean norm, \mathbf{B}_k is the unknown parameters vector for the k^{th} algorithm iteration described in Section 5.2.2, $\boldsymbol{\tau}_{\text{fly}}$ with $\tilde{\boldsymbol{\tau}}_{\text{fly}}$ represent the Fourier transformation vector of the simulated ICT in Equation 5.18 and the measured data respectively, and $\frac{\partial \boldsymbol{\tau}_{\text{fly}}}{\partial \mathbf{B}_k}$ is the Fourier transformation vector of the sensitivity matrices in Equation 5.48. Finally, $\max\{\boldsymbol{\tau}_{\text{fly}}\}$ is utilised as a scaling factor of the objective function to improve the algorithm performance.

Having evaluated the objective function and its gradient, in the next step if the first-order optimality tolerance is satisfied, a local minimum is possible, hence the algorithm terminates and returns as output the optimised unknown in-cylinder pressure parameters \mathbf{B}^* . If the tolerance is not fulfilled the algorithm proceeds to the next step which calculates the trial LM step by making a linear approximation of the objective function according to the following equation:

$$\Delta \mathbf{B}_k = \left(\frac{\partial \boldsymbol{\tau}_{\text{fly}}}{\partial \mathbf{B}_k}^T \frac{\partial \boldsymbol{\tau}_{\text{fly}}}{\partial \mathbf{B}_k} + \nu_k \mathbf{I} \right)^{-1} \nabla O_{\text{I},k} \quad (5.55)$$

where ν_k is the LM damping parameter which determines the size and direction of the trial step. This is accomplished by employing a self-adaptive method which considers the damping parameter as a function of the modified LM ratio and the objective function value. This method induces a behaviour similar to the more robust gradient descent step when further from the minimum, or the faster converging Newton-Gauss step when closer to the minimum. The specific calculation procedures of the LM step can be found in [178].

In the next step, the LM ratio $\hat{\rho}_k$ is calculated which is once again specific to the NSALMN algorithm, and is a measure of the agreement of the linear approximation made by the LM step, as compared to the exact value of the objective function in the current iteration. Subsequently, in the following step, if the LM ratio lies within the user-defined tolerance μ , it is accepted and the damping parameter ν_k is modified such that that a larger step can be taken in the next iteration. The LM step is then added to the unknown parameter vector to define its new value such that $\mathbf{B}_{k+1} := \mathbf{B}_k + \Delta \mathbf{B}_k$, and the process repeats itself until the first-order optimality criterion is fulfilled. Conversely if the LM ratio lies outside the user-defined tolerance, the damping parameter ν_k is recalculated to obtain a shorter trial step, thereby following more closely the shape of the objective function.

5.2.6 Inverse Model Verification Procedure

The verification of the inverse crankshaft dynamics model consists of a four part process which tests said model by emulating realistic and challenging conditions which could be encountered when deploying the proposed research methodology for engines of various conditions and in a wide range of operating points.

In specific, the first part consists of determining the optimal settings of the initial LM step damping ν_0 and LM step tolerance μ , which enable the convergence of the inverse crankshaft dynamics model over a wide operating envelope of the engine. The second part quantifies the performance of the inverse crankshaft dynamics model by considering deviations in the Torsional Vibration Damper (TVD) coefficients by changing the stiffness and damping coefficient factors x_1 and x_2 respectively, which could be unaccounted for by the user. This is likely to take place since the direct crankshaft dynamics model calibration techniques to determine these coefficients, such as the one presented in Section 5.1.8, may often be unsuccessful by yielding incorrect results [116]. Third, the performance of the inverse crankshaft dynamics model is quantified considering various levels of Signal-to-Noise Ratio (SNR) present in the ICT measurement which acts as input to the inverse crankshaft dynamics model in order to reconstruct the in-cylinder pressures. Fourth, the inverse crankshaft dynamics model is validated using the obtained ICT measurements for the respective reference system. The above four parts along with the relevant adjusted parameters and the range of their values, are listed in Table 5.3, and the procedure to achieve the objective of each part is described below.

For the first three parts, firstly five sample operating points are chosen which cover uniformly the entire engine operating envelope. For these points the healthy conditions digital twin is utilised to obtain the in-cylinder pressure curves which act as the in-cylinder pressure simulated measurements.

For the first part in Table 5.3, the in-cylinder pressure simulated measurements are utilised as input to the direct crankshaft dynamics model to obtain the ICT which act as the ICT simulated measurements. The ICT simulated measurements are then deployed as input to the inverse crankshaft dynamics model. In addition, the values of the user-defined settings for the inverse crankshaft dynamics model, ν_0 and μ are changed each in 11 equal increments within $[0.8, 1.1]$ and $[4, 10] \times 10^{-3}$

Table 5.3: Four part verification procedure of inverse crankshaft dynamics model.

Part	Objective	Parameters	Range	Runs*
1	Determination of optimal settings for convergence	Init. step damping, ν_0 Step tolerance, μ	[0.8, 1.1] [4, 10] $\times 10^{-3}$	605
2	Inverse crank. dyn. model performance quantification with TVD coefficient errors	Stiffness factor, x_1 Damping factor, x_2	[0.8, 1.2] [0.8, 1.2]	605
3	Inverse crank. dyn. model performance quantification with measurement noise	Signal-to-Noise Ratio	[10^4 , 3]	55
4	Inverse crank. dyn. model validation using ICT measurements from reference system	-	-	0

*Number of parametric runs.

respectively, and all their combinations are considered thus providing a total of $11^2 = 121$ unique pairs of the ν_0 and μ parameter values. By considering this in addition to the five operating points chosen, a total of $121 \times 5 = 605$ parametric runs of the inverse crankshaft dynamics model are performed. The performance of each parametric run is quantified according to a KPI which considers the error between the reconstructed in-cylinder pressure curves by the inverse crankshaft dynamics model and the in-cylinder pressure simulated measurements, as well as the number of iterations required to achieve convergence. As a result, the optimal settings are found where the sum of the KPIs for all sample operating points becomes minimum, thus implying the best combination of a small error together with only a few iterations required to reach convergence. The KPI is provided by the equation below:

$$\text{KPI}_I = \sum_{i=1}^5 (\tilde{\varepsilon}_{p,i} + w_{I,i} I_i) \quad (5.56)$$

where I is the number of iterations taken to achieve convergence, w_I is a user defined weight which can be set equal to $(\max\{\tilde{\varepsilon}_p\} - \min\{\tilde{\varepsilon}_p\}) (\max\{I\} - \min\{I\})^{-1}$ to ensure that both $\tilde{\varepsilon}_p$ and I contribute equally to the KPI value, and $\tilde{\varepsilon}_p$ is the NRME of the reconstructed in-cylinder pressure with the simulated measurements, which is calculated in accordance to the equation below:

$$\tilde{\varepsilon}_p = \frac{\|\mathbf{p}_{\text{sim}} - \tilde{\mathbf{p}}\|_2}{\text{mean}(\tilde{\mathbf{p}})} \quad (5.57)$$

where $\|\cdot\|_2$ is the Euclidean norm, $\tilde{\cdot}$ indicate measured quantities, and \mathbf{p} is the in-cylinder pressure vector including all cylinders.

For the second part in Table 5.3, the values of the TVD stiffness and damping factors, x_1 and x_2 are both changed in 11 equal increments within $[0.8, 1.2]$. By considering all combinations of the above parameters and the five operating points, a total of $11^2 \times 5 = 605$ parametric runs of the direct crankshaft dynamics model are performed to obtain the ICT simulated measurements. These are subsequently deployed as input to the inverse crankshaft dynamics model which is also deployed once for every parametric run, however by keeping the TVD stiffness and damping factors the same as determined by the direct crankshaft dynamics model calibration process described in Section 5.1.8. The performance quantification takes place by considering the in-cylinder pressure NRME according to Equation 5.57 above, as well as the maximum percentage difference between the peak in-cylinder pressure of the reconstructed curves by the inverse model and the simulated measurements. Therefore, via this procedure, this part provides insight on how TVD coefficient discrepancies effect the accuracy of the reconstructed in-cylinder pressure curves provided by the inverse crankshaft dynamics model.

For the third part in Table 5.3 the direct crankshaft dynamics model is deployed for the five operating points to obtain the simulated ICT. On the simulated ICT white Gaussian noise is added in 11 equal increments with SNR within $[1 \times 10^4, 3]$, providing a total of $11 \times 5 = 55$ ICT simulated measurements. For each ICT simulated measurement the inverse crankshaft dynamics model is employed thereby making a total 55 parametric runs, the performance of which is quantified using the the NRME of the in-cylinder pressures and the maximum percentage difference between the peak pressures, same as in the second part described above.

Finally, for the fourth part in Table 5.3, the inverse crankshaft dynamics model remains to be validated by utilising the actual ICT measurements obtained for the appropriate reference system. As a result since the actual ICT measurements are utilised there are no parametric runs performed as indicated on the table.

Chapter 6

Reference System, Available Data, and Case Studies

6.1 Reference Systems & Available Data

The research methodology described in Chapter 3 has been demonstrated by employing three reference systems presented in Table 6.1. Detailed information on reference system specifications, DOF coefficients and lumped mass model layout (including torque meter locations) is provided in Appendix B.

Table 6.1: Reference systems overview.

	W9L46C	6RTflex50	10L67GBE
Type	4-stroke	2-stroke	2-stroke
MCR (kW @ RPM)	9,450 @ 500	8,890 @ 116	15,500 @ 125
Number of Cylinders	9	6	10
Cylinder Bore (mm)	460	500	670
Load Type	CPP*	FPP**	Generator

*CPP: Controllable Pitch Propeller

**FPP: Fixed Pitch Propeller

The first reference system is a 4-stroke Wärstilä engine which is installed in a RoPax ferry as part of four-engine configuration with identical engines. Each pair of engines drives a gearbox which in turn provides power to a controllable pitch propeller and a power take-off generator. The measurement campaign was conducted for one of the engines in steady state for two the operating points of 2,949 kW at 401 RPM, and 5,491 kW at 450 RPM as shown in Figure 6.1. The in-cylinder pressures of all cylinders and the ICT between the camshaft drive and flywheel, were obtained using

a Kistler 6619AP35 pressure sensor, and a high-sample rate prototype torque meter respectively, more details on which are provided in Appendix C. Furthermore, the shop tests and torsional vibration study were obtained from when the engine was built in year 2000, as well as the T/C map and engine geometry data. Despite having two engines as part of the same lumped mass model system, the measurement campaign was conducted for only one engine, since the torque meter location was placed forward of the engine coupling, thereby completely isolating the one engine from the dynamics of the other under normal seagoing conditions. This was readily verified by the engine torsional vibration study.

The second reference system is a 2-stroke Wärstilä RT-flex engine installed in a bulk carrier, driving a fixed pitch propeller, the available data of which includes the shop tests and project guide as indicated in Table 6.2, which were obtained from the build year of the engine in 2014.

The third reference system is a 2-stroke MAN B&W land-based engine powering a constant speed generator, the data of which has been obtained from published works [92, 94, 179]. The measurements include the in-cylinder pressure of all cylinders and the ICT at four engine operating points from 7,800 kW to 13,800 kW, at a constant speed of 125 RPM as shown in Figure 6.2. The ICT measurements were obtained by a high-sample rate torque meter mounted between the flywheel and generator rotor. Most crucially, the updated torsional vibration study is available as indicated on Table 6.2, which includes the calibrated DOF coefficients from 2016, which is the same time the in-cylinder pressure and ICT were obtained.

Table 6.2: Overview of reference systems available data and case studies deployment.

Required Data	W9L46C	6RTflex50	10L67GBE
In-cylinder Pressure Measurement	✓	-	✓
Instantaneous Flywheel Torque (ICT) Measurement	✓	-	✓
Shop Tests	✓	✓	-
Torsional Vibration Study	✓	-	✓
Project Guide	✓	✓	-
T/C Maps & Geometry Data	✓	-	-
Case studies deployed	ALL ex. 3(a)	2(a)	3(a)

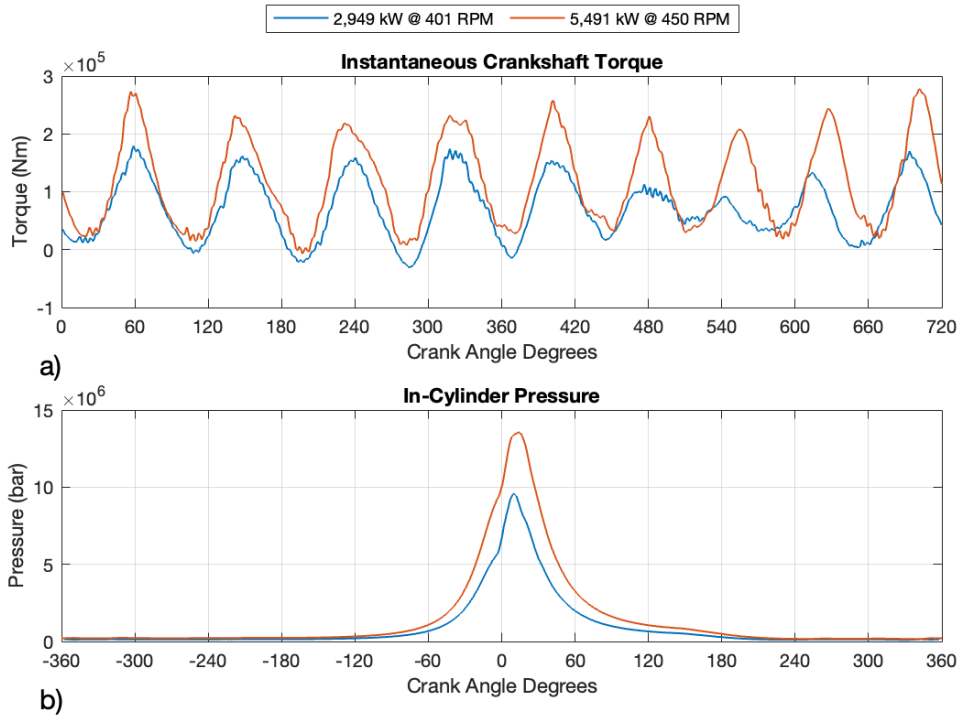


Figure 6.1: Measurement samples of the W946C reference system. a) Instantaneous Crankshaft Torque (ICT) measurement and b) in-cylinder pressure measurement of cylinder no. 1.

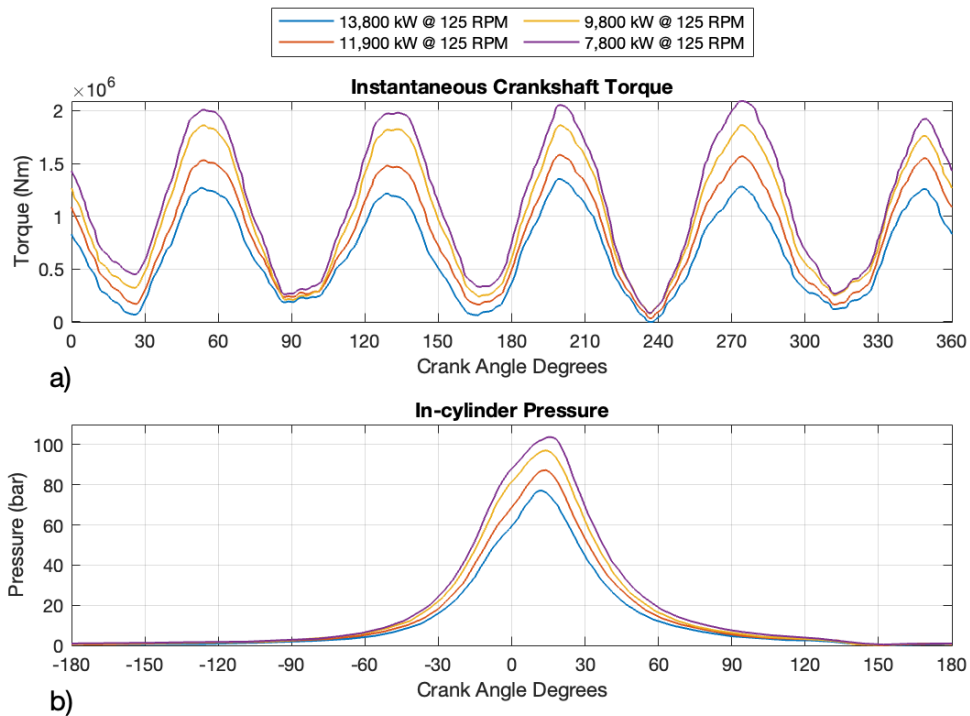


Figure 6.2: Measurement samples of the 10L67GBE reference system. a) Instantaneous Crankshaft Torque (ICT) measurement and b) in-cylinder pressure measurement of cylinder no. 1.

6.2 Case Studies

The methodology discussed in Chapter 3 is implemented via several case studies, the results of which are subsequently presented in Chapter 7. In specific, these case studies are listed in Table 6.3, and correspond to each stage of the methodology:

Table 6.3: Case studies pertaining to each stage of the methodology.

Stage*	Case Study Number	Description	Reference System	Section
2	2(a)	Healthy conditions digital twin calibration	W9L46C 6RTflex50	7.1
	2(b)	Healthy conditions performance maps	W9L46C	7.2
3	3(a)	Direct crankshaft dynamics model solution method determination	10L67GBE	7.3
4	4(a)	Direct crankshaft dynamics model calibration	W9L46C	7.4
	4(b)	Inverse crankshaft dynamics model verification	W9L46C	7.5
	4(c)	Current conditions digital twin configuration & performance maps	W9L456C	7.6
5	5(a)	Derivation of health assessment KPIs& maps	W9L46C	7.7

*Methodology stage

Regarding the first stage, there are no case studies included as it involves the development, setup and formulation of the thermodynamics model, the process of which is described in Chapter 4.

For the second stage including the healthy conditions digital twin, the case study 2(a) involves the calibration of the digital twin in healthy engine conditions. This is performed by using the shop test data as described in Section 4.5, for the W9L46C and 6RTflex50 reference systems. Using the calibrated digital twin, case study 2(b) involves parametric runs to derive the healthy conditions performance maps. This case study is performed for the W9L46C reference system, since the T/C map is available therefore the multi-cylinder thermodynamics model can be deployed with sufficient accuracy.

The third stage which includes the crankshaft dynamics model, contains study 3(a). This case study considers the three solution methods proposed in Section 5.1 of the direct crankshaft dynamics model, to determine the one with the best compromise between computational simplicity, execution time, and overall accuracy when compared to measured data. The quantification of the performance of each solution method is outlined in Section 5.1.6. The 10L67GBE reference system is selected to be employed in this case study, firstly due to the system's simplicity as a land-based generator which exclude propeller dynamic and damping effects, and secondly due to the fact that the calibrated DOF coefficients are already available.

The fourth stage including the current conditions digital twins, firstly involves case study 4(a) where the direct crankshaft dynamics model calibration takes place as described in Section 5.1.8. The output of case study 4(a) is utilised for case study 4(b) where the inverse crankshaft dynamics model is verified according to the procedure in Section 5.2.6, by employing parametric runs of the respective digital twins to quantify its performance as well as validate it using the ICT measurements. Subsequently, the in-cylinder pressure diagram parameters provided as output from case study 4(b) including the mass of fuel injected, duration of combustion and Wiebe exponent, are utilised as input to the thermodynamics model in case study 4(c) as described in Section 3.4, in order to configure the current conditions digital twin as well as to perform parametric runs to provide the current engine conditions performance maps. The fourth stage case studies are conducted for the W9L46C reference system since the in-cylinder pressure and ICT measurements were obtained by the author. Consequently this makes the system suitable to verify and validate the inverse crankshaft dynamics model which is one of the main aspects of the research methodology.

The fifth stage performs the engine health assessment which utilises the healthy and current engine performance maps derived from case studies 2(b) and 4(d) respectively. These maps are utilised to derive the health assessment KPIs for the entire engine operating envelope as described in Section 4.7, hence providing as final output the engine health assessment maps. The case studies in this stage are conducted for the W9L46C reference system, since it contains the most complete available data and measurements as shown in Table 6.2.

Chapter 7

Results & Discussion

7.1 Case Study 2(a): Healthy Conditions Digital Twin Calibration

The healthy conditions digital twin is developed by calibrating the thermodynamics model utilising the available measurements in the shop tests, according to the methodology in Chapter 3, for the reference systems of W9L46C and 6RTflex50, which are 4-stroke and 2-stroke propulsion engines respectively.

The first step of the calibration involves the determination of the combustion and friction mean effective pressure parameters for the reference system. This is performed at a reference operating point obtained from the shop tests, which is chosen to lie within the engine's most frequent operational envelope. In specific, for the W9L46C engine the most frequent operating point is from 4,000–6,000 kW at 400–450 RPM as advised by the crew, hence the reference point from the shop tests is chosen to be 4,725 kW at 400 RPM. Similarly for the 6RTflex50 engine, the most frequently operating point is again from 4,000–6,000 kW at 85–95 RPM as obtained from the literature for similar engines [6]. Therefore the reference point from the shop tests is chosen to be 4,469 kW at 92.2 RPM.

The second step of the calibration determines the values of the Woschni-Anisits model constants by considering all the remaining shop test operating points. Overall, for both steps of the calibration process the particle-swarm optimisation employed demonstrated its consistency, as inferred from the small deviation of the calibrated

values for every run, which are provided in Appendix E.

To verify the consistency of the particle-swarm optimisation algorithm, three separate runs were performed for each reference system, the results of which are shown in Appendix E. With minor deviations between each run, their average is shown in Table 7.1, where it is demonstrated that the calibrated parameters values lie well within the ranges reported in the pertinent literature for similar engine types [105, 149, 151, 180]. An exception is made of the two engine speed exponents g_1 and g_3 of the Woschni-Anisits model, however when constraining the particle-swarm optimisation algorithm to within the engine speed constants limits specified in the literature, a less optimal solution is obtained. Hence, considering that only a few sources in the literature discuss those limits with minor discrepancies between them, they can be considered as soft limits, and values exceeding those can be deemed acceptable.

Furthermore, comparing the calibrated combustion and FMEP values for both engines, it is observed that for the 4-stroke as compared to the 2-stroke engine, the combustion duration is significantly greater by 56.0°CA whilst the Wiebe exponent is reduced by 0.934, which will result to a more gradual increase to the in-cylinder pressure diagram following ignition. Furthermore, the FMEP factor is almost equivalent to 1 for the case of the 2-stroke engine which is reasonable as the coefficients of the Chen-Flynn FMEP model were obtained from a similar 2-stroke diesel engine as discussed in Section 4.2.1.2, whilst the FMEP losses appear to be much greater for the case of the 4-stroke engine.

Table 7.1: Healthy conditions digital twin calibrated values for W9L46C and 6RTflex50 reference systems.

Parameters	Calibrated Values		Limits
	W9L46C	6RTflex50	
Engine speed exponent, DOC (g_1)	0.723	0.455	$-0.65 \sim 0.5$
Equivalence ratio exponent (g_2)	0.078	0.420	$-0.30 \sim 0.60$
Engine speed exponent, Wiebe (g_3)	0.403	0.280	$-0.8 \sim 0.3$
Wiebe exponent delta (Δw)	0.142	0.011	-
Wiebe Exponent* (w)	0.323	1.257	$0.2 \sim 2.0$
DOC* (θ_{DOC})	90.5°CA	34.5°CA	$30 \sim 110^\circ\text{CA}$
Friction Factor (f_{mep_0})	2.277	1.023	-

*At reference operating points of: 4,725 kW @ 400 RPM for W9L46C
4,469 kW @ 92.2 RPM for 6RTflex50

Following the determination of calibration parameters, the thermodynamics digital twin was subsequently validated by comparing the simulated BSFC and peak in-cylinder pressure (p_{\max}) with the respective shop test measurements. Considering the results presented in Table 7.2, for the 4-stroke W9L46C reference system, the simulated BSFC and peak in-cylinder pressure exhibit a maximum error of 2.7% and 2.5% respectively, as compared to the shop tests. Similarly, for the 2-stroke 6RTflex50 reference system, the simulated BSFC and peak in-cylinder pressure exhibit a maximum error of 1.5% and -2.9% respectively, as compared to the shop tests.

The error appears to be the least at the reference operating points indicated by an asterisk in Table 7.2. This demonstrates the importance of properly choosing the reference operating point, so that the simulation results exhibit sufficient accuracy within of the most frequent engine operation points. Finally, the error for all operating points in the BSFC and maximum in-cylinder pressure can be considered as acceptably small by taking into account similar studies [105, 151], thereby validating the developed thermodynamics model.

Table 7.2: Digital twin validation results at healthy conditions following calibration, for W9L46C and 6RTflex50 reference systems.

	Operating Point (kW @ RPM)	BSFC		p_{\max}	
		Simulated (g/kWh)	Shop Test Δ (%)	Simulated (g/kWh)	Shop Test Δ (%)
W9L46C	4,725 @ 500	195.9	2.7	130	2.5
	7,088 @ 500	186.5	1.2	177	3.0
	8,033 @ 500	186.9	-0.1	188	0.0
	9,450 @ 500	189.8	-0.5	194	-0.4
	10,395 @ 500	193.4	-1.2	197	-0.1
	6,143 @ 440	186.3	1.04	156	1.2
	4,725 @ 400*	189.3	0.1	130	0.1
6RTflex50	4,469 @ 92.2*	168.8	0.1	120	0.4
	6,682 @ 105.4	167.0	-0.8	149	-2.9
	7,121 @ 107.7	166.8	1.1	151	-2.1
	8,915 @ 116.1	170.5	1.5	152	1.3

*Reference operating points.

7.2 Case Study 2(b): Healthy Conditions Performance Maps

The calibrated digital twin was used to simulate the engine operation for a wide operating envelope, thereby deriving engine performance parameters maps and qualitatively verifying the engine performance for the reference system of the 4-stroke W9L46C engine, as shown in Figure 7.1.

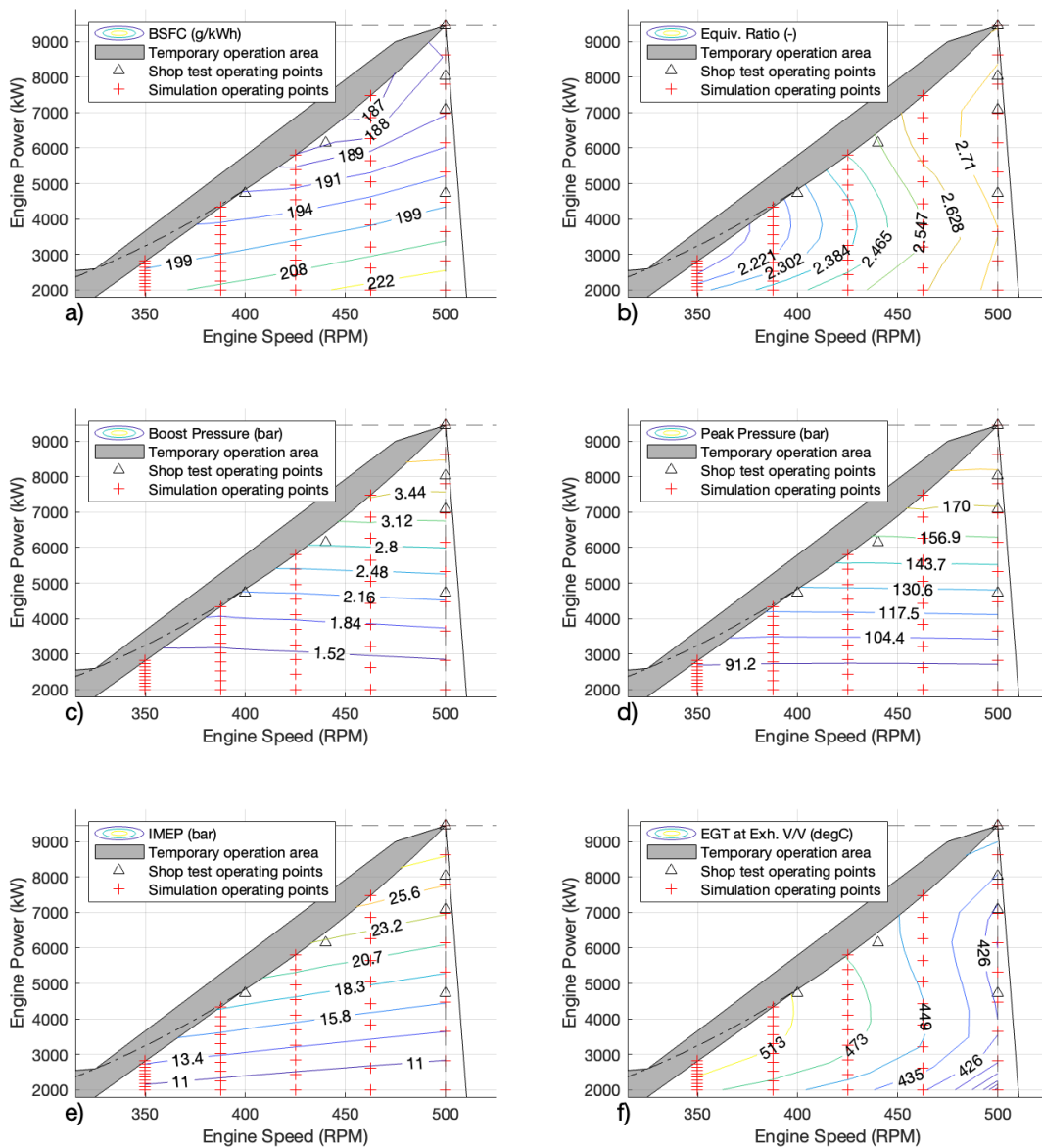


Figure 7.1: Performance maps of the W9L46C digital twin in healthy conditions: (a) BSFC map for healthy engine conditions. (b) Equivalence ratio map for healthy engine conditions. (c) Boost pressure map for healthy engine conditions. (d) Peak pressure map for healthy engine conditions. (e) IMEP map for healthy engine conditions. (f) Exhaust gas temperature at exhaust valve map for healthy engine conditions.

Figures 7.1 (a)–(c) provide the BSFC, equivalence ratio at the exhaust manifold, and boost pressure at the inlet manifold. Figures 7.1 (d)–(f) include the average values from all 9 cylinders of the maximum in-cylinder pressure, IMEP, and EGT at the exhaust valve. However, since the digital twin simulates healthy conditions, there are no deviations in the values of the three aforementioned parameters between the cylinders.

Figure 7.1 (a) demonstrates that the engine BSFC exhibits a minimum near 80% load on the lower boundary of the temporary operation range shown in gray, similar to the manufacturer reference map [181]. The rapid increase of the BSFC away from the minimum of up to 10 g/kWh for loads close to 4,000 kW, enforces the importance of matching the actual vessel operation as close to the engine design point as possible, or de-rating the engine to achieve better fuel efficiency at lower loads if the vessel operational profile changes significantly. Figure 7.1 (b) demonstrates that the equivalence ratio values exceeds 2, indicating lean combustion conditions, which are typical of large four-stroke diesels, resulting lower NOx emissions [156].

Figures 7.1 (c) and (d) demonstrate that the boost pressure and peak in-cylinder pressure vary almost exclusively as a linear function of the engine load, as expected [107]. Furthermore, Figure 7.1 (e) illustrates that the IMEP varies linearly both as an increasing function of the engine load and rotational speed. Comparing the IMEP to the peak in-cylinder pressure map, it is deduced that the latter is not an inclusive indicator of the cylinder performance, since distinct in-cylinder pressure curves with the same peak pressure can result in different IMEP values.

Figure 7.1 (f) shows that the EGT at the exhaust valve exhibits a minimum near 5,000 kW (45% load) on the lower boundary of the engine temporary operation range. The map contour lines follow approximately the direction of the lower boundary of the engine temporary operation, which is consistent with the literature [107], thus adequately capturing the thermal loading and subsequently defining possible operational limits of the engine.

7.3 Case Study 3(a): Direct Crankshaft Dynamics Model Solution Method Determination

The direct crankshaft dynamics model solution method entails an investigation and subsequent determination of the most suitable solution method out of the three numerical schemes proposed which include the TR-BDF2, piecewise LTI, and harmonic balancing. As also described in Section 6.2, this case study will be performed utilising the 10L67GBE reference system, which is a 2-stroke diesel engine driving a generator, and is selected due to its simplicity and availability of already calibrated DOF coefficients. The numerical schemes quantification of performance is accomplished by changing the settings of each numerical scheme to perform parametric runs, and determine the minimum of the numerical schemes performance KPI described in Section 5.1.6.

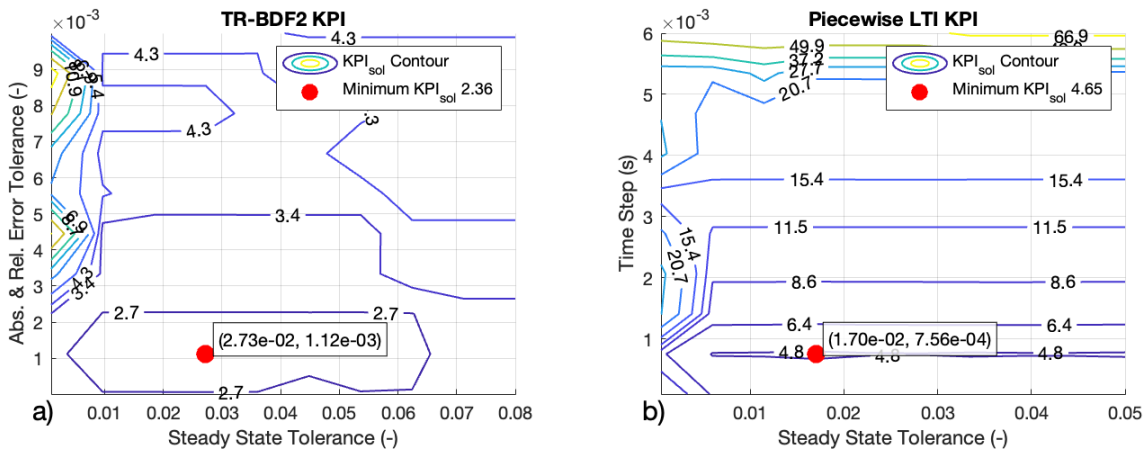


Figure 7.2: Numerical schemes performance KPI for (a) TR-BDF2 and (b) piecewise LTI, with weight $w_{\text{sol}} = 10$.

The parametric runs for TR-BDF2 are shown in Figure 7.2 (a), where, it is observed that when the steady state tolerance and the absolute and relative error tolerances are all reduced, the simulation increases its execution time at a greater rate as compared to the reduction of the NRME error. As a result the numerical scheme performance KPI increases. Similarly, the KPI also increases when all aforementioned user-defined settings are increased in value, thereby increasing the NRME error, compensating for the reduction in execution time. Consequently with the appropriate combination of user-defined settings, the numerical scheme performance KPI for

TR-BDF2 provided a minimum value of $KPI_{sol} = 2.36$, which was obtained by setting the absolute and relative error tolerances at 1.12×10^{-3} and the steady state tolerance at 2.73×10^{-2} as demonstrated in Figure 7.2 (a).

The piecewise LTI numerical scheme performance KPI reacts in a similar way when changing the time step as shown in Figure 7.2 (b). However, when increasing the steady state tolerance particularly above 0.01, it is observed that it bears a nearly negligible effect on the KPI. This is due to the fact that this numerical scheme converges really fast to steady state for a broad range of time steps. Nevertheless, a minimum on the numerical scheme performance KPI can still be obtained at $KPI_{sol} = 4.65$, by setting the time step at 7.56×10^{-4} s and the steady state tolerance at 1.70×10^{-2} .

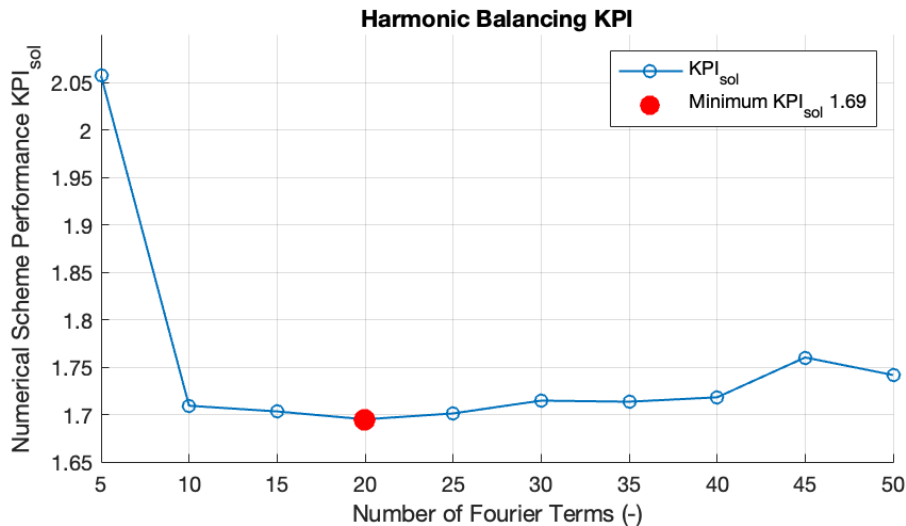


Figure 7.3: Numerical scheme performance KPI for Harmonic Balancing, with weight $w_{sol} = 10$.

The harmonic balancing numerical scheme performance KPI reaches a minimum at 1.69 when the user-defined setting reaches 20 Fourier Terms, and subsequently increases gradually. This is because as the number of Fourier terms increases there is only marginal improvement in the error of the solution, however the size of the linear system of equations solved increases by the square of the Fourier terms number. Consequently, the execution time increases greatly in proportion to any change in the NRME, thereby increasing the numerical scheme performance KPI.

The settings resulting to the best performance for each numerical scheme are summarised in Table 7.3. Subsequently, a comparison takes place in Table 7.4 to determine the best performing numerical scheme, with the smallest KPI value.

Therefore, the harmonic balancing numerical scheme has the smallest KPI, which indicates the least NRME with respect to the measured data, and also the fastest execution time. The second best performing numerical scheme is the TR-BDF2, which is both the second fastest and the second smallest NRME. This is expected as a powerful and complicated algorithm is utilised which is suitable for a vast number of problems. The worst performing numerical scheme is the piecewise LTI, however it is very easy and simple to setup and code, in contrast to the very complex and not freely available TR-BDF2 which is included as part of MATLAB.

Furthermore, the selection of the numerical schemes performance KPI weight, which was set to $w_{\text{sol}} = 10$ can be justified through Table 7.4. This is because the NRME is always an order of magnitude greater than the execution time. As a result, this weight was chosen to remove this bias and equalise the contribution of the NRME and execution time in the overall result of the KPI.

Table 7.3: Numerical scheme user-defined settings to achieve best performance.

Numerical Scheme	User Settings	Value	Minimum KPI
TR-BDF2	Abs. & Rel. Tolerance	1.12×10^{-3}	2.359
	Steady State Tolerance	2.73×10^{-2}	
Piecewise LTI	Time Step (s)	7.56×10^{-4}	4.654
	Steady State Tolerance	1.70×10^{-2}	
Harmonic Balancing	Number of Fourier Terms	20	1.695

Table 7.4: Numerical schemes selection, considering NRME and execution time.

Numerical Scheme	Minimum KPI (-)	NRME (-)	Execution Time (s)
TR-BDF2	2.359	2.275	0.105
Piecewise LTI	4.654	4.183	0.589
Harmonic Balancing*	1.695	1.684	0.014

*Selected numerical scheme

Considering the KPI of all numerical schemes, it is apparent that the harmonic balancing scheme is the best performing. To visualise this, the simulated ICT at the flywheel can be compared to the measurements for all numerical numerical schemes when these are configured with the settings resulting to the minimum KPI, as demonstrated in Figure 7.4. Despite the differences in KPIs, the simulated torque lies close to the measurements in all cases. As a result, all numerical schemes could be considered as appropriate alternatives to validate the direct crankshaft dynamics model.

Furthermore, differences between the measured and the simulated ICT can be shown in the vicinity of 170°CA , 200°CA , 220°CA , and 320°CA . These can be attributed to several reasons such as choosing the appropriate bearings and piston friction model [182], including the higher frequency components of the generator dynamics, or correcting and calibrating the in-cylinder pressure measurements appropriately which were averaged over a number of cycles [179].

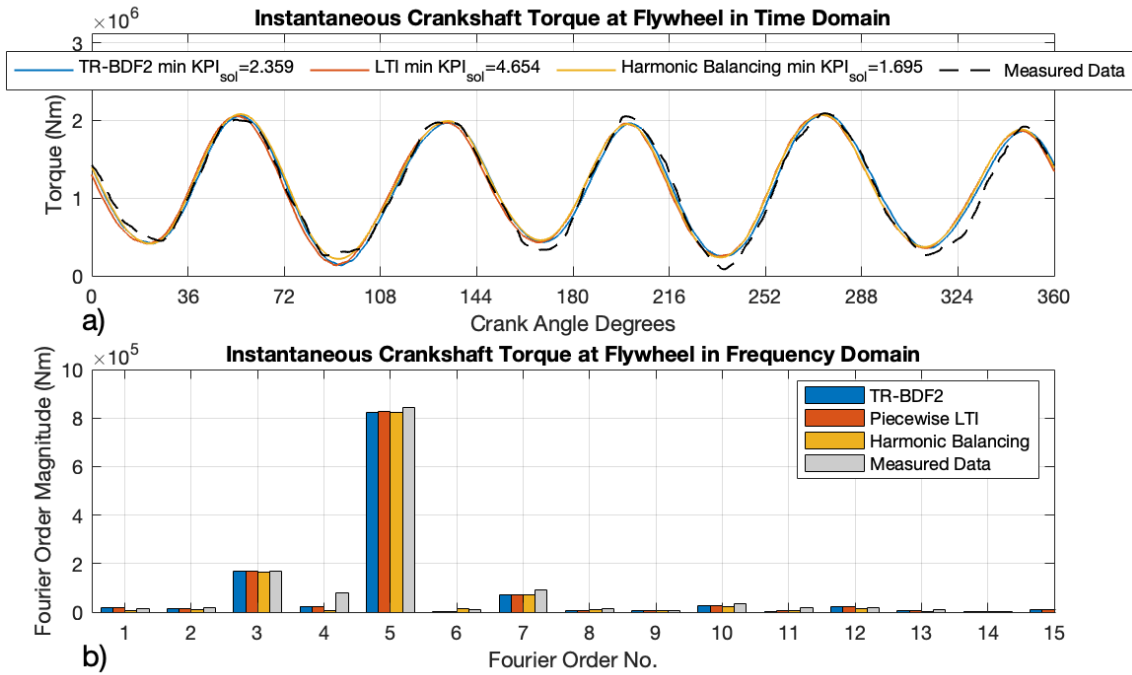


Figure 7.4: Comparison of 10L67GBE engine measured and simulated ICT at the flywheel for all numerical schemes, utilising best performing combination of settings in (a) the time domain and (b) the frequency domain.

Furthermore, it is noted that even though the reference system is a 10-cylinder engine, only 5 peaks are observed in the time domain of the ICT as shown in Figure 7.4 (a), with the cylinders reaching top dead center at either side of the peak as indicated by the x-axis tick marks. This is also demonstrated in the frequency domain since the dominant order is the 5th in Figure 7.4 (b). In addition, the frequency domain demonstrates the simplistic dynamics of this reference system which justifies its selection for this case study, as correctly predicted in Section 6.2. That because only the 3rd, 5th and 7th orders contribute significantly to the ICT. Finally, the frequency domain analysis identifies better the source of the differences between the measured and simulated ICT, which seems to be the 4th order. This

indicates that an event which occurs 4 times per engine cycle has not been included in the direct crankshaft dynamics models, which could stem from generator dynamics or camshaft excitation torques which were not considered.

7.4 Case Study 4(a): Direct Crankshaft Dynamics Model Calibration

The direct crankshaft dynamics model calibration takes place for the W9L46C reference system, which is a 4-stroke propulsion engine. The engine torsional damper stiffness and viscous damping coefficients are calibrated as described in Section 5.1.8, and the results both operating points where measurements were obtained are listed on Table 7.5. Further details on the algorithm iterations and performance are provided in Appendix E.

Table 7.5: Direct crankshaft dynamics model calibration results for W9L46C reference system.

Operating Point (kW @ RPM)	Viscous Damping		Stiffness	
	Calibrated (Nms/rad)	Manufacturer Δ (%)	Calibrated (Nm/rad)	Manufacturer Δ (%)
2,949 @ 401	5.048×10^4	-26.0	2.503×10^7	-19.3
5,491 @ 450	5.217×10^4	-23.5	2.359×10^7	-23.9
% Difference	3.2%	-	6.1%	-
Average	5.133×10^4	-24.8	2.430×10^7	-21.6

The calibration results indicate that there is a difference in the values of the torsional vibration damper calibrated coefficients between the engine operating points by 3.2% for the case of the viscous damping coefficient and 6.1% for the case of the stiffness coefficient. These coefficients should remain constant regardless of the operating point, however such differences can be attributed to measurement and modelling errors. Such errors may arise from the in-cylinder pressure measurement used as input to the direct crankshaft dynamics model, which is averaged over a number of cycles, in contrast to the ICT which is measured instantaneously for only one cycle. However, the percentage differences of 3.2% and 6.1% for each coefficient respectively as shown in Table 7.5 are fairly small, thus the calibration results can be considered as acceptable. As a result, average of 24.8% and 21.6% reduction in the

viscous damping and stiffness coefficients is observed respectively, on the torsional vibration damper of the W9L46C reference system.

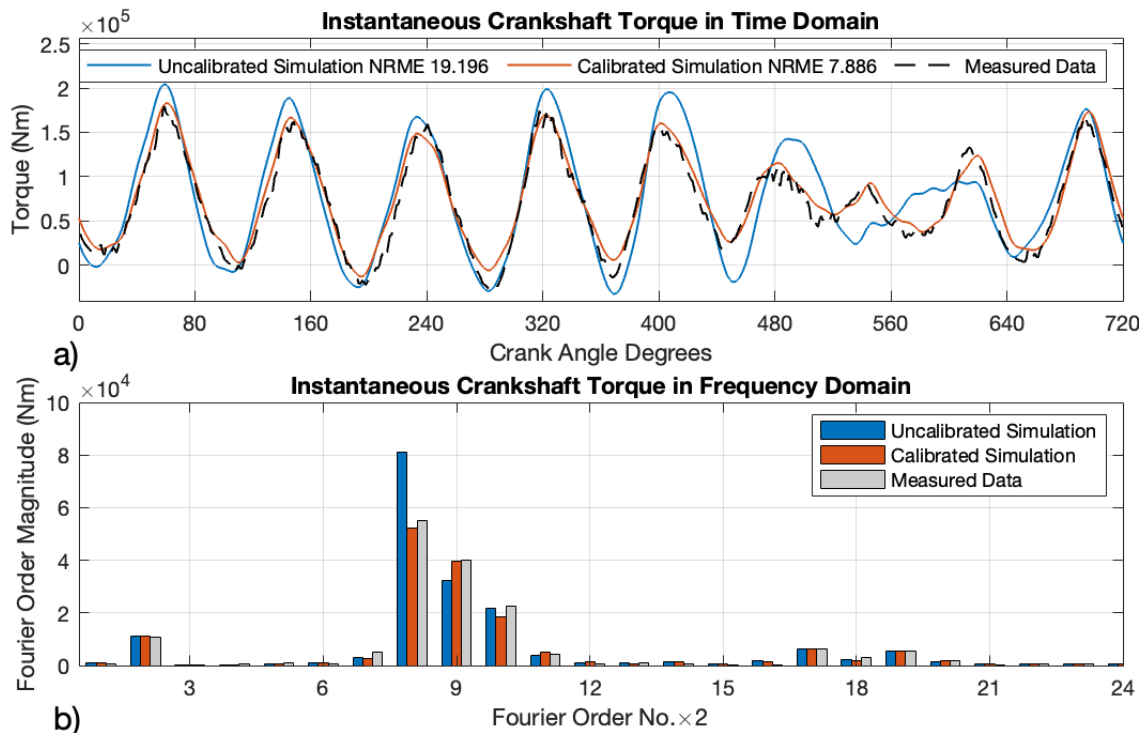


Figure 7.5: Direct crankshaft dynamics model calibration of W9L46C reference system for 2,949 kW at 401 RPM, with ICT shown in (a) the time domain and (b) frequency domain.

Firstly the above result demonstrates a significant difference between the values provided by the manufacturer. This is demonstrated in Figure 7.5 for the one operating point, where the ICT of the uncalibrated simulation employing the manufacturer values varies considerably between 400°CA and 640°CA . The same is true for the second operating point, the figure of which can be found in Appendix E. This is primarily observed in the frequency domain results, where the dominant order following the calibration, becomes the 9th instead of the 8th before the calibration. Consequently, values quoted by the manufacturer in the torsional vibration studies are subject to change depending on the age and degradation of the system at the time of measurements.

Secondly, calibration results indicate significant degradation exceeding 20% of the engine torsional vibration damper. The effect of this should be investigated by considering the Frequency Response Function (FRF) of the flywheel response per unit of excitation force in any of the cylinders as shown in Figure 7.6. However, it is

observed that the aforementioned FRF remains largely unaffected, with a resonance observed at 407 RPM for both calibrated and uncalibrated systems. Furthermore, the FRF has a maximum magnitude of 6.721×10^{-6} and 6.614×10^{-6} for the calibrated and uncalibrated systems respectively, which is just a 1.6% difference. As a result, the degradation of the torsional vibration damper can be deemed as acceptable, since it bears minimum impact on the natural frequency and potential vibration amplitude at resonance. Finally, this conclusion has been validated by vibration analysis experts EMHA B.V., who conducted order tracking using stationary accelerometers and proximity sensors on the flywheel, one month preceding the measurements made for this study.

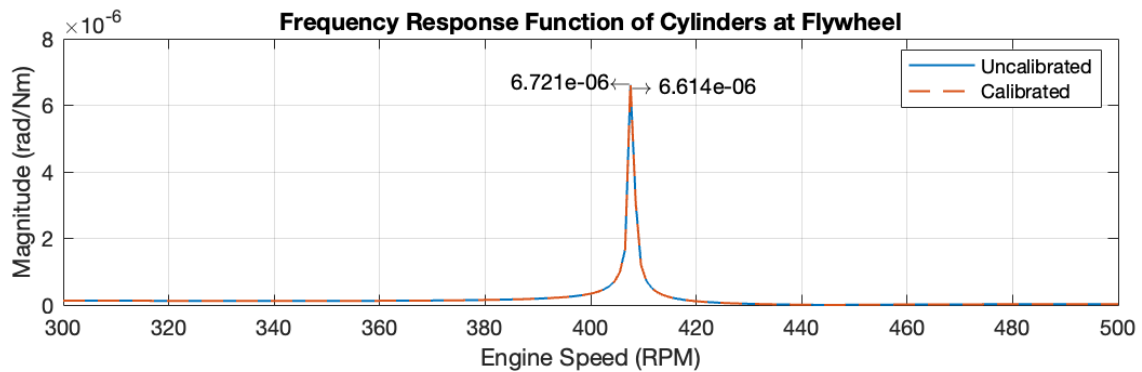


Figure 7.6: FRF for W9L46C reference system of flywheel response per unit of excitation force in the cylinders.

7.5 Case Study 4(b): Inverse Crankshaft Dynamics Model Verification

The inverse crankshaft dynamics model verification is performed for the W9L46C reference system, and contains a four part procedure described in Section 5.2.6. In short, the first three parts utilise simulated measurements of the in-cylinder pressure and ICT from the healthy conditions digital twin and direct crankshaft dynamics models respectively, at five sample operating points as shown in Figure 7.7. These operating points were chosen by the author to cover evenly the most frequently operating area of the engine and also lie far from the operating points selected to provide the inverse crankshaft dynamics model initial conditions as described in Section 5.2.5. As a result, the robustness of said model is tested.

The simulated measurements from these operating points are utilised to firstly determine the optimal settings of the inverse crankshaft dynamics model algorithm, secondly to determine the effect of discrepancies in the TVD stiffness and damping coefficients in the algorithm performance, and third to determine the effect of noise in the algorithm performance. The fourth part consists of the validation using the collected ICT data from the reference system.

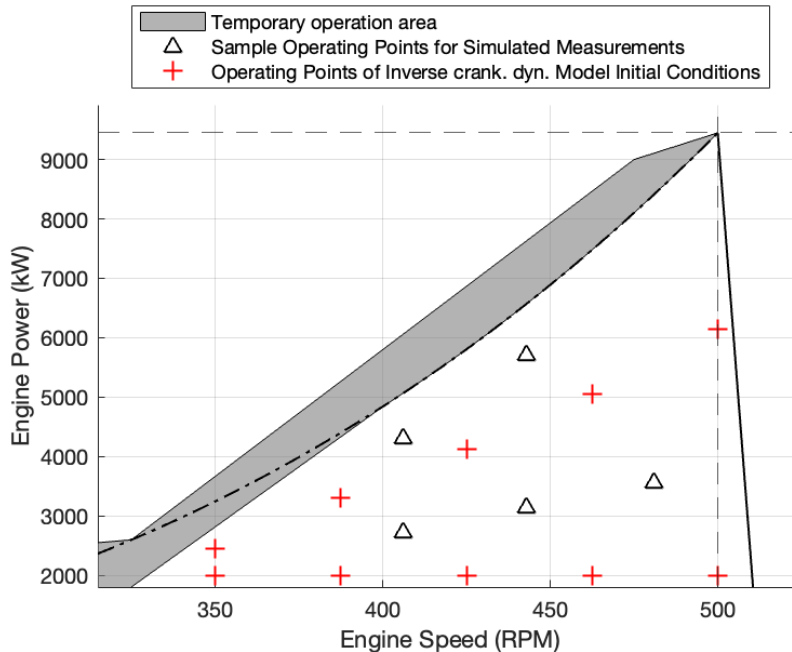


Figure 7.7: Sample operating points of simulated measurements utilised for the verification of the inverse crankshaft dynamics model for the W9L46C engine.

7.5.1 Determination of Optimal Settings

In the first part of the verification procedure, the parametric runs of the inverse crankshaft dynamics model shown in Figure 7.8, provide a global minimum at $KPI_I = 111.2$, for LM step tolerance of $\mu = 5.333 \times 10^{-3}$ and LM step initial damping of $\nu_0 = 0.867$. Alternative combinations of these settings result to various local minima with approximate KPI values of 118, 138 and 131, however unlike the global minimum they are narrower and localised.

Furthermore, the initial LM step damping parameter ν_0 is observed to have a considerable impact in the inverse crankshaft dynamics model performance, since as its value increases a smaller initial step is taken thus increasing the number of

iterations for convergence. Conversely, when its value decreases a larger initial step is taken resulting to overall reduced number of iterations leading up to convergence, which ultimately increases the in-cylinder pressure NRME thereby also increasing the KPI value. The LM step tolerance μ does not contribute significantly to the inverse model above the KPI contour line of 157, however it does impact the inverse crankshaft dynamics model performance for values less than that. In specific, as the tolerance reduces, more steps are rejected which increase the total number of iterations, whilst if the tolerance increases the NSALMN algorithm takes steps which do not conform well to the objective function shape thereby increasing the in-cylinder pressure NRME.

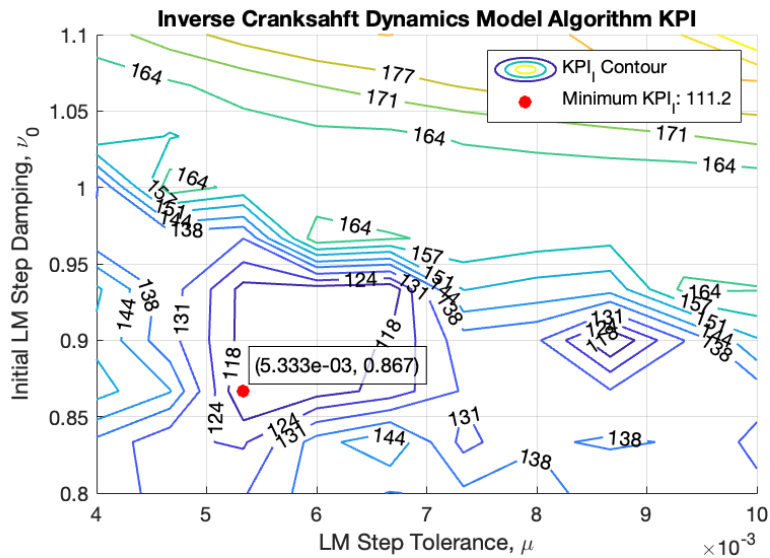


Figure 7.8: Inverse crankshaft dynamics model KPI for the first part of the verification procedure.

Considering the optimum settings for the inverse crankshaft dynamics model, the convergence of the unknown parameters which are utilised to reconstruct the in-cylinder pressure for cylinder no. 1 is shown in Figure 7.9 (a)–(e). This demonstrates the robustness of the algorithm employed, where convergence is achieved within 4 to 6 iterations for all the sample operating points. Furthermore, by utilising the operating points providing the initial conditions (or in-cylinder pressure parameters map as referred to in Section 5.2.5), a very good estimation of the initial conditions is obtained. This is indicated by Figure 7.9 (f)–(j), since the first iteration for all sample points already lies very close to the simulated measurements. This is particularly prevalent in the sample operating point of 5,704 kW at 443 RPM, which

lies very close to the initial conditions operating point of 6,139 kW at 500 RPM. Furthermore, this is improved further by the fact that the inlet air pressure is utilised as a measured input to the inverse crankshaft dynamics model thus the compression part of the curve is always consistent. Therefore the initial conditions of the unknown parameters are the furthest 9% less than the final converged value, as observed for the case of the DOC for the first iteration of Figure 7.9 (e).

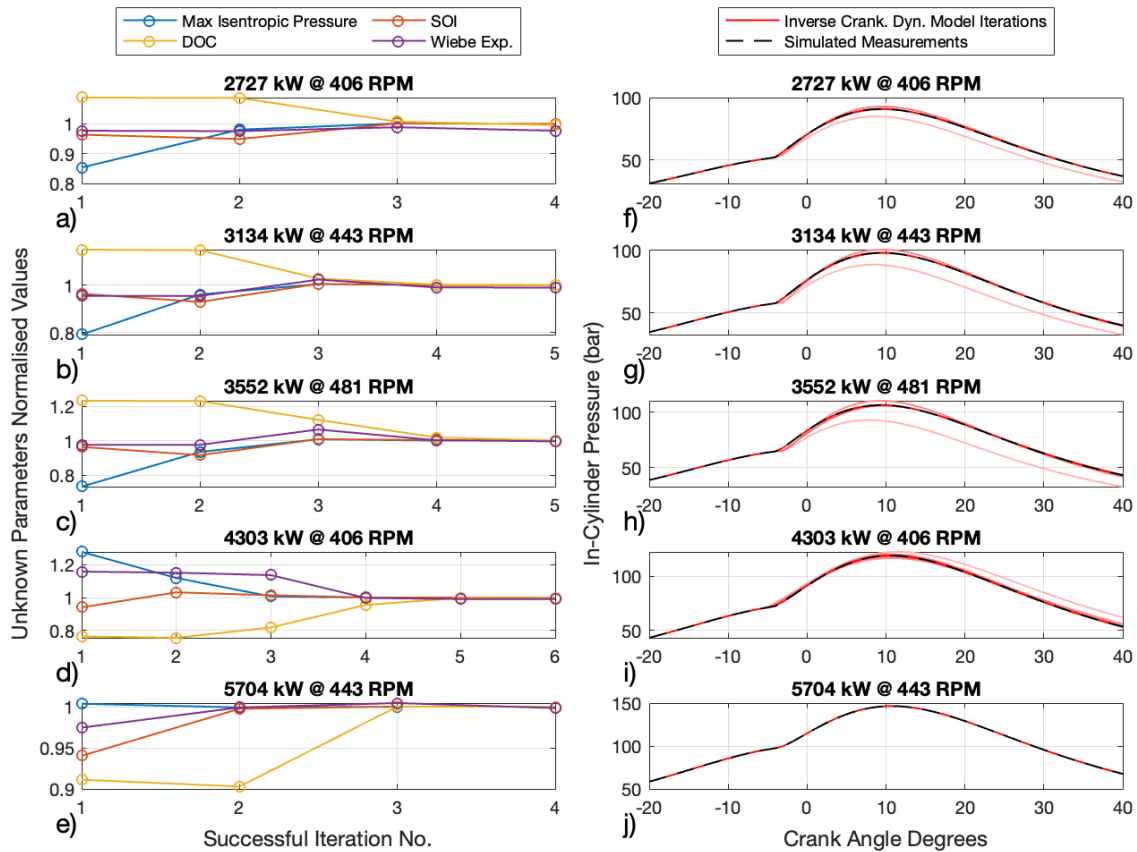


Figure 7.9: Inverse crankshaft dynamics model convergence utilising the optimal settings determined of $\mu = 5.333 \times 10^{-3}$ and $\nu_0 = 0.867$ at the sample operating points for cylinder 1 demonstrating (a)–(e) the unknown parameters normalised values convergence and (f)–(j) the reconstructed in-cylinder pressure curves at every iteration.

7.5.2 Torsional Vibration Damper Coefficient Discrepancies

In the second part of the verification procedure, the parametric runs of the inverse crankshaft dynamics model are shown in Figure 7.10 (a)–(b), in addition to the reconstructed in-cylinder pressures of three selected points at the sample operating point of 3,134 kW at 443 RPM in Figure 7.10 (c)–(e).

The in-cylinder pressure NRME indicates in Figure 7.10 (a) that as expected, it increases as the viscous damping and stiffness factors move away from 1 which represents its true value, and both factors seem to impact on the NRME equally between the values of 0.9 and 1.1. The same does not hold for the peak in-cylinder pressure maximum percentage difference in Figure 7.10 (b), where by changing the viscous damping factor to greater than 1, does not result to appreciable change when the stiffness factor lies within 1.00 and 1.08, as observed by the -6% contour.

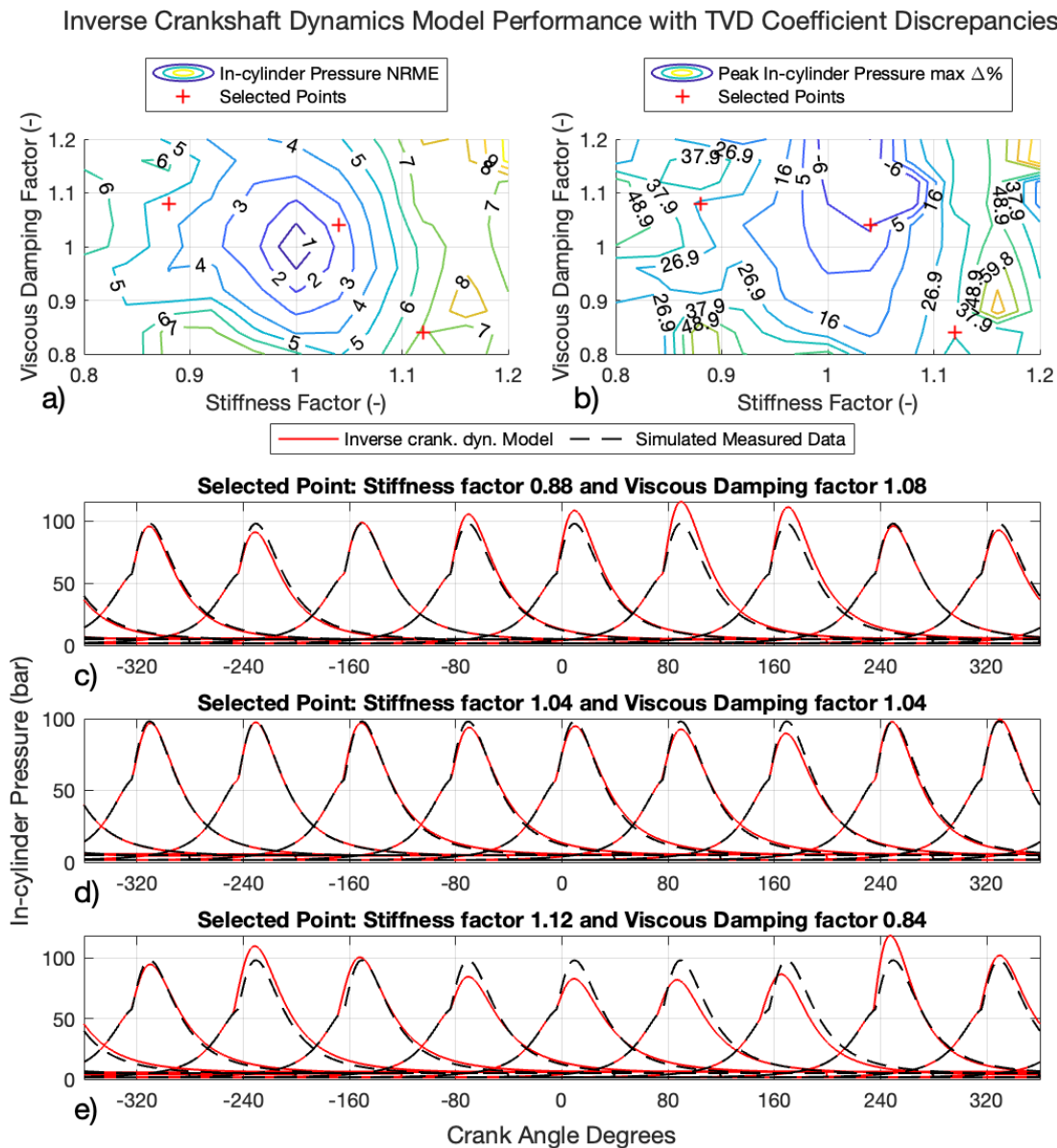


Figure 7.10: Inverse crankshaft dynamics model performance with torsional vibration damper coefficients discrepancies demonstrating the (a) in-cylinder pressure NRME, (b) peak in-cylinder pressure maximum percentage difference, and (c)–(e) in-cylinder pressure curves at selected points for 3, 134 kW at 443 RPM.

When investigating the in-cylinder pressures at the selected points, it becomes clear that for a NRME greater than 4, as demonstrated by Figures 7.10 (c) and (e), inverse crankshaft dynamics model is unable to handle discrepancies in the TVD coefficients thereby increasing the error in the reconstructed in-cylinder pressure. However, for NRME less than 3 which lies within 0.95 and 1.05 of both the viscous damping and stiffness factors, as indicated by Figure 7.10 b), the in-cylinder pressures can be reconstructed effectively, by also considering a peak in-cylinder pressure percentage difference of approximately 5%. This indicates that for the inverse crankshaft dynamics model to perform effectively, the values of the TVD coefficients should be identified correctly within $\pm 5\%$ of their true value. This provides the upper and lower error limits of the direct crankshaft dynamics calibration process, the results of which are presented in Section 7.4.

7.5.3 Noise in the Instantaneous Crankshaft Torque Measurements

In the third part of the verification procedure, the parametric runs of the inverse crankshaft dynamics model including various levels of noise in the ICT simulated measurements, are shown in Figures 7.11 (a)–(b). In specific, as the Signal-to-Noise Ratio (SNR) increases, the in-cylinder pressure NRME and peak in-cylinder pressure maximum percentage difference both decrease. That is because the inverse crankshaft dynamics model cannot distinguish between noise and system dynamics, therefore it adjusts accordingly the in-cylinder pressure curves such that the noisy measurements can be matched. This effect is minimised when formulating the objective function in the frequency domain as described in Section 5.2.5, particularly since the higher frequency noise components are not considered there since a maximum of 25 Fourier orders is used.

Furthermore, the sample points of the in-cylinder pressure in Figures 7.11 (c)–(e) indicate that the inverse crankshaft dynamics model is able to perform well for SNR values greater than 1.136×10^2 . In specific, only minor differences are observed in the reconstructed curves with the simulated measurements for the aforementioned SNR value, since in-cylinder pressure NRME is at 2.06 and the peak in-cylinder pressure maximum percentage difference is at 4.64%. As a result, this can be set as

the lower SNR limit of the measured ICT data, below which the robustness of the inverse crankshaft dynamics model algorithm may be compromised.

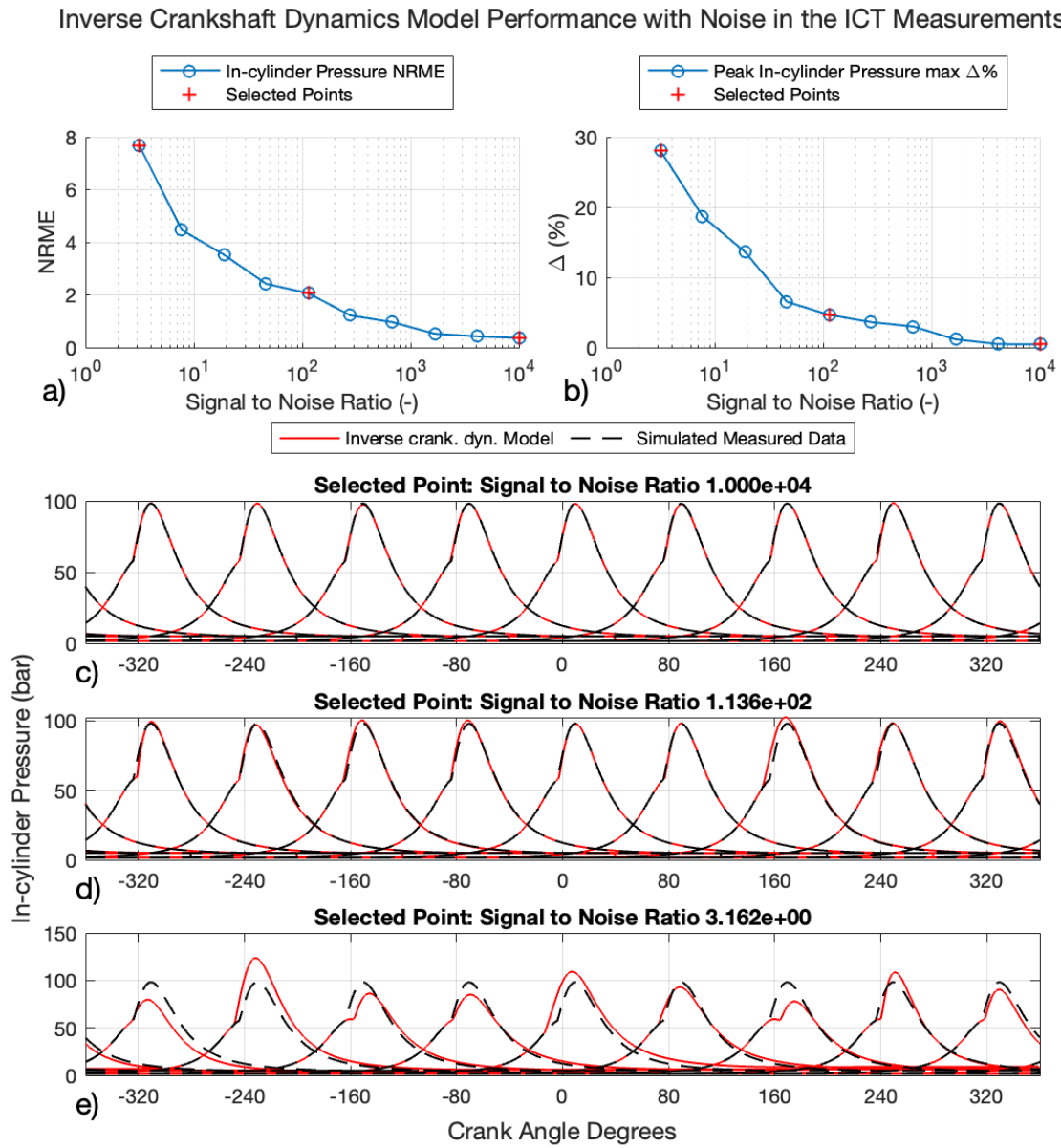


Figure 7.11: Inverse crankshaft dynamics model performance with noise in the input ICT demonstrating (a) in-cylinder pressure NRME (b) peak in-cylinder pressure maximum percentage difference, and (c)–(e) in-cylinder pressure curves at selected points for 3,314 kW at 443 RPM.

7.5.4 Validation Utilising Instantaneous Crankshaft Torque Measurements

The fourth part of the verification procedure involves the validation of the inverse crankshaft dynamics model utilising the measured ICT at the two operating points of the W9L46C reference system shown in Section 6.1. This process firstly ensures that the measured ICT is smoothed using a Gaussian-weighted moving average such that the SNR in the measurements is above the threshold established in Section 7.5.3, which is shown in Appendix D.3.

Subsequently, the measured ICT is utilised by the inverse crankshaft dynamics model, to reconstruct the in-cylinder pressure for the first measured operating point of 2,949 kW at 401 RPM, where a number of parametric runs are performed with different TVD coefficients as shown in Figure 7.12. That is because, using the results obtained from the direct crankshaft dynamics model calibration from Section 7.4 (corresponding to damping and stiffness factors of 1.0) large errors between the measured and the reconstructed in-cylinder pressure curves are observed as shown in Figure 7.12 (d).

Therefore, through this process, it is observed in Figures 7.12 (a)–(c) that the in-cylinder pressure NRME and peak in-cylinder pressure maximum difference can both reduce to 242 and 6.5% respectively for the case of cylinder 9 with TDC at 320°. The NRME can be considered as large, particularly because the expansion part of the in-cylinder pressure curves for the cylinders with TDC at -80°, 0°, 240° and 320° is considerably reduced compared to the measured data. However considering the map of the parametric runs this appears to be the best compromise between a reasonably small NRME and a near zero peak in-cylinder pressure maximum difference.

The above takes place for damping and stiffness factors of 0.92 and 1.08 respectively, hence given that the calibrated values of the TVD coefficients derived in Section 7.4 are 5.133×10^4 Nms/rad and 2.430×10^7 Nm/rad, the new TVD coefficients become $5.133 \times 10^4 \cdot 0.92 = 4.722 \times 10^4$ Nms/rad and $2.430 \times 10^7 \cdot 1.08 = 2.624 \times 10^7$ Nm/rad respectively.

For the same damping and stiffness factors as above the inverse crankshaft dynamics model is deployed for the measured ICT of the second operating point of 5,491 kW at 450 RPM. For the sake of brevity only the in-cylinder pressure results

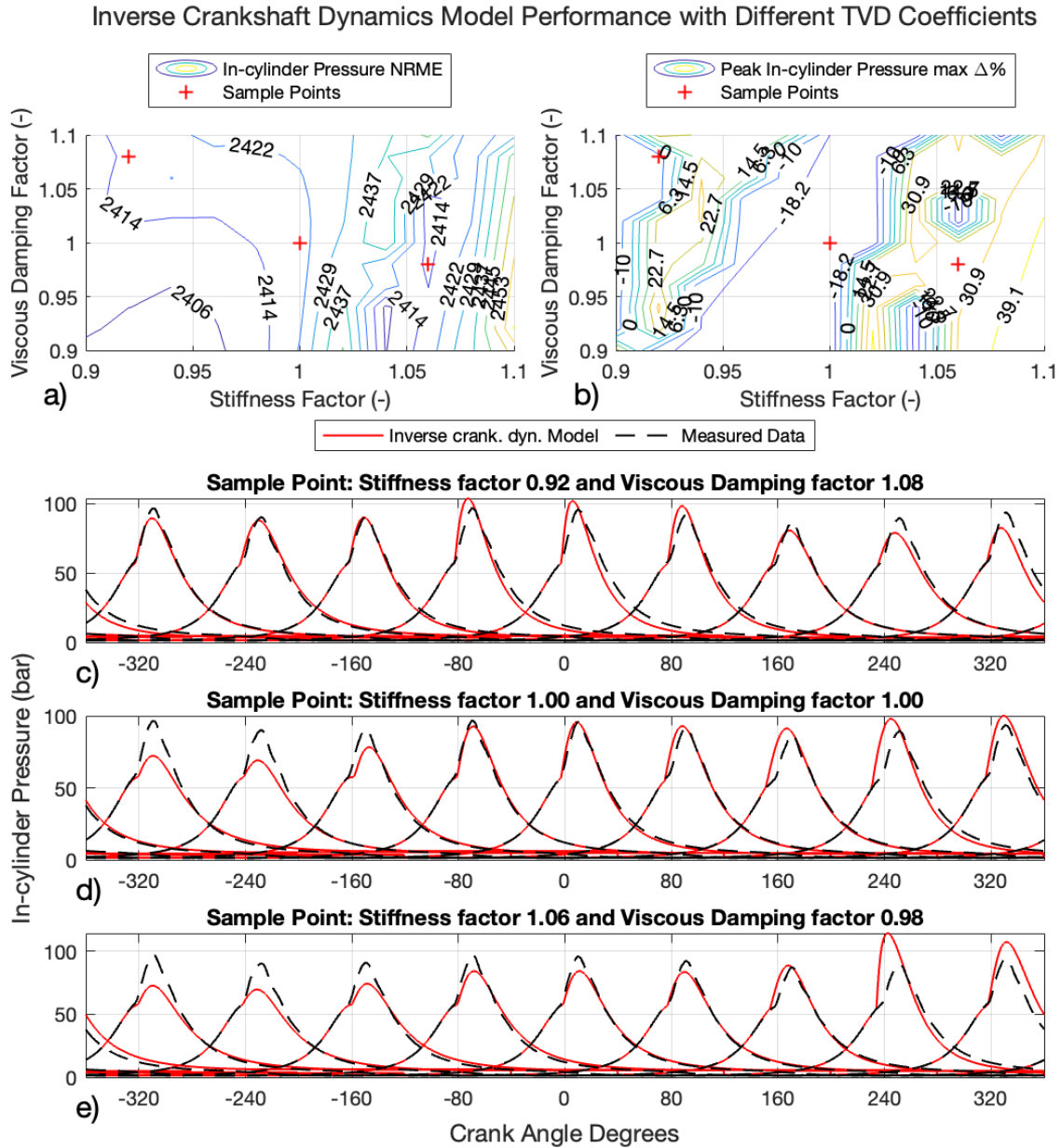


Figure 7.12: Inverse crankshaft dynamics model performance using measured ICT, with parametric runs for different TVD coefficients demonstrating the (a) in-cylinder pressure NRME, (b) peak in-cylinder pressure maximum percentage difference, and (c)–(e) in-cylinder pressure curves at selected points for 2,949 kW at 401 RPM.

are shown in Figure 7.13, whilst the maps for the parametric runs along with the in-cylinder pressures obtained at two sample points on said maps, can be seen in Appendix E.3. In this case the in-cylinder pressure NRME and peak in-cylinder pressure maximum difference are 281 and 15.7% respectively (for the case of cylinder 6 with TDC at -240°).

From the above process, by utilising the measured ICT the inverse crankshaft dynamics model has demonstrated its ability to reconstruct the in-cylinder pressure

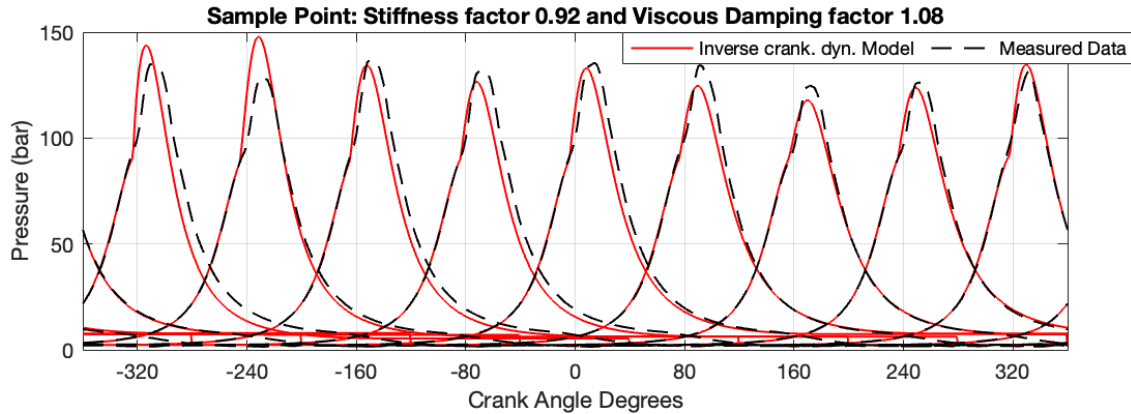


Figure 7.13: Measured and reconstructed in-cylinder pressures by the inverse crankshaft dynamics model for validation of the inverse crankshaft dynamics model, at operating point of 5,491 kW at 450 RPM.

curves. However the validation process can not be considered as conclusive particularly due to the large errors demonstrated between the measured and reconstructed in-cylinder pressure curves. This can be due to a number of reasons that either include the errors in the direct crankshaft dynamics model such as erroneously modelled or neglected dynamics, or the input data for the DOF coefficients which might not only include degradation in the TVD coefficients, but also in the DOF inertias, shaft stiffness and friction damping. Finally, the lack of precise data synchronisation between the measured in-cylinder pressure and ICT complicates the validation process further, since it may be the case that the inverse crankshaft dynamics model provides a good result considering the cycle-to-cycle in-cylinder pressure fluctuations, however these are not being measured since the pressure analyser averages the results over 40 cycles.

7.6 Case Study 4(c): Current Conditions Digital Twin Configuration & Performance Maps

The current conditions digital twin configuration is performed by extracting the in-cylinder pressure parameters of duration of combustion, start of combustion, Wiebe exponent and mass of fuel injected from the inverse crankshaft dynamics model, and subsequently deploying those in the thermodynamics model as described in Section 6.2. Since the inverse crankshaft dynamics model was unable to be validated utilising the measured ITC for reasons described in Section 7.5.4, the

unknown parameters for each cylinder will be extracted by the in-cylinder pressure measurements obtained instead.

In specific, the in-cylinder pressure measurement which lies the closest to the reference point from the calibration of the healthy conditions digital twin will be employed, since this enables the Woschni-Anisits model to perform the best. To extract the unknown parameters for the in-cylinder pressure measurements, a standard heat release analysis is performed with a best-fit curve fitted on the heat release curves shown in Appendix D.2, whilst the values of said parameters (in addition to the indicated power) are listed in Table 7.6.

Table 7.6: Heat release analysis results for operating point of 5,491 kW at 450 RPM for W9L46C reference system, with underperforming cylinders highlighted.

Cyl.	DOC	SOC	Wiebe Exp.	Fuel Injected		Indicated Power	
	(°CA)	(°CA)	(-)	(kg/cycle)	(%)	(kW)	(%)
1	58.8	9.3	0.817	7.663×10^{-3}	11.2	675.4	11.2
2	51.7	8.8	1.014	7.787×10^{-3}	11.4	693.9	11.5
3	63.4	9.0	0.713	7.834×10^{-3}	11.5	694.7	11.5
4	65.6	8.9	0.730	7.079×10^{-3}	10.4	615.6	10.2
5	59.6	9.4	0.733	7.987×10^{-3}	11.7	713.0	11.8
6	61.6	9.1	0.802	7.243×10^{-3}	10.6	639.7	10.6
7	60.1	8.7	0.779	7.071×10^{-3}	10.4	634.3	10.5
8	78.7	8.6	0.479	7.791×10^{-3}	11.4	683.5	11.3
9	54.5	9.2	0.888	7.843×10^{-3}	11.5	705.2	11.6
Total:				6.830×10^{-2}	100.0	6,055.3	100.0

Considering the results of the heat release analysis, cylinders 4, 6, and 8 are identified to be under-performing due to the reduced indicated power. Subsequently, the unknown parameters identified can be deployed to the thermodynamics model, thereby configuring the current conditions digital twin by the process described in Section 4.6. Following this, the performance of individual cylinders using the current conditions digital twin is summarised, by plotting the mean peak in-cylinder pressure, IMEP, and EGT at the exhaust valve for all cylinders as well as the standard deviations in Figure 7.14.

All standard deviation parameter maps have similar shapes to their counterparts

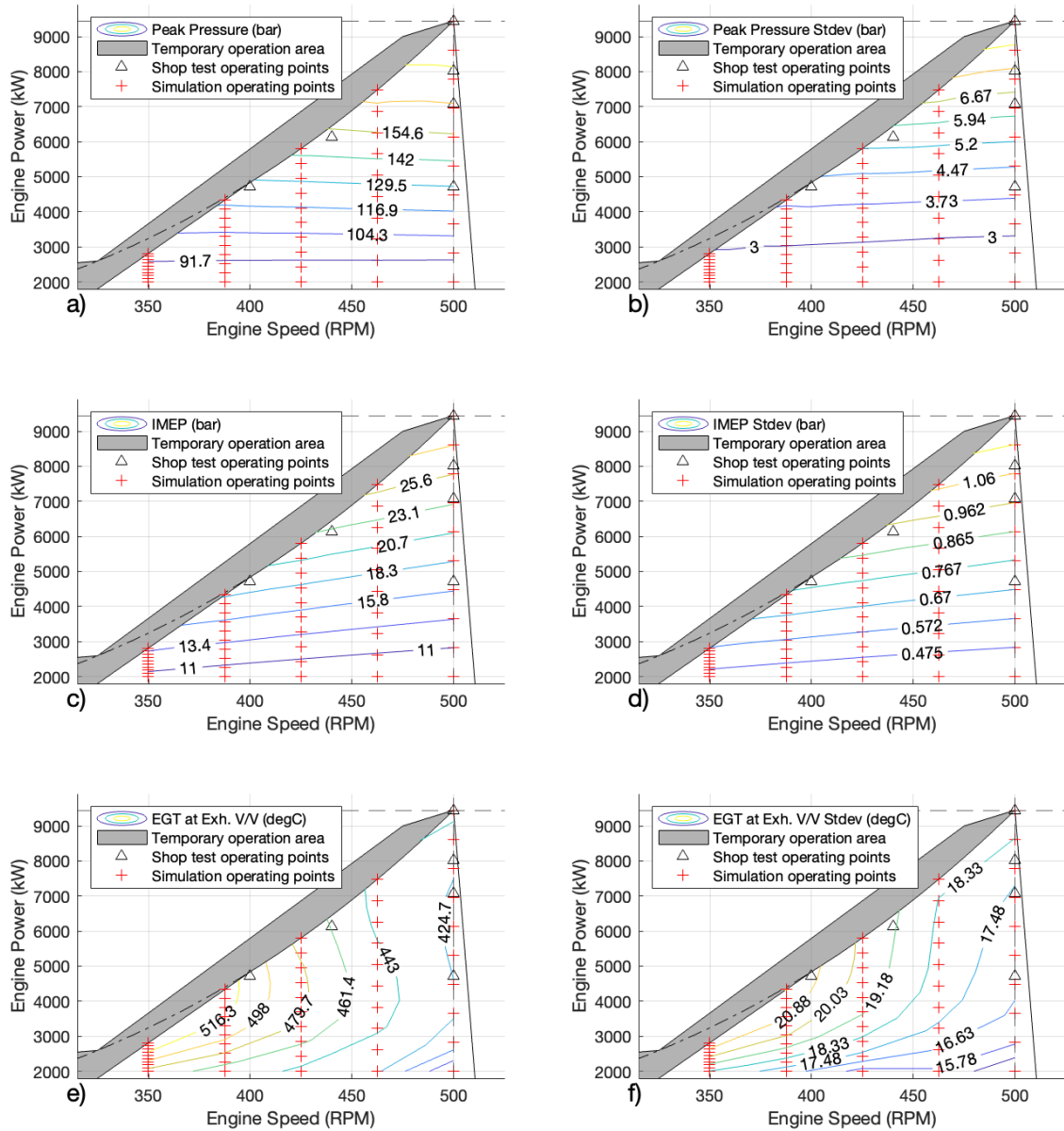


Figure 7.14: Performance maps of W9L46C engine current conditions digital twin. (a)–(b) Peak pressure average and standard deviation between all cylinders respectively. (c)–(d) IMEP average and standard deviation between all cylinders respectively. (e)–(f) EGT average and standard deviation between all cylinders respectively.

for the mean parameter values. This indicates that differences between cylinders gets magnified as the respective parameters increase in value. In specific, Figure 7.14 (a)–(b) show that as the peak in-cylinder pressure increases to 167 bar, the standard deviation between all cylinders also increases to 6.7 bar; the same trend is observed for the IMEP presented in Figure 7.14 (c)–(d). Regarding the EGT at the exhaust valve outlet, the standard deviation between all cylinders reaches a maximum of 20°C in line with the maximum mean EGT of 516° presented in

Figure 7.14 (e)-(f), respectively. Overall the standard deviation values appear to be close when considering all engine cylinders which provide a first indication regarding the current health of the engine, however a rigorous analysis is required to draw definite conclusions which follows in the next section.

7.7 Case Study 5(a): Derivation of Health Assessment KPIs & Maps

The health assessment KPIs and maps are derived by comparing the current conditions against the healthy conditions digital twin these include the BSFC, peak in-cylinder pressure, IMEP and EGT at exhaust valve percentage differences, as described in Section 7.7. The BSFC KPI is shown in Figure 7.15 where in its current condition the engine examined demonstrates an average increase by 2.1% for the entire engine operating envelope. This demonstrates that the engine efficiency at the time of the measurement is reduced compared to its healthy state for the entire operating envelope, with a more pronounced efficiency drop occurring for operating points closer to the lower boundary of the temporary operation area.

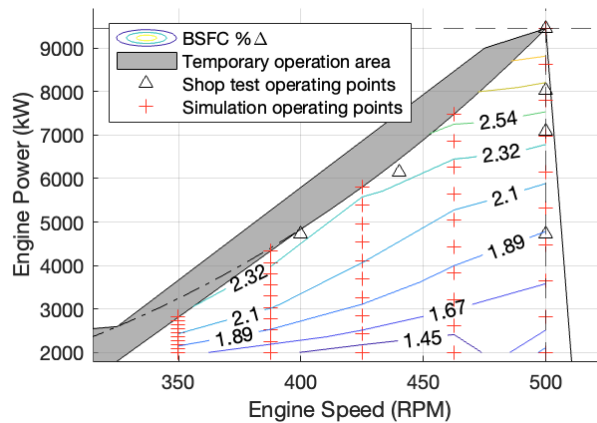


Figure 7.15: BSFC percentage difference of current engine conditions with reference to healthy conditions of W9L46C engine.

The EGT KPI is shown in Figures 7.16 (a), (c) and (e) for the cylinders with reduced performance identified from Table 7.6. Additionally, the same KPI for another three randomly chosen engine cylinders is provided in Figures 7.16 (b), (d) and (f). The presented results demonstrate that the cylinders 4, 6 and 7 with reduced performance exhibit a very similar temperature decrease by 6.1% on average compared

to the healthy conditions, with similarly shaped contours. This is attributed to the reduced quantity of fuel injected in the under-performing cylinders. Hence, for the engine to retain its power output, the remaining cylinders need to burn more fuel, and as a result an average temperature increase of 1.5% is observed for cylinders 2, 8 and 9, as illustrated in Figures 7.16 (b), (d) and (f). However, this increase is considered reasonably small, hence the engine in its current condition can run comfortably at higher loads without danger of thermal overload.

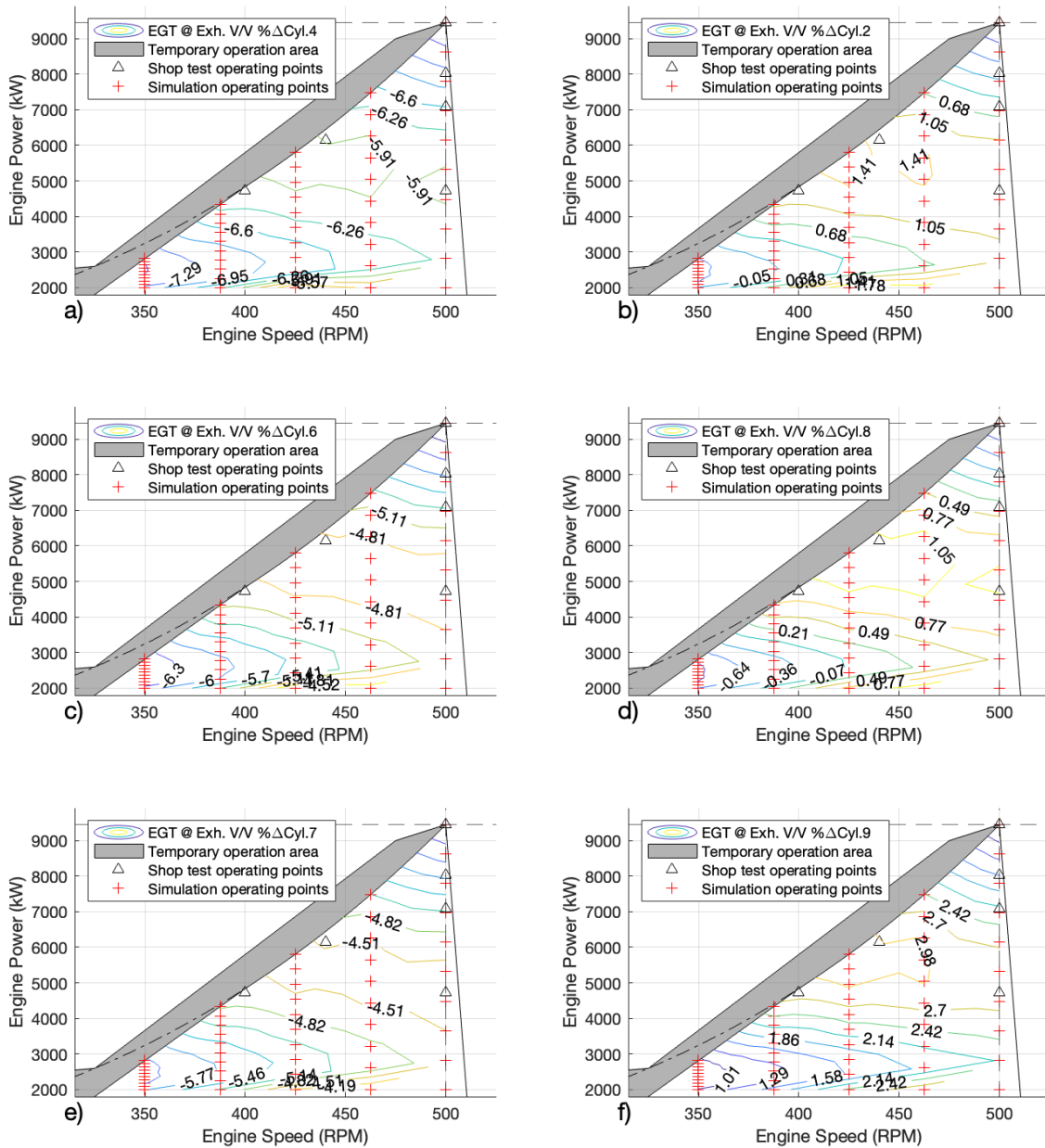


Figure 7.16: Cylinder EGT percentage difference of current engine conditions with reference to healthy conditions of W9L46C engine of (a) cylinder 4, (b) cylinder 6, (c) cylinder 7, (d) cylinder 2, (e) cylinder 8, (f) cylinder 9.

The IMEP comparisons are shown in Figure 7.17. The presented results demonstrate significant reduction for the under-performing cylinders 4, 6 and 7 by an average of 6.7%, 4.8% and 3.7% respectively, as shown in Figures 7.17 (a), (c) and (e). Thus, to retain the engine power output, the cylinders 2, 8 and 9 demonstrate average increases of 3.0%, 1.8% and 3.1% respectively, as shown in Figures 7.17 (b), (d) and (f).

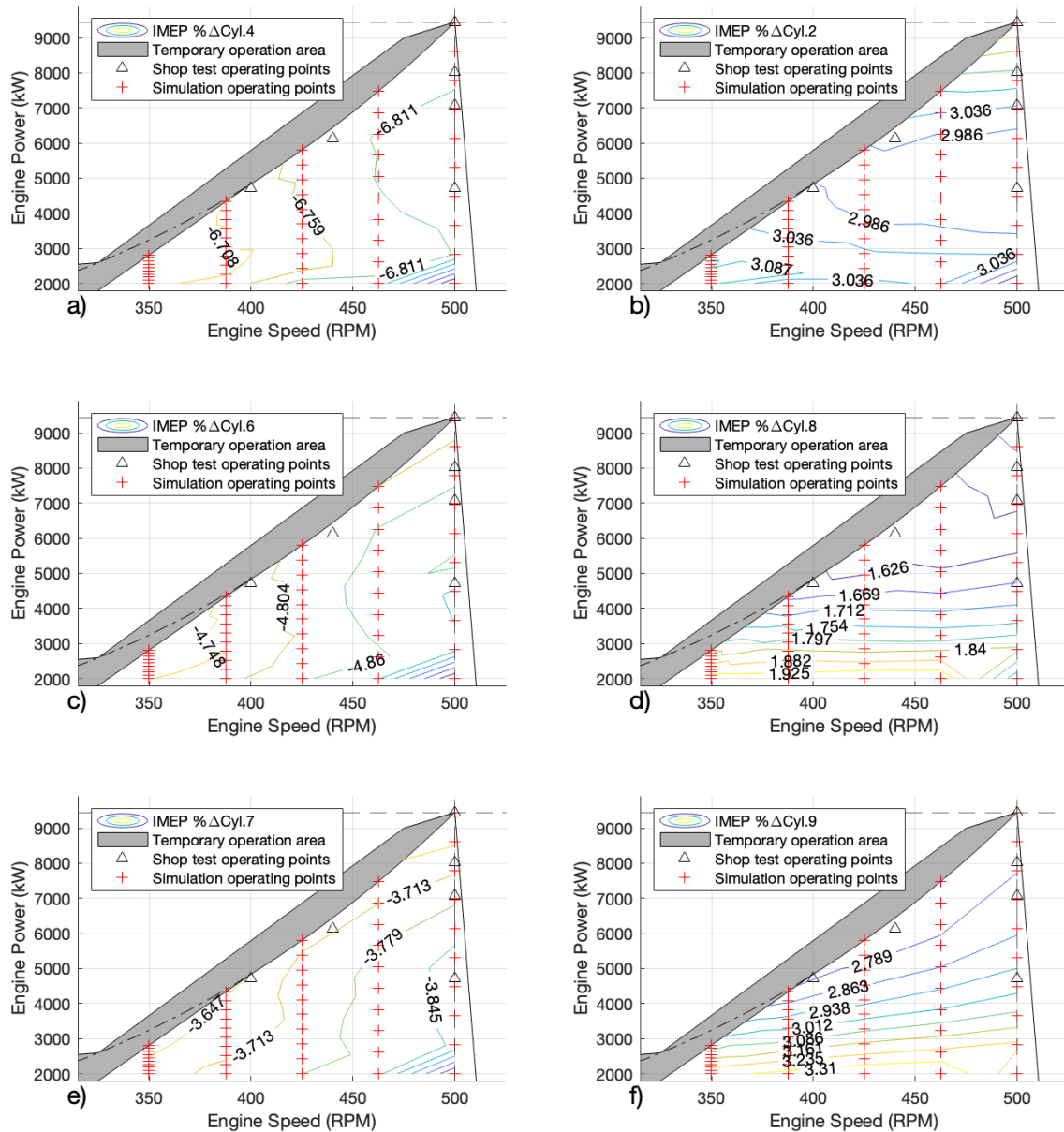


Figure 7.17: Cylinder IMEP percentage difference of current engine conditions with reference to healthy conditions of W9L46C engine of (a) cylinder 4, (b) cylinder 6, (c) cylinder 7, (d) cylinder 2, (e) cylinder 8, (f) cylinder 9.

An identical trend with IMEP is exhibited for the peak in-cylinder pressure, hence for the sake of brevity it is not included as part of the three KPIs. In specific,

the encountered differences between the current and healthy conditions results are less than 2%, which can be considered as minor or marginal difference. As a result, the peak in-cylinder pressure may not be reflect directly to the engine power output, on the contrary to IMEP. Nonetheless, it is useful to monitor the peak in-cylinder pressure (especially for engines using variable injection timing technologies), as it is directly linked to the mechanical stresses on the engine components, and it also effects the BSFC. Moreover, large deviations in the peak in-cylinder pressure may indicate faults in the relevant components,²² whereas high peak pressure levels may jeopardise the engine integrity.

Chapter 8

Final Remarks & Future Work

8.1 Case Studies Findings

The five stages of the research methodology were tested via seven case studies, employing three reference systems of a 4-stroke W9L46C engine installed in a ferry, a 2-stroke 6RTflex50 propulsion engine installed in a bulk carrier, and a 2-stroke 10L67GBE land-based generator.

The first case study involved the healthy conditions digital twin calibration, where the particle-swarm optimisation algorithm employed was able to return consistent results for the Wiebe combustion model, for both investigated engines. The main weakness of the calibration approach was the Woschni-Anisits model, which demonstrated increasing error trends near the edge of the engine operating envelope. Regardless, the BSFC and peak in-cylinder pressure errors of the digital twin compared to the shop tests reached a maximum of 2.7% and 2.5% respectively for the W9L46C engine, as well as 1.5% and 2.9% respectively for the 6RTflex50 engine, demonstrating sufficient accuracy. In the second case study, the healthy conditions digital twin performance maps were derived which were verified qualitatively against expected behaviour from the literature.

The third case study investigated the solution method of the crankshaft dynamics models for the 10L67GBE land-based generator, where the harmonic balancing numerical scheme was found to be the best performing. In specific, compared to the TR-BDF2 and piecewise LTI, it demonstrated the least NRME of 1.684 for the measured compared to the simulated ICT, as well as the fastest execution time of

0.014 s. The drawbacks of the harmonic balancing scheme include the inability to simulate transients since the governing equations are solved in the frequency domain. In addition, by considering that the thermodynamics model governing equations are solved always in the time domain, this may prohibit said governing equations to be combined in the time domain with those of the direct crankshaft dynamics model as part of a holistic engine modelling approach.

The fourth case study included the direct crankshaft dynamics model calibration which was performed for the W9L46C propulsion engine. The calibration identified a degradation of the engine TVD, where both its viscous damping and stiffness coefficients reduced by 24.8% and 21.6% in value respectively. This result was demonstrated to be consistent for both the operating points for which in-cylinder pressure and ICT measurements were obtained. A degradation in excess of 20% in the engine TVD may seem alarming, however the change in the shafting system's frequency response function was found to be negligible thereby posing no threat to the engine normal operation. This conclusion which was also verified by an independent third party study.

The fifth case study included the inverse crankshaft dynamics model verification for the W9L46C propulsion engine, where a four part procedure was followed using simulated ICT measurements for the first three parts and the actual ICT measurements for the last. Firstly, the optimal user-defined settings to achieve a good compromise between quick convergence and accuracy were determined to be $\mu = 5.333 \times 10^{-3}$ for the LM step tolerance, and $\nu_0 = 0.867$ for initial LM step damping. Secondly, it was determined that a discrepancy in the TVD stiffness and damping coefficients greater than $\pm 5\%$ from their true values, will result to a difference between the actual and reconstructed peak in-cylinder pressure to exceed 5%. Thirdly, an upper threshold of the SNR in the ICT measured data was determined to be 1.136×10^2 , below which the difference between the actual and reconstructed in-cylinder pressure curves peak would exceed 4.56%. Fourth, the actual ICT measurements were utilised to reconstruct the in-cylinder pressures however the results did not demonstrate satisfactory accuracy. Since the SNR in the measured ICT was above the indicated threshold, this can be attributed primarily in three factors:

1. Omission of important dynamics in the direct crankshaft dynamics model.

2. Errors in the direct crankshaft dynamics calibration process.
3. Lack of measured ICT and in-cylinder pressure data synchronisation.

The confirmation if the above holds true could ultimately be confirmed subject to a more extensive measurement campaign to verify modelling discrepancies (if any), calibrate the direct crankshaft dynamics model even effectively considering multiple operating points, and possibly circumvent data synchronisation issues, which will be discussed as part of the future work in Section 8.5.

In the sixth and seventh case studies, the current conditions digital twin was configured and the health assessment for the W9L46C engine were performed respectively. Through this process a slight increase in the engine BSFC by an average of 2.1% across the entire operating envelope was exhibited which was deemed as reasonable for a 20-year old engine. Furthermore, the EGT at the exhaust valves outlet exhibited a notable decrease by an average of 6.1% for under-performing cylinders, and an increase by 1.5% for the rest cylinders. When expanding this to the entire engine operating envelope, there exists no danger of thermal overload or any operational restrictions. Significant reduction in the IMEP of under-performing cylinders was observed by a maximum of 6.8%, which particularly affects the higher load areas over 6,000 kW. Finally, the peak in-cylinder pressure was not found to be the most effective engine health indicator for this case study, since only minor differences were exhibited between the under-performing and the other cylinders.

8.2 Research Methodology Remarks

The systematic methodology proposed in Chapter 3 demonstrated its effectiveness through the case studies results discussed above, leading to the following overarching conclusions. Firstly, the two-step calibration process of thermodynamics model was successfully demonstrated for the healthy conditions digital twin of both 4-stroke and 2-stroke engine types. This was aided by exploiting the mathematical simplicity of the single cylinder thermodynamics model, whilst only minimal data were available from the engine shop tests.

The systematic methodology proposed was also able to exploit the link between the engine mechanical and thermodynamics performance, by combining both crankshaft

dynamics and thermodynamics models. This proved that an integrated modelling approach can be successfully deployed with to gain improved insight on the engine performance, which is further reinforced by the minimal measuring requirements used to obtain the engine's current condition.

Furthermore, by employing engine ICT measurements their reliability and importance as a critical engine measurement parameter was demonstrated through this systematic methodology. In specific, the ICT measurements were able to be deployed utilising a novel approach developed involving the inverse crankshaft dynamics model, to reconstruct the in-cylinder pressures and thus obtain information regarding the thermodynamic performance of each cylinder.

Finally, the systematic methodology proposed set a basic framework for the quantification of engine health assessment, by developing the healthy and current conditions digital twins. As a result, comparisons were facilitated at any selected operating point as well as for a wide engine operating envelope, allowing for a detailed examination of the engine performance. Moreover, the applicability of this methodology to a variety of engine types and configurations was demonstrated.

8.3 Novelty & Implications

The novelty of this research stems from addressing particular gaps identified in the literature review in Chapter 2, as listed in Table 8.1. In specific, the literature review gaps 3–6 were addressed in the following manner:

3. A systematic methodology was developed incorporating a holistic modelling approach which included both thermodynamics and crankshaft dynamics models. These were deployed using flexible formulations to establish both healthy and current engine conditions digital twins for engines of any type (4-stroke, 2-stroke) and configuration, to enable health assessment.
4. A rigorous calibration procedure for the numerous constants was developed and demonstrated for both 4-stroke and 2-stroke engines. This exploited the mathematical and computational simplicity of the single-cylinder thermodynamics model and utilised minimal data available for the engine shop test, to develop the healthy engine conditions digital twin.

Table 8.1: Addressed literature review gaps.

Gap*	Description	Addressed?
1	Lack of systematic approaches that provide actionable diagnostics information	-
2	Lack of techniques and methods exploiting continuous and instantaneous measurements	-
3	Lack of a systematic methodology incorporating thermodynamics and crankshaft dynamics models for marine engines	✓
4	Lack of rigorous calibration procedure for thermodynamics model	✓
5	Lack of utilisation of ICT measurements as the means to reconstruct in-cylinder pressures for marine engines	✓
6	Lack of investigation on numerical schemes and solution methods of crankshaft dynamics models	✓

*Literature review gap.

5. A novel approach was developed and demonstrated involving an inverse crankshaft dynamics model which reconstructs the in-cylinder pressure curves utilising ICT measurements of marine engines.
6. A rigorous study of the direct crankshaft dynamics model numerical schemes and solution methods which remain largely unpublished, to enable optimum performance of the inverse crankshaft dynamics model.

The wider implications of this research lead to improved health monitoring and diagnostics of marine engines for the academia. This takes place by enabling improved quantification of current engine conditions, as well as the expansion of the current engine condition digital twin to predict the effects of degradation and failures on engine performance. This can lead to accurate predictions on the remaining useful life of components, as well as lifecycle costs.

Regarding the wider industry, this research provides incentives of improving digitalisation in the shipping industry by underpinning the value of digital twin which utilise instantaneous signals such as the ICT. Furthermore, the systematic methodology proposed enables more rigorous and scientific benchmarking practices to assess engine performance, which lead to improved scheduling of overhaul periods as well as optimising spare part logistics.

8.4 Achievement of Aims & Objectives

The first objective was to develop a systematic methodology to benchmark, quantify and assess the marine engine health. This was achieved by incorporating the development process of both thermodynamics and crankshaft dynamics models within one methodology to formulate, calibrate and deploy said models for both healthy and current engine conditions. Therefore, this systematic methodology enabled the simulation of marine engine performance at various conditions and engine operating points through the vital metrics of BSCF, IMEP and EGTs. Therefore, the benchmarking and quantification of engine performance was facilitated.

The second objective was to develop modelling tools based on first-principles and digital twins, which utilise critical measurements to accurately simulate the mechanical and thermodynamic performance of marine engines. This was achieved by the by the development of first-principles thermodynamics and crankshaft dynamics models. In specific, the former successfully simulated the engine operation by deriving vital performance metrics utilised for health assessment. The latter was employed as part of a novel approach utilising ICT measurements to reconstruct the engine in-cylinder pressures, which were deployed to configure the current engine conditions digital twin. Moreover, the flexible and generic formulations employed within the first-principles models, enabled the digital twins to be engine-agnostic, hence they can be configured for any engine type and configuration (as also demonstrated in the case studies).

The third objective was to demonstrate the application of the methodology and developed tools, for several representative case studies including marine engines of any type (4-stroke, 2-stroke) and configuration. This was achieved by employing three separate reference system which included one 4-stroke and two 2-stroke engines. The 4-stroke engine was part of a dual engine arrangement driving a CPP, whilst the two 2-stroke engines where installed as a main propulsion engine of a bulk carrier and as a stationary generator respectively. This demonstrated the flexibility of the developed methodology and as a consequence the usefulness of the digital twins.

Overall, through the above objectives the aim of this dissertation was addressed, which was to develop a systematic methodology enabling marine engine health assessment, by employing first-principles digital twins. The relevant first-principles

model formulations were presented, and incorporated within the context of a novel approach involving the inverse crankshaft dynamics model which reconstructs the in-cylinder pressures, a rigorous two-step calibration process for the healthy condition digital twin, and an overarching systematic methodology than enables engine health assessment.

8.5 Future Work

Following the conclusions from the individual case studies and the literature review research gaps which were not addressed, the future work can be considered in a short and long term outlook respectively. In the short-term, the thermodynamics model can be made more robust by utilising alternative methods from the Woschni-Anisits model to predict the values of combustion parameters. This would potentially improve the thermodynamics model accuracy since the Woschni-Anisits model is semi-empirical and was not originally developed for larger engines [149].

Furthermore, the calibration of the crankshaft dynamics model should take place by considering the frequency response of the engine for a wide operating envelope by utilising at least 10 measurement points, particularly including near or on the natural frequencies. This allows for a more robust calibration approach as the system becomes more sensitive near the natural frequencies, and furthermore since the governing equations become linear in the frequency domain, the optimisation process robustness and accuracy will improve.

The direct crankshaft dynamics model can be further improved by considering also the camshaft excitation forces and parasitic drag forces of the relevant oil and water pumps, where the literature is lacking on such studies for large 4-stroke engines. Even though for larger engines these dynamics (where applicable) had a negligible effect [182], they could improve the inverse model performance particularly for the case of the 4-stroke engines as these excitation forces may influence the engine ICT.

The long term outlook the digital twins derived from the proposed systematic methodology can be used in tandem with AI-enabled algorithms to provide component-wise health assessment capabilities. This addresses a major gap identified in the literature, where the crew can utilise actionable information on replacing and

overhauling specific components to improve or upkeep the engine efficiency. Furthermore, this can exploit the ability of the digital twins to simulate the engine efficiency and BSFC for degraded conditions which can provide an accurate life cycle cost assessment of the ship's engine.

Finally, a rigorous data processing methodology can be integrated to the systematic methodology proposed which considers continuous monitoring of the engine using the ICT measurement, thereby being able to identify and provide trends on the engine degradation over time. This is another gap identified in the literature, which would be particularly useful when trying to estimate and predict the remaining useful life of certain engine components, which that have significant commercial implications.

Bibliography

- [1] United Nations Conference on Trade and Development. *Review of maritime transport 2021*. Review of Maritime Transport. United Nations, New York, NY, March 2022.
- [2] Andreas Papandreou, Phoebe Koundouri, and Lydia Papadaki. *Sustainable Shipping: Levers of Change*, pages 153–171. Springer International Publishing, Cham, 2021. ISBN 978-3-030-56847-4. doi: 10.1007/978-3-030-56847-4_10. URL https://doi.org/10.1007/978-3-030-56847-4_10.
- [3] Jasper Faber; Shinichi Hanayama; Shuang Zhang; Paula Pereda; Bryan Comer; Elena Hauerhof; Wendela Schim van der Loeff ; Tristan Smith; Yan Zhang; Hiroyuko Kosaka; Masaki Adachi; Jean-Marc Bonello; Connor Galbraith; Ziheng Gong; Koichi Hirata; David Hummels; Anne Kleijn; David S. Lee; Yiming Liu; Andrea Lucchesi; Xiaoli Mao; Eiichi Muraoka; Liudmila Osipova; Haoqi Qian; Dan Rutherford; Santiago Suárez de la Fuente; Haichao Yuan; Camilo Velandia Perico; Libo Wu; Deping Sun; Dong-Hoon Yoo ; Hui Xing. Fourth IMO GHG Study 2020. Technical report, International Maritime Organisation, 4 Albert Embankment, London SE1 7SR, 2021.
- [4] Gordon Darroch. Reality check: Are ships more polluting than germany? *BBC*, 2018. URL <https://www.bbc.co.uk/news/world-43714029>.
- [5] International Maritime Organisation. International maritime organisation. <https://imo.org/>, 2022. [Online; accessed 19-July-2022].
- [6] Konstantinos-Marios Tsitsilonis and Gerasimos Theotokatos. A novel systematic methodology for ship propulsion engines energy management. *Journal of cleaner production*, 204:212–236, 2018.

- [7] International Maritime Organisation. Imo action to reduce greenhouse gas emissions from international shipping. https://sustainabledevelopment.un.org/content/documents/26620IMO_ACTION_TO_REDUCE_GHG_EMISSIONS_FROM_INTERNATIONAL_SHIPPING.pdf, 2019. Accessed: 11-07-2022.
- [8] Francesco Baldi, Fredrik Ahlgren, Tuong-Van Nguyen, Marcus Thern, and Karin Andersson. Energy and exergy analysis of a cruise ship. *Energies*, 11 (10):2508, 2018.
- [9] T. W. P. Smith, J. P. Jalkanen, B. A. Anderson, J. J. Corbett, J. Faber, S. Hanayama, E. O’Keeffe, S. Parker, L. Johansson, L. Aldous, C. Raucci, M. Traut, S. Ettinger, D. Nelissen, D. S. Lee, S. Ng, A. Agrawal, J. J. Winebrake, M. Hoen, S. Chesworth, and A. Pandey. Third IMO GHG Study 2014. Technical report, International Maritime Organisation, 4 Albert Embankment, London SE1 7SR, 2021.
- [10] RESOLUTION MEPC. 2016 guidelines for the development of a ship energy efficiency management plan (seemp). *International Maritime Organization. London*, 2, 2012.
- [11] Edmund Hughes. Implications of application of the eu emissions trading system (ets) to international shipping, and potential benefits of alternative market-based measures (mbms). *European Community Shipowners’ Association (ECSA): London, UK*, 2020.
- [12] Poseidon Principles. Poseidon principles; a global framework for responsible finance. <https://www.poseidonprinciples.org/>, 2019. Accessed: 07 Jun 2022.
- [13] Nishatabbas Rehmatulla and Tristan Smith. Barriers to energy efficiency in shipping: A triangulated approach to investigate the principal agent problem. *Energy Policy*, 84:44–57, 2015.
- [14] Chetna Chauhan, Amol Singh, and Sunil Luthra. Barriers to industry 4.0 adoption and its performance implications: An empirical investigation of emerging economy. *Journal of Cleaner Production*, 285:124809, 2021.

- [15] Fang Dao, Yun Zeng, Yidong Zou, Xiang Li, and Jing Qian. Acoustic vibration approach for detecting faults in hydroelectric units: A review. *Energies*, 14 (23):7840, 2021.
- [16] Peter Dörfler, Mirjam Sick, and André Coutu. *Flow-induced pulsation and vibration in hydroelectric machinery: engineer's guidebook for planning, design and troubleshooting*. Springer, 2013.
- [17] Zepeng Liu and Long Zhang. A review of failure modes, condition monitoring and fault diagnosis methods for large-scale wind turbine bearings. *Measurement*, 149:107002, 2020.
- [18] Jack P Salameh, Sebastien Cauet, Erik Etien, Anas Sakout, and Laurent Rambault. Gearbox condition monitoring in wind turbines: A review. *Mechanical Systems and Signal Processing*, 111:251–264, 2018.
- [19] Shengnan Tang, Shouqi Yuan, and Yong Zhu. Deep learning-based intelligent fault diagnosis methods toward rotating machinery. *Ieee Access*, 8:9335–9346, 2019.
- [20] Leonardo Presoto de Oliveira, Marco Aurélio Wehrmeister, and André Schneider de Oliveira. Systematic literature review on automotive diagnostics. In *2017 VII Brazilian Symposium on Computing Systems Engineering (SBESC)*, pages 1–8. IEEE, 2017.
- [21] Deepak Agarwal and Chandan Kumar Singh. *Model-Based Fault Detection on Modern Automotive Engines*, pages 167–204. Springer Singapore, Singapore, 2019. ISBN 978-981-13-3275-3. doi: 10.1007/978-981-13-3275-3_9. URL https://doi.org/10.1007/978-981-13-3275-3_9.
- [22] Amare D Fentaye, Aklilu T Baheta, Syed I Gilani, and Konstantinos G Kyprianidis. A review on gas turbine gas-path diagnostics: State-of-the-art methods, challenges and opportunities. *Aerospace*, 6(7):83, 2019.
- [23] Wang, H, Faber, J, Nelissen, D, Russell, B and St Amand, D. Reduction of ghg emissions from ships. marginal abatement costs and cost effectiveness of energy-efficiency measures, Jul 2010.

- [24] Terence Coghlin, Andrew W Baker, Julian Kenny, John D Kimball, and Thomas H Belknap. *Time charters*. Informa Law from Routledge, 2014.
- [25] Ícaro Aragão Fonseca and Henrique Murilo Gaspar. Challenges when creating a cohesive digital twin ship: a data modelling perspective. *Ship Technology Research*, 68(2):70–83, 2021.
- [26] Giuseppe Aiello, Antonio Giallanza, and Giuseppe Mascarella. Towards shipping 4.0. a preliminary gap analysis. *Procedia Manufacturing*, 42:24–29, 2020.
- [27] European Commission. The european green deal. https://ec.europa.eu/info/sites/default/files/european-green-deal-communication_en.pdf, 2019. Accessed: 06-07-2022.
- [28] Zero-Emission Shipping Mission. Industry roadmap for zero-emissions shipping. <https://dma.dk/Media/637847381174295461/ZESM%20Roadmap.pdf>, 2022. Accessed: 12-05-2022.
- [29] International Maritime Organisation. National action plans. <https://www.imo.org/en/OurWork/Environment/Pages/RELEVANT-NATIONAL-ACTION-PLANS-AND-STRATEGIES.aspx>, 2022. Accessed: 01-05-2022.
- [30] Lokukaluge P Perera and Brage Mo. Marine engine operating regions under principal component analysis to evaluate ship performance and navigation behavior. *IFAC-PapersOnLine*, 49(23):512–517, 2016.
- [31] Panos Deligiannis. Ship performance indicator. *Marine Policy*, 75:204–209, 2017.
- [32] Michael I Foteinos, Efstratios I Tzanos, and Nikolaos P Kyrtatos. Ship hull fouling estimation using shipboard measurements, models for resistance components, and shaft torque calculation using engine model. *Journal of Ship Research*, 61(2):64–74, 2017.
- [33] Clara Borén, Marcella Castells-Sanabra, and Manel Grifoll. Ship emissions reduction using weather ship routing optimisation. *Proceedings of the Institution*

- of Mechanical Engineers, Part M: Journal of Engineering for the Maritime Environment*, page 14750902221082901, 2022.
- [34] Christine Natalia, Michael Holine, and Agustinus Silalahi. A simultaneous container assignment and ship scheduling optimisation model in container shipping. *The Asian Journal of Shipping and Logistics*, 37(3):213–219, 2021.
- [35] Ramez Kian, Tolga Bektaş, and Djamila Ouelhadj. Optimal spare parts management for vessel maintenance scheduling. *Annals of operations research*, 272(1):323–353, 2019.
- [36] Rosmaini Ahmad and Shahrul Kamaruddin. An overview of time-based and condition-based maintenance in industrial application. *Computers & industrial engineering*, 63(1):135–149, 2012.
- [37] Albert W Veenstra and Jan Van Dalen. Ship speed and fuel consumption quotation in ocean shipping time charter contracts. *Journal of Transport Economics and Policy (JTPEP)*, 45(1):41–61, 2011.
- [38] Pratham Agarwala, Sanjay Chhabra, and Nitin Agarwala. Using digitalisation to achieve decarbonisation in the shipping industry. *Journal of International Maritime Safety, Environmental Affairs, and Shipping*, 5(4):161–174, 2021.
- [39] Ronald Dela Cruz Barro, Jun-Seong Kim, and Don-Chool Lee. Real time monitoring of energy efficiency operation indicator on merchant ships. *Journal of the Korean Society of Marine Engineering*, 35(3):301–308, 2011.
- [40] Hongtao Chi, Giulia Pedrielli, Szu Hui Ng, Thomas Kister, and Stéphane Bressan. A framework for real-time monitoring of energy efficiency of marine vessels. *Energy*, 145:246–260, 2018.
- [41] Andrea Coraddu, Massimo Figari, and Stefano Savio. Numerical investigation on ship energy efficiency by monte carlo simulation. *Proceedings of the institution of mechanical engineers, part M: journal of engineering for the maritime environment*, 228(3):220–234, 2014.
- [42] Z Bazari. Ship energy performance benchmarking/rating: methodology and application. *Journal of Marine Engineering & Technology*, 6(1):11–18, 2007.

- [43] Shuang Zhang, Ying Li, Haichao Yuan, and Deping Sun. An alternative benchmarking tool for operational energy efficiency of ships and its policy implications. *Journal of Cleaner Production*, 240:118223, 2019.
- [44] Francesco Baldi, Fredrik Ahlgren, Francesco Melino, Cecilia Gabriellii, and Karin Andersson. Optimal load allocation of complex ship power plants. *Energy Conversion and Management*, 124:344–356, 2016.
- [45] Zhi-Min Yao, Zuo-Qin Qian, Rong Li, and Eric Hu. Energy efficiency analysis of marine high-powered medium-speed diesel engine base on energy balance and exergy. *Energy*, 176:991–1006, 2019.
- [46] Pierre Marty, Jean-François Hétet, David Chalet, and Philippe Corrigan. Exergy analysis of complex ship energy systems. *Entropy*, 18(4):127, 2016.
- [47] George G Dimopoulos, Chariklia A Georgopoulou, Iason C Stefanatos, Alexandros S Zymaris, and Nikolaos MP Kakalis. A general-purpose process modelling framework for marine energy systems. *Energy conversion and management*, 86:325–339, 2014.
- [48] Oktay Çetin and M Ziya Sogut. A new strategic approach of energy management onboard ships supported by exergy and economic criteria: A case study of a cargo ship. *Ocean Engineering*, 219:108137, 2021.
- [49] George G Dimopoulos, Chariklia A Georgopoulou, and Nikolaos MP Kakalis. The introduction of exergy analysis to the thermo-economic modelling and optimisation of a marine combined cycle system. In *The 25th international conference on efficiency, cost, optimisation, simulation and environmental impact of energy systems*, pages 26–29, 2012.
- [50] Francesco Baldi, Cecilia Gabriellii, Karin Andersson, and Bengt-Olof Petersen. From energy flows to monetary flows-an innovative way of assessing ship performances through thermo-economic analysis. In *International Association of Maritime Economists Conference (IAME 2012 Taipei).*, 2012.
- [51] Carolin Wagner, Philipp Saalman, and Bernd Hellingrath. An overview of useful data and analyzing techniques for improved multivariate diagnostics

- and prognostics in condition-based maintenance. In *Proceedings of Annual Conference of the Prognostics and Health Management Society*, pages 3–6, 2016.
- [52] Michael Knowles and David Baglee. Condition management of marine lube oil and the role of intelligent sensor systems in diagnostics. In *Journal of Physics: Conference Series*, volume 364, page 012007. IOP Publishing, 2012.
- [53] Mohammad Rahimi, Mohammad-Reza Pourramezan, and Abbas Rohani. Modeling and classifying the in-operando effects of wear and metal contaminations of lubricating oil on diesel engine: A machine learning approach. *Expert Systems with Applications*, 203:117494, 2022.
- [54] O Cardona-Morales, LD Avendaño, and German Castellanos-Dominguez. Non-linear model for condition monitoring of non-stationary vibration signals in ship driveline application. *Mechanical Systems and Signal Processing*, 44(1-2): 134–148, 2014.
- [55] Christos Gkerekos, Iraklis Lazakis, and Gerasimos Theotokatos. Ship machinery condition monitoring using vibration data through supervised learning. In *Smart ship technology conference*, 01 2017.
- [56] Sangharatna M Ramteke, H Chelladurai, and M Amarnath. Diagnosis and classification of diesel engine components faults using time–frequency and machine learning approach. *Journal of Vibration Engineering & Technologies*, 10(1):175–192, 2022.
- [57] Yiannis Raptodimos and Iraklis Lazakis. Using artificial neural network-self-organising map for data clustering of marine engine condition monitoring applications. *Ships and Offshore Structures*, 13(6):649–656, 2018.
- [58] Oihane C Basurko and Zigor Uriondo. Condition-based maintenance for medium speed diesel engines used in vessels in operation. *Applied Thermal Engineering*, 80:404–412, 2015.
- [59] Andrea Coraddu, Luca Oneto, Aessandro Ghio, Stefano Savio, Davide Anguita, and Massimo Figari. Machine learning approaches for improving condition-based maintenance of naval propulsion plants. *Proceedings of the Institution*

- of Mechanical Engineers, Part M: Journal of Engineering for the Maritime Environment*, 230(1):136–153, 2016.
- [60] Donghyun Kim, Sangbong Lee, and Jihwan Lee. An ensemble-based approach to anomaly detection in marine engine sensor streams for efficient condition monitoring and analysis. *Sensors*, 20(24):7285, 2020.
- [61] Christian Velasco-Gallego and Iraklis Lazakis. Radis: a real-time anomaly detection intelligent system for fault diagnosis of marine machinery. *Expert Systems with Applications*, page 117634, 2022.
- [62] Ruihan Wang, Hui Chen, and Cong Guan. A bayesian inference-based approach for performance prognostics towards uncertainty quantification and its applications on the marine diesel engine. *ISA transactions*, 118:159–173, 2021.
- [63] Peihua Han, Andre Listou Ellefsen, Guoyuan Li, Vilmar Æsøy, and Houxiang Zhang. Fault prognostics using lstm networks: application to marine diesel engine. *IEEE Sensors Journal*, 21(22):25986–25994, 2021.
- [64] Magnus Gribbestad, Muhammad Umair Hassan, and Ibrahim A Hameed. Transfer learning for prognostics and health management (phm) of marine air compressors. *Journal of Marine Science and Engineering*, 9(1):47, 2021.
- [65] Turker Ince, Serkan Kiranyaz, Levent Eren, Murat Askar, and Moncef Gabbouj. Real-time motor fault detection by 1-d convolutional neural networks. *IEEE Transactions on Industrial Electronics*, 63(11):7067–7075, 2016.
- [66] AL Michala, I Lazakis, and G Theotokatos. Predictive maintenance decision support system for enhanced energy efficiency of ship machinery. In *International Conference on Shipping in Changing Climates*, pages 195–205, 2015.
- [67] Christina Diakaki, Natalia Panagiotidou, Anastasios Pouliezios, Georgios D Kontes, George S Stavrakakis, Kostas Belibassakis, Theodoros P Gerostathis, George Livanos, Dimitrios-Nikolaos Pagonis, and Gerasimos Theotokatos. A decision support system for the development of voyage and maintenance plans for ships. *International Journal of Decision Support Systems*, 1(1):42–71, 2015.

- [68] Louise Wright and Stuart Davidson. How to tell the difference between a model and a digital twin. *Advanced Modeling and Simulation in Engineering Sciences*, 7(1):1–13, 2020.
- [69] Xiaojian Xu, Xinping Yan, Kun Yang, Jiangbin Zhao, Chenxing Sheng, and Chengqing Yuan. Review of condition monitoring and fault diagnosis for marine power systems. *Transportation Safety and Environment*, 3(2):85–102, 2021.
- [70] Iraklis Lazakis, Yannis Raptodimos, and T Varelas. Predicting ship machinery system condition through analytical reliability tools and artificial neural networks. *Ocean Engineering*, 152:404–415, 2018.
- [71] George A Livanos, Gerasimos Theotokatos, and Dimitrios-Nikolaos Pagonis. Techno-economic investigation of alternative propulsion plants for ferries and ro-ro ships. *Energy Conversion and Management*, 79:640–651, 2014.
- [72] Andrea Coraddu, Miltiadis Kalikatzarakis, Gerasimos Theotokatos, Rinze Geertsma, and Luca Oneto. Physical and data-driven models hybridisation for modelling the dynamic state of a four-stroke marine diesel engine. In *Engine Modeling and Simulation*, pages 145–193. Springer, 2022.
- [73] S d’Ambrosio, A Ferrari, and L Galleani. In-cylinder pressure-based direct techniques and time frequency analysis for combustion diagnostics in ic engines. *Energy Conversion and Management*, 99:299–312, 2015.
- [74] DA Kouremenos, CD Rakopoulos, DT Hountalas, and AD Kouremenos. The maximum compression pressure position relative to top dead centre as an indication of engine cylinder condition and blowby. *Energy Conversion and Management*, 35(10):857–870, 1994.
- [75] Giulio Panzani, Fredrik Östman, and Christopher H Onder. Engine knock margin estimation using in-cylinder pressure measurements. *IEEE/ASME transactions on Mechatronics*, 22(1):301–311, 2016.
- [76] VT Lamaris and DT Hountalas. A general purpose diagnostic technique for marine diesel engines—application on the main propulsion and auxiliary diesel

- units of a marine vessel. *Energy conversion and management*, 51(4):740–753, 2010.
- [77] Fredrik Östman and Hannu T Toivonen. Active torsional vibration control of reciprocating engines. *Control Engineering Practice*, 16(1):78–88, 2008.
- [78] Terry Lin, Andy Tan, and Joseph Mathew. Condition monitoring and diagnosis of injector faults in a diesel engine using in-cylinder pressure and acoustic emission techniques. In *Proceedings of the 14th Asia Pacific Vibration Conference-Dynamics for Sustainable Engineering-Volume 1*, pages 454–463. Department of Civil and Structural Engineering, The Hong Kong Polytechnic . . . , 2011.
- [79] Stefan Larsson and Stefan Schagerberg. Si-engine cylinder pressure estimation using torque sensors. Technical Report 2004-01-1369, SAE Technical Paper, 2004.
- [80] Hans Aulin, Per Tunestal, Thomas Johansson, and Bengt Johansson. Extracting cylinder individual combustion data from a high precision torque sensor. In *Internal Combustion Engine Division Fall Technical Conference*, volume 49446, pages 619–625, 2010.
- [81] Feilong Liu, Gehan AJ Amaratunga, Nick Collings, and Ahmed Soliman. An experimental study on engine dynamics model based in-cylinder pressure estimation. Technical report, SAE Technical Paper, 2012.
- [82] DT Hountalas, RG Papagiannakis, G Zovanos, and A Antonopoulos. Comparative evaluation of various methodologies to account for the effect of load variation during cylinder pressure measurement of large scale two-stroke diesel engines. *Applied energy*, 113:1027–1042, 2014.
- [83] Rakesh Kumar Maurya, Maurya, and Luby. *Reciprocating engine combustion diagnostics*. Springer, 2019.
- [84] Winterthur Gas & Diesel Ltd. Low pressure x-df engines faq. <https://www.wingd.com/en/documents/general/brochures/x-df-faq-brochure.pdf/>, 2020. Accessed: 2021-12-06.

- [85] Urban Žvar Baškovič, Rok Vihar, Igor Mele, and Tomaž Katrašnik. A new method for simultaneous determination of the tdc offset and the pressure offset in fired cylinders of an internal combustion engine. *Energies*, 10(1):143, 2017.
- [86] Antonis Antonopoulos and Dimitrios Hountalas. Identification and correction of the error induced by the sampling method used to monitor cylinder pressure of reciprocating internal combustion engines. In *SAE 2012 World Congress & Exhibition*, number 2012-01-1155 in 01820274, 2012.
- [87] F Taglialatela, N Cesario, M Porto, SS Merola, P Sementa, and BM Vaglieco. Use of accelerometers for spark advance control of si engines. *SAE International Journal of Engines*, 2(1):971–981, 2009.
- [88] Christopher J Polonowski, Vivek K Mathur, Jeffrey D Naber, and Jason R Blough. Accelerometer based sensing of combustion in a high speed hpcr diesel engine. *SAE Transactions*, pages 592–607, 2007.
- [89] Stuart Trimby, Julian F Dunne, Colin Bennett, and Dave Richardson. Unified approach to engine cylinder pressure reconstruction using time-delay neural networks with crank kinematics or block vibration measurements. *International Journal of Engine Research*, 18(3):256–272, 2017.
- [90] Runzhe Han, Christian Bohn, and Georg Bauer. Recursive engine in-cylinder pressure estimation using kalman filter and structural vibration signal. *IFAC-PapersOnLine*, 51(31):700–705, 2018.
- [91] C Bennett, JF Dunne, S Trimby, and D Richardson. Engine cylinder pressure reconstruction using crank kinematics and recurrently-trained neural networks. *Mechanical systems and signal processing*, 85:126–145, 2017.
- [92] Francisco J Jiménez Espadafor, José A Becerra Villanueva, Daniel Palomo Guerrero, Miguel Torres García, Elisa Carvajal Trujillo, and Francisco Fernández Vacas. Measurement and analysis of instantaneous torque and angular velocity variations of a low speed two stroke diesel engine. *Mechanical Systems and Signal Processing*, 49(1-2):135–153, 2014.

- [93] Mathieu Desbazeille, RB Randall, François Guillet, Mohamed El Badaoui, and Christian Hoisnard. Model-based diagnosis of large diesel engines based on angular speed variations of the crankshaft. *Mechanical Systems and Signal Processing*, 24(5):1529–1541, 2010.
- [94] Daniel Palomo Guerrero and Francisco J Jiménez-Espadafor. Torsional system dynamics of low speed diesel engines based on instantaneous torque: Application to engine diagnosis. *Mechanical Systems and Signal Processing*, 116:858–878, 2019.
- [95] Gerasimos Theotokatos, Cong Guan, Hui Chen, and Iraklis Lazakis. Development of an extended mean value engine model for predicting the marine two-stroke engine operation at varying settings. *Energy*, 143:533–545, 2018.
- [96] Alberto Diez-Olivan, Jose A Pagan, Ricardo Sanz, and Basilio Sierra. Data-driven prognostics using a combination of constrained k-means clustering, fuzzy modeling and lof-based score. *Neurocomputing*, 241:97–107, 2017.
- [97] Michail Cheliotis, Iraklis Lazakis, and Gerasimos Theotokatos. Machine learning and data-driven fault detection for ship systems operations. *Ocean Engineering*, 216:107968, 2020.
- [98] Xiaojian Xu, Zhuangzhuang Zhao, Xiaobin Xu, Jianbo Yang, Leilei Chang, Xinping Yan, and Guodong Wang. Machine learning-based wear fault diagnosis for marine diesel engine by fusing multiple data-driven models. *Knowledge-Based Systems*, 190:105324, 2020.
- [99] Andrea Coraddu, Luca Oneto, Davide Ilardi, Sokratis Stoumpos, and Gerasimos Theotokatos. Marine dual fuel engines monitoring in the wild through weakly supervised data analytics. *Engineering Applications of Artificial Intelligence*, 100:104179, 2021.
- [100] Yanghui Tan, Hui Tian, Ruizheng Jiang, Yejin Lin, and Jundong Zhang. A comparative investigation of data-driven approaches based on one-class classifiers for condition monitoring of marine machinery system. *Ocean Engineering*, 201:107174, 2020.

- [101] Dileep N. Malkhede, Bhartendu Seth, and H.C. Dhariwal. Mean value model and control of a marine turbocharged diesel engine. In *SAE Technical Paper Series*. SAE International, October 2005. doi: 10.4271/2005-01-3889. URL <https://doi.org/10.4271/2005-01-3889>.
- [102] Kamyar Nikzadfar and Amir H Shamekhi. Investigating the relative contribution of operational parameters on performance and emissions of a common-rail diesel engine using neural network. *Fuel*, 125:116–128, 2014.
- [103] RD Geertsma, K Visser, and RR Negenborn. Adaptive pitch control for ships with diesel mechanical and hybrid propulsion. *Applied energy*, 228:2490–2509, 2018.
- [104] Xavier Llamas and Lars Eriksson. Control-oriented modeling of two-stroke diesel engines with exhaust gas recirculation for marine applications. *Proceedings of the Institution of Mechanical Engineers, Part M: Journal of Engineering for the Maritime Environment*, 233(2):551–574, 2019.
- [105] Cong Guan, Gerasimos Theotokatos, and Hui Chen. Analysis of two stroke marine diesel engine operation including turbocharger cut-out by using a zero-dimensional model. *Energies*, 8(6):5738–5764, 2015.
- [106] Ulrik Larsen, Leonardo Pierobon, Francesco Baldi, Fredrik Haglind, and Anders Ivarsson. Development of a model for the prediction of the fuel consumption and nitrogen oxides emission trade-off for large ships. *Energy*, 80:545–555, 2015.
- [107] Harsh Sapra, Milinko Godjevac, Klaas Visser, Douwe Stapersma, and Chris Dijkstra. Experimental and simulation-based investigations of marine diesel engine performance against static back pressure. *Applied Energy*, 204:78–92, 2017.
- [108] Nikola Matulić, Gojmir Radica, and Sandro Nižetić. Engine model for onboard marine engine failure simulation. *Journal of Thermal Analysis and Calorimetry*, 141(1):119–130, 2020.

- [109] Sokratis Stoumpos and Gerasimos Theotokatos. A novel methodology for marine dual fuel engines sensors diagnostics and health management. *International Journal of Engine Research*, 23(6):974–994, 2022.
- [110] Jose Antonio Pagán Rubio, Francisco Vera-García, Jose Hernandez Grau, Jose Muñoz Cámara, and Daniel Albaladejo Hernandez. Marine diesel engine failure simulator based on thermodynamic model. *Applied Thermal Engineering*, 144:982–995, 2018.
- [111] Francisco Vera-García, José Antonio Pagán Rubio, José Hernández Grau, and Daniel Albaladejo Hernández. Improvements of a failure database for marine diesel engines using the rcm and simulations. *Energies*, 13(1):104, 2019.
- [112] Spiridon I Raptotasios, Nikolaos F Sakellaris, Roussos G Papagiannakis, and Dimitrios T Hountalas. Application of a multi-zone combustion model to investigate the nox reduction potential of two-stroke marine diesel engines using egr. *Applied Energy*, 157:814–823, 2015.
- [113] Michael I Foteinos, Alexandros Papazoglou, Nikolaos P Kyrtatos, Anastassios Stamatelos, Olympia Zogou, and Antiopi-Malvina Stamatellou. A three-zone scavenging model for large two-stroke uniflow marine engines using results from cfd scavenging simulations. *Energies*, 12(9):1719, 2019.
- [114] Gerasimos Theotokatos. On the cycle mean value modelling of a large two-stroke marine diesel engine. *Proceedings of the Institution of Mechanical Engineers, Part M: Journal of engineering for the maritime environment*, 224(3):193–205, 2010.
- [115] Jer-Nan Juang. *Applied system identification*. Prentice-Hall, Inc., 1994.
- [116] Yuriy Batrak. Torsional vibration calculation issues with propulsion systems. <http://www.shaftdesigner.com/downloads/Yuriy-Batruk-CALCULATION-OF-TORSIONAL-VIBRATION.pdf>, 2011. Accessed: 2022-10-06.
- [117] Lech Murawski and Adam Charchalis. Simplified method of torsional vibration

- calculation of marine power transmission system. *Marine structures*, 39:335–349, 2014.
- [118] Ivo Senjanović, Neven Hadžić, Lech Murawski, Nikola Vladimir, Neven Alujević, and Dae-Seung Cho. Analytical procedures for torsional vibration analysis of ship power transmission system. *Engineering Structures*, 178:227–244, 2019.
- [119] Stefan Schagerberg and Tomas McKelvey. Instantaneous crankshaft torque measurements-modeling and validation. Technical Report 2003-01-0713, SAE Technical Paper, 2003.
- [120] Fredrik Ostman and Hannu T Toivonen. Adaptive cylinder balancing of internal combustion engines. *IEEE Transactions on Control Systems Technology*, 19(4):782–791, 2010.
- [121] Mingquan Zhang, Yanyang Zi, Linkai Niu, Songtao Xi, and Yiqing Li. Intelligent diagnosis of v-type marine diesel engines based on multifeatures extracted from instantaneous crankshaft speed. *IEEE Transactions on Instrumentation and Measurement*, 68(3):722–740, 2018.
- [122] Mikael Thor, Bo Egardt, Tomas McKelvey, and Ingemar Andersson. Using combustion net torque for estimation of combustion properties from measurements of crankshaft torque. *Control Engineering Practice*, 26:233–244, 2014.
- [123] Jie Chen and Guoxiang Gu. *Control-oriented system identification: an H_{∞} approach*, volume 19. Wiley-Interscience, 2000.
- [124] JR Raol. Neural network based parameter estimation of unstable aerospace dynamic systems. *IEE Proceedings-Control Theory and Applications*, 141(6):385–388, 1994.
- [125] Peter Englezos and Nicolas Kalogerakis. *Applied parameter estimation for chemical engineers*. CRC Press, 2000.
- [126] Mo R Banan, Ma R Banan, and KD Hjelmstad. Parameter estimation of structures from static response. ii: Numerical simulation studies. *Journal of structural engineering*, 120(11):3259–3283, 1994.

- [127] J-H Heo and JD Salas. Estimation of quantiles and confidence intervals for the log-gumbel distribution. *Stochastic Hydrology and Hydraulics*, 10(3):187–207, 1996.
- [128] Yu Chen, Jin Cheng, Yu Jiang, and Keji Liu. A time delay dynamical model for outbreak of 2019-ncov and the parameter identification. *Journal of Inverse and Ill-posed Problems*, 28(2):243–250, 2020.
- [129] Gérard Favier. An overview of system modeling and identification. In *11th International conference on Sciences and Techniques of Automatic control & computer engineering (STA'2010)*, Monastir, Tunisia, 2010.
- [130] Jaume Llibre and Rafael Ramírez. *Inverse problems in ordinary differential equations and applications*. Springer, 2016.
- [131] Yonathan Bard. *Nonlinear parameter estimation*. Academic press, New York City, 1974.
- [132] Antônio H Ribeiro and Luis A Aguirre. Shooting methods for parameter estimation of output error models. *IFAC-PapersOnLine*, 50(1):13998–14003, 2017.
- [133] PW Hemker. Numerical methods for differential equations in system simulation and in parameter estimation. *Analysis and Simulation of biochemical systems*, 28:59–80, 1972.
- [134] Maurice W Benson. *Numerical parameter estimation in differential equations*. PhD thesis, University of British Columbia, 1977.
- [135] Hans Georg Bock, Ekaterina Kostina, and Johannes P Schlöder. Direct multiple shooting and generalized gauss-newton method for parameter estimation problems in ode models. In *Multiple Shooting and Time Domain Decomposition Methods*, pages 1–34. Springer, 2015.
- [136] Hans Georg Bock. Recent advances in parameteridentification techniques for ode. In *Numerical treatment of inverse problems in differential and integral equations*, pages 95–121. Springer, 1983.

- [137] M Peifer and J Timmer. Parameter estimation in ordinary differential equations for biochemical processes using the method of multiple shooting. *IET Systems Biology*, 1(2):78–88, 2007.
- [138] John Villadsen and Michael L Michelsen. *Solution of differential equation models by polynomial approximation*. Prentice-Hall, Inc., Englewood Cliffs, New Jersey, 1978.
- [139] Niels Baden and John Villadsen. A family of collocation based methods for parameter estimation in differential equations. *The Chemical Engineering Journal*, 23(1):1–13, 1982.
- [140] James M Varah. A spline least squares method for numerical parameter estimation in differential equations. *SIAM Journal on Scientific and Statistical Computing*, 3(1):28–46, 1982.
- [141] Sastry S Isukapalli and Panos G Georgopoulos. Computational methods for sensitivity and uncertainty analysis for environmental and biological models. Technical report, National Exposure Research Laboratory, US Environmental Protection Agency, EPA/600/R-01-068, 2001.
- [142] S Reynold Chu, Rahmat Shoureshi, and Manoel Tenorio. Neural networks for system identification. *IEEE Control systems magazine*, 10(3):31–35, 1990.
- [143] Alexander S Poznyak, Edgar N Sanchez, and Wen Yu. *Differential neural networks for robust nonlinear control: identification, state estimation and trajectory tracking*. World Scientific, 2001.
- [144] Oliver Nelles. *Nonlinear system identification: from classical approaches to neural networks and fuzzy models*. Springer Science & Business Media, 2013.
- [145] Panagiotis Mizythras, Evangelos Boulougouris, and Gerasimos Theotokatos. A novel objective oriented methodology for marine engine–turbocharger matching. *International Journal of Engine Research*, page 14680874211039705, 2021.
- [146] John B Heywood. *Internal combustion engine fundamentals*. McGraw-Hill Education, 2018.

- [147] William Cecil Gardiner and Alexander Burcat. *Combustion chemistry*. Springer, 1984.
- [148] CIMAC HFO Working Group et al. Recommendations regarding fuel quality for diesel engines. *Publisher: City, Country*, 2003.
- [149] Günter P Merker, Christian Schwarz, Gunnar Stiesch, and Frank Otto. *Simulating Combustion: Simulation of combustion and pollutant formation for engine-development*. Springer Science & Business Media, 2005.
- [150] Simon K Chen and Patrick F Flynn. Development of a single cylinder compression ignition research engine. Technical report, SAE Technical Paper 650733, 1965.
- [151] Francesco Baldi, Gerasimos Theotokatos, and Karin Andersson. Development of a combined mean value-zero dimensional model and application for a large marine four-stroke diesel engine simulation. *Applied Energy*, 154:402–415, 2015.
- [152] La Xiang, Gerasimos Theotokatos, Haining Cui, Keda Xu, Hongkai Ben, and Yu Ding. Parametric knocking performance investigation of spark ignition natural gas engines and dual fuel engines. *Journal of Marine Science and Engineering*, 8(6):459, 2020.
- [153] Neil Watson and Marian Janota. *Turbocharging the internal combustion engine*. Macmillan International Higher Education, 1982.
- [154] Cong Guan, Gerasimos Theotokatos, Peilin Zhou, and Hui Chen. Computational investigation of a large containership propulsion engine operation at slow steaming conditions. *Applied Energy*, 130:370–383, 2014.
- [155] Seyed Mohsen Momeni, Gholamreza Salehi, and Majid Eshagh Nimvari. Modeling and thermoeconomic optimization of marine diesel charge air cooler. *Energy*, 162:753–763, 2018.
- [156] G Theotokatos, S Stoumpos, I Lazakis, and G Livanos. Numerical study of a marine dual-fuel four-stroke engine. *Maritime Technology and Engineering III*, pages 777–783, 2016. doi: [\url{https://doi.org/10.1201/b21890-100}](https://doi.org/10.1201/b21890-100).

- [157] Sokratis Stoumpos, Gerasimos Theotokatos, Christoforos Mavrelou, and Evangelos Boulougouris. Towards marine dual fuel engines digital twins—integrated modelling of thermodynamic processes and control system functions. *Journal of Marine Science and Engineering*, 8(3):200, 2020.
- [158] Per Öberg. *A DAE Formulation for Multi-Zone Thermodynamic Models and its Application to CVCP Engines*. PhD thesis, Linköping UniversityLinköping University, Vehicular Systems, The Institute of Technology, 2009.
- [159] Brian R Hunt, Ronald L Lipsman, John E Osborn, and Jonathan M Rosenberg. *Differential equations with MATLAB*. John Wiley & Sons, 2019.
- [160] Lars Eriksson and Ingemar Andersson. An analytic model for cylinder pressure in a four stroke si engine. *Sae Transactions*, pages 726–733, 2002.
- [161] MG Calgin. *Lagrangian and Hamiltonian Mechanics: Solutions to the Exercises*. World Scientific Publishing Company, Incorporated, 1999.
- [162] AS Mendes, PS Meirelles, and DE Zampieri. Analysis of torsional vibration in internal combustion engines: modelling and experimental validation. *Proceedings of the Institution of Mechanical Engineers, Part K: Journal of Multi-body Dynamics*, 222(2):155–178, 2008.
- [163] DJ Henwood. Approximating the hysteretic damping matrix by a viscous matrix for modelling in the time domain. *Journal of sound and Vibration*, 254(3):575–593, 2002.
- [164] Uwe Kiencke and Lars Nielsen. *Automotive control systems: for engine, driveline, and vehicle*. IOP Publishing, Bristol, United Kingdom, 2000.
- [165] DNV. Rules for classification of ships, part 4, chapter 2. <https://rules.dnv.com/docs/pdf/DNV/RU-SHIP/2015-10/DNVGL-RU-SHIP-Pt4Ch2.pdf>, 2015. Accessed: 2022-06-06.
- [166] MAN Energy Solutions. Basic principles of ship propulsion. https://www.man-es.com/docs/default-source/marine/tools/basic-principles-of-ship-propulsion_web_links.pdf?sfvrsn=12d1b862_10, 2018. Accessed: 2022-06-06.

- [167] Gerhard Wanner and Ernst Hairer. *Solving ordinary differential equations II*, volume 375. Springer Berlin Heidelberg New York, 1996.
- [168] Cleve B Moler. *Numerical computing with MATLAB*. SIAM, 2004.
- [169] Martin Schetzen. *Linear time-invariant systems*. Wiley–Blackwell, 2003.
- [170] E Brusa, C Delprete, and G Genta. Torsional vibration of crankshafts: effects of non-constant moments of inertia. *Journal of sound and vibration*, 205(2): 135–150, 1997.
- [171] Felix Martinek. Torsional vibration damping in a marine propulsion system driven by a two-cycle diesel engine. In *Internal Combustion Engine Division Spring Technical Conference*, volume 36789, pages 321–327, 2003.
- [172] Konstantinos-Marios Tsitsilonis and Gerasimos Theotokatos. A novel method for in-cylinder pressure prediction using the engine instantaneous crankshaft torque. *Proceedings of the Institution of Mechanical Engineers, Part M: Journal of Engineering for the Maritime Environment*, 236(1):131–149, 2022.
- [173] M Tadros, M Ventura, and C Guedes Soares. Simulation of the performance of marine genset based on double-wiebe function. In *Sustainable Development and Innovations in Marine Technologies*, pages 292–299. CRC Press, 2019.
- [174] Joseph Hilsenrath. *Tables of thermal properties of gases: comprising tables of thermodynamic and transport properties of air, argon, carbon dioxide, carbon monoxide, hydrogen, nitrogen, oxygen, and steam*, volume 564. US Department of Commerce, National Bureau of Standards, 1955.
- [175] Haosheng Shen, Jundong Zhang, Baicheng Yang, and Baozhu Jia. Development of a marine two-stroke diesel engine mvem with in-cylinder pressure trace predictive capability and a novel compressor model. *Journal of Marine Science and Engineering*, 8(3):204, 2020.
- [176] Arkady Pikovsky and Antonio Politi. *Lyapunov exponents: a tool to explore complex dynamics*. Cambridge University Press, 2016.

- [177] Oliver Nelles. Nonlinear dynamic system identification. In *Nonlinear System Identification*, pages 547–577. Springer, 2001.
- [178] Morteza Kimiaei. Nonmonotone self-adaptive levenberg–marquardt approach for solving systems of nonlinear equations. *Numerical Functional Analysis and Optimization*, 39(1):47–66, 2018.
- [179] Daniel Palomo Guerrero. *Aportaciones al mantenimiento predictivo de plantas de potencia: aplicación a motores diesel lentos de 2 tiempos*. PhD thesis, Universidad de Sevilla, 2017.
- [180] Byong-Seok Kim, Wook Hyeon Yoon, Sung Hyup Ryu, and Ji Soo Ha. Effect of the injector nozzle hole diameter and number on the spray characteristics and the combustion performance in medium-speed diesel marine engines. Technical report, SAE Technical Paper 2005-01-3853, 2005.
- [181] Wartsila. Project guide for marine applications: Wartsila 46c, 2001. Accessed: 2022-10-06.
- [182] Konstantinos-Marios Tsitsilonis, Gerasimos Theotokatos, Nikolaos Xiros, and Malcolm Habens. Systematic investigation of a large two-stroke engine crankshaft dynamics model. *Energies*, 13(10):2486, 2020.
- [183] Piezotron pressure sensor – for engine diagnostics, type 6619ap25/ap35. https://kistler.cdn.celum.cloud/SAPCommerce_Download_original/003-398e.pdf, 2019.
- [184] Doctor diesel dk-20 analyser from icon research. <https://iconresearch.co.uk/wp-content/uploads/2018/02/dk-20-brochure.pdf>, 2020.
- [185] F. Espadafor, D. Guerrero, F. Vacas, and M. Amo. Torsional system modelling: balancing and diagnosis application in two-stroke low speed power plant diesel engine. In *Proceedings of the 28th CIMAC world congress*, 2016.

Appendix A

Derivation of Equations

A.1 Direct Crankshaft Dynamics Model

The derivatives of the viscous damping found in the right hand side of the Lagrangian equation (Eq. 5.1), are shown below for each DOF:

$$\begin{aligned}\frac{\partial \mathcal{R}}{\partial \dot{\theta}_1} &= c_1 (\dot{\theta}_2 - \dot{\theta}_1) - d_1 \dot{\theta}_1 \\ &= -(c_1 + d_1) \dot{\theta}_1 + c_2 \dot{\theta}_2\end{aligned}\tag{A.1}$$

$$\begin{aligned}\frac{\partial \mathcal{R}}{\partial \dot{\theta}_2} &= -c_1 (\dot{\theta}_2 - \dot{\theta}_1) + c_2 (\dot{\theta}_3 - \dot{\theta}_2) - d_2 \dot{\theta}_2 \\ &= c_1 \dot{\theta}_1 - (c_1 + c_2 + d_2) \dot{\theta}_2 + c_2 \dot{\theta}_3\end{aligned}\tag{A.2}$$

\vdots

$$\begin{aligned}\frac{\partial \mathcal{R}}{\partial \dot{\theta}_j} &= c_{j-1} (\dot{\theta}_j - \dot{\theta}_{j-1}) - c_j (\dot{\theta}_{j+1} - \dot{\theta}_j) - d_j \dot{\theta}_j \\ &= c_{j-1} \dot{\theta}_{j-1} - (c_{j-1} + c_j + d_j) \dot{\theta}_j + c_j \dot{\theta}_{j+1}\end{aligned}\tag{A.3}$$

Similarly, the derivatives of the hysteretic damping found in the right hand side of the Lagrangian equation (Eq. 5.1), are shown below for each DOF:

$$\begin{aligned}\frac{\partial \mathcal{H}}{\partial \theta_1} &= i k_1 \sigma_1 (\theta_2 - \theta_1) \\ &= -i k_1 \sigma_1 \theta_1 + i k_2 \sigma_2 \theta_2\end{aligned}\tag{A.4}$$

$$\begin{aligned}\frac{\partial \mathcal{H}}{\partial \theta_2} &= -i k_1 \sigma_1 (\theta_2 - \theta_1) + i k_2 \sigma_2 (\theta_3 - \theta_2) \\ &= i k_1 \sigma_1 \theta_1 - i (k_1 \sigma_1 + k_2 \sigma_2) \theta_2 + i k_2 \sigma_2 \theta_3\end{aligned}\tag{A.5}$$

$$\begin{aligned}
 & \vdots \\
 \frac{\partial \mathcal{H}}{\partial \theta_j} &= i k_{j-1} \sigma_{j-1} (\theta_j - \theta_{j-1}) - i k_j \sigma_j (\theta_{j+1} - \theta_j) \\
 &= i k_{j-1} \sigma_{j-1} \theta_{j-1} - i (k_{j-1} \sigma_{j-1} + k_j \sigma_j) \theta_j + i k_j \sigma_j \theta_{j+1}
 \end{aligned} \tag{A.6}$$

Subsequently, both of the above systems of equations can be gathered in matrix format for the case of the viscous and hysteretic damping as demonstrated by the below equations respectively:

$$\frac{\partial \mathcal{R}}{\partial \dot{\Theta}} = - \overbrace{\begin{bmatrix} c_1 & -c_1 & & & \\ -c_1 & c_1 + c_2 & -c_2 & & \\ & & \ddots & & \\ & & & -c_{j-1} & c_{j-1} + c_j & -c_j \\ & & & & \ddots & \end{bmatrix}}^{\mathcal{C}} \overbrace{\begin{bmatrix} \dot{\theta}_1 \\ \dot{\theta}_2 \\ \vdots \\ \dot{\theta}_j \\ \vdots \end{bmatrix}}^{\dot{\Theta}} \tag{A.7}$$

$$- \overbrace{\begin{bmatrix} d_1 & & & & \\ & d_2 & & & \\ & & \ddots & & \\ & & & d_j & \\ & & & & \ddots \end{bmatrix}}^{\mathcal{D}} \overbrace{\begin{bmatrix} \dot{\theta}_1 \\ \dot{\theta}_2 \\ \vdots \\ \dot{\theta}_j \\ \vdots \end{bmatrix}}^{\dot{\Theta}}$$

$$\frac{\partial \mathcal{H}}{\partial \Theta} = -i \overbrace{\begin{bmatrix} k_1 \sigma_1 & -k_1 \sigma_1 & & & \\ -k_1 \sigma_1 & k_1 \sigma_1 + k_2 \sigma_2 & -k_2 \sigma_2 & & \\ & & \ddots & & \\ & & & -k_{j-1} \sigma_{j-1} & k_{j-1} \sigma_{j-1} + k_j \sigma_j & -k_j \sigma_j \\ & & & & \ddots & \end{bmatrix}}^{\mathcal{H}} \overbrace{\begin{bmatrix} \theta_1 \\ \theta_2 \\ \vdots \\ \theta_j \\ \vdots \end{bmatrix}}^{\Theta} \tag{A.8}$$

Regarding the left hand side of the Lagrangian equation (Eq. 5.1), the derivatives of the total kinetic and potential energy are shown below:

$$\begin{aligned}
 \frac{d}{dt} \left(\frac{\partial \mathcal{L}}{\partial \dot{\theta}_1} \right) - \frac{\partial \mathcal{L}}{\partial \theta_1} &= J_1 \ddot{\theta}_1 - k_1 (\theta_2 - \theta_1) \\
 &= J_1 \ddot{\theta}_1 + k_1 \theta_1 - k_1 \theta_2
 \end{aligned} \tag{A.9}$$

$$\begin{aligned}
 \frac{d}{dt} \left(\frac{\partial \mathcal{L}}{\partial \dot{\theta}_2} \right) - \frac{\partial \mathcal{L}}{\partial \theta_2} &= J_2 \ddot{\theta}_2 + k_1(\theta_2 - \theta_1) - k_2(\theta_3 - \theta_2) \\
 &= J_2 \ddot{\theta}_2 - k_1 \theta_1 + (k_1 + k_2) \theta_2 - k_2 \theta_3
 \end{aligned} \tag{A.10}$$

$$\vdots$$

$$\begin{aligned}
 \frac{d}{dt} \left(\frac{\partial \mathcal{L}}{\partial \dot{\theta}_j} \right) - \frac{\partial \mathcal{L}}{\partial \theta_j} &= J_j \ddot{\theta}_j + k_{j-1}(\theta_j - \theta_{j-1}) - k_j(\theta_{j+1} - \theta_j) \\
 &= J_j \ddot{\theta}_j - k_{j-1} \theta_{j-1} + (k_{j-1} + k_j) \theta_j - k_j \theta_{j+1}
 \end{aligned} \tag{A.11}$$

The resulting system of equations of the Lagrangian derivatives can be presented compactly in matrix format as shown below:

$$\begin{aligned}
 \frac{d}{dt} \left(\frac{\partial \mathcal{L}}{\partial \dot{\Theta}} \right) - \frac{\partial \mathcal{L}}{\partial \Theta} &= \overbrace{\begin{bmatrix} J_1 & & & & \\ & J_2 & & & \\ & & \ddots & & \\ & & & J_j & \\ & & & & \ddots \end{bmatrix}}^{\mathbf{J}} \overbrace{\begin{bmatrix} \ddot{\theta}_1 \\ \ddot{\theta}_2 \\ \vdots \\ \ddot{\theta}_j \\ \vdots \end{bmatrix}}^{\ddot{\Theta}} \\
 + &\overbrace{\begin{bmatrix} k_1 & -k_1 & & & \\ -k_1 & k_1 + k_2 & -k_2 & & \\ & & \ddots & & \\ & & & -k_{j-1} & k_{j-1} + k_j & -k_j \\ & & & & \ddots & \end{bmatrix}}^{\mathbf{K}} \overbrace{\begin{bmatrix} \theta_1 \\ \theta_2 \\ \vdots \\ \theta_j \\ \vdots \end{bmatrix}}^{\Theta}
 \end{aligned} \tag{A.12}$$

Appendix B

Reference Systems Data & Layout

B.1 W9L46C Reference System

Table B.1: Reference system data of W9L46C engine.

Bore	0.46 m
Crank radius	0.29 m
Con. rod length	1.37 m
Firing order	1-3-5-7-9-8-6-4-2
Compression ratio	14.00
Reciprocating mass	450.00 kg
<hr/>	
Turbocharger	ABB TPL77-A30
<hr/>	
Nominal speed	500 RPM
Idling speed	360 RPM
Maximum power per cylinder	1,050 kW
<hr/>	
Propeller type	LIPS 4C16
Propeller diameter	4.9 m
No. of propeller blades	4
<hr/>	
Main reduction ratio	108/33
PTO reduction ratio	29/105
<hr/>	
Vibration Damper	Geislinger D140/30
Main coupling	Vulkan Rato S 5127
PTO coupling	Vulkan Rato S 2547

Table B.2: Port engine shaft uncalibrated DOF coefficients for W9L46C reference system.

DOF	Inertia (kgm ²)	Stiffness (Nm/rad)	Structural	Absolute — Relative
			Damping (-)	Viscous Damping (Nms/rad)
Damper 1	651.0	3.100×10^7	0	0 — 68200
Damper 2	48.7	4.240×10^8	4.500×10^{-3}	0 — 0
Cylinder 9	376.1	3.210×10^8	4.500×10^{-3}	26 — 0
Cylinder 8	362.2	3.210×10^8	4.500×10^{-3}	26 — 0
Cylinder 7	376.1	3.210×10^8	4.500×10^{-3}	26 — 0
Cylinder 6	376.1	3.210×10^8	4.500×10^{-3}	26 — 0
Cylinder 5	376.1	3.210×10^8	4.500×10^{-3}	26 — 0
Cylinder 4	376.1	3.210×10^8	4.500×10^{-3}	26 — 0
Cylinder 3	376.1	3.210×10^8	4.500×10^{-3}	26 — 0
Cylinder 2	362.2	3.210×10^8	4.500×10^{-3}	26 — 0
Cylinder 1	376.1	3.720×10^8	0	26 — 0
Cam. Drive	139.5	4.700×10^8	0	0 — 0
Flywheel	2,341.5	1.600×10^6	8.400×10^{-3}	0 — 0
Coupling 1	222.0	1.600×10^6	8.400×10^{-3}	0 — 0
Coupling 2	391.7	2.480×10^6	0	0 — 0
Flange	29.5	1.269×10^7	0	0 — 0
Clutch	84.0	2.058×10^8	0	0 — 0
Pinion Gear	93.1	0	0	0 — 0

Table B.3: Starboard engine, propeller and generator shaft uncalibrated DOF coefficients for W9L46C reference system.

	DOF	Inertia (kgm ²)	Stiffness (Nm/rad)	Structural Damping (-)	Abs. — Rel. Viscous Damping (Nms/rad)
Starboard Engine	Damper 1	651.0	3.100×10^7	0	0 — 68200
	Damper 2	48.7	4.240×10^8	4.500×10^{-3}	0 — 0
	Cylinder 9	376.1	3.210×10^8	4.500×10^{-3}	26 — 0
	Cylinder 8	362.2	3.210×10^8	4.500×10^{-3}	26 — 0
	Cylinder 7	376.1	3.210×10^8	4.500×10^{-3}	26 — 0
	Cylinder 6	376.1	3.210×10^8	4.500×10^{-3}	26 — 0
	Cylinder 5	376.1	3.210×10^8	4.500×10^{-3}	26 — 0
	Cylinder 4	376.1	3.210×10^8	4.500×10^{-3}	26 — 0
	Cylinder 3	376.1	3.210×10^8	4.500×10^{-3}	26 — 0
	Cylinder 2	362.2	3.210×10^8	4.500×10^{-3}	26 — 0
	Cylinder 1	376.1	3.720×10^8	0	26 — 0
	Cam. Drive	139.5	4.700×10^8	0	0 — 0
	Flywheel	2,341.5	1.600×10^6	8.400×10^{-3}	0 — 0
	Coupling 1	222.0	1.600×10^6	8.400×10^{-3}	0 — 0
	Coupling 2	322.3	4.386×10^7	0	0 — 0
	Pinon Gear	180.7	1.456×10^7	0	0 — 0
	Clutch	82.3	2.058×10^8	0	0 — 0
Pinion Gear	72.8	0	0	0 — 0	
Propeller	Main Gear	3,955.2	4.219×10^8	0	0 — 0
	Flange	488.0	2.719×10^7	0	0 — 0
	Int. Shaft	474.0	8.186×10^7	0	0 — 0
	Sleeve Coup.	1,032	2.881×10^7	0	0 — 0
	Propeller	33,112	0	0	0* — 0
Gen'tor	Pinion Gear	3.8	$3.2270e+06$	0	0 — 0
	Gen. Coupling	19.5	$4.000E+04$	0.175	0 — 0
	Flange	10.2	$1.507E+07$	0	0 — 0
	Gen. Rotor	254.5	0	0	0 — 0

*Propeller damping calculated using Archer's method [116]

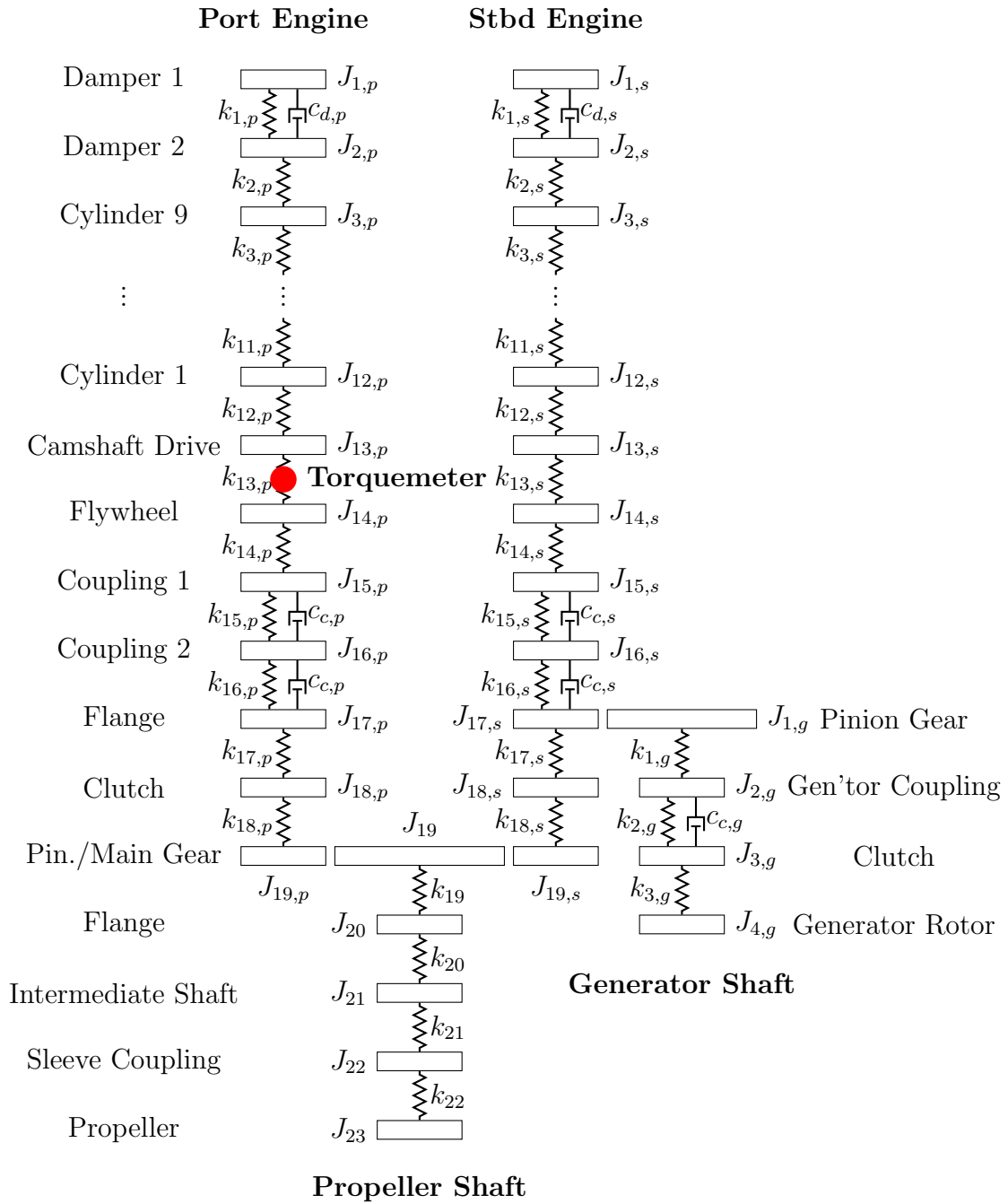


Figure B.1: Lumped mass model layout of W9L46C reference system.

B.2 1067LGBE Reference System

Table B.4: Reference system data of 10L67GBE engine [92].

Bore	0.67 m
Crank radius	0.85 m
Con. rod length	2.538 m
Firing order	1-9-4-6-3-10-2-7-5-8
Reciprocating mass	4,550.00 kg
Nominal speed	125 RPM
Maximum power per cylinder	1,648 kW

Table B.5: Calibrated DOF coefficients for 10L67GBE reference system [94].

DOF	Inertia (kgm ²)	Stiffness (Nm/rad)	Abs.* — Rel.
			Viscous Damping (Nms/rad)
Damper Casing	8.540×10^3	1.000×10^4	0 — 5.705×10^5
Damper Inertia	4.480×10^3	1.000×10^{12}	0 — 0
Flange	4.420×10^2	1.342×10^9	0 — 0
Cylinder 1	6.520×10^3	1.202×10^9	2.287×10^4 — 50
Cylinder 2	6.890×10^3	1.202×10^9	2.287×10^4 — 50
Cylinder 3	6.520×10^3	1.196×10^9	2.287×10^4 — 50
Cylinder 4	6.615×10^3	1.206×10^9	2.287×10^4 — 50
Cylinder 5	6.890×10^3	1.302×10^9	2.287×10^4 — 50
Chain Drive	3.807×10^3	1.410×10^9	2.287×10^4 — 50
Cylinder 6	6.890×10^3	1.212×10^9	2.287×10^4 — 50
Cylinder 7	6.890×10^3	1.202×10^9	2.287×10^4 — 50
Cylinder 8	6.520×10^3	1.202×10^9	2.287×10^4 — 50
Cylinder 9	6.895×10^3	1.202×10^9	2.287×10^4 — 50
Cylinder 10	6.520×10^3	8.150×10^8	2.287×10^4 — 0
Output Shaft	3.058×10^3	6.928×10^8	3.290×10^5 — 0
Generator Rotor	8.536×10^5	5.940×10^6	2.691×10^4 — 0

*Absolute damping values provided for harmonic balancing numerical scheme, see Eq. 5.28

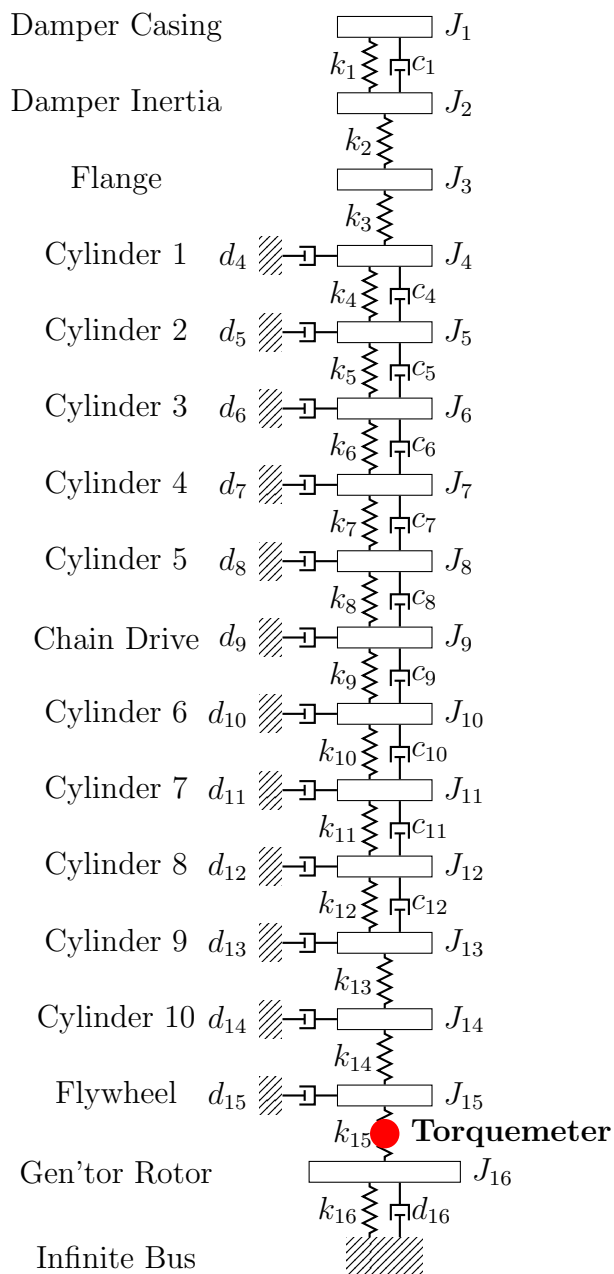


Figure B.2: Lumped mass model layout of 10L67GBE reference system.

Appendix C

Measuring Equipment

C.1 In-cylinder Pressure Sensor & Analyser

The in-cylinder pressure sensor utilised for the measurements of the W9L46C reference system is a Kistler 6619AP35 with a 6513AK Thompson adapter shown in Figure C.1, which acts as a heat sink. The sensor is developed specifically for low and medium speed engines and has very low thermal sensitivity and maintain linearity. The primary technical features of the in-cylinder pressure sensor are listed in Table C.1, and more information can be accessed from the relevant data sheet [183].

Table C.1: Specifications of Kistler 6619AP35 pressure sensor.

Range (bar)	0 ··· 350
Overload (bar)	450
Operating temperature range (°C)	
Continuous	−40 ··· 350
Short time (< 20 mins)	−40 ··· 400
Sensitivity 200 ··· ± 150°C	±0.7%
Tightening torque (Nm)	15



Figure C.1: Kistler 6619AP35 in-cylinder pressure sensor with a 6513AK Thompson adapter [183].

The in-cylinder pressure analyser utilised was the Doctor Diesel DK-20, which employs the in-cylinder sensor and a proximity sensor at the flywheel as input, to plot the in-cylinder pressure curves versus the crank angle. Furthermore, it employs the boost/scavenge air pressure as input inserted by the user at the time of the measurement, which is used to peg the minimum value of the measured in-cylinder pressure curves. The in-cylinder pressure data is time-stamped and exported in .csv files. The specifications overview of the DK-20 analyser is listed on Table C.2, with greater details available on the specification brochure [184].

Table C.2: Specifications of Doctor Diesel DK-20 in-cylinder pressure analyser [184].

Engine speed range (RPM)	20 ··· 3,000
Resolution	0.1°CA up to 1,820 RPM 0.2°CA from 1,820 – 3,000 RPM
Max. sampling rate (kHz)	102.4
Measurement storage	500 full engine sets

C.2 Prototype High-Sample Rate Torquemeter

The prototype high-sample rate torquemeter was installed in the W9L46C reference system and its simplified schematic is shown in Figure C.2. The control unit was provided with power from the ship's low voltage local 220V switchboard, which in turn provided power to the stator mounted on the engine block. The stator transmitted the power through the small air gap to the belt which via wired connection powered the strain gauges located under the transmitter housing and epoxy-glued on the engine shaft. The transmitter wirelessly transmitted the strain gauge data to the control panel, which displayed and saved the data on a removable hard drive. The on-shaft installation of the torquemeter and the control panel are shown in Figure C.3.

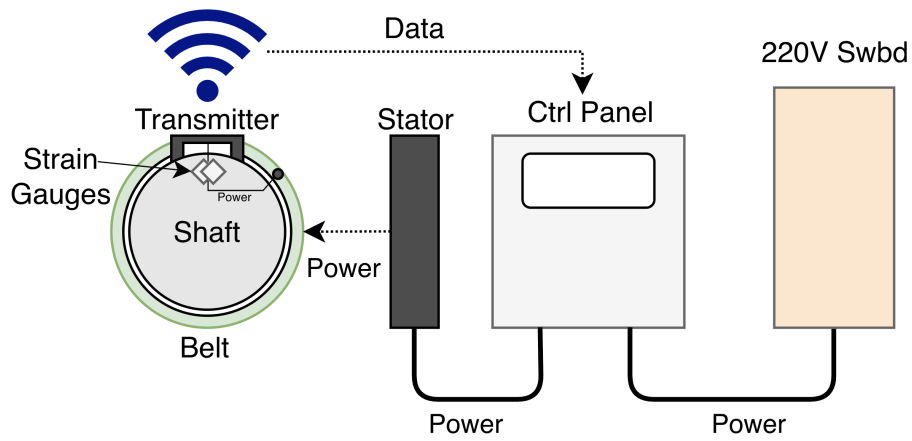
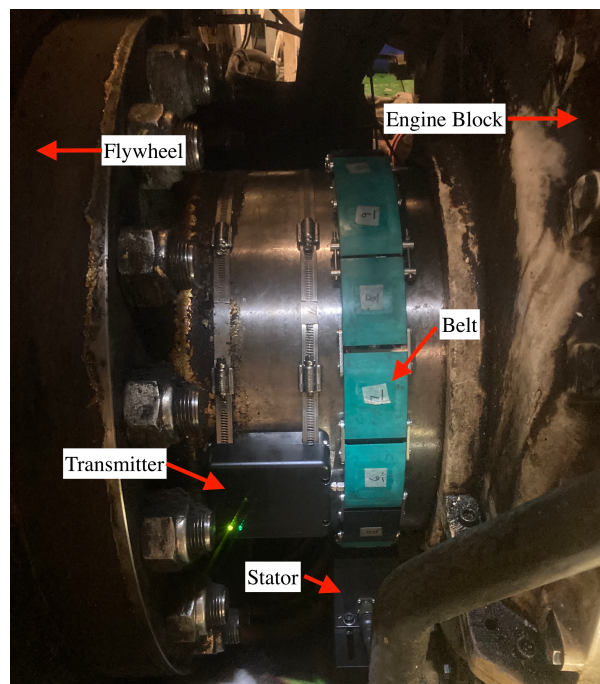
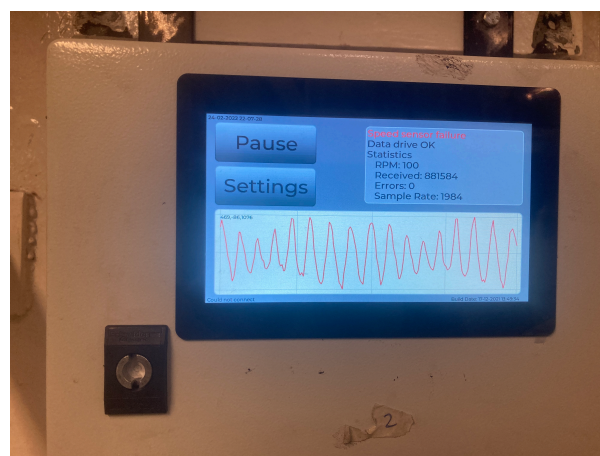


Figure C.2: Schematic of prototype high-sample rate torquemeter.



(a) On-shaft torquemeter installation.



(b) Torquemeter control panel.

Figure C.3: Prototype high-sample rate torquemeter installation for W9L46C referene system.

Appendix D

Experimental Measurements Rectification & Processing

D.1 In-Cylinder Pressure Rectification

The measured in-cylinder pressure curves are corrected by adjusting their offset both in the x and y-axis. The first step in the correction process is to model the compression curve by utilising the healthy conditions digital twin and setting the fuel injected per cycle to zero. The second step is to extract the part of the measured in-cylinder pressure curve representing the compression process, the end of which is located at the start of combustion, denoted by the first local minimum, as shown in Figure D.1.

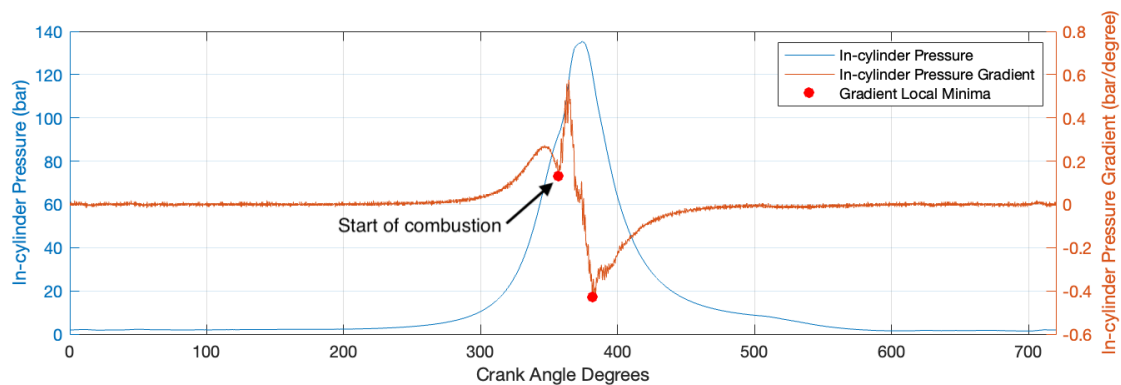


Figure D.1: Start of combustion identification in measured in-cylinder pressure diagram.

The third step includes the correction of the in-cylinder pressure measurement by comparing the simulated with the measured in-cylinder pressure compression curves

extracted above, by employing a Levenberg-Marquardt optimisation algorithm to perform a least squares curve fitting with the below objective function:

$$O = \min_{x,y} \left\{ \frac{1}{2} \|\mathbf{p}_{\text{data}}(\theta - \mathbf{x}) - y - \mathbf{p}_{\text{sim}}\|_2^2 \right\} \quad (\text{D.1})$$

where $\|\cdot\|_2$ denotes the Euclidean norm, \mathbf{p}_{data} , \mathbf{p}_{sim} indicate the vectors containing the compression part of the measured and simulated in-cylinder pressure curves respectively, and x , y indicate the x and y -axis offset calibration factors respectively.

The results of the in-cylinder pressure calibration for both measured operating points are presented in Table D.1, and the corrected in-cylinder pressure measurements are shown in Figure D.2.

Table D.1: In-cylinder pressure measurement correction for W9L46C engine.

Cylinder	Measured Operating Point			
	2,949 kW @ 401 RPM		5,491 kW @ 450 RPM	
	X-axis Offset (°CA)	Y-axis Offset (bar)	X-axis Offset (°CA)	Y-axis Offset (bar)
1	-3.2	-0.150	-1.9	-0.527
2	-5.0	-0.345	-4.3	-0.585
3	-2.8	-0.240	-2.0	-0.593
4	-3.5	-0.108	-3.1	-0.464
5	-2.9	-0.408	-4.2	-0.515
6	-4.1	-0.192	-3.5	-0.607
7	-3.5	-0.274	-3.5	-0.559
8	-2.8	-0.117	-3.9	-0.489
9	-3.8	-0.082	-2.6	-0.525

The x -axis offset is observed to be negative presumably because of an error in placement of the reflective tape marking the cylinder TDC. However, in this case the offset would remain constant for all cylinders, therefore the crankshaft torsion and flexibility during the measurements could contribute to said offset which is an phenomenon that has been observed for large internal combustion engines [185].

The y -axis offset is observed to be negative for all cylinders in both operating points. The reason stems from the fact that the in-cylinder pressure analyser sets the minimum of the measured in-cylinder pressure curve to be equal to the inlet air pressure. For non-scientific purposes involving comparisons between in-cylinder pressure curves of different cylinders this method would suffice, however engine

theory dictates that the minimum of the in-cylinder pressure diagram should be less in pressure than the inlet air pressure [146]. Therefore, the in-cylinder pressures correction identifies this error and accounts for it accordingly by returning negative y-axis offsets.

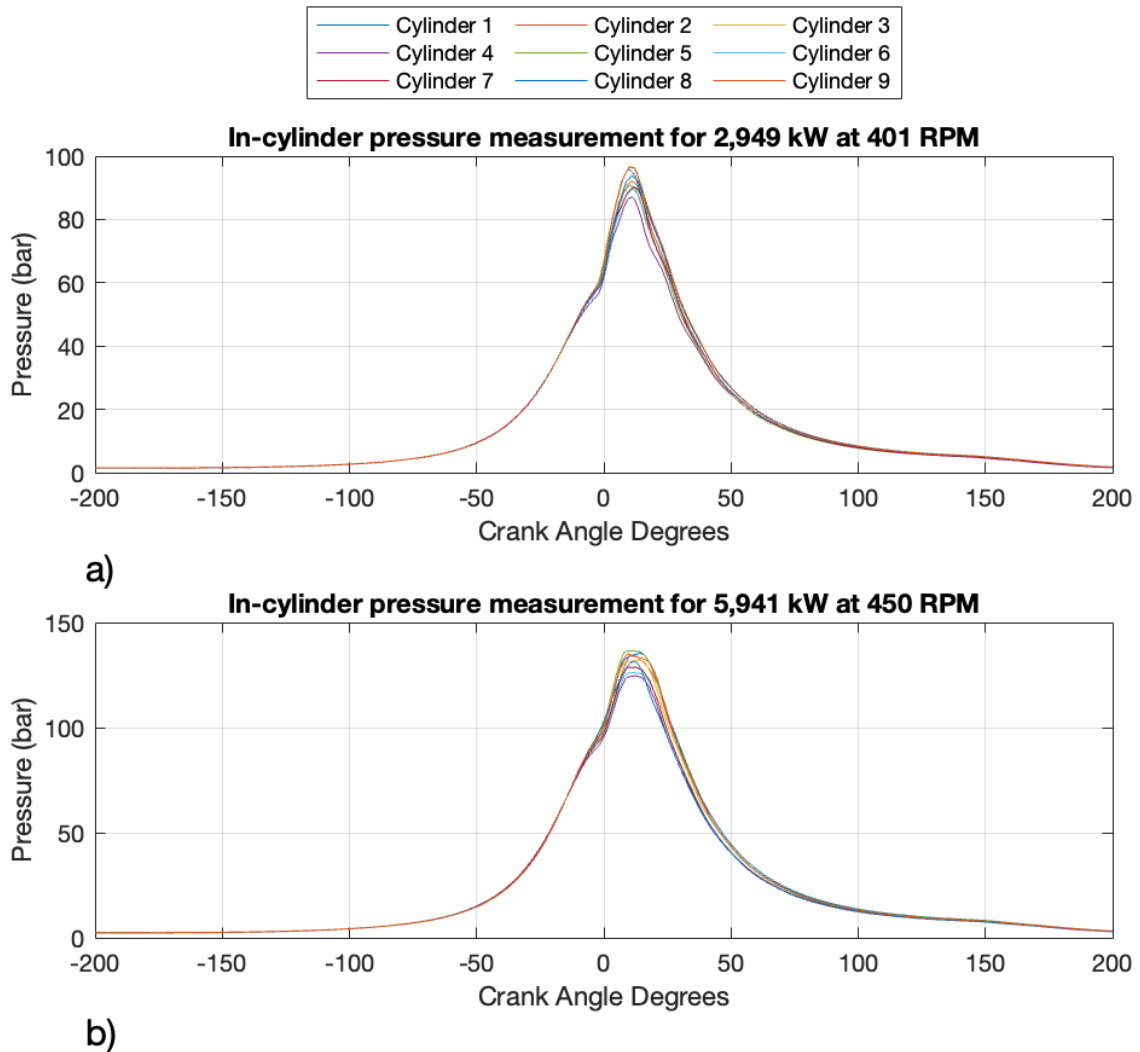


Figure D.2: Corrected in-cylinder pressure measurements for W9L46C engine for a) 2,949 kW @ 401 RPM obtained on 23-Apr-2021, and b) 5,491 kW @ 450 RPM, obtained on 24-Mar-2022.

D.2 Heat Release Curves

Table D.2: Heat release analysis results for operating point of 5,491 kW at 450 RPM for W9L46C reference system.

Cyl.	DOC	SOC	Wiebe Exp.	Fuel Injected		Indicated Power	
	(°CA)	(°CA)	(-)	(kg/cycle)	(%)	(kW)	(%)
1	58.8	9.3	0.817	7.663×10^{-3}	11.2	675.4	11.2
2	51.7	8.8	1.014	7.787×10^{-3}	11.4	693.9	11.5
3	63.4	9.0	0.713	7.834×10^{-3}	11.5	694.7	11.5
4	65.6	8.9	0.730	7.079×10^{-3}	10.4	615.6	10.2
5	59.6	9.4	0.733	7.987×10^{-3}	11.7	713.0	11.8
6	61.6	9.1	0.802	7.243×10^{-3}	10.6	639.7	10.6
7	60.1	8.7	0.779	7.071×10^{-3}	10.4	634.3	10.5
8	78.7	8.6	0.479	7.791×10^{-3}	11.4	683.5	11.3
9	54.5	9.2	0.888	7.843×10^{-3}	11.5	705.2	11.6
Total:				6.830×10^{-2}	100.0	6,055.3	100.0

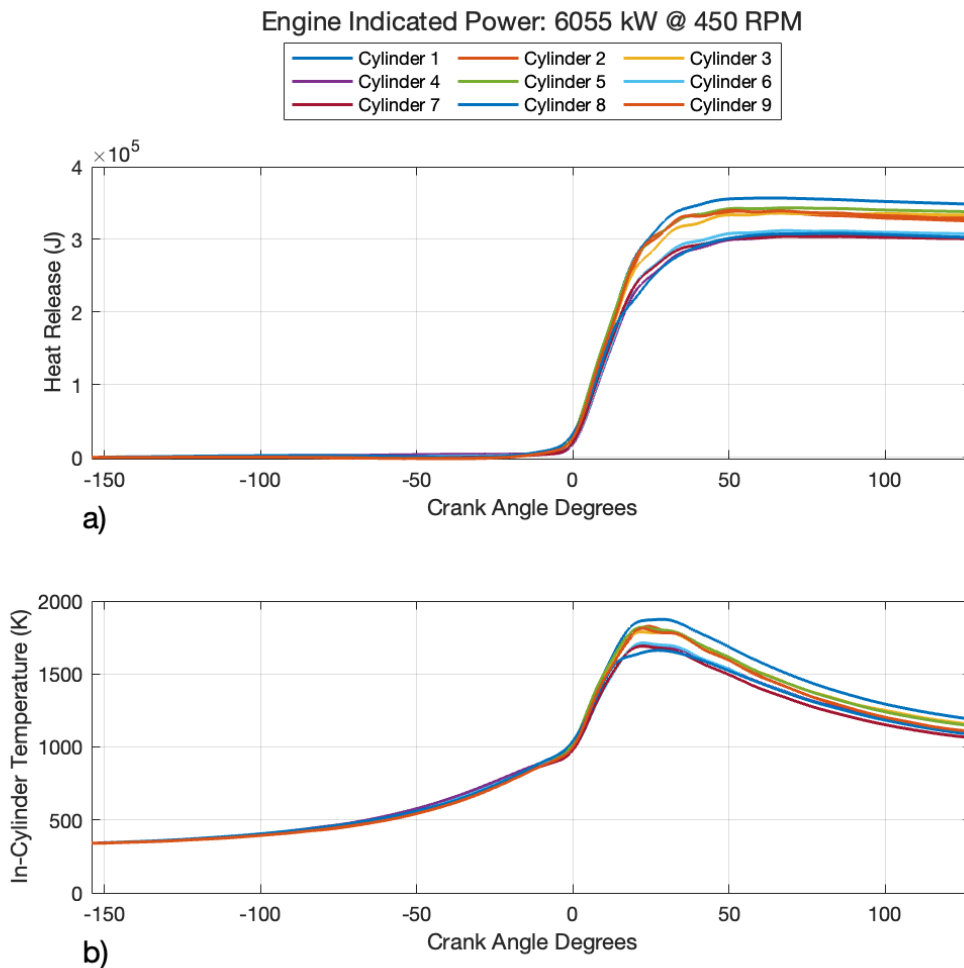


Figure D.3: Heat release analysis curves for W9L46C engine at operating point 5,491 kW @ 450 RPM.

Table D.3: Heat release analysis results for operating point of 2,949 kW at 401 RPM for W9L46C reference system.

Cyl.	DOC	SOC	Wiebe Exp.	Fuel Injected		Indicated Power	
	(°CA)	(°CA)	(-)	(kg/cycle)	(%)	(kW)	(%)
1	58.7	7.2	0.597	5.204×10^{-3}	11.5	409.4	11.5
2	56.3	6.9	0.669	4.766×10^{-3}	10.5	377.1	10.6
3	54.1	7.1	0.716	5.092×10^{-3}	11.2	405.3	11.4
4	72.6	7.4	0.499	4.854×10^{-3}	10.7	369.8	10.4
5	59.7	7.3	0.582	4.809×10^{-3}	10.6	380.5	10.7
6	56.6	7.0	0.719	5.119×10^{-3}	11.3	400.5	11.3
7	61.0	7.5	0.619	5.061×10^{-3}	11.2	397.2	11.2
8	56.2	7.2	0.723	5.326×10^{-3}	11.8	417.5	11.7
9	58.1	7.1	0.572	5.075×10^{-3}	11.2	401.9	11.3
Total:				4.530×10^{-2}	100.0	3,559.2	100.0

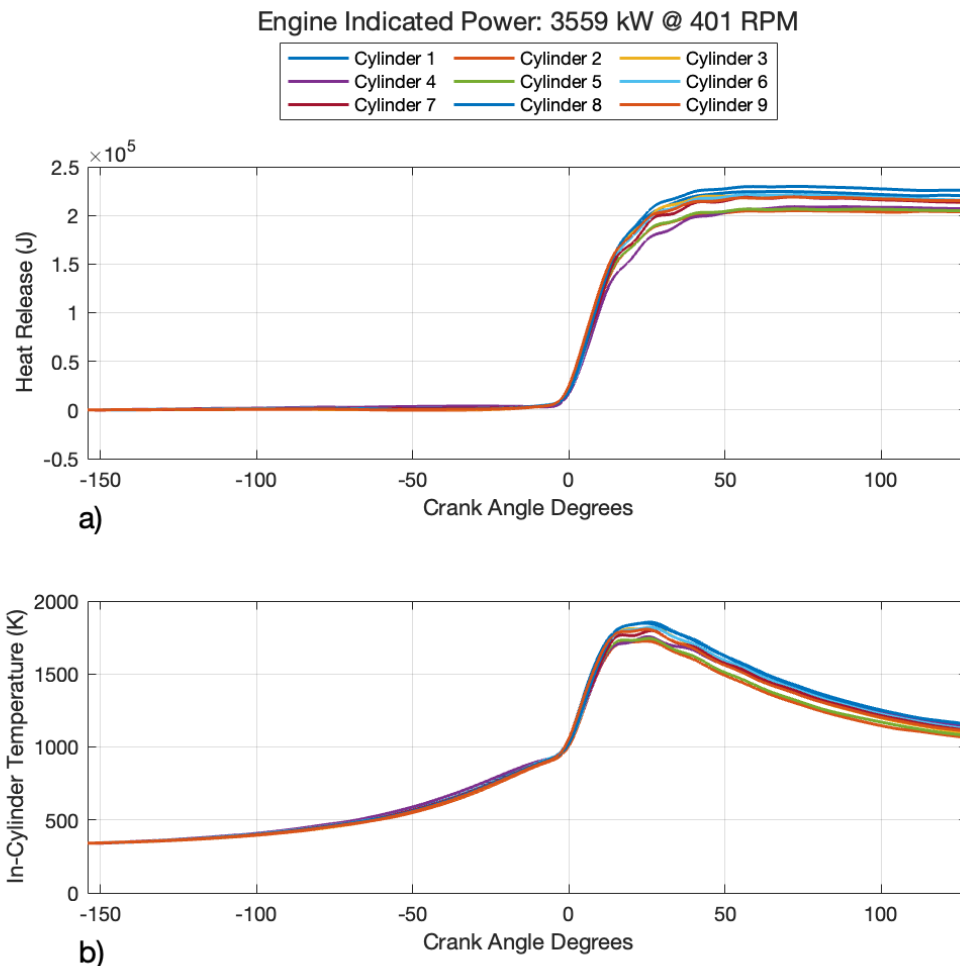


Figure D.4: Heat release analysis curves for W9L46C engine at operating point 2,949 kW @ 401 RPM.

D.3 Instantaneous Crankshaft Torque

The signal obtained from the torquemeter is in mV/V (milliVolts per Volt), hence it needs to be converted to Nm (Newton-meters), according to the below equation:

$$\tilde{T} = \pi \frac{Gr^3N_g}{2G_f n} \quad (\text{D.2})$$

where

- G is the shaft shear modulus, equal to 80×10^9 Pa
- G_f is the gauge factor for metal-foil strain gauge equal to 2.02.
- r is the shaft radius equal to 0.225 m.
- N_g takes the value of 2 for a full-bridge strain gauge with two active arms.
- n is the V/V in ADC count equal to 2^{23} for a 24-bit system where the 24th bit is reserved for the positive or negative sign.

The measured raw versus the smoothed ICT data are shown below for a Gaussian-weighted moving average with 20 samples averaging window.

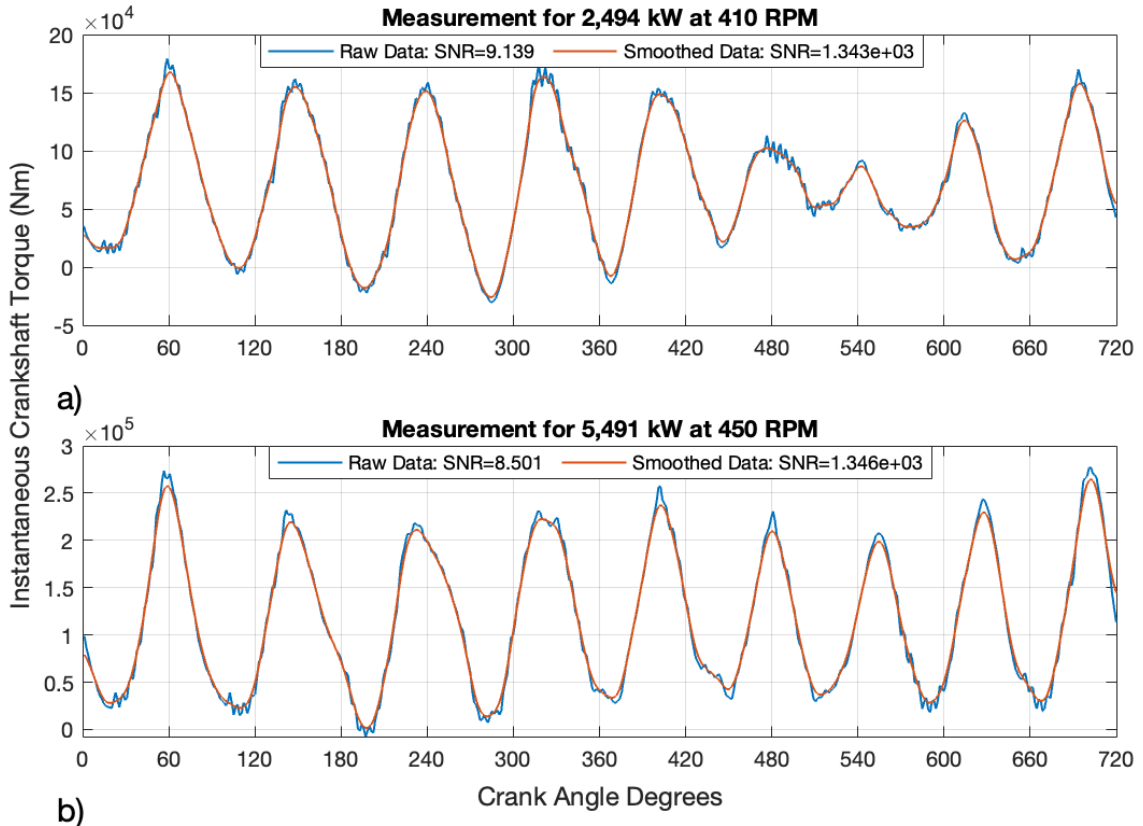


Figure D.5: Measured ICT SNR for raw and smoothed data using Gaussian-weighted moving average with 20 samples window.

Appendix E

Optimisation Algorithms Results & Performance

E.1 Healthy Conditions Digital Twin Calibration

Table E.1: Step 1 of thermodynamics model calibration using particle swarm optimisation algorithm; Wiebe function and FMEP constants.

Reference System	Run	Objective Value at Minimum	Run Time (s)	Calibration Results [$\theta_{\text{DOC}}, w, \text{fmep}_0$]
W9L46C	1	5.102×10^{-5}	119.1	[91.5, 0.306, 2.029]
	2	1.367×10^{-5}	134.6	[89.4, 0.350, 2.500]
	3	2.492×10^{-5}	122.2	[90.6, 0.312, 2.303]
	Results Average:			[90.5, 0.323, 2.277]
6RTflex50	1	5.080×10^{-5}	202.6	[34.0, 1.290, 1.047]
	2	6.694×10^{-5}	218.4	[35.1, 1.293, 0.999]
	3	9.135×10^{-5}	192.3	[36.0, 1.225, 1.050]
	Results Average:			[34.5, 1.257, 1.023]

Table E.2: Step 2 of thermodynamics model calibration using particle swarm optimisation algorithm; Woschni-Anisits model constants.

Reference System	Run	Objective Value at Minimum	Run Time (s)	Calibration Results $[g_1, g_2, g_3, \Delta w] \times 10^{-2}$
W9L46C	1	8.082×10^{-4}	821.8	[76.2, 8.2, 36.0, 13.9]
	2	1.033×10^{-3}	850.4	[72.5, 7.2, 39.1, 14.8]
	3	7.194×10^{-4}	789.2	[68.1, 7.9, 45.9, 13.9]
	Results Average:			[72.3, 7.8, 40.3, 14.2]
6RTflex50	1	5.080×10^{-5}	940.1	[48.2, 36.5, 29.4, 0.8]
	2	6.694×10^{-5}	861.9	[43.3, 46.3, 30.5, 1.3]
	3	9.135×10^{-5}	907.4	[44.9, 42.8, 24.2, 1.2]
	Results Average:			[45.5, 42.0, 28.0, 1.1]

E.2 Direct Crankshaft Dynamics Model Calibration

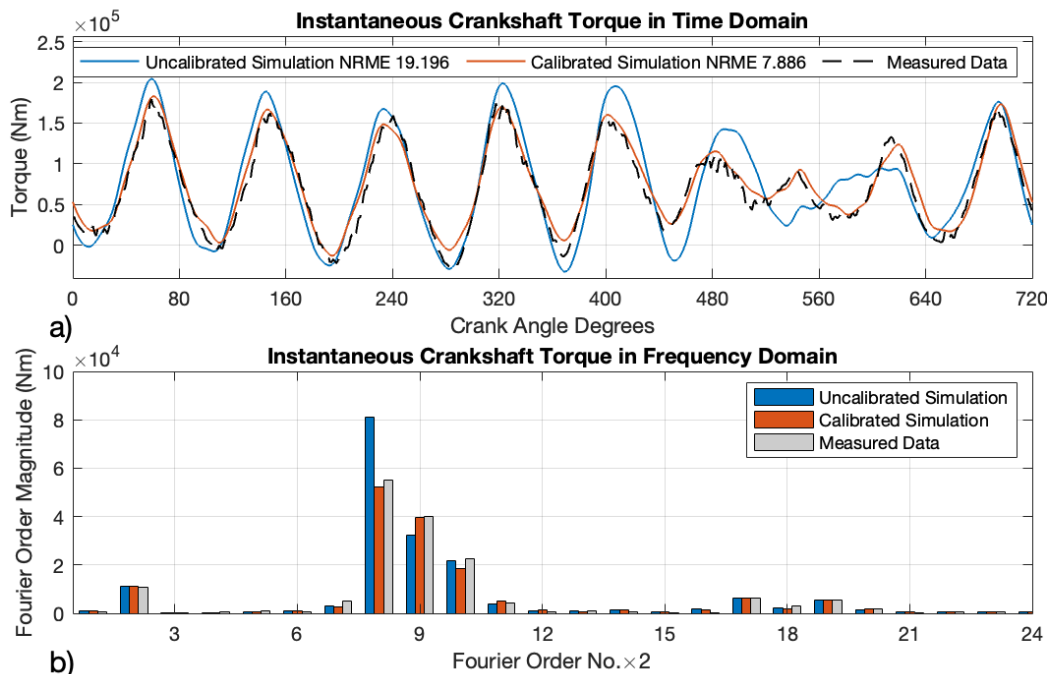


Figure E.1: Direct crankshaft dynamics model calibration of W9L46C reference system for 2,949 kW at 401 RPM, with ICT shown in **a)** the time domain and **b)** frequency domain.

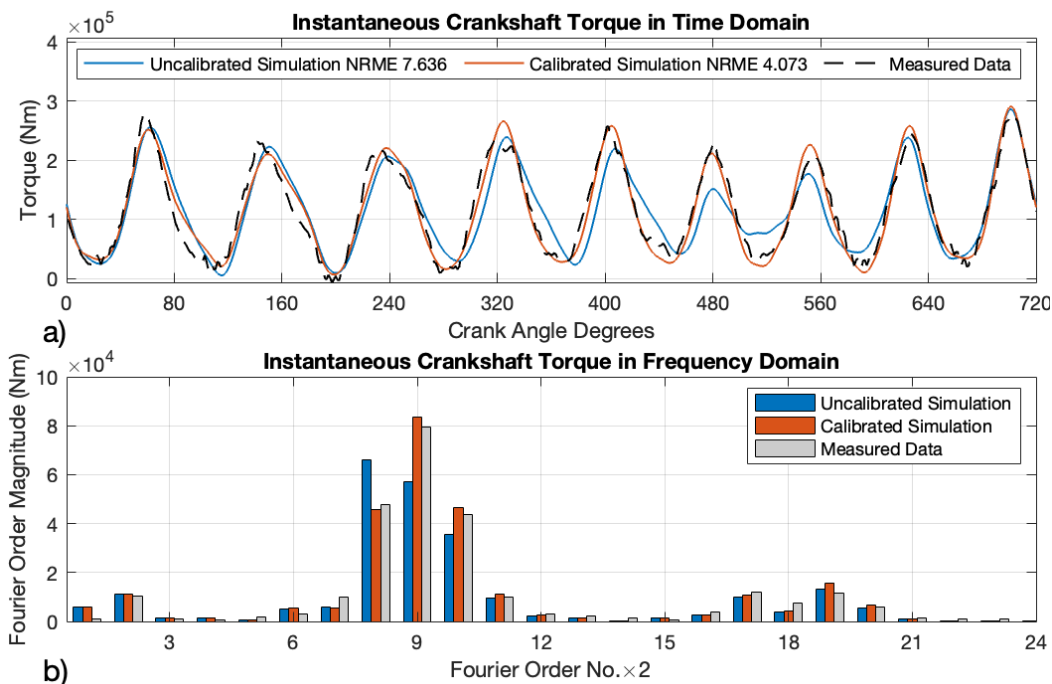


Figure E.2: Direct crankshaft dynamics model calibration of W9L46C reference system for 5,491 kW at 450 RPM, with ICT shown in **a)** the time domain and **b)** frequency domain.

Table E.3: Direct crankshaft dynamics model calibration algorithm performance for W9L46C reference system, for 2,949 kW at 401 RPM.

Iter.	Evals	Objective	Line-Search Step Length	Directional Derivative	1 st -Order Optimality
0	3	7.043×10^{-1}	0.000	0.000	0.000
1	7	5.917×10^{-1}	0.500	-2.780×10^0	4.090×10^0
2	10	2.659×10^{-1}	1.000	-1.590×10^0	1.210×10^0
3	15	2.641×10^{-1}	0.250	-1.050×10^0	1.270×10^0
4	18	2.371×10^{-1}	1.000	-1.080×10^0	9.600×10^{-2}
5	22	2.371×10^{-1}	0.500	-3.990×10^{-2}	2.610×10^{-2}
6	25	2.370×10^{-1}	1.000	-3.130×10^{-2}	2.590×10^{-2}
7	28	2.370×10^{-1}	1.000	-1.970×10^{-2}	7.440×10^{-4}

Execution Time: 20.586 s.

Table E.4: Direct crankshaft dynamics model calibration algorithm performance for W9L46C reference system, for 5,491 kW at 450 RPM

Iter.	Evals	Objective	Line-Search Step Length	Directional Derivative	1 st -Order Optimality
0	3	6.303×10^{-1}	0.000	0.000	0.000
1	7	5.765×10^{-1}	0.500	-1.260×10^0	2.700×10^0
2	10	4.137×10^{-1}	1.000	-2.100×10^0	1.180×10^0
3	13	3.479×10^{-1}	1.000	-1.110×10^0	1.230×10^{-1}
4	17	3.475×10^{-1}	0.500	-6.630×10^{-2}	3.490×10^{-2}
5	20	3.475×10^{-1}	1.000	-3.870×10^{-2}	5.860×10^{-2}
6	23	3.474×10^{-1}	1.000	-4.920×10^{-2}	4.470×10^{-3}
7	26	3.474×10^{-1}	1.000	-3.600×10^{-3}	2.670×10^{-4}

Execution Time: 19.123 s.

E.3 Inverse Crankshaft Dynamics Model

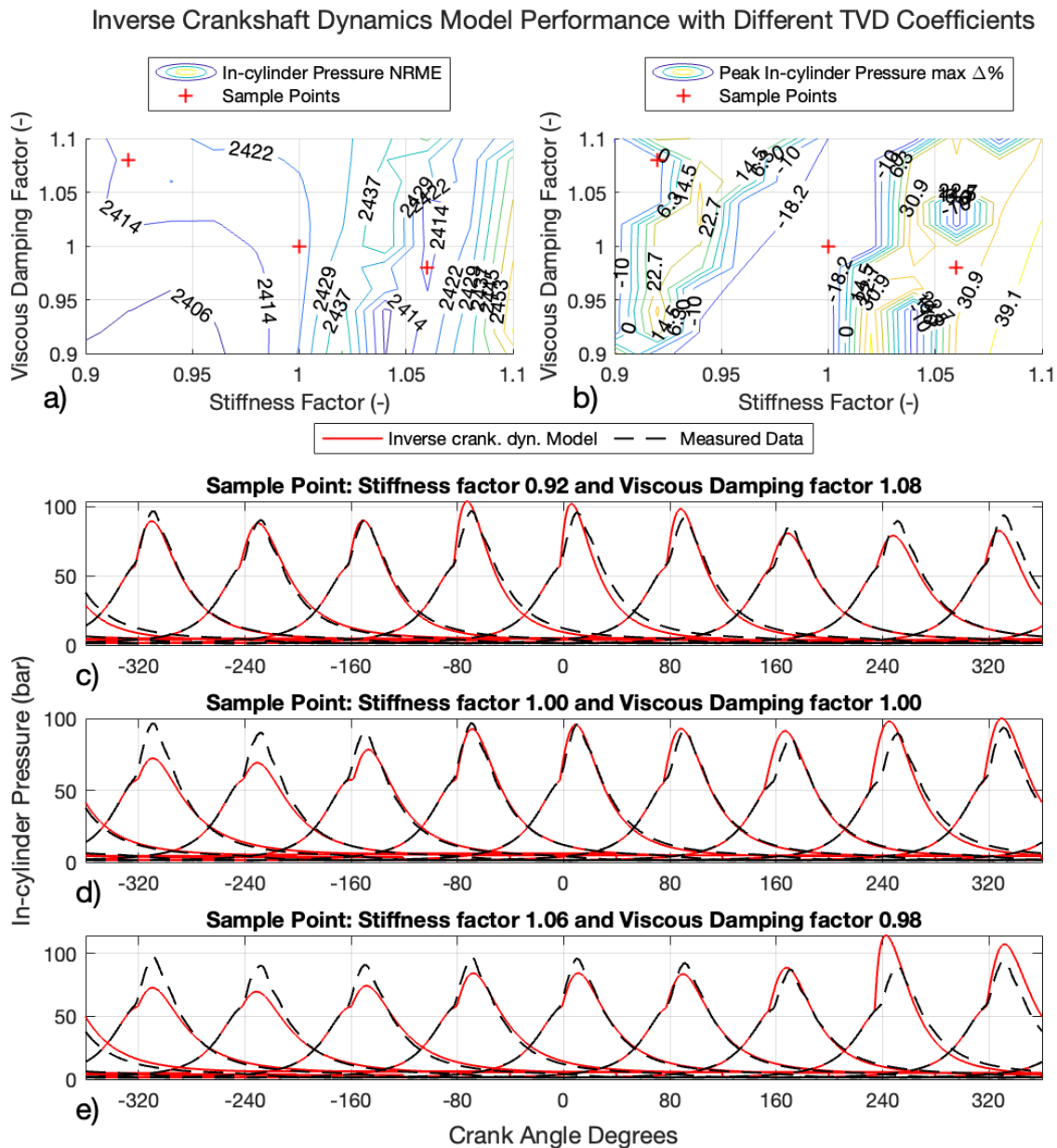


Figure E.3: Inverse crankshaft dynamics model performance using measured ICT, with parametric runs for different TVD coefficients demonstrating the **a)** in-cylinder pressure NRME, **b)** peak in-cylinder pressure maximum percentage difference, and **c)–e)** in-cylinder pressure curves at selected points for 2,949 kW at 401 RPM.

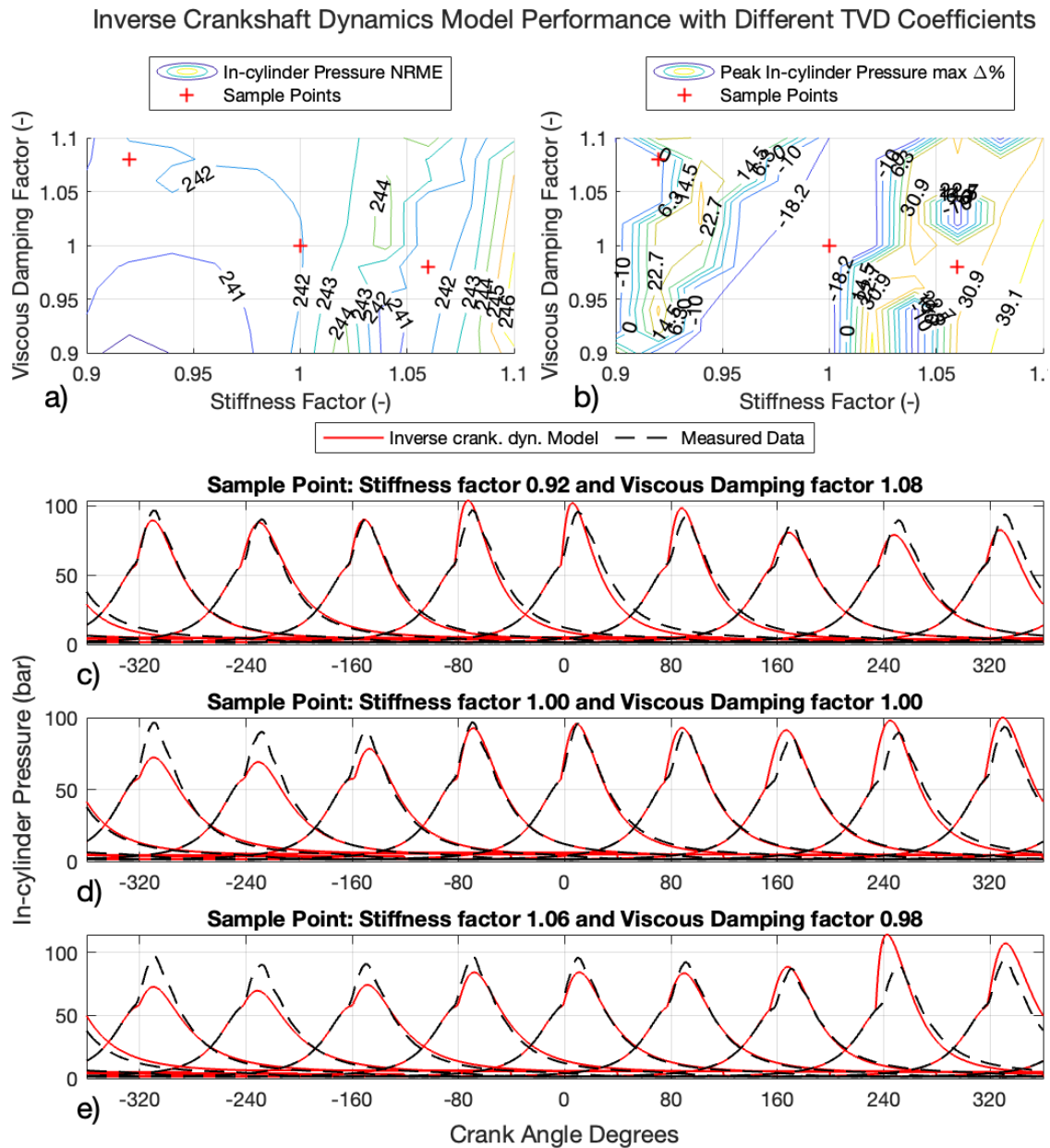


Figure E.4: Inverse crankshaft dynamics model performance using measured ICT, with parametric runs for different TVD coefficients demonstrating the **a)** in-cylinder pressure NRME, **b)** peak in-cylinder pressure maximum percentage difference, and **c)–e)** in-cylinder pressure curves at selected points for 5,491 kW at 450 RPM.